P-doped semiconducting polymers : process optimization, characterization and investigation of air stability

Tamara Nunes Domschke

▶ **To cite this version:**

Tamara Nunes Domschke. P-doped semiconducting polymers : process optimization, characterization and investigation of air stability. Electronics. Université de Lyon, 2020. English. NNT : 2020LYSES020 . tel-03207268

HAL Id: tel-03207268
https://theses.hal.science/tel-03207268

Submitted on 24 Apr 2021

HAL is a multi-disciplinary open access archive for the deposit and dissemination of scientific research documents, whether they are published or not. The documents may come from teaching and research institutions in France or abroad, or from public or private research centers.

L'archive ouverte pluridisciplinaire **HAL**, est destinée au dépôt et à la diffusion de documents scientifiques de niveau recherche, publiés ou non, émanant des établissements d'enseignement et de recherche français ou étrangers, des laboratoires publics ou privés.

N°d'ordre NNT : 2020LYSES020

THESE de DOCTORAT DE L'UNIVERSITE DE LYON
opérée au sein du
Laboratoire Hubert Curien

École Doctorale N° 488
(SCIENCES, INGÉNIERIE, SANTÉ)

Spécialité de doctorat : Microélectronique
Discipline : Sciences et technologies de l'information et de la communication

Soutenue publiquement le 23/10/2020, par :
Tamara Nunes Domschke

P-doped semiconducting polymers: process optimization, characterization, and investigation of air stability.

Devant le jury composé de :

Bonnassieux, Yvan Professeur École polytechnique		Président
Müller, Christian Professeur Chalmers University		Rapporteur
Vignau, Laurence Professeur Bordeaux INP		Rapporteure
Biniek, Laure Chargée de Recherche CNRS		Examinatrice
Clerc, Raphäel Professeur Université Jean Monnet de Saint-Etienne		Directeur de thèse
Pereira, Alexandre Ingénieur de Recherche CEA Grenoble		Encadrant de thèse
Demadrille, Renaud Ingénieur de Recherche CEA Grenoble		invité

ACKNOWLEDGEMENTS

During this experience, I meet several exceptional scientists that made me realize how exciting the work of a researcher can be. This work was possible thanks to the help of colleagues, friends and family members, which I would like to thank in the following lines.

First, I would like to sincerely thank Yvan Bonnassieux, Christian Müller, Laurence Vignau, Laure Biniek and Renaud Demadrille for taking time to evaluate my work. I feel very honored. It was a great pleasure to present and discuss the results of my PhD thesis with you during my defense.

Je souhaiterai particulièrement remercier Alexandre Pereira et Raphael Clerc pour cette opportunité et pour m'avoir guidée pendant ces 3 ans (et quelques mois...). Je tiens aussi à vous remercier pour votre confiance et votre patience avec ma façon un peu particulière de finir les choses au dernier moment. C'était très formateur comme expérience, même si pas toujours facile, et je le dois à vous deux. Merci beaucoup!

Je tiens aussi à remercier tous mes collègues du LCO et du LCH pour votre accueil et pour les moments partagés autour d'un café, d'un repas, lors d'une réunion ou au laboratoire. Merci à Christelle Laugier pour m'avoir formée et aidée avec les manips en boite à gants. Merci à Simon Charlot pour toutes les formations et pour ton aide en salle blanche. Merci Julien Routin pour ton aide et ta compagnie dans la salle PALMIRE. Merci à Stéphanie Jacob pour m'avoir aidée avec des simulations sur Silvaco/TCAD. Merci Sébastien Noel pour ton aide dans l'installation des bancs de vieillissement. Merci à Olivier Aon pour m'avoir formée et aidée avec le profilomètre. Merci Laurent Tournon pour ton aide dans la fabrication des masques de photolithographie. Merci à Géraldine Lorin pour m'avoir formée et aidée avec le spectro UV-Vis-NIR. Merci Amélie Revaux pour ton support et pour les discussions. Merci à Fabrice Emieux pour les images MEB de mes échantillons. Merci Nicolas Dunoyer pour tes connaissances en programmation. Merci à Jamal Tallal, pour les conseils, pour l'écoute, et pour m'avoir aidée à nettoyer la tournette de la boite à gants (!). Un grand merci aux thésards, stagiaires, alternants et postdocs que j'ai pu rencontrer pendant ces 3 ans et qui ont rendu cette expérience encore plus mémorable : Julie Euvrard, Clara Haddad, Pierre Lheritier, Alex Gaïtis, Smail Amari, Agathe Brodu, Marie Fontana, Yoann Dini, Amélie Schultheiss, Claudette Mansour, Sophie Delprat, Florent Marlec, Bastien Guy, Erwan Troussel. Je garde des très bons souvenirs avec vous tous!

Anne Pouchot, merci pour ton aide dans l'organisation des rendezvous, des réunions, des conférences et de ma soutenance. Je ne sais pas comment je l'aurais fait sans toi.

Alexandre Carella, merci pour les discussions, pour l'écoute, pour les relectures, pour l'aide avec les manips (sans toi je n'aurais peut-être jamais identifié mon problème de bouchon !)

et pour la mise en relation avec Renaud, Olivier et Stéphanie. Je te souhaite une bonne continuation dans le Sud!

L'équipe des chimistes du STEP, merci pour votre accueil, bonne humeur et leçons de chimie organique. Merci Renaud Demadrille, pour les discussions, les relectures et pour l'accès à ton super labo. Je tiens à remercier en particulier Olivier Bardagot. C'était génial de t'avoir rencontré et d'avoir partagé des moments de brainstorming, discussions, manips et fermeture du CEA avec toi ! Je suis extrêmement reconnaissante pour tout ce que tu m'as apporté et j'espère que nos chemins se croiseront dans le futur. Bis Bald!

Stéphanie Pouget, merci pour avoir partagé ton temps et tes connaissances de GIWAXs avec moi. J'ai passé des très bons moments avec le diffractomètre et toi.

Anass Benayad, c'était un énorme plaisir de découvrir cette puissante technique qu'est l'XPS avec toi. Tu m'impressionneras toujours avec ton œil pour fiter n'importe quel spectre. Merci beaucoup pour ton temps et pour tous tes enseignements.

Dennis Mariolle et François Saint-Antonin, merci pour les mesures et leçons AFM. J'ai passé de très bons moments avec vous et vos différents types d'AFM.

Orlane Fanget, merci pour ton aide dans la salle anhydre et pour ta gentillesse ! Les manips organisées avec toi ont été très importantes pour ma thèse.

Antoine Kahn, merci pour m'avoir fourni ce dopant-p très prometteur ($Mo(tdf\text{-}COCF_3)_3$) et pour les discussions qu'on a pu avoir en conférences et par téléphone.

Lilian, merci pour ton soutien, ta patience, ton amour. Merci de croire en moi et de m'avoir accompagnée dans cette expérience éprouvante. Tu as été très important pour cette réussite. J'aimerais aussi remercier ma nouvelle famille savoyarde pour votre accueil et gentillesse.

Liebe Familie Domschke, ich danke Euch ganz herzlich für die Unterstützung und für das Daumendrücken. Papa, danke fürs Zuhören und Aufmuntern, besonders in Momenten, wo ich keine Lust mehr auf Polymere hatte. Oma, wir haben es endlich geschafft! Opa, dein Geburtstag war dieses Jahr ein bisschen aufregend, aber wir haben alle zusammen gefeiert!

Querida mãe, querida irmã, obrigada por escutar meus lamentos e dramas durante os momentos mais complicados desse doutorado, pelos incentivos, pelas releituras e pelas repetições à distância! Agradeço também à minha família carioca, por serem essas pessoas maravilhosas, cheias de alegria e por me transmitirem boas energias apesar da distância. Um agradecimento especial para minha avó Lina, aonde quer que a senhora esteja, saiba que o seu amor pelo ensino e educação foram muito inspiradores durante meus estudos. Sou muito grata pela sua ajuda. Viva às doutoras dessa família!

LIST OF ABBREVIATIONS AND SYMBOLS

σ	Electrical conductivity
μ_e	Electron mobility
μ_h	Hole mobility
CB	Conduction Band
CPX	Charge-Transfer Complex
CT	Charge-Transfer
CV	Cyclic Voltammetry
DCM	DiChloroMethane
DOS	Density Of States
EA	Electron Affinity
E_C	Conduction band edge
E_F	Fermi level
E_G	Electronic or transport band Gap
E_{GOPT}	Optical band gap
EPR	Electron Paramagnetic Resonance
E_V	Valence band edge
E_{VAC}	Vacuum level
F4TCNQ	2,3,5,6-Tetrafluoro-7,7,8,8-tetracyanoquinodimethane
GIWAXS	Grazing Incidence Wide Angle X-ray Scattering
HOMO	Highest Occupied Molecular Orbital
IE	Ionization Energy
IPA	Ion-Pair
LUMO	Lowest Unoccupied Molecular Orbital
$Mo(tfd\text{-}COCF_3)_3$	tris[1-(trifluoroethanoyl)-2-(trifluoromethyl) ethane-1,2-dithiolene]
OFET	Organic Field-Effect Transistor
OLED	Organic Light-Emitting Diode
OPV	Organic PhotoVoltaics
OSC	Organic SemiConductor
RR-P3HT	RegioRegular Poly(3-HexylThiophene-2,5-diyl)

RRa-P3HT	RegioRandom Poly(3-HexylThiophene-2,5-diyl)
PBDTTT-c	Poly[(4,8-bis-(2-ethylhexyloxy)-benzo(1,2-b:4,5-b')dithiophene)-2,6-diyl-alt-(4-(2-ethylhexanoyl)-thieno[3,4-b]thiophene-)-2-6-diyl)]
PEDOT	Poly(3,4-EthyleneDiOxyThiophene)
PSS	PolyStyrene Sulfonate
PTB7	Poly[[4,8-bis[(2-ethylhexyl)oxy]benzo[1,2-b:4,5-b']dithiophene-2,6-diyl][3-fluoro-2-[(2-ethylhexyl)carbonyl]thieno[3,4-b]thiophenediyl]]
TLM	Transmission Line Measurement
THF	TetraHydroFuran
UV-Vis	UltraViolet-Visible
UV-Vis-NIR	UltraViolet-Visible-Near InfraRed
VB	Valance Band
WF	Work Function
XRD	X-Ray Diffraction

ABSTRACT

Organic semiconductors (OSCs) are promising materials for low-cost, flexible, large-area production of printed electronic devices. In this context, molecular doping allows controlling the electrical properties of OSCs, offering a powerful tool to improve the performances of different electronic devices. Despite the progress in the fundamental understanding of the doping mechanism and processing techniques, stability aspects of *p*-doped OSCs have received little attention. Nevertheless, the stability of the *p*-doped state in the presence of oxygen and humidity is a crucial factor to be investigated for the integration of doped layers in organic devices.

In this thesis, we have studied the molecular doping of disordered polymer semiconductors and the stability of the *p*-doped state in the presence of oxygen and water-related species. PBDTTT-c and RRa-P3HT were used as polymer hosts and F4TCNQ and Mo(tfd-$COCF_3)_3$ as *p*-dopants. The process conditions have been carefully studied to achieve controlled doping and to optimize the electrical properties. The impact of the dopant concentration was investigated in terms of electrical (conductivity), optical (UV-Vis-NIR) and structural (GIWAXS) properties of doped layers.

The stability of the *p*-doped state was investigated by monitoring the evolution of the doping signatures under three different atmospheres: argon, anhydrous air, and ambient air. XPS analyses were carried out to investigate the impact of air exposure on the chemical state of *p*-doped layers. Simulations have been used to support our findings.

Present results highlighted the presence of an important dedoping mechanism for *p*-doped semiconducting polymers in the presence of water-related species.

Keywords: Organic electronics, pi-conjugated polymers, *p*-type, Molecular doping, Dedoping, Air Stability

RESUME

Les semi-conducteurs organiques (OSCs) sont des matériaux prometteurs pour la production à faible coût de dispositifs électroniques imprimés flexibles et de grandes surfaces. Dans ce contexte, le dopage moléculaire permet de contrôler les propriétés électriques des OSC, offrant un outil puissant pour améliorer les performances de différents dispositifs électroniques. Malgré les progrès dans la compréhension fondamentale du mécanisme de dopage et de leurs procédés, la stabilité des OSC dopés *p* ont reçu peu d'attention. Or, la stabilité de l'état dopé *p* en présence d'oxygène et d'humidité est un facteur crucial pour l'intégration de couches dopées dans des dispositifs organiques.

Dans cette thèse, nous avons étudié le dopage moléculaire de semi-conducteurs polymères désordonnés et la stabilité du dopage *p* en présence d'oxygène et d'espèces liées à l'eau. PBDTTT-c et RRa-P3HT ont été utilisés comme matrice de polymères et F4TCNQ et $Mo(tfd\text{-}COCF_3)_3$ comme dopants de type *p*. Les paramètres du procédé de dopage ont été soigneusement étudiés pour obtenir un dopage contrôlé et optimiser les propriétés électriques. L'impact de la concentration de dopant a été étudié en termes de propriétés électriques (conductivité), optiques (UV-Vis-NIR) et structurelles (GIWAXS).

La stabilité de l'état dopé *p* a été analysée en surveillant l'évolution des signatures de dopage sous trois atmosphères différentes : l'argon, l'air anhydre et l'air ambiant. Des analyses XPS ont été effectuées pour étudier l'impact de l'exposition à l'air sur l'état chimique des couches dopées *p*. Des simulations ont été utilisées pour étayer nos résultats.

Les résultats actuels ont mis en évidence la présence d'un mécanisme de dédopage important pour les polymères semi-conducteurs dopés-p en présence d'espèces liées à l'eau.

Mots clés: Electronique organique, polymères π conjugués, dopage *p*, dopage moléculaire, stabilité à l'air.

TABLE OF CONTENTS

GENERAL INTRODUCTION

We live in an electronic world. Advances in electronic technology positively impacted our lives in terms of comfort, mobility, leisure but also security and health. New needs and markets continuously arise to supply and support this development. Flexible and conformable electronic components, with transparent displays and smart packaging, will be part of the Internet of Things (IoT) era[1]. Flexible electronics are also of great interest for medical applications since they offer the possibility of wearable, implantable, and biocompatible electronic devices[2]. In this context, despite the excellent performances, the current electronic technology based on inorganic semiconductors (e.g. silicon-based devices) is not adapted for the applications mentioned above due to their brittleness, thickness, absence of transparency, incompatibility with organic tissues, etc. Besides, the resources and methodologies used to manufacture inorganic electronic devices raise urgent questions about their negative environmental impacts[3].

To continue powering and developing this modern lifestyle, the world needs a significant transition in its energy sources towards more sustainable solutions, to reduce our environmental impact and replenish the resources we consume. Historical and current energy systems are dominated by fossil fuels (coal, oil, and gas), which produce carbon dioxide and other greenhouse gases, fundamental drivers of global climate change[4]. As a result, the energy transition is one of the 21st century's major challenges. Considering that 60% of the total greenhouse gas emissions originate from energy demand and supply, the investigation and promotion of low-carbon energy sources are primordial[5]. In this context, organic semiconductors offer a huge potential for an energy transition towards clean and green solutions with an ultra-low carbon footprint.

The discovery of organic materials with semiconducting properties in the late 1970s by *A.* J. Heeger, A. G. MacDiarmid and H. Shirakawa was awarded the 2000 Nobel Prize in Chemistry and initiated a new technological era[6]. These organic small molecules and polymers can be used for a variety of applications in technical industries (e.g. circuitry, energy harvesting/storage, etc.) and medical applications (e.g. bioelectronics for sensors, tissue scaffolds for tissue engineering, etc.)[2,7]. Besides these diverse applications, the use of organic materials to build electronic devices offers a more sustainable and affordable approach compared to silicon-based electronics: the materials are synthesized rather than mined from the earth, and the ending devices are biodegradable or recyclable[8]. Additionally, organic semiconductors can be processed using solution printing techniques on glass, plastic, paper, metal, almost any type of substrate with a low thermal budget[9]. Finally, the next generation of flexible, low weight, transparent, and eco-friendly electronics devices can be fabricated with these organic materials.

Nevertheless, major limitations are still hampering the growth and industrial development of organic electronics. Achieving performant and stable devices, which are compatible with large scale printing techniques is the major challenge to be considered in the years to come.

In this context, molecular doping emerged as a potential technique to improve the performance of organic electronic devices since it allows manipulating the electrical properties of OSCs, for instance improving transport properties as well as electrical contacts of devices. Even though the doping process has been used for years in inorganic semiconductors, the underlying principles are fundamentally different for OSCs. To overcome the lack of understanding and consequently improve the doping efficiencies, the research over the last years mainly focused on the fundamental principles governing the molecular doping of OSCs. Very little attention was given to the stability of *p*-doped OSCs under ambient air, although it is a crucial aspect for the future integration of these materials into commercial organic devices. Air instability is commonly associated with electron trapping and oxidation of materials with low ionization energies (IE)[10,11]. Not surprisingly, the existing studies on the stability of molecular doped OSCs consider mainly n-doped OSCs. However, hole traps are also present in conjugated polymers and have recently received more attention in the literature.

In this context, this thesis aims to investigate the potential of *p*-doped semiconducting polymer for the industrial development of flexible electronic devices, where performance, stability, and scalability are essential aspects.

The first chapter introduces the basis to appreciate the context and objectives of this Ph.D. thesis. A brief theoretical background on organic semiconductors (OSCs) will be provided and the principles, mechanisms, applications, and challenges of doped OSCs detailed, before presenting the motivations and main objectives of this work.

In the second chapter, we present a detailed study of the doping process by solution-based techniques, aiming to achieve controlled and reproducible results. The initial electrical, optical, electrochemical, and structural properties of pristine materials will be characterized, the optimization of the doping conditions detailed and the doping signatures discussed.

The third chapter will focus on the stability of the *p*-doped state under different atmospheres. An extensive state-of-the-art survey air-related hole and electron traps will be provided. The stability of the doping signatures under different atmospheres will be presented and potential degradation mechanisms discussed. Simulations will be used to help understanding our experimental results.

To conclude this thesis, we will summarize the major achievements and suggest outlooks based on the progress of this work.

INTRODUCTION GENERALE

Nous vivons dans un monde électronique. Les progrès des technologies ont eu un impact positif sur nos vies en termes de confort, de mobilité, de loisirs mais aussi de sécurité et de santé. De nouveaux besoins et de nouveaux marchés surgissent continuellement pour stimuler ce développement. Par exemple, l'Internet des objets (IoT) encourage le développement de composants électroniques flexibles et conformables, avec des écrans transparents et une encapsulation adaptée[1]. L'électronique flexible présente également un grand intérêt pour les applications médicales, car elle offre la possibilité de réaliser des dispositifs électroniques portables, implantables et biocompatibles[2]. Dans ce contexte, malgré ses excellentes performances, la technologie électronique actuelle à base de semi-conducteurs inorganiques (par exemple les dispositifs à base de silicium) n'est pas adaptée aux applications mentionnées ci-dessus en raison de leur fragilité, leur poids, leur absence de transparence, leur incompatibilité avec les tissus organiques, etc. Par ailleurs, les ressources et méthodologies utilisées pour fabriquer ces dispositifs électroniques inorganiques soulèvent aussi des interrogations sur leur excessif impact environnemental[3].

Pour continuer à alimenter et à développer ce mode de vie moderne, le monde a besoin d'une transition de ses sources d'énergie et de ses modes de consommation vers des solutions plus durables, permettant de réduire notre impact environnemental et de reconstituer les ressources consommées. Les systèmes énergétiques historiques et actuels demeurent dominés par les combustibles fossiles (charbon, pétrole et gaz), qui produisent du dioxyde de carbone et d'autres gaz à effet de serre, moteurs fondamentaux du changement climatique mondial[4]. Par conséquent, la transition énergétique est l'un des défis majeurs du XXIe siècle. Considérant que 60% des émissions totales de gaz à effet de serre proviennent de la demande et de l'offre d'énergie, la recherche et la promotion de sources d'énergie à faible émission de carbone sont primordiales[5]. Dans ce contexte, les semi-conducteurs organiques (OSCs) ont un énorme potentiel pour la transition énergétique, pour des solutions plus propres à très faible empreinte carbone.

La découverte de matériaux organiques aux propriétés semi-conductrices à la fin des années 1970 par A. J. Heeger, A. G. MacDiarmid et H. Shirakawa a donné lieu au prix Nobel de chimie 2000 et a lancé une nouvelle ère technologique[6]. Ces petites molécules et polymères organiques peuvent être utilisés pour une variété d'applications dans les industries techniques (par exemple, circuits, récupération / stockage d'énergie, etc.) et les applications médicales (par exemple, bioélectronique pour capteurs, échafaudages tissulaires pour l'ingénierie tissulaire, etc.)[2,7]. Outre ces différentes applications, l'utilisation de matériaux organiques pour construire des appareils électroniques offre une approche plus durable et plus abordable par rapport à l'électronique à base de silicium : les matériaux sont synthétisés plutôt que extraits de la terre, et les dispositifs finaux sont plus facilement biodégradables ou recyclables[8]. De plus, les semi-conducteurs organiques peuvent être traités en utilisant des techniques d'impression sur une grande variété de substrat : verre, plastique, papier, métaux, presque tous les types de substrat[9]. En conclusion, la prochaine

génération d'appareils électroniques flexibles, légers, transparents et écologiques pourrait être fabriquée avec ces matériaux organiques.

Néanmoins, des limitations majeures entravent toujours la croissance et le développement industriel de l'électronique organique. Réaliser des dispositifs performants et stables, compatibles avec les techniques d'impression à grande échelle demeure le défi majeur pour cette technologie pour les années à venir.

Dans ce contexte, le dopage moléculaire est apparu comme une technique intéressante pour améliorer les performances des dispositifs électroniques organiques car il permet de modifier les propriétés électriques des OSCs, par exemple en améliorant les propriétés de transport ainsi que les contacts électriques des dispositifs. Même si le processus de dopage est utilisé depuis des années dans les semi-conducteurs inorganiques, les principes sous-jacents sont fondamentalement différents pour les OSCs. Pour pallier le manque de compréhension et par conséquent améliorer l'efficacité du dopage, les recherches ces dernières années se sont principalement concentrées sur la compréhension des principes fondamentaux régissant le dopage moléculaire des OSCs. Très peu d'attention a été accordée à la stabilité des OSCs dopés p sous l'air ambiant, bien qu'il s'agisse d'un aspect crucial pour l'intégration future de ces matériaux dans des dispositifs organiques commerciaux.

L'instabilité à l'air est généralement associée au piégeage d'électrons et à l'oxydation de matériaux à faibles énergies d'ionisation (IE)[10,11]. En conséquence, les études existantes sur la stabilité des OSCs dopées concernent principalement le dopage de type n. Cependant, les pièges à trous sont également présents dans les polymères conjugués et ont récemment reçu plus d'attention dans la littérature.

Dans ce contexte, cette thèse vise à étudier les potentialités du dopage p des polymères pour le développement industriel de dispositifs électroniques flexibles, où la performance et stabilité sont des aspects essentiels.

Le premier chapitre introduit les bases pour apprécier le contexte et les objectifs de ce travail de doctorat. Un bref rappel théorique sur les semi-conducteurs organiques sera fourni et les principes, mécanismes, applications et défis des OSCs dopés seront présentés, avant de préciser le sujet et les objectifs de cette thèse.

Dans le deuxième chapitre, nous présentons une étude détaillée du processus de dopage en solution, visant à obtenir des résultats contrôlés et reproductibles. Les propriétés électriques, optiques, électrochimiques et structurelles des matériaux vierges seront caractérisées, l'optimisation des conditions de dopage détaillée et les signatures de dopage discutées.

Le troisième chapitre se concentrera sur la stabilité de l'état dopé p sous différentes atmosphères. Un état de l'art concernant les pièges à électrons et à trous sera présenté. La stabilité des signatures de dopage sous différentes atmosphères sera exposée et les mécanismes de dégradation potentiels discutés. Des simulations seront utilisées pour aider à mieux comprendre les résultats expérimentaux.

Pour conclure cette thèse, nous résumerons les principales réalisations et proposerons des perspectives basées sur l'avancement de ces travaux.

1 INTRODUCTION AND FOUNDATIONS

This first chapter introduces the basis to appreciate the context and motivation of this work, and also the results of the experimental chapters. Principles, mechanisms, applications, and challenges of organic semiconductors and molecular doping are presented, before highlighting the main objectives of this thesis.

CHAPTER CONTENTS

1.1 ORGANIC SEMICONDUCTORS

Organic semiconductors (OSCs) are mostly composed of highly abundant atoms (e.g. C, S, O, N) and, therefore, capable of addressing the increasing demand for environment-friendly products due to the absence of scarce and toxic heavy metals[7]. These carbon chains can be processed either by evaporation or via solution. In both cases, deposition techniques enabling large-area and continuous deposition can be used[9]. Another advantage in terms of processing is short and low-temperature treatments. Besides, organic semiconductors have high absorption coefficients in the visible range, offering the possibility to develop very thin photodetectors and photovoltaic cells[12], meaning low material consumption. All these aspects allow a reduction of the overall manufacturing costs, justifying the appellation of low-cost technology. This term is used especially in comparison to inorganic semiconductors such as silicon, which presents an energy-intensive production, resulting in expensive fabrication costs.

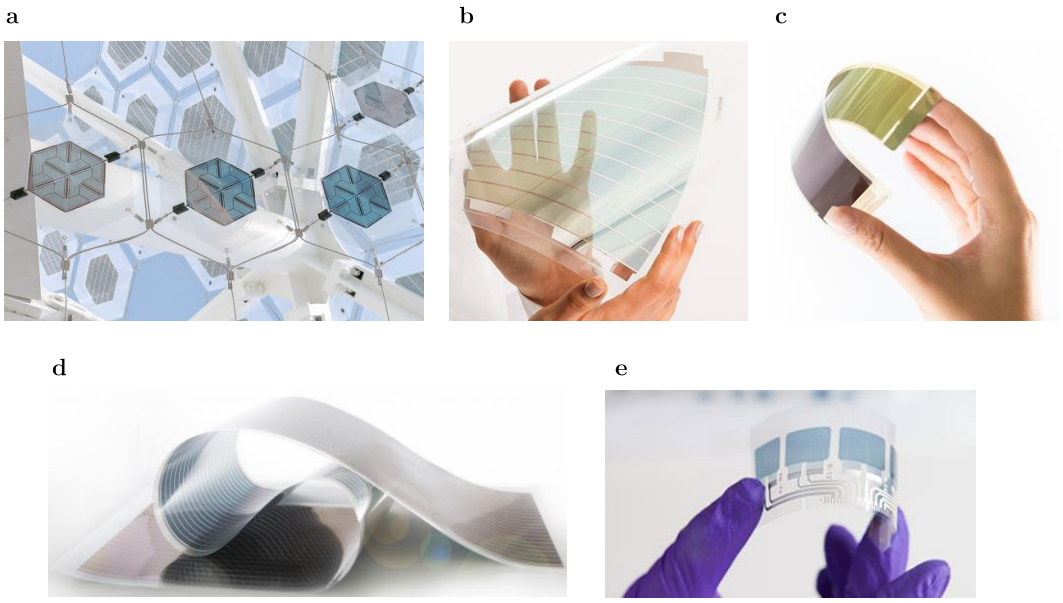

Figure 1.1 - Examples of organic electronic devices: a) OPV Solar Trees at EXPO 2015, (source: OPVIUS), b) Organic solar cell (source: Heliatek), c) organic photodiode (source: ISORG), d) organic solar cells (source: Armor), and d) example of printed electronic circuits (source: CEA tech).

This new generation of semiconductors allows the fabrication of ultrathin, lightweight, and transparent devices. Besides, the low fabrication temperatures and the mechanical tolerance of organic materials allow the use of flexible substrates and, consequently, the fabrication of flexible and conformable devices. These advantages are particularly exploitable for portable or wearable technologies[2,13].

Nevertheless, the interest in organic semiconductors is not only related to the technological aspects described above, but also to their versatility. The structure of organic semiconductors can be easily modified by chemical synthesis, for example, to tailor electronic properties such as the desired emission wavelength, to render it soluble, to improve the thermal stability or the mechanical robustness, etc. In addition, esthetic

applications also benefit from the possibility of adapting the color and the transparency of devices[14].In **Figure 1.1**, some examples of prototypes are given to illustrate the potential of organic electronic devices.

In the following, we present a brief review of definitions and basic principles of solid-state physics to recall the theory that gives rise to the semiconductor behavior. Then, organic semiconductors are introduced and their particular properties are highlighted, followed by some examples and an introduction to the solution processing techniques. Last, some degradation mechanisms of OSCs in the presence of light and air are discussed before presenting a discussion on the actual challenges and highlighting the interest of molecular doping for the development of organic electronic devices.

1.1.1 Principles of organic semiconductor

Band diagram and electronic energy levels

Semiconducting materials are the basis of electronic devices. They offer the possibility of controlling the behavior of charge carriers by applying an electrical field, light irradiation, doping, etc. These tunable electrical properties of semiconductors allow, for example, passing current more easily in one direction than the other, having variable resistance and also being sensitive to light and heat. In other words, amplification, switching, energy conversion, among other useful features, can be explored with these materials. Thus, diodes, transistors, integrated circuits, and all modern electronics are fabricated thanks to the semiconductors and their unique electrical properties.

From solid physics, semiconductors are defined as materials presenting electrical conductivities between that of a conductor (e.g. metallic copper) and an insulator (e.g. glass). The electrical conductivity describes the ability of a solid material to drive charge carriers (particles or quasi-particles that carry electric charges) in the presence of an external field. Charge carriers can be ions, electrons (if the charge is negative) or holes (if the charge is positive). Pristine semiconductors present a relatively low electrical conductivity which is, however, sensitive to a range of external factors such as temperature, illumination, magnetic fields, etc. Below, the origin of the high conductivity of metals, the low but variable electrical conductivity of semiconductors, and the extremely low conductivity of insulators is reviewed.

Solid materials are composed of a large number of atoms strongly bound together. In ordered materials, atomic positions are well defined. The electronic structure of such an atomic pattern can be described by the interaction of electron wave functions. As a consequence of the Pauli's exclusion principle, the interaction between atoms results in a splitting of energy levels: a lower-energetic binding and a higher energetic anti-binding energy level. The spacing between these energy levels decreases with increasing the number of atoms in interaction. In ordered solids, the closely spaced energy levels can be approximated to a continuum and obey the band theory[15]. A quasi-continuum of allowed levels is called a band, while the absence of level is a bandgap. In inorganic materials, the

highest energy band occupied with electrons is called valence band (E_v), whereas the lowest unoccupied band is called conduction band (E_c). Their equivalent in organic semiconductors (OSCs) are the Highest Occupied Molecular Orbital (HOMO) and the Lowest Unoccupied Molecular Orbital (LUMO), which are further discussed in the next section. The energy required for an electron in the valence band (HOMO) to be excited toward the conduction band (LUMO) is commonly referred to as E_G[16].

Figure 1.2 illustrates the band diagram of an insulator, a pristine semiconductor, and a metal. There are some important definitions to be clarified before highlighting the differences between each class of material (**Figure 1.2**a). First, all energy levels are referenced to the vacuum level (E_{VAC}), also known as the local vacuum level[17]. Since electrons are naturally bound to the solid, E_{VAC} corresponds to the energy barrier that needs to be overcome by an electron, at the surface of the material (with zero kinetic energy with respect to the latter), to escape to vacuum. In this context, the ionization energy (IE) is defined as the minimum energy necessary to remove an electron from a material and corresponds, therefore, to the energy difference between E_{VAC} and the VB (HOMO) edge. Conversely, the energy difference between E_{VAC} and the CB (LUMO) edge, i.e. the energy gained by adding an electron from the vacuum level to the lowest unoccupied state, corresponds to the electron affinity (EA) of the material. Another important definition is the Fermi energy E_F, which describes the statistical energy at which the occupation probability is exactly 50%. The distance between the E_{VAC} and the Fermi level is called work function WF, which represents the energy barrier that prevents an electron at E_F from escaping to vacuum.

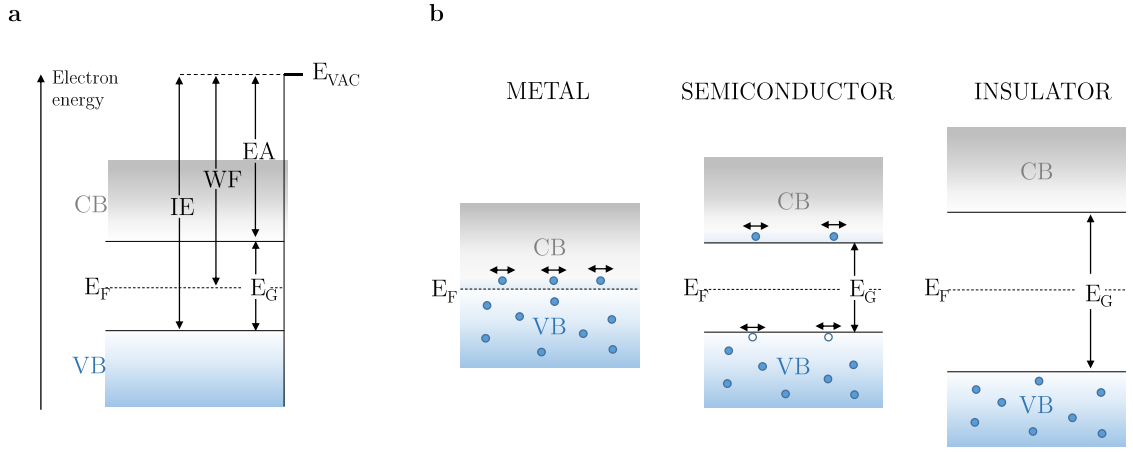

Figure 1.2 –Energy diagram of a semiconductor with several important denominations (a): Conduction and valence band (CB and VB, respectively and their edges. For organic semiconductors CB edge corresponds to LUMO and VB edge to HOMO), energy gap (E_G), vacuum level (E_{VAC}), work function (WF), ionization energy (IE) and electron affinity (EA). Illustration of band diagrams of a metal, a semiconductor, and an insulator (b).

In conductors, if the temperature is above absolute zero, E_F lies in the conduction band. In other words, the VB is only partially occupied, meaning that there are several empty states and electrons can move freely, resulting in high electrical conductivities (**Figure 1.2**b, left). Semiconductors present a completely occupied VB, which is separated by an

energy gap E_G from the completely empty CB (**Figure 1.2**b, middle). In an intrinsic semiconductor, the E_F is located in the middle of the bandgap, allowing electrons to populate CB upon excitation. Depending on the bandgap width, the temperature, and the doping conditions, the conductivity of semiconductors may vary from 10^{-8} to 10^{+5} $S.cm^{-1}$ [18]. Note that pure semiconductors are insulators at absolute zero, with a conductivity that increases with temperature. If the bandgap is larger than 3 eV, the material is commonly referred to as an insulator (**Figure 1.2**b, right). The difference between insulators and semiconductors is that the former requires unfeasibly large energy to raise charge carriers to an energy level at which it might conduct. Hence, regardless of the conditions, an insulator is characterized by a poor conductivity below 10^{-8} $S.cm^{-1}$.

Until the end of the XX century, semiconductors were represented by inorganic materials such as Silicon (Si), Germanium (Ge), Gallium-Arsenide (Ge-As), etc. These highly ordered materials were deeply studied, allowing scientists to build a solid understanding of semiconducting materials and devices[15]. The discovery of organic materials with semiconducting properties in the late 1970s by A. J. Heeger, A. G. MacDiarmid and H. Shirakawa initiated a new technological era[6]. The next section aims to give an overview of the semiconducting properties of OSCs and some important aspects of this class of materials.

Conjugated polymer chains

As the name indicates, OSCs are mainly composed of carbon (C) and hydrogen (H). Usually, additional heteroatoms such as oxygen (O), nitrogen (N), fluorine (F), or sulfur (S) are also added to the backbone to manipulate their optical and electrical properties. Organic semiconductors can be classified into two classes: small molecules and polymers. Small molecules are composed of one or a few monomers, whereas polymers are large molecules, or macromolecules, composed of several repeated subunits (monomers). Consequently, small molecules present lower molecular weight than polymers and, therefore, can be easily evaporated. The size and weight of OSCs have an important impact on the processing conditions as well as on the crystallinity of thin layers[19,20]. Generally speaking, small molecules are processed by evaporation under vacuum and present a better crystallinity than polymers, which are solution-processed with techniques such as spin-coating, inkjet printing, slot dye coating, etc. (see section 1.1.2 for printing techniques). This thesis studies semiconducting polymers chains since we are interested in using solution-processable deposition techniques, which offer advantages in terms of costs and simplicity. In the following, the semiconducting properties of polymers are reviewed, from the atomic scale up to thin polymer layers, to highlight important aspects of this class of semiconductors.

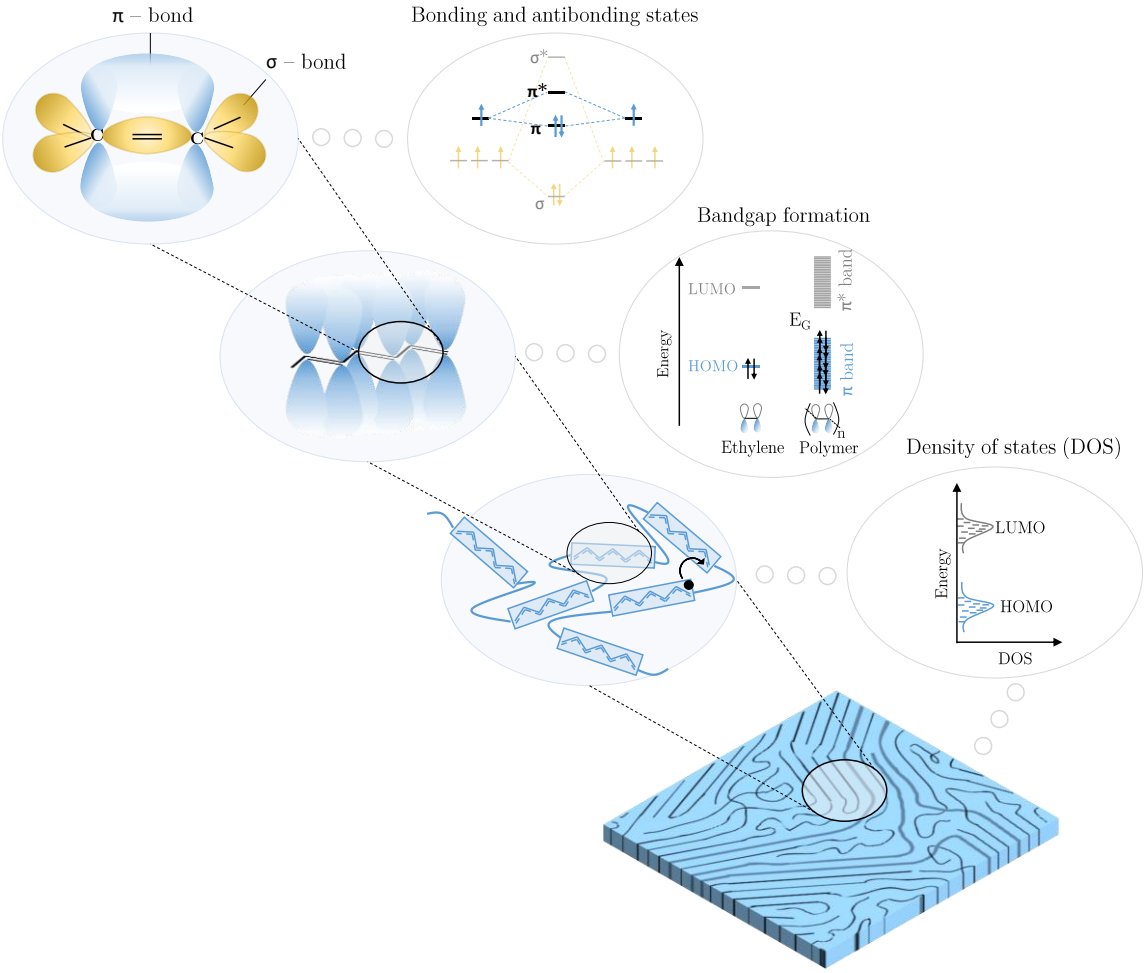

Figure 1.3- Schematic representation of several important morphological and energetic aspects of organic semiconductors.

The semiconducting properties of polymer chains originate from the alternation of single (σ) and double (π) bonds, called π-conjugation[21]. This can be better understood when looking at polymer chains at the atomic scale, with the respective atomic orbitals (**Figure 1.3**, top left). Depending on the neighboring atoms, carbon can have three different hybridization configurations: *sp*, sp_2, and sp_3. In conjugated carbon chains, carbons present their sp_2 configuration, meaning that one *s* and two *p* orbitals hybridize. The third *p* orbital (p_z), corresponding to the fourth valence electron, remains non-hybridized. The sp_2 orbitals are responsible for three σ-bonds with neighboring atoms (yellow orbitals, **Figure 1.3**) and are oriented in the plane of the carbon backbone. This is not the case of the non-hybridized p_z orbital (blue orbital, **Figure 1.3**), which is oriented perpendicularly to the carbon backbone. The overlapping of neighboring p_z orbitals forms π-bonds. Due to Pauli's exclusion principle, which states that two electrons cannot occupy the same quantum state, σ and π-bonds in conjugated polymer form bonding (σ, π) and antibonding (σ*, π*) states, (**Figure 1.3**, bonding and antibonding states)[21].

When extending such a system over several carbon units (**Figure 1.3**, middle left), the electrons in the p_z orbitals will become delocalized over several carbon units and give rise to a so-called π-band. Due to the symmetry breaking of C-C bond lengths in conjugated

polymer chains (Peierl's instability), the evolution of the π-band results in fully occupied π orbitals and unoccupied π* orbitals, separated by a gap[22]. This gap decreases with increasing the number of carbon atoms in a conjugated chain, i.e. of π and π* levels (**Figure 1.3**, bandgap formation). In conjugated polymers, the energy gap separating π orbitals from π* is in the order of a few eV (< 3 eV), characteristic of semiconductors. Hence, the motion of delocalized π-electrons (excited from π to π*) gives rise to semiconducting properties in conjugated polymer chains.

Different from inorganic semiconductors, the electronic structure of OSCs is more accurately described by the molecular orbital theory, implying discrete energy levels instead of energy bands. In this context, the HOMO level, resulting from the overlapping of π orbitals, can be approximated to the valence band edge. Analogically, the LUMO level, resulting from the overlapping of π* orbitals, can be approximated to the conduction band edge[23]. Thus, the electronic band gap (E_g) of organic semiconductors is defined by the HOMO-LUMO difference.

When considering several segments of a conjugated carbon chain, the effective length where carriers can be delocalized is called the conjugation length. Generally speaking, reducing the overlapping of π-orbitals hinders the mobility of charge carriers. However, differently from the strong covalent bonds in inorganic semiconductors, conjugated polymer chains interact only weakly by Van-der-Waals forces. Thus, these carbon chains present a relatively high conformational freedom, which may lead to variations in bond lengths, bent or twisted segments, etc. As a result, these materials are rather disordered concerning positional but also energetic order, resulting in local variations of HOMO and LUMO levels among different chain segments. Therefore, instead of a band edge, HOMO and LUMO levels often present a Gaussian distribution of the Density Of States (DOS), as illustrated in **Figure 1.3**, where higher disorder leads to broader distribution of energies and shorter conjugations length[23]. The presence of atomic or molecular disorder, as well as impurities, may also result in traps, i.e. electronic states in the gap of the semiconductor. As the word suggests, once an electron or a hole gets trapped, they no longer participate in the conduction. Traps that are near the middle of E_G are referred to as deep traps.

In terms of charge transport, this energetic disorder results in transport barriers to the delocalized electrons. In order to move, charge carriers must hope between localized inter or intramolecular states. **Figure 1.3** (bottom left) presents a conceptual illustration of the mechanism of charge transport by hopping in π-conjugated polymer chains, where the rectangular sections represent the conjugation length, separated by regions that are bent or twisted, or that have chemical defects that disrupt the conjugation. There are different transport models for OSCs, depending mainly on the organization, i.e. crystallinity of the material. For more information, a review of the existing mechanism was recently published by Liu *et al.*[24]. In general, higher crystallinities result in an increased overlap of π-orbitals, fewer traps, and consequently higher mobility[25]. This is why amorphous polymers have

particularly low mobility. Hence, favoring intramolecular and intermolecular π-interactions, such as π-stacking, improves the charge transport process.

Finally, the final properties of a conjugated polymer layer are highly dependent on the morphology, which can be influenced or even modulated by synthesis strategies[19,26], processing parameters[27], post-treatments[28], etc. Therefore, in this thesis, we carefully investigated the impact of process parameters on the final properties of semiconducting polymer layers. The morphology and aggregation of polymer chains are further discussed in section 2.1.1.

Below, some examples and properties of conjugated polymers are discussed. Besides, we introduce the conjugated polymers that were studied in this thesis.

Examples of conjugated polymers

Depending on the device and on the fabrication process, conjugated polymers with different optical, electrical, thermal, or chemical properties are required. Propitiously, organic chemistry offers the possibility of designing and synthesizing polymers with targeted properties to fulfill the requirements in terms of performance and processability. In this context, after the discovery of the semiconducting and conducting properties of conjugated polymers in 1977 by A. J. Heeger, A. G. MacDiarmid and H. Shirakawa[6], several studies have been carried out to develop convenient and efficient semiconducting polymers.

According to its structure, an intrinsic OSC conducts favorably electrons (*n*-type) or holes (*p*-type). This is related to the electronegativity of the functional groups or atoms present in the backbone, giving rise to an unequal sharing of electrons within the molecule[29]. For instance, the more electron-withdrawing groups (*e.g.* carbonyl, cyano groups, or halogenated atoms), the higher the electron affinity of the polymer, since these acceptor units will favorably conduct electrons (*n*-type material). On the other hand, if the molecule is composed of electron releasing groups (e.g. alkyl, alcohol, or amino groups), its ionization potential will be low and the molecule will favorably conduct holes (*p*-type material). Therefore, tuning the functional groups greatly influences the energetic structure and spatial distribution of the frontier molecular orbitals[29,30].

Additionally, varying the π-chain torsion or adding alkyl chains of variable lengths will impact the conformation, i.e. the overall structure disorder and, therefore, the charge transport properties of OSCs. Besides, the addition of alkyl side chains improves the solubility of conjugated polymer chains[31], which is an important requirement for solution-processed layers. For large-scale printing, OSCs should be soluble in non-toxic solvents, *e.g.* halogen-free solvents or even green, environmentally friendly solvents.

Poly(3-hexylthiophene) (P3HT) is the most widely studied polymer, consisting of polythiophene (PT) building blocks with alkyl side chains for improving the solubility (**Figure 1.4**a, b)[32]. It is a *p*-type semiconducting polymer. P3HT can be synthesized in the regiorandom (RRa) or regioregular (RR) form, which differs on the orientation of the alkyl side chains, as illustrated in **Figure 1.4**c, d. In RR-P3HT, the regularly oriented alkyl side

chains not only lead to fewer torsion angles in the polymer backbone, providing a longer conjugated pathway for charge carriers but also allow a more ordered intermolecular packing. Thus, semi-crystalline morphologies can be obtained with RR-P3HT, whereas amorphous layers are obtained with RRa-P3HT. As a consequence, RR-P3HT presents a substantial increase in the carrier mobility (0.05 to 0.1 $cm^2.Vs^{-1}$) compared with RRa-P3HT (usually below 10^{-3} $cm^2.Vs^{-1}$)[33].

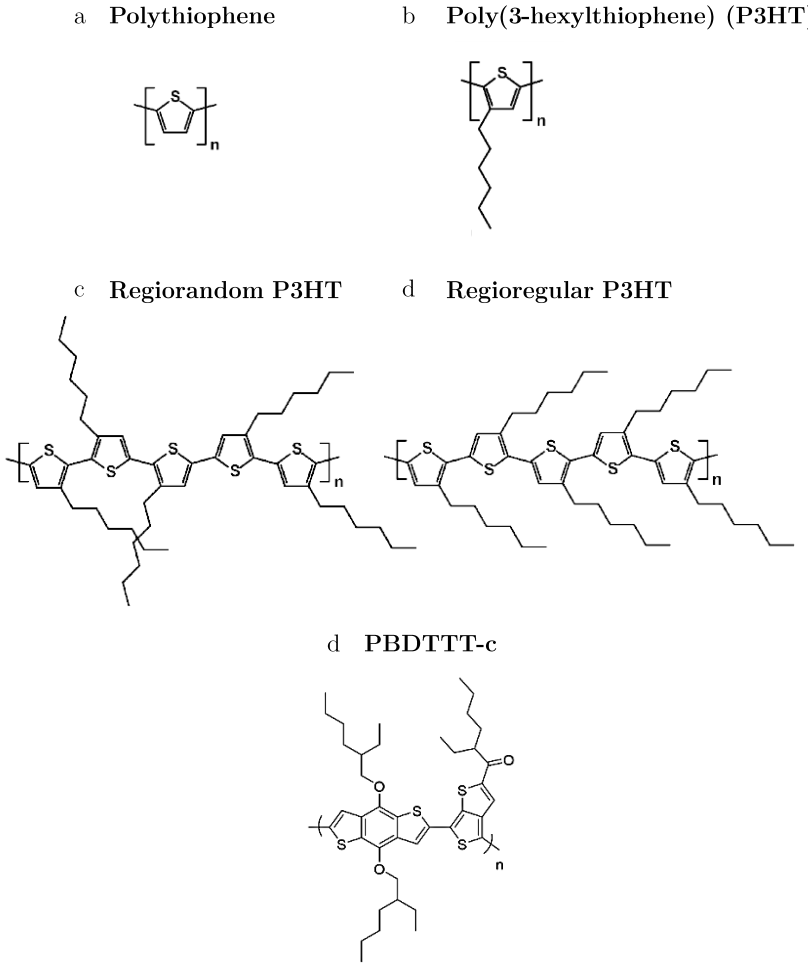

Figure 1.4 - Chemical structures (a) Polythiophene, (b) Poly(3-hexylthiophene) (P3HT), and (d) PBDTTT-c. Schematic representation of (c) regiorandom (RRa) and (d) regioregular (RR) poly(3-hexylthiophene).

As mentioned above, P3HT layers have been widely studied in the literature since they can be easily processed and exhibits good electrical properties in its semi-crystalline state[7,33]. Besides, due to the ability to obtain amorphous and ordered domains with the same composition, several research groups used P3HT to study the impact of morphology and packing of polymer chain on the properties of thin layers and devices[34-36]. This conjugated polymer can be considered as reference material in the field.

However, to increase the performance of organic devices, the synthesis of conjugated polymers focused on improving their mobility[20] and tuning the absorption range in the visible spectrum[30,37], among other properties. New building blocks have been synthesized to address these issues, such as donor–acceptor (D–A) conjugated polymers. D–A polymers

consist of at least two alternating moieties along the polymer backbone: an electron-rich donor (*p*-type building block) and an electron-deficient acceptor (*n*-type building block). Compared with homopolymers, i.e. polymers with only one moiety such as P3HT, the design of D–A polymers present a clear advantage for tuning of energy bandgap (E_G) of these semiconductors. As a result, these polymers allowed harvesting near-infrared energy from the solar spectrum, despite presenting lower HOMO levels, which increased considerably the power conversion efficiency (PCE) of organic solar cells[29,31,37].

Today, donor–acceptor (D–A) conjugated polymers are within the state-of-the-art *p*-type semiconducting polymers for OPV[29]. One example is the family of PTB polymers developed by Liang *et al.*, consisting in alternating thieno[3,4-b]thiophene (TT) and benzodithiophene (BDT) units[30,37].

In this work, we have chosen to study a D-A polymer of the PTB family, more precisely PBDTTT-c, due to the potential of this class of D-A polymers for organic solar cells and photodetectors. As a reference polymer, we also considered P3HT, which has been widely studied in this neutral and doped state[34,38,39]. The polymer choice is further developed in section 1.3.

1.1.2 Processing of organic semiconductor

As mentioned previously in this chapter, OSCs can be deposited by vacuum techniques, i.e. evaporation, or by solution-phase processes. In this work, the conjugated polymers are solution-processed, due to the advantages in terms of costs and simplicity for upscaling (large-scale production). Several techniques have been developed for processing conjugated polymer layers from solutions: spin-coating, dip-coating, screen printing, inkjet printing, etc. The variety of techniques attests to the versatility of solution-phase deposition. Here, we will describe both techniques used in this work: spin coating and drop-casting. More details on the other processes can be found in this review[40].

Spin coating is a technique particularly appreciated at the laboratory scale, where no patterning is required and where processing a single substrate at the time is not inconvenient. Despite the simplicity of setting up a spin coating process, thin and uniform layers can be achieved with this technique. One may mention the waste of material as a disadvantage, as a considerable amount of the deposited solution is spun off the substrate. This waste can be minimized, for example, by using smaller volumes and spreading out the solution manually before the rotation. However, this technique is usually not considered for industrial scale, due to the limitations for continuous and scalable deposition processes, but also the waste of material.

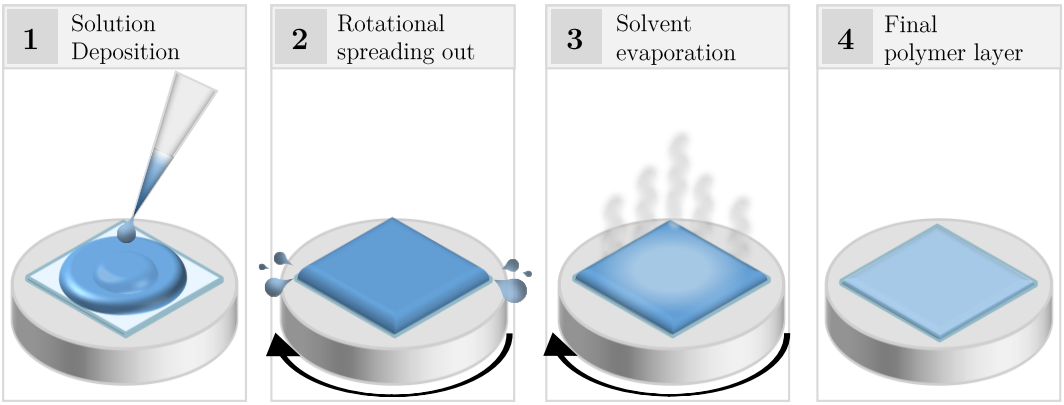

Figure 1.5 –Schematic representation of the spin-coating deposition technique.

The spin coating process is illustrated in **Figure 1.5**. First, the polymer solution is applied on the center of the substrate, which is held by a vacuum chuck (step 1). Then, the substrate is rotated to spread the solution by centrifugal force while the excess spins off the edges of the substrate (step 2). The rotation allows the formation of a homogeneous layer with a controlled thickness but is also responsible for the solvent evaporation (step 3). The main parameter controlling the layer thickness is the rotational speed: faster rotations result in thinner layers. Besides, the viscosity and concentration of the solution will also influence the final layer thickness[40]. For processing thicker layers, in the order of a few µm, this technique is not well suited. Using higher concentrations combined with slower rotations result in inhomogeneous layers with the so-called edge-bead effect, where the fluid on the edges dries first and disturbs the flow of the remaining solution[41]. Thicker layers were processed with the drop-casting technique in this thesis.

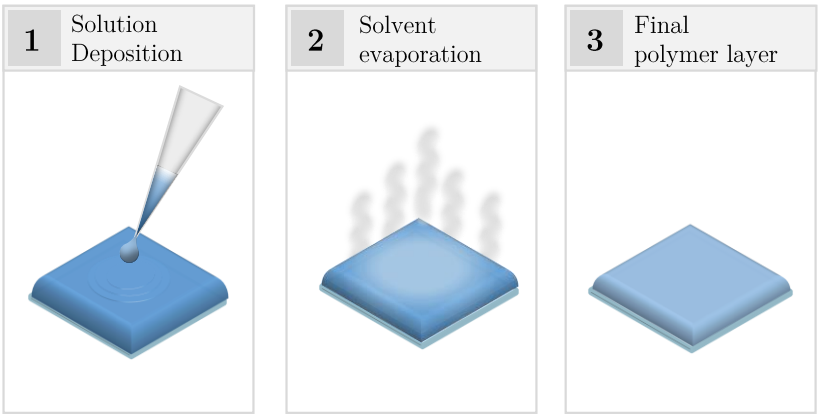

Figure 1.6 - Schematic representation of the drop-casting deposition technique.

Drop casting consists simply of spreading the solution over a substrate and allowing it to dry under controlled conditions, as illustrated in **Figure 1.6**. The solvent evaporation can be controlled by using solvents with a higher boiling point, or by using saturated solvent environments, among other strategies[40]. Compared to spin coating, the slower drying time can be beneficial to achieved layers with better crystallinities, especially for semi-crystalline polymers.

1.1.3 Stability of conjugated polymers

The stability of conjugated polymer and the resulting organic electronic devices is a complex and broad subject. In this thesis, we aim to study the stability of *p*-doped semiconducting polymer under ambient atmosphere, i.e. in the presence of oxygen and water. In this context, this section presents two important degradation routes identified for conjugated polymer layers in the presence of oxygen and light: photo-oxidation and oxygen doping. In section 1.1.4, we also present a brief overview of the stability challenges in organic devices (multilayer stacks). Besides, section 3.1 presents a detailed discussion on the presence of water and oxygen traps and their impact on pristine and doped OSCs.

Photo-oxidation

OSCs are synthesized to absorb photons of the solar spectrum. Upon irradiation, electrons will populate states with higher energies, i.e. excited states, which may lead to various photophysical or photochemical processes. Note that processes that are energetically unfavorable at ambient temperature (kT approx. 0.025 eV at 25°C) may rapidly take place under UV-visible irradiation (approx. 4.95 eV at 250 nm). Primary photochemical reactions can be classified as isomerization reactions (rearrangements), bond-forming reactions, or bond-breaking reactions[42]. However, absorbed photons can also generate reactive species, such as radicals or ions, which can further react with the polymer and result in bond breaking. In other words, the light may initiate several degradation processes in conjugated polymers.

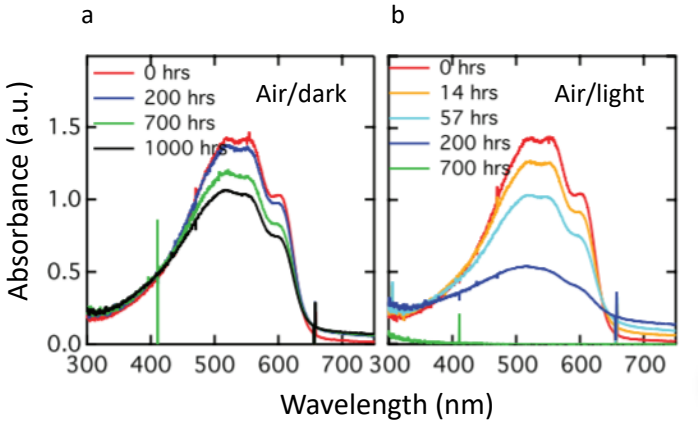

Figure 1.7 – Absorbance spectra of P3HT layers exposed to ambient atmosphere in the dark (a) and under 1 sun illumination (b). Adapted from [43].

In this context, important photochemical and photophysical processes have been reported to degrade OSCs[43–46]. For example, upon exposure to photo-oxidative conditions (presence of light and oxygen), organic materials are susceptible to undergo degradation processes that result in bleaching of the π-π* absorption, due to the loss of π-conjugation. In other words, semiconducting polymers lose their ability to absorb light (see **Figure 1.7**).

Differently from ground-state oxygen, which can be seen as a non-reactive molecule, radical oxygen species (e.g. superoxide radical anions O_2^-) and/or singlet oxygen ($^1O_2$) are highly

reactive species. Singlet oxygen corresponds to the lowest excited state of the diatomic oxygen molecule (O_2), which is kinetically unstable at ambient temperature and therefore more reactive toward organic compounds[47]. Up to date, two oxygen-dependent photo-degradation pathways have been highlighted in the literature for conjugated polymers: free-radical oxidation and photo-oxidation through singlet oxygen generation[48–51]. Both pathways are briefly described below.

In the free-radical oxidation process, once a free radical is introduced in a polymer, it propagates in the materials and breaks conjugated bonds, which results in the bleaching of the π-π^* absorption. This free-radical reaction is often initiated by the abstraction of hydrogen of the polymer side chain by a free-radical (e.g. superoxide anion O_2^-)[51]. Hence, the free-radical is transferred to the polymer and its propagation is accelerated in the presence of oxygen, which can diffuse throughout a polymer layer[44,46].

The second photo-oxidation mechanism identified in the literature involves the generation of singlet oxygen ($^1O_2$), which further oxidizes the polymer. To explain this mechanism lets introduce the definition of singlet and triplet excited states in OSCs. Upon absorption of photons by an OSC, there are several possible excited states in terms of orbitals (LUMO, LUMO +1…), configuration (distribution of electrons), and spin (parallel and antiparallel). Regarding the latter, when the spin of the electron in the π^* orbital and that of the remaining electron in the π-orbital are antiparallel, it is called a singlet-excited state (S), whereas parallel spins correspond to triplet excited states (T). Triplet states are lower in energy than singlet states. This terminology is correlated to the three different arrangements of the spin wavefunctions in the case of triplets compared to one single arrangement for singlets (For more details see[16]). The generation of singlet oxygen is associated with the molecular triplet state of OSCs, depending on their lifetime and energy[48,52]. In this photo-oxidation mechanism, the generated singlet oxygen species are reactive towards the polymer backbone, leading to photo-oxidation.

Though the nature of the chemical bonding among OSCs is relatively similar, the mechanism and the rate at which specific OSCs bleach can vary substantially[48,53]. Regarding the polymers studied in this thesis, for P3HT, it was shown that even though singlet oxygen may react with this polymer, the photo-oxidation mechanism responsible for the degradation of P3HT is the free radical process, starting at the polymer side chains[45,49]. On the other hand, for D-A polymers such as PTB7 (same family of PBDTTT-c), the photo-oxidation was shown to be mainly controlled by the $^1O_2$ attack.[49]. Compared to P3HT, D-A polymers have shown to be relatively unstable to light under ambient conditions[46,49].

Last, the morphology of conjugated polymers was also reported to play an important role in their photo-oxidative stability. For polymers that can be cast in both amorphous and semi-crystalline morphologies, the semi-crystalline layers presented better stability[44,52]. The film density was also correlated to the stability; denser films tend to be more stable to

photo-oxidation, possibly because the molecules are more confined and oxygen is less able to diffuse to reaction sites.[44]

Oxygen doping

Oxygen has shown to act as a *p*-dopant (acceptor level) for *p*-type conjugated polymers[54–56]. Unintentional doping can negatively affect the performance of devices where electronic semiconductor properties are desired, for example, for 'on–off' characteristics of organic field-effect transistors or the dark current of organic solar cells[55,56]. This unintentional doping process consists of an electron transfer from the polymer to the molecular oxygen, creating a free hole in the polymer, while the electron is trapped on an oxygen molecule. In the dark, oxygen doping has shown to be relatively slow (several days to reach a heavy doping level[56]). This slow equilibrium at room temperature can be associated with a considerably large energetic barrier. In other words, the doping kinetics is not controlled by the diffusion of oxygen through a polymer layer (within a few milliseconds for a 200 nm P3HT layer) but rather by the doping process itself[54].

Under illumination, the doping process is dramatically accelerated, as the absorption of a photon by the polymer readily provides the activation energy necessary for the doping process, accelerating the charge transfer process significantly[54–56]. In this context, Zhou *et al.* reported on photo-hole-doping of thiophene-based OSCs when exposed to ambient air and light, where photo-excited LUMO electrons were injected into acceptor levels such hydrated $0_2(H_20)_n$ species[55].

Oxygen doping was shown to be reversible upon oxygen desorption, which can be performed under vacuum or annealing under a controlled atmosphere (e.g. argon, or nitrogen)[54,56]. However, the reversibility of photo-assisted oxygen doping depends on the duration of illumination, the oxygen concentration, and the wavelength, since photo-oxidation and consequently irreversible degradations may occur for longer illumination periods in the presence of UV[56].

In conclusion, the degradation mechanisms identified for conjugated polymer exposed to ambient atmosphere and light are a critical aspect of the long-term stability of organic devices. Existing solutions, such as encapsulations, are discussed in the following, where we present an overview of the main challenges in the field of organic electronics.

1.1.4 Mains challenges

Despite the potential of semiconducting polymers for the next generation of electronic devices, there are major limitations still hampering their growth and industrial development. The main research axis over these last years concerned the performance. Nevertheless, this is not the only criterion hindering the industrial development of flexible electronic devices. The stability and the compatibility with large scale printing techniques, i.e. the scalability, are also major issues to be considered in the years to come. These three aspects are discussed separately below.

Performance

One actual challenge consists in improving the electrical properties of conjugated polymers. Due to the weak intermolecular interactions, polymer layers are subjected to disorder, which directly affects the transport of charge carriers[20,57]. As a consequence, the carrier mobility of RR-P3HT is over three orders of magnitude lower than the one in a silicon crystal[7]. Over the last decades, many efforts have been directed at improving the performance of organic optoelectronic devices. If we consider the development OPV, in 2005 the obtained power conversion efficiency (PCE) was in the order of 4-5%, whereas today several groups achieved PCE beyond 15% [58]. These performance improvements reflect the progress in terms of synthesis[29], control of morphology [19], interfaces[59,60], to mention a few examples.

Regarding interfaces, the quality of electrical contacts is an important aspect for all types of devices[61]. A good interface between the semiconducting active layer and the electrodes assures an efficient injection and collection of charges. In this context, doped conjugated polymers are of great interest to provide efficient ohmic contacts in electronic devices.

Scalability

As one might imagine, fabricating $1mm^2$ devices is considerably different from, for example, $1m^2$ devices. The transfer of technology from a spin coating fabrication inside a glovebox to a large area roll-to-roll (R2R) printing in the ambient atmosphere is challenging[62]. To be compatible with printed electronics, i.e. large scale production, the fabrication processes of materials and devices should be scalable, reliable, and cost effective[63]. Over the last years, some companies started the challenge of large scale fabrication of organic devices. One can mention OPVIUS and Armor for printed organic solar cells, Heliatek for evaporated ones, and ISORG for organic photodetectors.

In terms of materials, the first challenge concerns the actual price of the raw materials. For example, conjugated polymers with high performances usually require several synthesis steps and present low yield, which directly impacts their price. To lower the prices, the polymer synthesis should focus on fewer steps and higher yields. Besides, the price of raw polymers is strictly related to demand. Increasing the production volume is also an effective way of reducing the price of a product. However, the latter depends on the commercialization of organic devices. The second challenge in terms of material concerns the batch-to-batch reproducibility, since a high quality control of devices is required for industrial-scale production.

Now if we consider the processing, despite the challenge of achieving homogeneous layers in large areas, there are other important requirements for a process to be scalable. First, to agree with the industrial standards concerning the toxicity of the solvent, they should be halogen-free. Note that several high performing polymers are processed from halogenated solvents due to their poor solubility in halogen-free solvents. However, halogenated solvents are classified as carcinogenic and their use at an industrial-scale is restricted[64]. Another important requirement concerns the drying process: low temperature and quick drying

processes should be favored. Last, the materials should be air processable, i.e. stable at least for short periods of air exposure between different processing steps[62]. The need of air stable OSCs is further discussed in the following.

Finally, to be compatible with large scale production, conjugated polymers do not necessarily need record performances. However, they should present a simple synthesis route, reproducible performances, solubility in halogen-free solvents, simple and low-temperature drying process, and air stability.

Stability and lifetime of devices

Organic devices are commonly composed of a stack of several layers, including mainly a semiconducting active layer sandwiched between electrodes. Often, additional interlayers are included between the active layers and the electrodes (called buffer or blocking layers), to improve the interfaces and the charge collection/injection in the device. Hence, the stability of organic devices involves not only the stability of individual layers towards the fabrication and working conditions (ambient atmosphere, light, and heat) but also the stability of the device as a whole and the interfaces rising from the stacking of different layers.

The permeability of organic layers allows water and molecular oxygen to diffuse through the material and/or device. Therefore, when exposed to ambient conditions, organic semiconductors may undergo chemical reactions leading to significant performance loss over time[65–67]. Oxygen and water are known to react with the low work function materials, degrading electrical contacts of devices[46,65]. Also, photo-oxidation mechanisms can take place in the presence of oxygen and light, where polymers lose their ability to absorb light (see section 1.1.3)[44,45]. Water was also reported to create an insulating metal oxide layer in the interface between the electrode and the active layers of devices[68]. These are only some of the existing degradation routes highlighted in the literature when exposing organic devices to ambient air. A detailed discussion on the impact of oxygen and water traps on the stability of conjugated polymers is presented in chapter 3.

To increase the long-term stability of organic devices, encapsulation is required. Although glass encapsulation is effective to prevent water vapor and oxygen permeation, it renders the device rigid and heavy. Thus, thin-film encapsulation is widely studied to offer an effective gas barrier while preserving the flexibility of organic devices[69]. This is a viable alternative when devices can be prepared under inert atmosphere (argon or nitrogen) and encapsulated before exposing them to working conditions. However, for large-scale fabrication, it is important to have materials that are stable for short periods of air exposure, as technically it is complicated and expensive to consider a production line under an argon or nitrogen atmosphere. Besides, encapsulations are not perfect barriers against oxygen and water[69,70]. They will slow the extrinsic degradation mechanism, but these species will eventually enter the devices. In this context, improving the air-stability of organic devices is a crucial aspect for their future commercialization.

However, the ambient atmosphere is not the only critical degradation factor. Even when protected from atmospheric species, light and heat can provide sufficient stress to induce degradation in organic devices. The working temperature of organic devices is normally far below the decomposition temperature of active materials, but several heat-induced physical degradations have been observed[66,71]. Due to the absence of strong covalent bonds between polymer chains, they present some extent of mobility, especially when the environmental temperature is higher than their glass transition temperature (T_g). Thus, the heat might induce molecular rearrangements that can lead to phase separation in active layers (metastable morphologies)[72,73], or diffusion of atoms and/or molecules in the device[71]. Additionally, photochemical reactions can also result in light-induced degradations in conjugated polymer[46]. Hence, considering the intrinsic stability is also an important step of stability studies, as the discussed mechanisms are also detrimental for the performance or organic devices.

Last, interfaces are also a critical aspect of the stability of organic devices. Despite the significant performance improvement of organic devices by the addition of interlayers, their stability is still an important research subject. For example, electron contacts are often subjected to air instability due to their low ionization potentials (IP)[11,74]. Regarding the hole contacts, despite their higher IP, the commonly used PEDOT:PSS has also been identified as critical for the long-term stability[65,75].

Here, we only mentioned a few of the degradation mechanisms identified in the literature. Nevertheless, this brief discussion aimed to introduce the complexity and importance of studying their intrinsic and extrinsic stability of individual layers and devices.

In conclusion, the main challenges for the years to come can be divided into three axes: performance, stability, and scalability of organic devices. These three aspects are considered in this thesis to explore the potential and the limitations of molecular doped conjugated polymers for organic electronic devices. In the following section, despite providing a background knowledge in doped semiconductor, we present a broad overview of the interest, advances, and challenges in the field of molecular doped OSCs, before presenting the motivation and main objectives of this thesis.

1.2 MOLECULAR DOPING OF ORGANIC SEMICONDUCTORS

Despite the potential of OSCs for the next generation of electronic devices, there are still some challenges that need to be overcome to launch the commercialization of these devices (see section 1.1.4). Over the last years, increasing the performance of OSCs and, consequently, organic electronic devices has been the main focus of scientists in the field, motivated by the limited mobility of charge carriers[20] and the poor electrical contacts of the metal/OSC interfaces[61].

In this context, electrical doping was an important technological breakthrough for the performances of inorganic semiconductors and, consequently, for the multitude of electronic devices present in nowadays society[76]. Electrical doping is a mature technology for inorganic semiconductors and allows controlling or even tuning their electrical properties by increasing the concentration of free charge carriers in the material. Thus, aiming to achieve better performing organic devices, scientists studied techniques to doped OSCs. However, due to the significant chemical and physical differences of inorganic and organic semiconductors, the doping process of OSCs is fundamentally different from the controlled and commercialized doping process of inorganic semiconductors. Therefore, this section aims to provide background knowledge on the principles, mechanisms, and challenges of the doping process in OSCs.

1.2.1 Introduction to doped semiconductors

Electrical doping is a powerful technique to tune the electrical properties of semiconductors. This brief introduction will present the basic concepts of the doping process for inorganic semiconductors to allow a better understanding of the differences and challenges when doping OSCs.

As mentioned above, doping consists in increasing the concentration of free charge carriers in the semiconductors, which is an efficient approach to control the electrical conductivity of the material. As presented in **Equation 1.1**, the electrical conductivity (which is the reciprocal of the electrical resistivity) depends on the charge carrier concentration (electrons n and holes p) and their mobility (μ_e for electrons and $\mu_h$for holes). Hence, it can be defined as a sum of two terms, corresponding to the two types of charge carriers, where e is the elementary charge:

$$\sigma = \frac{1}{\rho} = ne\mu_e + pe\mu_h \qquad \textbf{Equation 1.1}$$

In inorganic semiconductors, the doping process consists in adding small amounts (ppm) of dopant atoms with a different number of valence electrons compared to the host atoms, i.e. the semiconductor. More precisely, atoms having more valence electrons than the semiconductor are *n*-dopants (also called donors) and, analogically, atoms with fewer valence electrons are *p*-dopants (also called donors). Thus, through covalent interactions between dopant and host atoms, electronic "defect" states arise inside the fundamental gap

of the semiconductor as illustrated in **Figure 1.8**. For *n*-doping, the "defect" state corresponds to a donor level slightly below the CB edge whereas for *p*-doping it corresponds to an acceptor level slightly above the VB edge. Exciting electrons from or to the dopant level and consequently creating free charge carriers requires only a few tens of meV, which is considerably less than the energy gap of the semiconductors[15]. Consequently, dopants are ionized at room temperature, increasing the density of mobile electrons (*n*-type doping) or holes (*p*-type doping) that contribute to the conduction in the semiconductor.

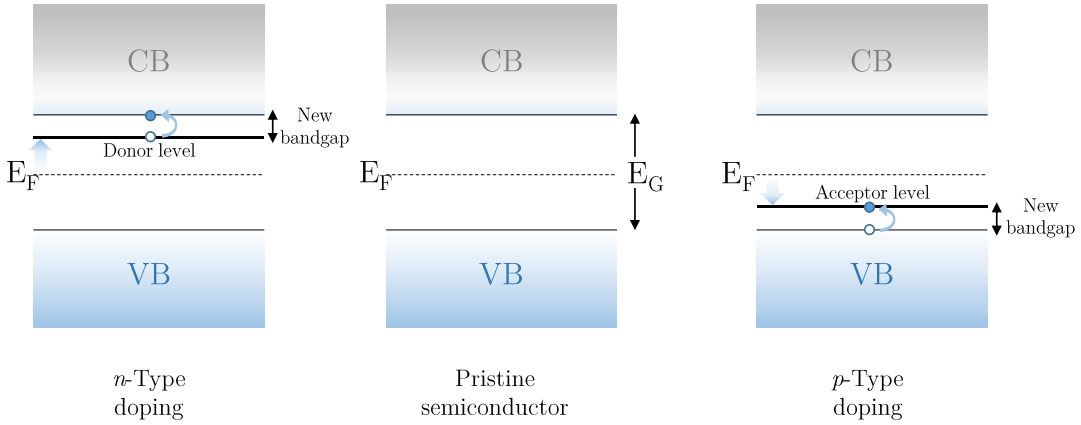

Figure 1.8 – Schematic representation of the *n*-type and *p*-type doping in inorganic semiconductors.

Despite the increase in conductivity, there is a second consequence of the doping process that is particularly important for the fabrication of devices: the fermi level (E_F) shift. By increasing the density of charge carriers in the conduction or valence band, the doping process changes the Fermi-Dirac occupation statistics in the semiconductor. As a result, a shift of E_F towards the VB (*p*-type doping) or CB (*n*-type doping) is observed[77]. Thus, the doping processes also allows tuning the WF of the semiconductor, which is an important tool for engineering surfaces and improving electrical contacts in devices (see section 1.2.6).

For organic semiconductors, the discovery of the possibility of improving the electrical properties of conjugated polymers dates from 1977, when J. Heeger, A. G. MacDiarmid and H. Shirakawa exposed polyacetylene to oxidizing and reducing agents and observed a conductivity increased from below 10^{-5} S cm^{-1} up to 10^{3} S cm^{-1} [6]. These results lead to the Nobel Prize in Chemistry in 2000[6] and triggered the research of organic semiconductors. Note that the existence of conductive polymers had been reported a few years earlier with polysulfur nitride $(SN)_x$, an inorganic polymer that also presented tunable properties when exposed to oxidizing agents[78]. By analogy to the doping of inorganic semiconductors, this process was also referred to as "doping". However, as highlighted by Bredas *et al.*[79], this is a misleading analogy since the doping of OSCs is fundamentally different from that of their inorganic counterparts, owing to their unique chemical structure. The process is best viewed as a redox reaction, where instead of adding donor or acceptor levels inside the bandgap (**Figure 1.8**), the semiconductor is either oxidized (*p*-doping) or reduced (*n*-doping).

The next section presents an overview of the charge carriers in OSCs (e.g. polarons) as well as some important concepts to understand the doping mechanism and the corresponding doping signatures discussed in the following.

1.2.2 Fundamental charge carriers in organic semiconductors

The molecular doping process of conjugated polymer chains occurs via redox reaction, where the neutral semiconducting polymer becomes an ionic complex composed of a polymeric ion (cation or anion) and a counterion (reduced form of the oxidizing agent or oxidized form of the reducing agent). Adding oxidizing agents corresponds to *p*-type doping whereas the addition of reducing agents corresponds to *n*-type doping. In OSCs, the act of injecting or extracting electrons is possible because electrons of π-bonds can be relatively easily removed or added from/to the polymer without disrupting the polymer chains (charge transport), differently from the electrons of σ-bonds, which are primarily responsible for holding the polymer together[79]. Here, we discuss some important fundamental aspects concerning the creation of charged states in conjugated polymers chains. These notions will be important to understand the existing doping mechanism as well as the optoelectronic properties of doped conjugated polymers presented in this thesis.

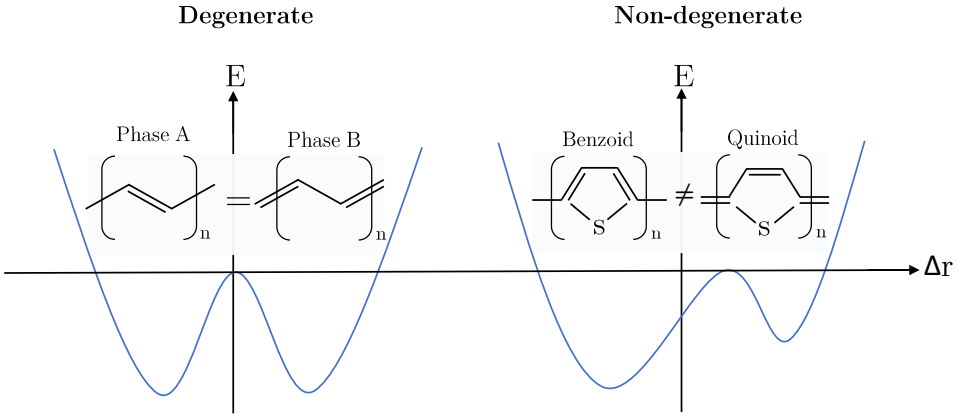

Figure 1.9 – Schematic representation of the potential energy change of different chains configurations, i.e. resonance forms, as a function of the degree of bond length alternation or distortion parameter Δr (Δr=0 when the bond lengths are equal). Left: trans-polyacetylene (degenerate). Right: polythiophene (non-degenerate). Adapted from[80].

In non-polar inorganic semiconductors such as silicon, the coordination of each atom to its neighbor through covalent bonds leads to a rigid structure, which is not influenced by the presence of charge carriers generated by the doping process (mobile electrons or holes). The scenario is considerably different for doped conjugated polymers, related to their susceptibility to structural distortions. As a result, the doping process was reported to create charge carriers that are inherently coupled to chain distortions: polarons (radical ions), bipolarons (dications or dianions), or solitons[79,81]. Note that polarons are also observed in ionic crystals[82] (like NaCl) and polar semiconductor[83] (like GaAs), but they are not reviewed here.

The type of charge carrier in conjugated systems will depend if the ground state is degenerate or non-degenerate, i.e. if it possesses two identical geometric structures with the same energy or two different structures with different energies, respectively (**Figure 1.9**)[84]. Polyacetylene is one example of polymer with a degenerated ground state, since moving one electron pair over one bond results in a geometric structure with the same total energy (**Figure 1.9**, left). This is not the case for non-degenerate systems such as polythiophenes. Moving one electron pair over one bond changes the structure from benzoid to quinoid, which presents higher total energy and a related distortion energy (**Figure 1.9**, right)[80,81]. In this context, solitons are identified as being the charge carriers in degenerate systems, and polarons as well as bipolarons are reported to be the charge carriers in non-degenerate systems[79]. Most of the conjugated polymers present non-degenerate ground state[81].

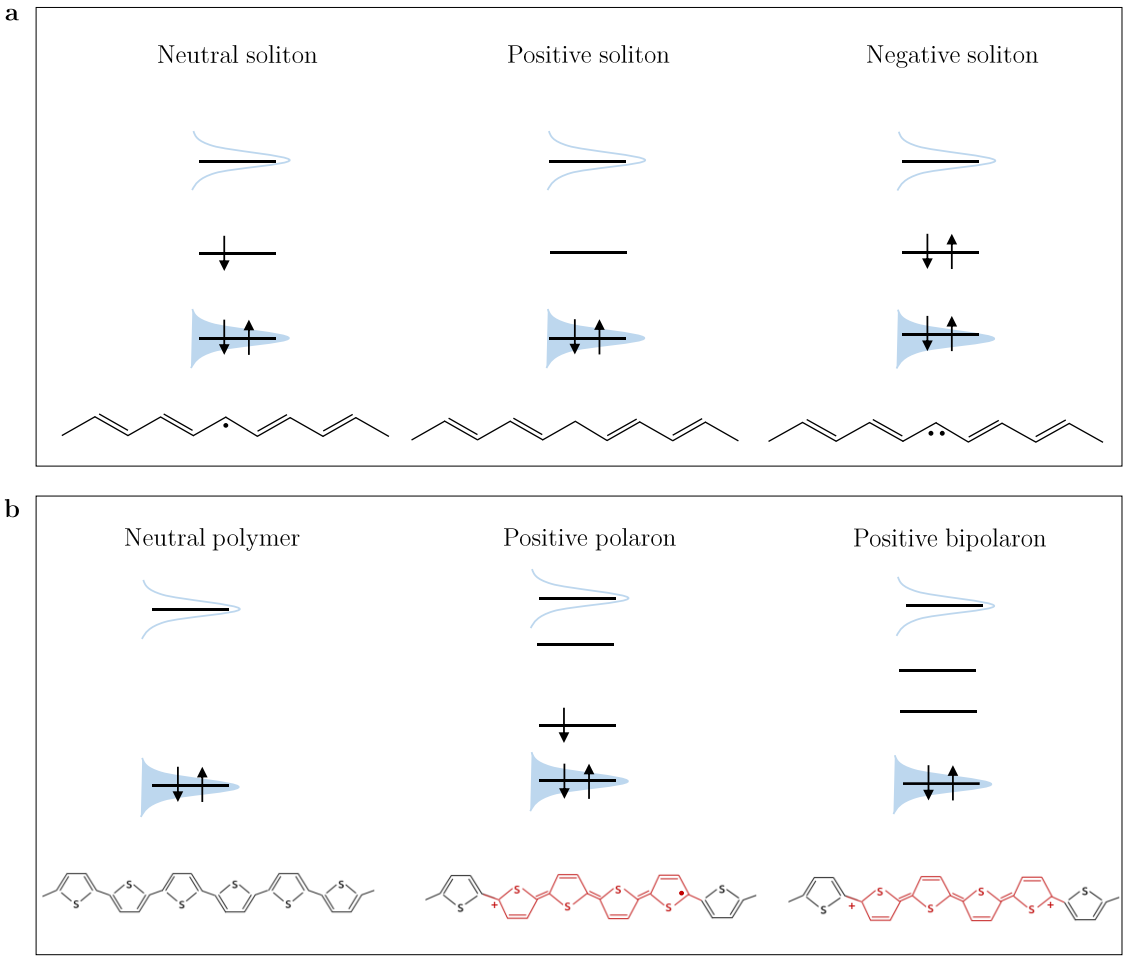

Figure 1.10 –Representation of solitons in polyacetylene (a) and polarons and bipolarons in polytiophene (b).

Solitons in polyacetylene can be neutral or charged, as illustrated in **Figure 1.10**a. Neutral solitons can be seen as defects and appear in carbon chains with an odd number of conjugated carbons. Neutral solitons are radicals containing an unpaired π electron and can propagate without deformations and dissipation by exchanging single and double bonds, as a result of the degenerate ground state[79,84]. Removing or adding electrons to a

polyacetylene chain can create positively and negatively charged solitons, respectively. As illustrated in **Figure 1.10**a, the presence of a soliton leads to the appearance of a localized electronic level at mid-gap, which is half-occupied in the case of a neutral soliton and empty (doubly occupied) in the case of a positively (negatively) charged soliton. As a consequence of the degenerate ground state, charge carriers formed upon oxidation and reduction of the material can move independently along the polymer chain, coulombically repealing one another [85]. A so-called soliton band can be formed by overlapping individual charged soliton chains[84].

In conjugated polymers other than polyacetylene, electrons removed or added to the π-bonded backbone will initially form polarons (radical ions), which may subsequently combine to form bipolarons (dianions or dications). Polarons are localized charges inherently coupled with a local distortion, from example from an benzoid to a quinoid structure[85]. This distortion is actually a relaxation of the lattice to a geometry that is energetically more favorable in the presence of an extra charge (positive or negative). Bipolarons are defined as a pair of like charges confined in the same location and associated to a stronger lattice distortion[79].

Figure 1.10b illustrates the representation of polarons and bipolarons proposed by Heeger and coworkers[81]. Removing an electron from a polymer chains leads to the formation of a polaron and its associated quinoid-like geometrical relaxation localized over a few polythiophene rings (represented by a red region **Figure 1.10**b). As a consequence of this reorganization energy, a shift of the singly occupied states was reported into the energy gap. A positive polaron is represented by a half-occupied HOMO level (radical cations) and negative polarons is represented by half occupied LUMO level (radical anion). In bipolarons, the geometry relaxation is stronger so the bipolaron electronic levels are supposed to shift further away from the band edges of the neutral polymer. Despite the coulomb repulsion between two similar charges, bipolarons were referred as being thermodynamically more stable than polarons due to the more important decrease in ionization energy[79].

This picture of polarons was established in the early 1980's in the organic electronic community and was only recently revisited and critically questioned by Nobert Koch and coworkers[86]. What motivated their research was the fact that the singly occupied polaron levels within the energy gap of the neutral OSCs described by Heeger *et al.* was not experimentally identified by photoelectron spectroscopy. Besides, this traditional polaron picture was developed for a structurally perfect polymer chain of infinite length and without considering electron correlation, which is less likely to be a realistic scenario in molecular doped OSCs.

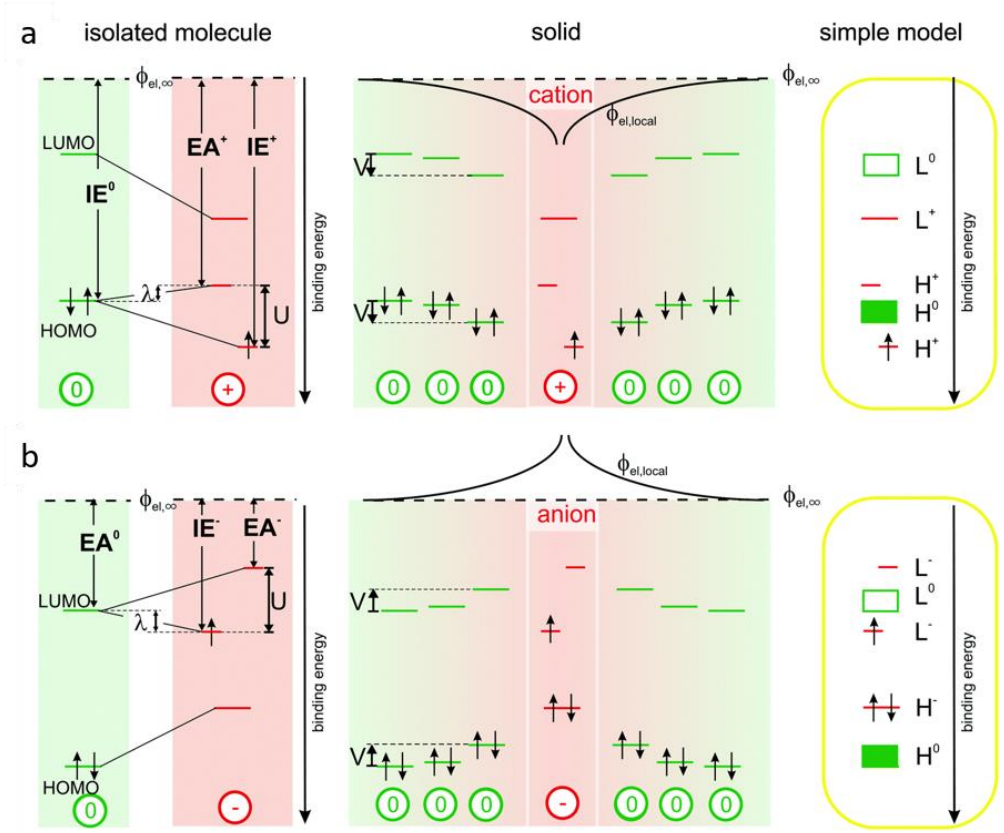

Figure 1.11 - Revised energy levels of polarons in doped OSC (with respect to the vacuum level $\phi_{el,\infty}$): (a) positive polarons: the left panel illustrates the reorganization energy λ in the presence a positive charge and the splitting of the HOMO level due to the on-site Coulomb-interaction U. The middle panel illustrates the energy shift ($\phi_{el,loc}$) of the neutral molecules close to the cations; and the right panel presents a simplified projection of the resulting energy levels. (b) Analogous to (a) for negative polarons. From[86].

The revised energy levels proposed by Koch and coworkers is presented in **Figure 1.11**. In this model, the introduction of an excess of electrons and holes also presented a reorganization energy (λ). However, due to strong on-site coulomb interaction (U – commonly known as Hubbard interactions), the singly occupied polaron level is split into two HOMO-derived sub-levels: an upper unoccupied and a lower occupied sub-level, where only the further is located within the semiconductor gap. They also reported on inter-site Coulomb interaction between neighboring neutral molecules, resulting in a distance dependent shift of the energy levels ($\phi_{el,loc}$) for neutral molecules close to a cation (or anion for *n*-doped OSCs). Thus, differently from the previous model, the ionization energy IE^+ of the cation is higher than the ionization energy of a neutral molecule IE^0, which can be explained by the coulomb attraction in the positively charge region. Analogically, the electron affinity of the anion (EA^-) is now lower than the electron affinity of a neutral molecule EA^0, which was justified by the coulomb repulsion in the negatively charge regions[87]. Recent results published by Peter Ho and coworkers are in agreement with the revised model, where additionally to the Hubbard interaction they also highlighted the energy shift of the frontier orbitals due to Madelung interactions, i.e. off-site coulomb interactions with counterions and other carriers[88].

Summarizing, regardless of the polaron model, charge carriers flowing in semiconducting polymers are coupled with local distortions of polymer chains and give rise to a complex energetic landscape, where the interaction with dopant counterions may also impact the electronic structure.

In this thesis, the presence of polarons is investigated with UV-vis-NIR measurements. For both polaron models discussed above, **Figure 1.12** illustrates the optical transitions expected for neutral (N) and doped (P1 and P2) chains. Only polarons are represented (no bipolarons). In both representations, conventional and revised, the polaronic transitions (P1 and P2) are smaller in energy than the π-π* transition of the neutral polymer chains (N). Hence, doping-related absorption should appear redshifted compared to neutral polymer chains.

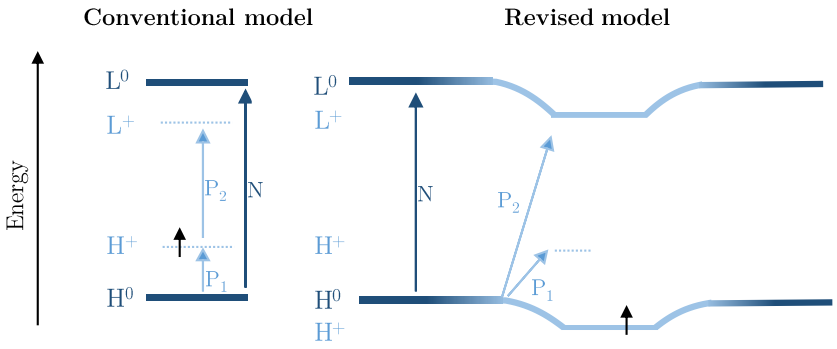

Figure 1.12 Representation of the optical transitions expected in doped conjugated polymers for neutral (N) and doped (P1 and P2) sites: conventional and revised polaron model.

Even though the polaronic transitions P1 and P2 seem similar in both models (**Figure 1.12**), some differences should be highlighted. In the conventional model, the presence of polarons results in localized intragap states, while the energy levels of neutral sites remain unaffected[79,81]. In this model, P1 corresponds to a transition from the HOMO of the neutral polymer (H^0) to the single occupied intragap state (H^+), whereas P2 designates the transition between the intragap states (from H^+ to L^+). In contrast, in the revised model, polarons interact with nearby neutral sites (on-site and inter-site Coulomb interaction), affecting the energy levels of neutral sites close to the charged region (represented by the gradient and the bending of energy levels in **Figure 1.12**, left)[87]. Besides, in this scenario, both polaronic transitions, P1 and P2, involve the HOMO of neutral sites (H^0). Recent results published by Banerji and coworkers on excited state dynamics of doped polymers are consistent with this revised polaron model[89].

Both polaron representations are currently used in the literature. In this thesis, we consider the revised polaron model. Examples of UV-vis-NIR spectra of doped polymers are shown in section 1.2.4, when discussing the mechanism governing the molecular doping of OSCs. In the following, some examples and properties of molecular *p*-dopants are discussed. Besides, we introduce the *p*-dopants that were studied in this thesis.

1.2.3 Molecular dopants

Molecular dopants are neutral, small molecules that can either accept or donate an electron to an OSCs without undergoing any covalent-bond-breaking reaction (reversible electron transfer). Since this thesis only studies *p*-type molecular doping, this section focuses on *p*-dopants, i.e. molecules that accept electrons from the OSC.

P-type molecular dopant should be able to oxidize OSCs, i.e. render the charge transfer process of an electron from the polymer to the dopant favorable (more details on the mechanism are presented in section 1.2.4). Since some OSCs present HOMO energies approaching 6 eV (e.g. 5.9 eV for polyfluorene[90]), maximizing the energy of the LUMO level is an important criterion when designing *p*-type dopant molecules.

As mentioned earlier in this chapter, initial studies on doped OSCs used diatomic halogens Cl_2, Br_2, and I_2 as *p*-type dopants[6]. Due to their volatility, doping was performed in the gas phase, where the dopant diffused into the sample. However, these small dopant molecules were reported to diffuse through and out of the film even at room temperature, leading to unstable doping properties[91,92]. One solution to circumvent the diffusion issue was the use of bigger molecules[59,93]. **Figure 1.13** presents some of the existing *p*-type molecular dopants, which can be classified into two categories: planar and 3D structures. Most *p*-type molecular dopants have an electron-poor core with electron-withdrawing groups such as fluorine, -CF_3, or nitrile functional groups to further reduce the EA.

The most studied *p*-type dopant in the literature, F4TCNQ, is an example of a planar molecular dopant. Its parent structure is TCNQ, an electron acceptor that was extensively studied due to its ability to form charge-transfer salts[94] but whose EA is not high enough to be used as a *p*-dopant for OSCs (-4.3 eV). By replacing hydrogen atoms by fluorine, to form F4TCNQ, researchers were able to increase the EA of this molecule (-5.2 eV)[95]. As shown in **Figure 1.13**, there are other more recent derivatives of TCNQ such as F6TCNNQ[96,97] or F2HCNQ[98], which were synthesized to further increase the EA of this molecular *p*-dopant.

However, despite the suitable energy levels to be used as *p*-dopants, F4TCNQ has shown to be rather prone to diffusion within doped layers, correlated to its volatility and poor sticking coefficient[95,97,99]. To limit the unwanted diffusion, some structural modifications of F4TCNQ were proposed as, for example, replacing fluorine by a bulkier side group[100]. Additionally, attention was drawn to the second dopant category, i.e. bulkier dopants with 3D structures.

Large and three-dimensional dopant molecules were identified as potential candidates for minimizing the diffusion issues in polymeric hosts. One example of this dopant category is $C_{60}F_{36}$, which consists in C_{60} molecules with additional fluorine as electron-withdrawing atoms to increase EA[101]. This *p*-dopant has shown better stability against thermal diffusion compared to F4TCNQ as well as a higher EA[59,102]. Another three-dimensional *p*-dopant that received significant attention in recent years is molybdenum tris-[1,2-

bis(trifluoromethyl)ethane-1,2-dithiolene] ($Mo(tfd)_3$), an organometallic molecule which also presents a stronger oxidizing power compared to F4TCNQ (EA of *ca.* -5.6 eV). This dopant has been well studied in vacuum-deposited samples and demonstrated good stability against diffusion[93,103]. Generally speaking, 3D dopant structures have shown better stability against diffusion when compared to planar molecules.

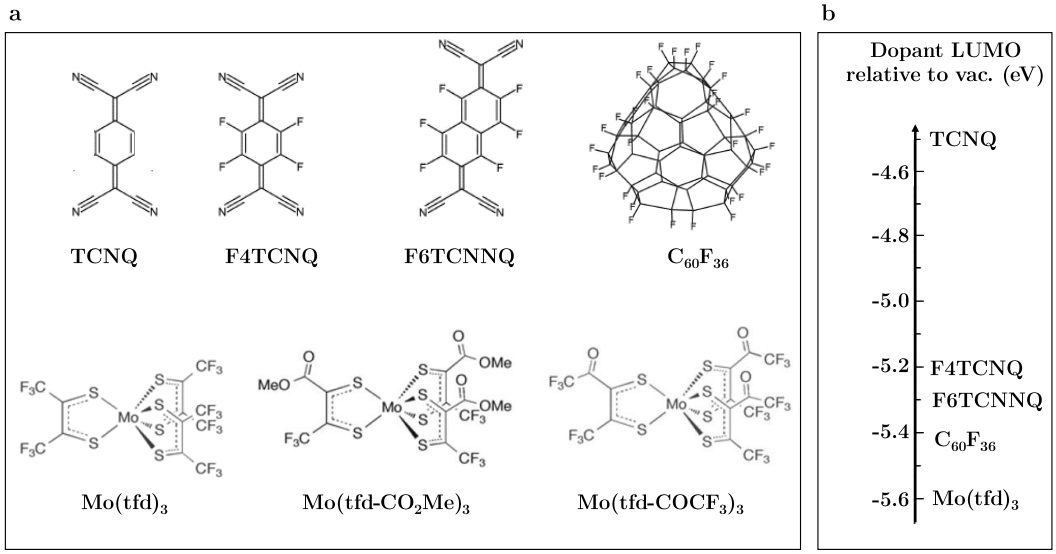

Figure 1.13 – Examples of molecular *p*-dopants and their respective LUMO levels. Adapted from[104].

The aforementioned dopant structures were originally developed to dope conjugated small molecules and, therefore, to be vacuum-processable. Consequently, most of the dopants are poorly soluble or even insoluble in organic solvents. In recent years, molecular doping was extended to conjugated polymers and solution-processable devices, triggering the research and the development of more soluble or miscible dopant molecules.

Recently, some design strategies were identified to tailor the solubility of some existing molecular dopants. For example, to improve the solubility of F4TCNQ in commonly used organic solvents (limited< 1 $g.L^{-1}$), Li *et al.* proposed to replace a nitrile by alkyl ester groups[105]. Another strategy proposed by Kroon *et al.* consists of adding polar side chains to polymer hosts, enabling the use of more polar solvents (e.g., acetonitrile and dimethylformamide)[106]. These solvents offer a better solubility for polar molecular dopants such as F4TCNQ.

Regarding the bulky molecule $Mo(tfd)_3$, the research group of Professor S. R. Marder at the Georgia Institute of Technology designed new derivatives by replacing one - CF_3 group on each side ring with ester or ketone functional groups[107]. As a result, a solubility of up to 10 $g.L^{-1}$ in chlorobenzene was reported for molybdenum tris-[1-(trifluoroethanoyl)-2-(trifluoromethyl)ethane-1,2-dithiolene] ($Mo(tfd\text{-}COCF_3)_3$) and molybdenum tris-[1-(methoxycarbonyl)- 2-(trifluoromethyl) ethane-1,2-dithiolene] ($Mo(tfd\text{-}CO2Me)_3$), where the further presented to be the strongest oxidizing derivative.

In conclusion, bulky and soluble molecular dopants are potential candidates for doping conjugated polymers, as they have shown better stability against diffusion and are adapted

to solution-processable fabrication processes. Besides, their EA should be high enough to allow an electron transfer from the polymer to the dopant (*p*-type doping). Considering these criteria, Mo(tfd-$COCF_3$)$_3$ and Mo(tfd-CO_2Me)$_3$ are potential *p*-type molecular dopant for conjugated polymers, as they present a 3D structure, high EA, and a good solubility in organic solvents.

In this thesis, two molecular dopants are studied: F4TCNQ and Mo(tfd-$COCF_3$)$_3$. The former was chosen as a reference dopant, since it is the most studied molecular *p*-dopant in the literature, and the latter was selected due to the higher solubility and better stability against diffusion.

1.2.4 Current understanding of the doping mechanism

In this section, we present an overview of the current understanding of the doping mechanisms occurring between OSCs and molecular dopants. This section will focus on *p*-type doping since this is the main topic of this thesis. Note that a full analogy of the presented mechanism can be used for *n*-doping.

As presented in the previous sections, *p*-type doping consists in extracting electrons from the OSC, i.e. creating a favorable electron transfer from the HOMO of the polymer to the LUMO of the electron acceptor. Two doping mechanisms were spectroscopically evidenced for several OSCs in the literature: ion-pair formation (IPA), also referred to as ground-state integer charge transfer (ICT), and formation of ground-state charge transfer complexes, where CPX or CTC can be found as acronyms[76]. Since ionized species exhibit characteristic absorption features in the visible (electronic transition) and infrared (vibrations) range of the light spectrum, UV-Vis and FTIR provide valuable information on the nature of charge transfer between OSCs and dopants. Both doping mechanisms are discussed separately below and the different signatures involved in each process are highlighted.

Ion-pair formation (IPA)

A simple picture of this process is illustrated in the top panel of **Figure 1.14**a, where a ground-state integer charge transfer is thought to occur between the HOMO of the OSCs to the LUMO of the dopant, resulting in an ion-pair, i.e. a positive polaron and a dopant anion. For this charge transfer to occur, the EA of the dopant should be equal or higher than the IE of the OSCs. As pointed out by Salzmann and Heimel[108], this representation is inferred from inorganic semiconductor physics but frequently found in the literature for both doped conjugated polymers[39] and conjugated organic molecules[109].

This doping mechanism has been spectroscopically evidenced for numerous OSCs[39,110,111]. **Figure 1.14**a presents UV-vis-NIR (central panel) and FTIR (bottom panel) characteristics of the P3HT:F4TCNQ system[112]. Regarding the UV-vis-NIR spectra, the observed features can be described by a superposition of the F4TCNQ anions and P3HT positive polarons, confirming the formation of an ion-pair. Besides, further evidence for this

doping mechanism is the energy of the C≡N vibrational stretch mode of F4TCNQ (measured by FTIR), which indicates the charge state of the molecule and allows, therefore, quantifying the degree of charge transfer (δ)[113]. According to the literature, when an electron is transferred to F4TCNQ ($\delta = 1$), the stretching mode of C≡N shifts by 33 cm^{-1}, corresponding to the vibration of a F4TCNQ radical anion[112,113]. This shift is observed in the FTIR spectra of P3HT:F4TCNQ (**Figure 1.14**a, bottom panel), further evidencing the formation of an ion-pair in this doped system ($\delta = 1$)[112].

Formation of ground state charge transfer complex (CPX)

For some OSCs:*p*-dopant systems, e.g. 4T:F4TCNQ, the doping signatures cannot be explained by the IPA mechanism, i.e. by the presence of polarons and dopant ions. In these systems, the HOMO of the donor (in this case 4T) and the LUMO of the acceptor (in this case F4TCNQ) were reported to hybridize, forming ground-state charge-transfer complexes (CPX). The formation of CPX creates new local HOMO ($HOMO_{CPX}$) and LUMO ($LUMO_{CPX}$) states, similar to bonding and antibonding states. Regarding the electron distribution, both electrons are located in $HOMO_{CPX}$ (bonding hybrid state), while the $LUMO_{CPX}$ (antibonding hybrid state) remains empty (**Figure 1.14**b, top panel).

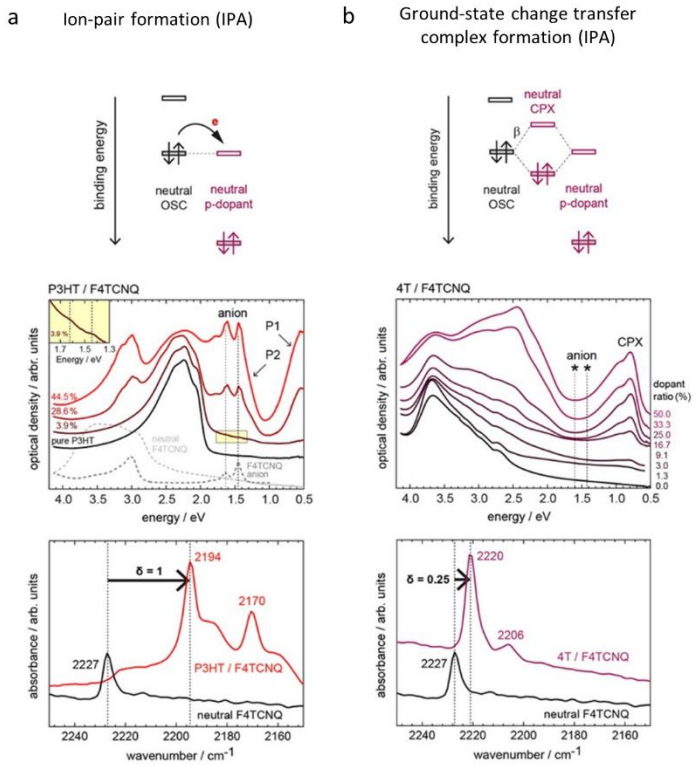

Figure 1.14 - Formation of Ion-pair (IPA) (a, top left) and of ground-state charge transfer complex (CPX) (b, top right). Spectral UV/vis/NIR signatures of IPA and CPX for P3HT:F4TCNQ (a, middle left) and 4T:F4TCNQ (b, middle right), respectively; P1 and P2 denote transitions of positive polarons in P3HT. Spectral FTIR signatures of IPA and CPX for P3HT:F4TCNQ (a, bottom, left) and 4T:F4TCNQ (b, bottom right); charge transfer δ is deduced from the shifts of the cyano vibrations. Adapted from[112].

In this model, the CPX presents an overall neutral charge and needs to be ionized to create mobile holes in the OSC. Since $LUMO_{CPX}$ states lie within the bandgap of OSCs, holes are

created as a consequence of the Fermi-Dirac statistics, resulting in a partial occupation of the $LUMO_{CPX}$ states at room temperature[108]. In this scenario, the generated holes are counterbalanced by ionized CPXs instead of ionized dopant molecules[114,115].

The degree of hybridization and the energetic splitting in CPXs have shown to depend not only on the individual energy levels of OSCs and dopants but also on the structure and orientation of the frontier orbitals[112,116]. The magnitude of the energy level split is often represented by the resonance integral (β), a parameter from the Hückel model referring to the intermolecular coupling between OSC and dopant (**Figure 1.14**b, top panel)[116]. Hence, the fundamental energy gap of the CPX (E_{gap}^{CPX}) is expected to be different for each OSCs:dopant system.

A characteristic UV-vis-NIR spectrum for this doping mechanism also presents optical transitions that grow upon doping, but they correspond neither to polarons nor dopant ions (**Figure 1.14**b, central panel). Besides, for F4TCNQ-doped OSCs, the FTIR spectra presented a smaller shift for the C≡N stretching mode compared to F4TCNQ anions (**Figure 1.14**b, bottom panel), which was interpreted as a partial electron transfer ($\delta < 1$)[112]. Hence, the CPX formation may be compared to polar covalent bonds, where electrons are also shared between atoms[104].

Additional considerations on CPX and IPA

Salzmann and coworkers proposed a unified mechanistic model for the doping process in OSCs, presented in **Figure 1.15** for *p*-doped OSCs[76]. The revised polaron model was used, which takes into account the reorganization energies (λ) and Hubbard (U) interactions related to the presence of charges in OSCs and dopants (see section 1.2.2)[86]. This schema summarizes the actual understanding of the doping mechanism in OSCs in terms of energy levels and DOS. Besides, it brings together the main aspects discussed in this section.

Currently, it is difficult to predict whether CPX or IPA formation will occur in a given OSC:dopant system. Besides, Jacobs *et al.* have recently shown that the doping mechanism of P3HT:F4TCNQ can be selectively chosen by controlling the polymorphism, i.e. packing of the P3HT chain[117]. This result is particularly interesting because it shows that a given OSC:dopant system is not restricted to a single doping mechanism.

In terms of performance, doping through CPX formation has shown to be less effective than doping through IPA. The hybridization process involved in the CPX formation pushes the relevant acceptor level of *p*-dopants into the gap of the OSCs, transforming a strong dopant into a week dopant. Hence, the energy barrier present for CPX ionization (β) and the fermi level pinning between the $LUMO_{CPX}$ and the HOMO level of the neutral OSC are the main reasons for the lower doping efficiencies of this doping mechanism[112,114].

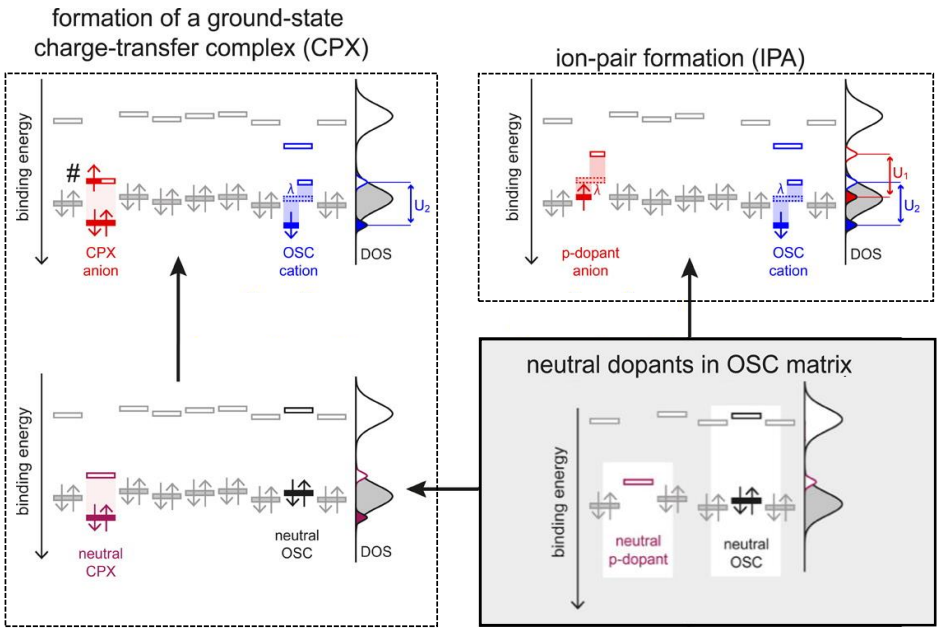

Figure 1.15 – Schematic representation of energy levels and the corresponding density of states (DOS) for molecular *p*-doped OSCs. Both doping mechanism IPA (top right) and CPX (bottom left for neutral CPX and top left for ionized CPX) are illustrated. The reorganization energy(λ) and Hubbard U (U_1 for the dopant and U_2 for the OSCs) are also represented. The levels of the ionized CPX (marked with #) are approximated by those of the neutral species. Adapted from[76].

The formation of CPXs has been reported for numerous conjugated molecules[108,112,116] but also a few examples with conjugated polymers[110,117]. However, to obtain higher doping efficiencies, researchers were interested in favoring the IPA doping mechanism. Increasing the driving force for an electron transfer from the OSCs to the *p*-dopant (i.e. increasing the EA of *p*-dopants) is not sufficient to avoid CPX formation[76]. Planar structures have shown to favor coupling between frontier orbitals resulting in CPX formation[112,114]. Therefore, in addition to high EA, hysterically shielding the frontier orbitals of dopant molecules has shown to be an important design rule to avoid CPX formation[76]. In other words, bulky dopant molecules present less accessible π-orbitals and, consequently, hinder the overlapping with π-orbitals of the OSC and the formation of CPX.

Finally, the doping efficiency in these organic systems is not only dependent on the doping mechanism. In the following section, we discuss the main aspects limiting the doping efficiency in OSCs.

1.2.5 Doping efficiency

The doping efficiency tells us the ratio between the added dopant molecules and the free charge carriers generated through the doping process. For example for *p*-doping, the doping efficiency is defined by p/N_A, where p and N_A represent the concentration in free holes and neutral acceptors (i.e. *p*-type dopants), respectively. For inorganic semiconductors, the doping process is highly efficient, i.e. typically generates one free charge carrier per dopant atom. As a result, ultralow dopant ratios (ppm order$<10^{-5}$) already result in considerable

improvement of electrical conductivity, leaving the crystalline order of the semiconductor unperturbed and therefore retaining the high mobilities of the pristine host[108].

The scenario is considerably different for organic semiconductors. The reported doping efficiencies are much lower (~5% measured for P3HT:F4TCNQ[39]), resulting in doping ratios significantly higher than for inorganic semiconductors, in the order of percent. Therefore, the term blend is commonly employed for doped OSCs. The important amount of dopant molecules added to the OSCs results in structural changes that might be detrimental for the charge transport, especially for crystalline OSCs[118]. Therefore, achieving higher doping efficiencies with lower doping ratios is imperative.

In this context, Kiefer *et al.* explored the fact that *p*-dopants such as F4TCNQ can accept two electrons per molecules, i.e. form dianions[119]. This concept of double doping was efficiently demonstrated for polymers with low IE, to allow a charge transfer to the EA^- of the *p*-dopant (~4.7 eV for F4TCNQ)[119]. Hence, doping efficiencies up to 200% can be reached in these systems.

However, energy levels are important but not the only criteria controlling the doping process. There are several additional explanations for the low doping efficiencies experimentally observed for OSCs: segregation of dopant molecules[120,121], local trapping of free charges[122,123], the formation of CPX states[76,108,112,116] and Coulombic binding between ionized species[39,124,125]. These aspects are discussed below (except for CPX formation that was already discussed in 1.2.4)

The **segregation of dopant molecules** can be related to a lack of miscibility with OSCs[120]. Dopant clusters decrease the intermolecular interaction between both materials, leaving several neutral dopant molecules is the system, which lower the doping efficiency. Besides, additional interface dipoles at phase boundaries may further lower the doping efficiencies[126]. The segregation of dopant molecules was also observed for higher dopant concentrations, associated to a lack of available doping sites are filled[38]. For example, for P3HT:F4TCNQ, the a precipitation of pristine F4TCNQ was observed when the dopant loading exceeded 4:1 (molar ratio)[38,118].

At low doping ratios, the low doping efficiencies were also associated with the **trapping of charge carriers** generated through the doping process. As discussed in 1.1.1, the energy levels of OSCs can be represented by broad Gaussian distributions due to their inherent disorder. These structural and chemical imperfections give rise to so-called tail states, i.e. localized electronic states that extend into the bandgap of OSCs. Tail states act as traps for charge carriers and are, therefore, detrimental for the charge transport and the performance of organic devices. In this context, ultra-low doping ratios (<<1 mol%) have shown to fill tail states and therefore passivate the traps in OSCs[122,127]. This passivation process results in low doping efficiency, as the generated charges get trapped. Nevertheless, this process increases the charge carrier mobility of OSCS and is therefore beneficial for the performance of devices.

The **dissociations of charges** generated through the doping process is also a critical aspect of the low doping efficiencies in OSCs. Despite the intense signatures of ionized dopant molecules and polarons observed in the UV-Vis-NIR spectrum of P3HT:F4TCNQ (see **Figure 1.14**a), Pingel *et al.* reported that only 5% of these molecules release mobile holes into the polymer[39,128]. The remaining holes would still Coulombically interact with ionized dopant molecules and consequently are not available for electrical conduction. Indeed, owing to the low dielectric constant of OSCs, the Coulomb attraction between ionized dopants and charge carriers is typically stronger than in inorganic semiconductors. Usually, thermal energy at room temperature (77meV at 300K) is not high enough to dissociate electron-hole pairs in OSCs[57]. Hence, the doping process was referred to as a two-step process[124,125]. First, it involves the ionization of molecular dopants (or CPX) and the formation of Coulombically bound electron-hole pairs, called charge-transfer complexes (CTCs, or integer charge transfer complexes ICTCs). Subsequently, the CTCs should be dissociated to generate mobile charge carriers. Although the dissociation of CTCs has been investigated over several years[129], the release of doped charge carriers in OSCs is not yet completely understood. It has shown to depend on the energetic disorder in the OSC:dopant system but also on the size and quadrupole moment of the dopant molecules[124,125].

In this context, several groups have studied the correlation between the doping efficiency and the doping ratio, by following the evolution in conductivity and mobility of doped layers. A sublinear conductivity increase is often observed at low to moderate doping ratios, followed by a superlinear increase at high doping ratios[38,125]. According to Arkhipov *et al.*, the conductivity evolution upon doping can be explained by the changes in the mobility of an OSC in the presence of dopant ions[130,131]. In their model, they considered a broadening of the DOS upon doping. Thus, low to moderate doping ratios present a decrease in mobility due to traps generated by dopant anions. At higher doping ratios, the Coulomb potential of individual traps overlaps and lower the barrier for releasing trapped holes, increasing the mobility[130]. In a more recent model proposed by Mityashin *et al.*, the correlation between the doping efficiency and the dopant concentration was explained by the existence of dissociation pathways for CTCs, which arise from the electrostatic energetic disorder introduced by neighboring doping molecules[124].

In summary, the presented discussion highlighted the close correlation between doping efficiency, local structural energetics, and the interaction strength between OSC and dopant. In other words, the doping efficiency seems not only to be specific to each OSC:dopant system but also dependent on the morphology and, consequently, on the processing conditions. This might explain some contradictions in terms of doping efficiency observed in the literature [39,108,124].

1.2.6 Applications for doped organic semiconductors

Molecular doping of OSCs is an increasingly explored tool for optimizing a range of optoelectronic devices. Here, we give a brief overview of how this technique has been applied in devices over the last years.

One very important application of doped layers is contact doping. Improving the charge carrier injection and extraction ensures good ohmic contacts in transistors, LEDs, solar cells, and photodetectors, which is crucial for good performances[132]. Several strategies have been explored over the last years to tailor the interfacial energetics and improve the contact of devices. Adding interlayers between the active layer and the electrodes to adjust their work function is a widely explored solution. Thin layers of zinc oxide (ZnO) or titanium oxide (TiOx) are commonly used to improve electron contacts and molybdenum oxide (MoOx), or PEDOT:PSS for hole contacts[133]. Another strategy consists of creating a dipole at the interface of the metal, which was achieved with self-assembled monolayers (SAMs) or with a thin physisorbed layer of poly(ethylenimine) ethoxylated (PEIE)[133]. In this context, the electrical doping of OSCs is also a valuable technique for interface engineering. It allows a controlled adjustment of the Fermi level and improves the conductivity of the semiconductor, enabling quasi-ohmic contacts between organic layers and metal electrodes[132]. Contact doping has been extremely important to the success of inorganic semiconductors.

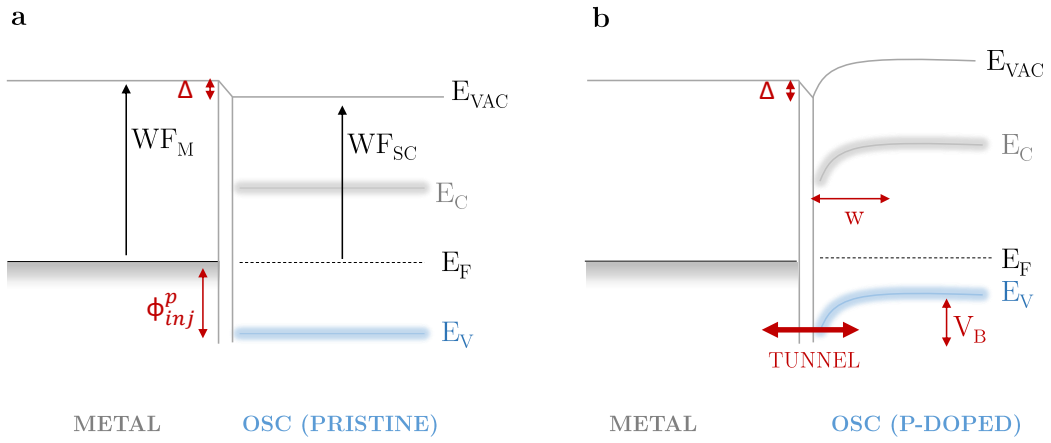

Figure 1.16 – Schematic representation of the energy level diagram between a metal electrode and a pristine (a) and *p*-doped semiconductor (b): Δ represents the interface dipole, w the thickness of the space charge layer (SCL), V_B the built-in voltage and ϕ^p_{inj} the injection barrier for holes.

The advantages of contact doping are illustrated in **Figure 1.16** for hole contacts. To form an ohmic contact between metal and semiconductor, the work function of the metal (WF_M) should be aligned with the corresponding carrier level of the semiconductor, i.e. with E_V (HOMO) levels for holes and E_C (LUMO) levels for electrons. When using intrinsic semiconductors, we are limited by the metals work functions available, and charge injection barriers (ϕ^p_{inj}) are often present (**Figure 1.16**a). With *p*-doped semiconductors, the Fermi level alignment between metal and semiconductor at the interface creates a space charge layer (SCL), whose thickness (w) depends on the doping concentration as well as the built-

in voltage (V_B). The higher the doping concentration, the thinner the SCL, and the stronger the band bending. Consequently, at higher doping concentrations charge carriers can tunnel through the thin SCL leading to quasi-ohmic contacts (**Figure 1.16**b)[132,134]. The thin SCL makes injection possible even if there is a considerable mismatch between the transport levels of the contact material and the organic semiconductor. Therefore, using doped OSCs as interlayers in devices offers the possibility to use a wider range of metallic materials as electrodes, without constraints on their work-function[135].

Additionally, molecular doping is also used to improve the transport properties of organic semiconductors through carrier generation and trap filling in devices [123,127]. Increasing the charge carrier density and consequently improving the electrical conductivity of OSCs is particularly interesting for thermoelectric applications. Compared to inorganic thermoelectric materials, doped polymers have great potential for wearable heating and cooling devices and near-room-temperature energy generation[2,136]. Therefore, highly doped OSCs, i.e. conducting polymers, have received increasing attention. Recently, Brinkmann *et al.* attained the highest electrical conductivity ever reported for an organic semiconductor by rubbing doped films at high temperature (PBTTT:$FeCl_3$ system, σ ~220,000 $S.cm^{-1}$, equivalent to platinum)[137]. Metallic-like electrical conductivities were also achieved with PEDOT, a *p*-doped conductive polymer that has received considerable attention in both academic studies and industrial applications. This polymer presents high conductivities and transparency, as well as good stability under ambient conditions[138]. Differently from the molecular *p*-type doping process presented in this thesis, which happens by exposing conjugated polymers to acceptor molecules, the *p*-doping of PEDOT occurs during the polymerization process (oxidative polymerization of EDOT). An extensive overview of this conductive polymer can be found in[138].

Recently, molecular doping was also used as a patterning tool, by exploring the insoluble character of highly doped semi-crystalline polymers[139].

Depending on the application of doped OSCs, different doping levels and, consequently, different properties are required. When doping contact layers (also called interlayers), we are interested in aligning the Fermi level with the corresponding carrier level to decrease the charge injection barrier in devices. For thermoelectric applications, one might be interested in increasing the electrical conductivity of OSCs to optimize the thermoelectric figure of merit.

In this thesis, we are interested in exploring the potential of molecular doping for nearly amorphous conjugated polymers. D-A conjugated polymers have received very little attention in the literature in their doped state, even though they are widely used in organic solar cells. These polymers present a great potential for doped interlayers in organic devices.

1.2.7 Stability of doped layers

The existing studies on the stability of molecular *p*-doped OSCs are mainly focused on the thermal stability and the diffusion of *p*-dopants in organic hosts. In molecular doped OSCs, the dopant molecules are not covalently bound to the polymer, and the weak van der Waals interaction between polymer chains allows for higher mobility of dopants within the host material[102]. Hence, *p*-dopants may diffuse into other layers within the device under thermal or electronic stress, causing unwanted interaction with other materials and compromising the stability of devices[140].

As discussed in section 1.2.3, the first *p*-dopants used in the literature were di-atoms such as iodine (I_2), bromine (Br_2), and chloride (Cl_2)[141]. However, these dopants are too small and exhibit a tendency to diffuse in organic hosts, resulting in unstable doping properties[91,92]. In this context, larger molecular dopants were introduced to reduce diffusivity. Planar dopants such as F4TCNQ have also shown to diffuse in organic hosts, even at room temperature[142]. Better stabilities against diffusion were obtained with molecular dopants presenting 3D structures such as $C_{60}F_{36}$ and $Mo(tfd)_3$. Increasing the steric hindrance of the host has also shown to be beneficial to limit bias-driven molecular migration in OLEDs[140].

Thermal instability is also a consequence of the week polymer:dopant interaction in molecular doped OSCs. For F4TCNQ-doped OSCs, dopants desorption through thermal annealing was observed at temperatures above 100°C[143,144]. This process was referred to as thermal dedoping since the conductivity and the microstructure of pristine polymers are recovered. When using polar dopants such as F4TCNQ, improved thermal stability was observed when doping hosts with polar side chains[106,142]. These studies suggested that increasing the compatibility of polymer hosts and molecular dopants is also a promising strategy to improve the thermal stability of these systems. Another solution that presented improved thermal stability consists of exchanging conventional *p*-type dopant anions with a second anion provided by an ionic liquid, called anion-exchange[145].

Nevertheless, the stability of the *p*-doped state over time and when exposed to the ambient atmosphere are also crucial aspects to evaluate the potential of *p*-doped OSCs for organic devices. In this context, *n*-type doped OSCs have received considerable attention. Due to the low IE of *n*-type dopants, which is however a requirement for an efficient electron transfer to *n*-type OSCs, these molecules are sensitive to immediate oxidation in ambient air[11]. A literature overview of the stability of pristine and doped OSCs in the presence of oxygen and water is presented in chapter 3 (section 3.1), which deeply investigates the stability of the *p*-doped state under different atmospheres. Here, we aim to highlight that the few existing studies that verified the stability of the *p*-doped state in molecular doped OSCs (under argon and/or ambient atmosphere) observed unstable doping signatures[137,146]. Hence, even though molecular *p*-dopants have shown to be stable in air, the stability of the *p*-doped state (i.e. positive polarons and ionized dopants, or neutral and ionized CPX) should be investigated.

1.3 THESIS OBJECTIVES

1.3.1 Motivations

Doping emerged as a potential technique to improve the performance of organic electronic devices since it allows manipulating the electrical properties of OSCs, for instance improving transport properties as well as electrical contacts of devices (interface engineering)[104,132]. Even though the doping process has been used for years in inorganic semiconductors, the underlying principles are fundamentally different for OSCs. Therefore, to overcome the lack of understanding and consequently improve the doping efficiencies, the research over the last years mainly focused on the fundamental principles governing the molecular doping of OSCs[104].

As discussed throughout this introductory chapter, considerable improvements have been achieved concerning the understanding of electrostatic interactions and the resulting energetic landscape in organic hosts in the presence of molecular dopants. As a result, researchers were able to draw a more precise picture of the underlying doping mechanism in these systems [76,86,112]. Besides, it allowed developing design rules and identifying energetic and structural requirements to improve the doping efficiency[112,117,119,145]. However, researchers are not yet capable of predicting the doping mechanism and the efficiency of a given polymer:dopant system before experimental results, indicating that the key parameters controlling the doping process are not yet completely understood. Additionally, the doping efficiency has shown to be correlated to structural and morphological aspects of the polymer:dopant blend[39,117,147]. In other words, the doping process is not only controlled by the choice of materials but also by processing conditions, as the latter highly impacts the morphology of polymer layers.

In terms of conjugated polymers, most of the existing studies with molecular dopants focused on RR-P3HT and PBTTT, two semi-crystalline polymers, mainly due to the better charge transport properties of semi-crystalline polymer layers. Very few articles reported on the doping of donor:acceptor conjugated polymers, even though they represent the state-of-art polymers for OPV[29,37]. These polymers have a great potential to be used as interlayers in their doped state[135].

Additionally, stability is a crucial factor in the development of organic electronic devices. Therefore, the potential of molecular doping is highly dependent on its stability. As mentioned in section 1.2.7, diffusion was identified as a critical stability issue, especially for small and planar molecular dopants[102,106,142]. This issue has been potentially solved by using bigger molecular dopants with 3D structures[93,102,107]. However, very little attention was given to the stability of the *p*-doped state under argon and ambient atmosphere, although these are crucial aspects for the future integration of these doped layers into printed devices. Only recently, an article questioned the intrinsic stability of the CPX and IPA charge transfer states in *p*-doped layers[146]. Stability studies under ambient air are

mainly performed for *n*-doped OSCs, due to the low IE of molecular dopants and the existence of electron traps in polymer hosts (see 3.1). However, *p*-doped OSCs have also shown unstable doping signatures under ambient air[137,146].

Finally, even though there are still some questions concerning fundamental aspects of the molecular doping process in OSCs, the stability of the *p*-doped state in the presence of oxygen and humidity are key factors to be investigated for the integration of doped layers in organic devices.

1.3.2 Outline

The main objectives of this thesis are to infer the **scalability**, **performance**, and **air stability** of the *p*-doped conjugated polymers to evaluate their potential and limitations for organic electronic devices. This study is interested in *p*-doping disordered hosts, which present great potential as hole transport layers of organic devices and have received little attention in their doped state.

In terms of polymer host, this thesis focused on PBDTTT-c, which is a donor:acceptor polymer widely used as a donor material in OPV cells[30,148]. Additionally, P3HT was selected as a reference polymer, as it has been thoroughly studied in its pristine and doped state[38,104,149]. Since this work is interested in doping disordered polymer hosts, we used RRa-P3HT, which has received much less attention in its doped state due to its amorphous nature.

Regarding the *p*-dopants, Mo(tfd-$COCF_3$)$_3$ is the main dopant studied in this thesis. This molecule was specially developed for *p*-type doping of OSCs in solution, presenting an improved solubility in organic solvents[150]. Besides, its 3D structure was reported to limit the diffusion in OSCs[93,102]. As for the polymer hosts, we added F4TCNQ as a reference dopant molecule to our study. This *p*-dopant was also selected due to its planarity, allowing the comparison between planar and 3D structures.

To investigate the **scalability**, molecular doping was performed in solution and from a non-halogenated solvent (o-Xylene), to be in agreement with the toxicity requirements and with large scale printing techniques. Besides, a particular attention was given to the reproducibility and, consequently, to the control of the doping process, to highlight possible complications and challenges for molecular doping in industrial scale.

In terms of **performance**, we studied the doping signatures of the four polymer:dopant systems considered in this thesis: PBDTTT-c:Mo(tfd-$COCF_3$)$_3$, RR-P3HT:Mo(tfd-$COCF_3$)$_3$, PBDTTT-c:F4TCNQ and our reference system RR-P3HT:F4TCNQ. This comparison allows analyzing the impact of the energy levels, dopant geometry, and polymer nature on the doping limits and mechanisms. As discussed in this chapter, it is still difficult to predict the doping efficiency and mechanism of a given polymer:dopant system before experimental results.

Finally, we investigated the **stability** of free holes and ionized dopant molecules in the presence of humidity and oxygen, but also their intrinsic stability in doped layers. This study was performed by exposing *p*-doped layers to different atmospheres: argon, anhydrous air, and ambient air.

The results will be presented in two main chapters: chapter 2 characterizes the initial properties of pristine materials and presents a thorough investigation of the doping process, to highlight the important parameters and to optimize the doping conditions. Besides, the initial properties of the doped layers are characterized and discussed. Once we analyzed the initial state of our *p*-doped layers, chapter 3 investigates their intrinsic stability as well as their air stability.

1.4 REFERENCES

(1) Al-Fuqaha, A.; Guizani, M.; Mohammadi, M.; Aledhari, M.; Ayyash, M. Internet of Things: A Survey on Enabling Technologies, Protocols, and Applications. *IEEE Commun. Surv. Tutor.* **2015**, *17* (4), 2347–2376. https://doi.org/10.1109/COMST.2015.2444095.

(2) Russ, B.; Glaudell, A.; Urban, J. J.; Chabinyc, M. L.; Segalman, R. A. Organic Thermoelectric Materials for Energy Harvesting and Temperature Control. *Nat. Rev. Mater.* **2016**, *1* (10), 1–14. https://doi.org/10.1038/natrevmats.2016.50.

(3) Chepesiuk, R. Where the Chips Fall: Environmental Health in the Semiconductor Industry. *Environ. Health Perspect.* **1999**, *107* (9), A452–A457.

(4) Jacoby, G. C.; D'Arrigo, R. D. Tree Rings, Carbon Dioxide, and Climatic Change. *Proc. Natl. Acad. Sci.* **1997**, *94* (16), 8350–8353. https://doi.org/10.1073/pnas.94.16.8350.

(5) V. Smil. *Energy Transitions: Global and National Perspectives*; Praeger, An Imprint Of ABC-CLIO, LLC,: Santa Barbara, California, 2017.

(6) Shirakawa, H.; Louis, E. J.; MacDiarmid, A. G.; Chiang, C. K.; Heeger, A. J. Synthesis of Electrically Conducting Organic Polymers: Halogen Derivatives of Polyacetylene, (CH)x. *J. Chem. Soc. Chem. Commun.* **1977**, No. 16, 578–580. https://doi.org/10.1039/C39770000578.

(7) Shaw, J. M.; Seidler, P. F. Organic Electronics: Introduction. *IBM J. Res. Dev.* **2001**, *45* (1), 3–9. https://doi.org/10.1147/rd.451.0003.

(8) Zhou, Y.; Fuentes-Hernandez, C.; Khan, T. M.; Liu, J.-C.; Hsu, J.; Shim, J. W.; Dindar, A.; Youngblood, J. P.; Moon, R. J.; Kippelen, B. Recyclable Organic Solar Cells on Cellulose Nanocrystal Substrates. *Sci. Rep.* **2013**, *3* (1), 1536. https://doi.org/10.1038/srep01536.

(9) G. Nisato, D. Lupo, and S. Ganz. *Organic and Printed Electronics Fundamentals and Applications*; Pan Stanford, 2016.

(10) Nicolai, H. T.; Kuik, M.; Wetzelaer, G. a. H.; Boer, B. de; Campbell, C.; Risko, C.; Brédas, J. L.; Blom, P. W. M. Unification of Trap-Limited Electron Transport in Semiconducting Polymers. *Nat. Mater.* **2012**, *11* (10), 882–887. https://doi.org/10.1038/nmat3384.

(11) Tietze, M. L.; Rose, B. D.; Schwarze, M.; Fischer, A.; Runge, S.; Blochwitz-Nimoth, J.; Lüssem, B.; Leo, K.; Brédas, J.-L. Passivation of Molecular N-Doping: Exploring the Limits of Air Stability. *Adv. Funct. Mater.* **2016**, *26* (21), 3730–3737. https://doi.org/10.1002/adfm.201505092.

(12) Tang, C. W. Two-layer Organic Photovoltaic Cell. *Appl. Phys. Lett.* **1998**, *48* (2), 183. https://doi.org/10.1063/1.96937.

(13) Lund, A.; van der Velden, N. M.; Persson, N.-K.; Hamedi, M. M.; Müller, C. Electrically Conducting Fibres for E-Textiles: An Open Playground for Conjugated Polymers and Carbon Nanomaterials. *Mater. Sci. Eng. R Rep.* **2018**, *126*, 1–29. https://doi.org/10.1016/j.mser.2018.03.001.

(14) Brus, V. V.; Lee, J.; Luginbuhl, B. R.; Ko, S.-J.; Bazan, G. C.; Nguyen, T.-Q. Solution-Processed Semitransparent Organic Photovoltaics: From Molecular Design to Device Performance. *Adv. Mater.* **2019**, *31* (30), 1900904. https://doi.org/10.1002/adma.201900904.

(15) Sze, S. M. *Physics of Semiconductor Devices: 2nd Ed*, 2nd edition.; John Wiley and Sons Ltd: New York, 1981.

(16) Köhler, A.; Bässler, H. *Electronic Processes in Organic Semiconductors: An Introduction*; John Wiley & Sons, 2015.

(17) Kahn, A. Fermi Level, Work Function and Vacuum Level. *Mater. Horiz.* **2015**, *3* (1), 7–10. https://doi.org/10.1039/C5MH00160A.

(18) Electrical Conductivity | Physics.

(19) Brinkmann, M. Structure and Morphology Control in Thin Films of Regioregular Poly(3-Hexylthiophene). *J. Polym. Sci. Part B Polym. Phys.* **2011**, *49* (17), 1218–1233. https://doi.org/10.1002/polb.22310.

(20) Noriega, R.; Rivnay, J.; Vandewal, K.; Koch, F. P. V.; Stingelin, N.; Smith, P.; Toney, M. F.; Salleo, A. A General Relationship between Disorder, Aggregation and Charge Transport in Conjugated Polymers. *Nat. Mater.* **2013**, *12* (11), 1038–1044. https://doi.org/10.1038/nmat3722.

(21) Geoghegan, M.; Hadziioannou, G. *Polymer Electronics*; OUP Oxford, 2013.

(22) Patterson, J.; Bailey, B. C. *Solid-State Physics: Introduction to the Theory*, 2nd ed.; Springer-Verlag: Berlin Heidelberg, 2010. https://doi.org/10.1007/978-3-642-02589-1.

(23) Coropceanu, V.; Cornil, J.; da Silva Filho, D. A.; Olivier, Y.; Silbey, R.; Brédas, J.-L. Charge Transport in Organic Semiconductors. *Chem. Rev.* **2007**, *107* (4), 926–952. https://doi.org/10.1021/cr050140x.

(24) Liu, C.; Huang, K.; Park, W.-T.; Li, M.; Yang, T.; Liu, X.; Liang, L.; Minari, T.; Noh, Y.-Y. A Unified Understanding of Charge Transport in Organic Semiconductors: The Importance of Attenuated Delocalization for the Carriers. *Mater. Horiz.* **2017**, *4* (4), 608–618. https://doi.org/10.1039/C7MH00091J.

(25) Dimitrakopoulos, C. D.; Malenfant, P. R. L. Orga. *Adv. Mater.* **2002**, *14* (2), 99–117. https://doi.org/10.1002/1521-4095(20020116)14:2<99::AID-ADMA99>3.0.CO;2-9.

(26) Leclerc, N.; Chávez, P.; Ibraikulov, O. A.; Heiser, T.; Lévêque, P. Impact of Backbone Fluorination on π-Conjugated Polymers in Organic Photovoltaic Devices: A Review. *Polymers* **2016**, *8* (1). https://doi.org/10.3390/polym8010011.

(27) Clark, J.; Silva, C.; Friend, R. H.; Spano, F. C. Role of Intermolecular Coupling in the Photophysics of Disordered Organic Semiconductors: Aggregate Emission in Regioregular Polythiophene. *Phys. Rev. Lett.* **2007**, *98* (20), 206406. https://doi.org/10.1103/PhysRevLett.98.206406.

(28) Müller, C.; Andersson, L. M.; Peña-Rodríguez, O.; Garriga, M.; Inganäs, O.; Campoy-Quiles, M. Determination of Thermal Transition Depth Profiles in Polymer Semiconductor Films with Ellipsometry. *Macromolecules* **2013**, *46* (18), 7325–7331. https://doi.org/10.1021/ma400871u.

(29) Li, G.; Chang, W.-H.; Yang, Y. Low-Bandgap Conjugated Polymers Enabling Solution-Processable Tandem Solar Cells. *Nat. Rev. Mater.* **2017**, *2* (8), 1–13. https://doi.org/10.1038/natrevmats.2017.43.

(30) Chen, H.-Y.; Hou, J.; Zhang, S.; Liang, Y.; Yang, G.; Yang, Y.; Yu, L.; Wu, Y.; Li, G. Polymer Solar Cells with Enhanced Open-Circuit Voltage and Efficiency. *Nat. Photonics* **2009**, *3* (11), 649–653. https://doi.org/10.1038/nphoton.2009.192.

(31) Liang, Y.; Yu, L. A New Class of Semiconducting Polymers for Bulk Heterojunction Solar Cells with Exceptionally High Performance. *Acc. Chem. Res.* **2010**, *43* (9), 1227–1236. https://doi.org/10.1021/ar1000296.

(32) Assadi, A.; Svensson, C.; Willander, M.; Inganäs, O. Field-effect Mobility of Poly(3-hexylthiophene). *Appl. Phys. Lett.* **1988**, *53* (3), 195–197. https://doi.org/10.1063/1.100171.

(33) Klauk, H. Organic Thin-Film Transistors. *Chem. Soc. Rev.* **2010**, *39* (7), 2643–2666. https://doi.org/10.1039/B909902F.

(34) Böckmann, M.; Schemme, T.; Jong, D. H. de; Denz, C.; Heuer, A.; Doltsinis, N. L. Structure of P3HT Crystals, Thin Films, and Solutions by UV/Vis Spectral Analysis. *Phys. Chem. Chem. Phys.* **2015**, *17* (43), 28616–28625. https://doi.org/10.1039/C5CP03665H.

(35) McFarland, F. M.; Ellis, C. M.; Guo, S. The Aggregation of Poly(3-Hexylthiophene) into Nanowires: With and without Chemical Doping. *J. Phys. Chem. C* **2017**, *121* (8), 4740–4746. https://doi.org/10.1021/acs.jpcc.7b00816.

(36) Gao, J.; Stein, B. W.; Thomas, A. K.; Garcia, J. A.; Yang, J.; Kirk, M. L.; Grey, J. K. Enhanced Charge Transfer Doping Efficiency in J-Aggregate Poly(3-Hexylthiophene) Nanofibers. *J. Phys. Chem. C* **2015**, *119* (28), 16396–16402. https://doi.org/10.1021/acs.jpcc.5b05191.

(37) Liang, Y.; Wu, Y.; Feng, D.; Tsai, S.-T.; Son, H.-J.; Li, G.; Yu, L. Development of New Semiconducting Polymers for High Performance Solar Cells. *J. Am. Chem. Soc.* **2009**, *131* (1), 56–57. https://doi.org/10.1021/ja808373p.

(38) Duong, D. T.; Wang, C.; Antono, E.; Toney, M. F.; Salleo, A. The Chemical and Structural Origin of Efficient P-Type Doping in P3HT. *Org. Electron.* **2013**, *14* (5), 1330–1336. https://doi.org/10.1016/j.orgel.2013.02.028.

(39) Pingel, P.; Neher, D. Comprehensive Picture of P-Type Doping of P3HT with the Molecular Acceptor F4TCNQ. *Phys. Rev. B* **2013**, *87* (11), 115209. https://doi.org/10.1103/PhysRevB.87.115209.

(40) Diao, Y.; Shaw, L.; Bao, Z.; Mannsfeld, S. C. B. Morphology Control Strategies for Solution-Processed Organic Semiconductor Thin Films. *Energy Environ. Sci.* **2014**, *7* (7), 2145–2159. https://doi.org/10.1039/C4EE00688G.

(41) Atthi, N.; Nimittrakoolchai, O.; Jeamsaksiri, W.; Supothina, S.; Hruanun, C.; Poyai, A. Study of Optimization Condition for Spin Coating of the Photoresist Film on Rectangular Substrate by Taguchi Design of an Experiment. *Songklanakarin J. Sci. Technol.* **2009**, *31*.

(42) Chatani, S.; Kloxin, C. J.; Bowman, C. N. The Power of Light in Polymer Science: Photochemical Processes to Manipulate Polymer Formation, Structure, and Properties. *Polym. Chem.* **2014**, *5* (7), 2187–2201. https://doi.org/10.1039/C3PY01334K.

(43) Reese, M. O.; Nardes, A. M.; Rupert, B. L.; Larsen, R. E.; Olson, D. C.; Lloyd, M. T.; Shaheen, S. E.; Ginley, D. S.; Rumbles, G.; Kopidakis, N. Photoinduced Degradation of Polymer and Polymer–Fullerene Active Layers: Experiment and Theory. *Adv. Funct. Mater.* **2010**, *20* (20), 3476–3483. https://doi.org/10.1002/adfm.201001079.

(44) Mateker, W. R.; Heumueller, T.; Cheacharoen, R.; Sachs-Quintana, I. T.; McGehee, M. D.; Warnan, J.; Beaujuge, P. M.; Liu, X.; Bazan, G. C. Molecular Packing and Arrangement Govern the Photo-Oxidative Stability of Organic Photovoltaic Materials. *Chem. Mater.* **2015**, *27* (18), 6345–6353. https://doi.org/10.1021/acs.chemmater.5b02341.

(45) Manceau, M.; Rivaton, A.; Gardette, J.-L.; Guillerez, S.; Lemaître, N. The Mechanism of Photo- and Thermooxidation of Poly(3-Hexylthiophene) (P3HT) Reconsidered. *Polym. Degrad. Stab.* **2009**, *94* (6), 898–907. https://doi.org/10.1016/j.polymdegradstab.2009.03.005.

(46) Mateker, W. R.; McGehee, M. D. Progress in Understanding Degradation Mechanisms and Improving Stability in Organic Photovoltaics. *Adv. Mater.* **2017**, *29* (10), 1603940. https://doi.org/10.1002/adma.201603940.

(47) Kearns, D. R. Physical and Chemical Properties of Singlet Molecular Oxygen. *Chem. Rev.* **1971**, *71* (4), 395–427. https://doi.org/10.1021/cr60272a004.

(48) Soon, Y. W.; Cho, H.; Low, J.; Bronstein, H.; McCulloch, I.; Durrant, J. R. Correlating Triplet Yield, Singlet Oxygen Generation and Photochemical Stability in Polymer/Fullerene Blend Films. *Chem. Commun.* **2013**, *49* (13), 1291–1293. https://doi.org/10.1039/C2CC38243A.

(49) Perthué, A.; Fraga Domínguez, I.; Verstappen, P.; Maes, W.; Dautel, O. J.; Wantz, G.; Rivaton, A. An Efficient and Simple Tool for Assessing Singlet Oxygen Involvement in the Photo-Oxidation of Conjugated Materials. *Sol. Energy Mater. Sol. Cells* **2018**, *176*, 336–339. https://doi.org/10.1016/j.solmat.2017.10.019.

(50) Manceau, M.; Rivaton, A.; Gardette, J.-L. Involvement of Singlet Oxygen in the Solid-State Photochemistry of P3HT. *Macromol. Rapid Commun.* **2008**, *29* (22), 1823–1827. https://doi.org/10.1002/marc.200800421.

(51) Silva, H. S.; Domínguez, I. F.; Perthué, A.; Topham, P. D.; Bussière, P.-O.; Hiorns, R. C.; Lombard, C.; Rivaton, A.; Bégué, D.; Pépin-Donat, B. Designing Intrinsically Photostable Low Band Gap Polymers: A Smart Tool Combining EPR Spectroscopy and DFT Calculations. *J. Mater. Chem. A* **2016**, *4* (40), 15647–15654. https://doi.org/10.1039/C6TA05455B.

(52) Soon, Y. W.; Shoaee, S.; Ashraf, R. S.; Bronstein, H.; Schroeder, B. C.; Zhang, W.; Fei, Z.; Heeney, M.; McCulloch, I.; Durrant, J. R. Material Crystallinity as a Determinant of Triplet Dynamics and Oxygen Quenching in Donor Polymers for Organic Photovoltaic Devices. *Adv. Funct. Mater.* **2014**, *24* (10), 1474–1482. https://doi.org/10.1002/adfm.201302612.

(53) Manceau, M.; Bundgaard, E.; Carlé, J. E.; Hagemann, O.; Helgesen, M.; Søndergaard, R.; Jørgensen, M.; Krebs, F. C. Photochemical Stability of π-Conjugated Polymers for Polymer Solar Cells: A Rule of Thumb. *J. Mater. Chem.* **2011**, *21* (12), 4132–4141. https://doi.org/10.1039/C0JM03105D.

(54) Seemann, A.; Sauermann, T.; Lungenschmied, C.; Armbruster, O.; Bauer, S.; Egelhaaf, H.-J.; Hauch, J. Reversible and Irreversible Degradation of Organic Solar Cell Performance by Oxygen. *Sol. Energy* **2011**, *85* (6), 1238–1249. https://doi.org/10.1016/j.solener.2010.09.007.

(55) Zhuo, J.-M.; Zhao, L.-H.; Png, R.-Q.; Wong, L.-Y.; Chia, P.-J.; Tang, J.-C.; Sivaramakrishnan, S.; Zhou, M.; Ou, E. C.-W.; Chua, S.-J.; Sim, W.-S.; Chua, L.-L.; Ho, P. K.-H. Direct Spectroscopic Evidence for a Photodoping Mechanism in Polythiophene and Poly(Bithiophene-Alt-Thienothiophene) Organic Semiconductor Thin Films Involving Oxygen and Sorbed Moisture. *Adv. Mater.* **2009**, *21* (46), 4747–4752. https://doi.org/10.1002/adma.200901120.

(56) Liao, H.-H.; Yang, C.-M.; Liu, C.-C.; Horng, S.-F.; Meng, H.-F.; Shy, J.-T. Dynamics and Reversibility of Oxygen Doping and De-Doping for Conjugated Polymer. *J. Appl. Phys.* **2008**, *103* (10), 104506. https://doi.org/10.1063/1.2917419.

(57) Bässler, H.; Köhler, A. Charge Transport in Organic Semiconductors. In *Unimolecular and Supramolecular Electronics I: Chemistry and Physics Meet at Metal-Molecule Interfaces*;

Metzger, R. M., Ed.; Topics in Current Chemistry; Springer Berlin Heidelberg: Berlin, Heidelberg, 2012; pp 1–65. https://doi.org/10.1007/128_2011_218.

(58) Green, M. A.; Dunlop, E. D.; Levi, D. H.; Hohl-Ebinger, J.; Yoshita, M.; Ho-Baillie, A. W. Y. Solar Cell Efficiency Tables (Version 54). *Prog. Photovolt. Res. Appl.* **2019**, *27* (7), 565–575. https://doi.org/10.1002/pip.3171.

(59) Meerheim, R.; Olthof, S.; Hermenau, M.; Scholz, S.; Petrich, A.; Tessler, N.; Solomeshch, O.; Lüssem, B.; Riede, M.; Leo, K. Investigation of C60F36 as Low-Volatility p-Dopant in Organic Optoelectronic Devices. *J. Appl. Phys.* **2011**, *109* (10), 103102. https://doi.org/10.1063/1.3590142.

(60) Seah, W.-L.; Tang, C. G.; Png, R.-Q.; Keerthi, V.; Zhao, C.; Guo, H.; Yang, J.-G.; Zhou, M.; Ho, P. K. H.; Chua, L.-L. Interface Doping for Ohmic Organic Semiconductor Contacts Using Self-Aligned Polyelectrolyte Counterion Monolayer. *Adv. Funct. Mater.* **2018**, *27* (18), 1606291. https://doi.org/10.1002/adfm.201606291.

(61) Ma, H.; Yip, H.-L.; Huang, F.; Jen, A. K.-Y. Interface Engineering for Organic Electronics. *Adv. Funct. Mater.* **2010**, *20* (9), 1371–1388. https://doi.org/10.1002/adfm.200902236.

(62) Wantz, G.; Szymanski, R.; Vongsaysy, U.; Hirsch, L.; Chambon, S. Organic Photovoltaics, from Lab to Fab. In *MRS Fall Meeting 2019*; Boston, United States, 2019.

(63) C. Krebs, F.; Tromholt, T.; Jørgensen, M. Upscaling of Polymer Solar Cell Fabrication Using Full Roll-to-Roll Processing. *Nanoscale* **2010**, *2* (6), 873–886. https://doi.org/10.1039/B9NR00430K.

(64) Manufacturing Restricted Substances List (MRSL) & Conformity Guidance: Halogenated Solvents.

(65) Norrman, K.; Madsen, M. V.; Gevorgyan, S. A.; Krebs, F. C. Degradation Patterns in Water and Oxygen of an Inverted Polymer Solar Cell. *J. Am. Chem. Soc.* **2010**, *132* (47), 16883–16892. https://doi.org/10.1021/ja106299g.

(66) Mateker, W. R.; McGehee, M. D. Progress in Understanding Degradation Mechanisms and Improving Stability in Organic Photovoltaics. *Adv. Mater.* **2017**, *29* (10), 1603940. https://doi.org/10.1002/adma.201603940.

(67) Nikolka, M.; Nasrallah, I.; Rose, B.; Ravva, M. K.; Broch, K.; Sadhanala, A.; Harkin, D.; Charmet, J.; Hurhangee, M.; Brown, A.; Illig, S.; Too, P.; Jongman, J.; McCulloch, I.; Bredas, J.-L.; Sirringhaus, H. High Operational and Environmental Stability of High-Mobility Conjugated Polymer Field-Effect Transistors through the Use of Molecular Additives. *Nat. Mater.* **2017**, *16* (3), 356–362. https://doi.org/10.1038/nmat4785.

(68) Cao, H.; He, W.; Mao, Y.; Lin, X.; Ishikawa, K.; Dickerson, J. H.; Hess, W. P. Recent Progress in Degradation and Stabilization of Organic Solar Cells. *J. Power Sources* **2014**, *264*, 168–183. https://doi.org/10.1016/j.jpowsour.2014.04.080.

(69) Cros, S.; de Bettignies, R.; Berson, S.; Bailly, S.; Maisse, P.; Lemaitre, N.; Guillerez, S. Definition of Encapsulation Barrier Requirements: A Method Applied to Organic Solar Cells. *Sol. Energy Mater. Sol. Cells* **2011**, *95*, S65–S69. https://doi.org/10.1016/j.solmat.2011.01.035.

(70) Yu, D.; Yang, Y.-Q.; Chen, Z.; Tao, Y.; Liu, Y.-F. Recent Progress on Thin-Film Encapsulation Technologies for Organic Electronic Devices. *Opt. Commun.* **2016**, *362*, 43–49. https://doi.org/10.1016/j.optcom.2015.08.021.

(71) Müller, C. On the Glass Transition of Polymer Semiconductors and Its Impact on Polymer Solar Cell Stability. *Chem. Mater.* **2015**, *27* (8), 2740–2754. https://doi.org/10.1021/acs.chemmater.5b00024.

(72) He, D.; Du, X.; Zhang, W.; Xiao, Z.; Ding, L. Improving the Stability of P3HT/PC61BM Solar Cells by a Thermal Crosslinker. *J. Mater. Chem. A* **2013**, *1* (14), 4589–4594. https://doi.org/10.1039/C3TA01525D.

(73) Collins, B. A.; Tumbleston, J. R.; Ade, H. Miscibility, Crystallinity, and Phase Development in P3HT/PCBM Solar Cells: Toward an Enlightened Understanding of Device Morphology and Stability. *J. Phys. Chem. Lett.* **2011**, *2* (24), 3135–3145. https://doi.org/10.1021/jz2014902.

(74) Prosa, M.; Tessarolo, M.; Bolognesi, M.; Margeat, O.; Gedefaw, D.; Gaceur, M.; Videlot-Ackermann, C.; Andersson, M. R.; Muccini, M.; Seri, M.; Ackermann, J. Enhanced Ultraviolet Stability of Air-Processed Polymer Solar Cells by Al Doping of the ZnO Interlayer. *ACS Appl. Mater. Interfaces* **2016**, *8* (3), 1635–1643. https://doi.org/10.1021/acsami.5b08255.

(75) Jørgensen, M.; Norrman, K.; Krebs, F. C. Stability/Degradation of Polymer Solar Cells. *Sol. Energy Mater. Sol. Cells* **2008**, *92* (7), 686–714. https://doi.org/10.1016/j.solmat.2008.01.005.

(76) Salzmann, I.; Heimel, G.; Oehzelt, M.; Winkler, S.; Koch, N. Molecular Electrical Doping of Organic Semiconductors: Fundamental Mechanisms and Emerging Dopant Design Rules. *Acc. Chem. Res.* **2016**, *49* (3), 370–378. https://doi.org/10.1021/acs.accounts.5b00438.

(77) Blochwitz, J.; Fritz, T.; Pfeiffer, M.; Leo, K.; Alloway, D. M.; Lee, P. A.; Armstrong, N. R. Interface Electronic Structure of Organic Semiconductors with Controlled Doping Levels. *Org. Electron. Phys. Mater. Appl.* **2001**, *2* (2), 97–104. https://doi.org/10.1016/S1566-1199(01)00016-7.

(78) Labes, M. M.; Love, P.; Nichols, L. F. Polysulfur Nitride - a Metallic, Superconducting Polymer. *Chem. Rev.* **1979**, *79* (1), 1–15. https://doi.org/10.1021/cr60317a002.

(79) Bredas, J. L.; Street, G. B. Polarons, Bipolarons, and Solitons in Conducting Polymers. *Acc. Chem. Res.* **1985**, *18* (10), 309–315. https://doi.org/10.1021/ar00118a005.

(80) Ahn, S.; Jeong, S.-H.; Han, T.-H.; Lee, T.-W. Conducting Polymers as Anode Buffer Materials in Organic and Perovskite Optoelectronics. *Adv. Opt. Mater.* **2017**, *5* (3), 1600512. https://doi.org/10.1002/adom.201600512.

(81) Heeger, A. J. Charge Storage in Conducting Polymers: Solitons, Polarons, and Bipolarons. *Polym. J.* **1985**, *17* (1), 201. https://doi.org/10.1295/polymj.17.201.

(82) Bennett, H. S. F Center in Ionic Crystals: Semicontinuum Polaron Models. *Phys. Rev.* **1968**, *169* (3), 729–745. https://doi.org/10.1103/PhysRev.169.729.

(83) Wu, Z.; Li, H.; Yan, L.; Liu, B.; Tian, Q. The Polaron in a GaAs Film Deposited on AlxGa1−xAs Influenced by the Thickness of the Substrate. *Superlattices Microstruct.* **2013**, *55*, 16–25. https://doi.org/10.1016/j.spmi.2012.11.026.

(84) Le, T.-H.; Kim, Y.; Yoon, H. Electrical and Electrochemical Properties of Conducting Polymers. *Polymers* **2017**, *9* (4), 150. https://doi.org/10.3390/polym9040150.

(85) Ponder, J. F.; Reynolds, J. R. Conducting Polymers: Redox States in Conjugated Systems. In *The WSPC Reference on Organic Electronics: Organic Semiconductors*; Materials and Energy; WORLD SCIENTIFIC, 2016; pp 1–18. https://doi.org/10.1142/9789813148611_0001.

(86) Winkler, S.; Amsalem, P.; Frisch, J.; Oehzelt, M.; Heimel, G.; Koch, N. Probing the Energy Levels in Hole-Doped Molecular Semiconductors. *Mater. Horiz.* **2015**, *2* (4), 427–433. https://doi.org/10.1039/C5MH00023H.

(87) Heimel, G. The Optical Signature of Charges in Conjugated Polymers. *ACS Cent. Sci.* **2016**, *2* (5), 309–315. https://doi.org/10.1021/acscentsci.6b00073.

(88) Png, R.-Q.; Ang, M. C. Y.; Teo, M.-H.; Choo, K.-K.; Tang, C. G.; Belaineh, D.; Chua, L.-L.; Ho, P. K. H. Madelung and Hubbard Interactions in Polaron Band Model of Doped Organic Semiconductors. *Nat. Commun.* **2016**, *7*, 11948. https://doi.org/10.1038/ncomms11948.

(89) Tsokkou, D.; Peterhans, L.; Cao, D. X.; Mai, C.-K.; Bazan, G. C.; Nguyen, T.-Q.; Banerji, N. Excited State Dynamics of a Self-Doped Conjugated Polyelectrolyte. *Adv. Funct. Mater. n/a* (n/a), 1906148. https://doi.org/10.1002/adfm.201906148.

(90) Hu, L.; Liang, J.; Zhong, W.; Guo, T.; Zhong, Z.; Peng, F.; Fan, B.; Ying, L.; Cao, Y. Improving the Electroluminescence Performance of Blue Light-Emitting Poly(Fluorene-Co-Dibenzothiophene-S,S-Dioxide) by Tuning the Intra-Molecular Charge Transfer Effects and Temperature-Induced Orientation of the Emissive Layer Structure. *J. Mater. Chem. C* **2019**, *7* (19), 5630–5638. https://doi.org/10.1039/C9TC00842J.

(91) Parthasarathy, G.; Shen, C.; Kahn, A.; Forrest, S. R. Lithium Doping of Semiconducting Organic Charge Transport Materials. *J. Appl. Phys.* **2001**, *89* (9), 4986–4992. https://doi.org/10.1063/1.1359161.

(92) Jakabovič, J.; Vincze, A.; Kováč, J.; Srnánek, R.; Kováč, J.; Dobročka, E.; Donoval, D.; Heinemeyer, U.; Schreiber, F.; Machovič, V.; Uherek, F. Surface and Interface Analysis of Iodine-Doped Pentacene Structures for OTFTs. *Surf. Interface Anal.* **2011**, *43* (1–2), 518–521. https://doi.org/10.1002/sia.3420.

(93) Qi, Y.; Sajoto, T.; Kröger, M.; Kandabarow, A. M.; Park, W.; Barlow, S.; Kim, E.-G.; Wielunski, L.; Feldman, L. C.; Bartynski, R. A.; Brédas, J.-L.; Marder, S. R.; Kahn, A. A Molybdenum Dithiolene Complex as P-Dopant for Hole-Transport Materials: A Multitechnique Experimental and Theoretical Investigation. *Chem. Mater.* **2010**, *22* (2), 524–531. https://doi.org/10.1021/cm9031623.

(94) Torrance, J. B. The Difference between Metallic and Insulating Salts of Tetracyanoquinodimethone (TCNQ): How to Design an Organic Metal. *Acc. Chem. Res.* **1979**, *12* (3), 79–86. https://doi.org/10.1021/ar50135a001.

(95) Gao, W.; Kahn, A. Controlled P-Doping of Zinc Phthalocyanine by Coevaporation with Tetrafluorotetracyanoquinodimethane: A Direct and Inverse Photoemission Study. *Appl. Phys. Lett.* **2001**, *79* (24), 4040–4042. https://doi.org/10.1063/1.1424067.

(96) Zhang, F.; Kahn, A. Investigation of the High Electron Affinity Molecular Dopant F6-TCNNQ for Hole-Transport Materials. *Adv. Funct. Mater. 28* (1), 1703780. https://doi.org/10.1002/adfm.201703780.

(97) Koech, P. K.; Padmaperuma, A. B.; Wang, L.; Swensen, J. S.; Polikarpov, E.; Darsell, J. T.; Rainbolt, J. E.; Gaspar, D. J. Synthesis and Application of 1,3,4,5,7,8-Hexafluorotetracyanonaphthoquinodimethane (F6-TNAP): A Conductivity Dopant for Organic Light-Emitting Devices. *Chem. Mater.* **2010**, *22* (13), 3926–3932. https://doi.org/10.1021/cm1002737.

(98) Rangger, G. M.; Hofmann, O. T.; Bröker, B.; Zojer, E. A Particularly Strong Organic Acceptor for Tuning the Hole-Injection Barriers in Modern Organic Devices. *Synth. Met.* **2010**, *160* (13), 1456–1462. https://doi.org/10.1016/j.synthmet.2010.05.004.

(99) Bruder, I.; Watanabe, S.; Qu, J.; Müller, I. B.; Kopecek, R.; Hwang, J.; Weis, J.; Langer, N. A Novel P-Dopant with Low Diffusion Tendency and Its Application to Organic Light-Emitting Diodes. *Org. Electron.* **2010**, *11* (4), 589–593. https://doi.org/10.1016/j.orgel.2009.12.019.

(100) Rainbolt, J. E.; Koech, P. K.; Polikarpov, E.; Swensen, J. S.; Cosimbescu, L.; Ruden, A. V.; Wang, L.; Sapochak, L. S.; Padmaperuma, A. B.; Gaspar, D. J. Synthesis and Characterization of P-Type Conductivity Dopant 2-(3-(Adamantan-1-Yl)Propyl)-3,5,6-Trifluoro-7,7,8,8-Tetracyanoquinodimethane. *J. Mater. Chem. C* **2013**, *1* (9), 1876–1884. https://doi.org/10.1039/C3TC00068K.

(101) Solomeshch, O.; Yu, Y. J.; Goryunkov, A. A.; Sidorov, L. N.; Tuktarov, R. F.; Choi, D. H.; Jin, J.-I.; Tessler, N. Ground-State Interaction and Electrical Doping of Fluorinated C60 in Conjugated Polymers. *Adv. Mater.* **2009**, *21* (44), 4456–4460. https://doi.org/10.1002/adma.200900798.

(102) Li, J.; Rochester, C. W.; Jacobs, I. E.; Friedrich, S.; Stroeve, P.; Riede, M.; Moulé, A. J. Measurement of Small Molecular Dopant F4TCNQ and C60F36 Diffusion in Organic Bilayer Architectures. *ACS Appl. Mater. Interfaces* **2015**, *7* (51), 28420–28428. https://doi.org/10.1021/acsami.5b09216.

(103) Qi, Y.; Sajoto, T.; Barlow, S.; Kim, E.-G.; Brédas, J.-L.; Marder, S. R.; Kahn, A. Use of a High Electron-Affinity Molybdenum Dithiolene Complex to p-Dope Hole-Transport Layers. *J. Am. Chem. Soc.* **2009**, *131* (35), 12530–12531. https://doi.org/10.1021/ja904939g.

(104) Jacobs, I. E.; Moulé, A. J. Controlling Molecular Doping in Organic Semiconductors. *Adv. Mater.* **2017**, *29* (42), n/a-n/a. https://doi.org/10.1002/adma.201703063.

(105) Li, J.; Zhang, G.; Holm, D. M.; Jacobs, I. E.; Yin, B.; Stroeve, P.; Mascal, M.; Moulé, A. J. Introducing Solubility Control for Improved Organic P-Type Dopants. *Chem. Mater.* **2015**, *27* (16), 5765–5774. https://doi.org/10.1021/acs.chemmater.5b02340.

(106) Kroon, R.; Kiefer, D.; Stegerer, D.; Yu, L.; Sommer, M.; Müller, C. Polar Side Chains Enhance Processability, Electrical Conductivity, and Thermal Stability of a Molecularly p-Doped Polythiophene. *Adv. Mater.* **2017**, *29* (24), n/a-n/a. https://doi.org/10.1002/adma.201700930.

(107) Mohapatra, S. K.; Zhang, Y.; Sandhu, B.; Fonari, M. S.; Timofeeva, T. V.; Marder, S. R.; Barlow, S. Synthesis, Characterization, and Crystal Structures of Molybdenum Complexes of Unsymmetrical Electron-Poor Dithiolene Ligands. *Polyhedron* **2016**, *116*, 88–95. https://doi.org/10.1016/j.poly.2016.04.025.

(108) Salzmann, I.; Heimel, G. Toward a Comprehensive Understanding of Molecular Doping Organic Semiconductors (Review). *J. Electron Spectrosc. Relat. Phenom.* **2015**, *204*, 208–222. https://doi.org/10.1016/j.elspec.2015.05.001.

(109) Harada, K.; Riede, M.; Leo, K.; Hild, O. R.; Elliott, C. M. Pentacene Homojunctions: Electron and Hole Transport Properties and Related Photovoltaic Responses. *Phys. Rev. B* **2008**, *77* (19), 195212. https://doi.org/10.1103/PhysRevB.77.195212.

(110) Ghani, F.; Opitz, A.; Pingel, P.; Heimel, G.; Salzmann, I.; Frisch, J.; Neher, D.; Tsami, A.; Scherf, U.; Koch, N. Charge Transfer in and Conductivity of Molecularly Doped Thiophene-Based Copolymers. *J. Polym. Sci. Part B Polym. Phys.* **2015**, *53* (1), 58–63. https://doi.org/10.1002/polb.23631.

(111) Gao, W.; Kahn, A. Controlled p Doping of the Hole-Transport Molecular Material N,N′-Diphenyl-N,N′-Bis(1-Naphthyl)-1,1′-Biphenyl-4,4′-Diamine with Tetrafluorotetracyanoquinodimethane. *J. Appl. Phys.* **2003**, *94* (1), 359–366. https://doi.org/10.1063/1.1577400.

(112) Méndez, H.; Heimel, G.; Winkler, S.; Frisch, J.; Opitz, A.; Sauer, K.; Wegner, B.; Oehzelt, M.; Röthel, C.; Duhm, S.; Többens, D.; Koch, N.; Salzmann, I. Charge-Transfer Crystallites as Molecular Electrical Dopants. *Nat. Commun.* **2015**, *6*, 8560. https://doi.org/10.1038/ncomms9560.

(113) Kampar, E.; Neilands, O. Degree of Charge Transfer in Donor-Acceptor Systems of the π-π Type. *Russ. Chem. Rev.* **1986**, *55*, 334–342. https://doi.org/10.1070/RC1986v055n04ABEH003193.

(114) Salzmann, I.; Heimel, G.; Duhm, S.; Oehzelt, M.; Pingel, P.; George, B. M.; Schnegg, A.; Lips, K.; Blum, R.-P.; Vollmer, A.; Koch, N. Intermolecular Hybridization Governs Molecular Electrical Doping. *Phys. Rev. Lett.* **2012**, *108* (3), 035502. https://doi.org/10.1103/PhysRevLett.108.035502.

(115) Heimel, G.; Salzmann, I.; Koch, N. On the Fundamental Processes in Molecular Electrical Doping of Organic Semiconductors. *AIP Conf. Proc.* **2012**, *1456* (1), 148–156. https://doi.org/10.1063/1.4730654.

(116) Méndez, H.; Heimel, G.; Opitz, A.; Sauer, K.; Barkowski, P.; Oehzelt, M.; Soeda, J.; Okamoto, T.; Takeya, J.; Arlin, J.-B.; Balandier, J.-Y.; Geerts, Y.; Koch, N.; Salzmann, I. Doping of Organic Semiconductors: Impact of Dopant Strength and Electronic Coupling. *Angew. Chem. Int. Ed.* **2013**, *52* (30), 7751–7755. https://doi.org/10.1002/anie.201302396.

(117) Jacobs, I. E.; Cendra, C.; Harrelson, T. F.; Valdez, Z. I. B.; Faller, R.; Salleo, A.; Moulé, A. J. Polymorphism Controls the Degree of Charge Transfer in a Molecularly Doped Semiconducting Polymer. *Mater. Horiz.* **2018**, *5* (4), 655–660. https://doi.org/10.1039/C8MH00223A.

(118) Jacobs, I. E.; Aasen, E. W.; Oliveira, J. L.; Fonseca, T. N.; Roehling, J. D.; Li, J.; Zhang, G.; Augustine, M. P.; Mascal, M.; Moulé, A. J. Comparison of Solution-Mixed and Sequentially Processed P3HT:F4TCNQ Films: Effect of Doping-Induced Aggregation on Film Morphology. *J. Mater. Chem. C* **2016**, *4* (16), 3454–3466. https://doi.org/10.1039/C5TC04207K.

(119) Kiefer, D.; Kroon, R.; Hofmann, A. I.; Sun, H.; Liu, X.; Giovannitti, A.; Stegerer, D.; Cano, A.; Hynynen, J.; Yu, L.; Zhang, Y.; Nai, D.; Harrelson, T. F.; Sommer, M.; Moulé, A. J.; Kemerink, M.; Marder, S. R.; McCulloch, I.; Fahlman, M.; Fabiano, S.; Müller, C. Double Doping of Conjugated Polymers with Monomer Molecular Dopants. *Nat. Mater.* **2019**, *18* (2), 149–155. https://doi.org/10.1038/s41563-018-0263-6.

(120) Hamwi, S.; Meyer, J.; Winkler, T.; Riedl, T.; Kowalsky, W. P-Type Doping Efficiency of MoO3 in Organic Hole Transport Materials. *Appl. Phys. Lett.* **2009**, *94* (25), 253307. https://doi.org/10.1063/1.3159824.

(121) Euvrard, J.; Revaux, A.; Bayle, P.-A.; Bardet, M.; Vuillaume, D.; Kahn, A. The Formation of Polymer-Dopant Aggregates as a Possible Origin of Limited Doping Efficiency at High Dopant Concentration. *Org. Electron.* **2018**, *53*, 135–140. https://doi.org/10.1016/j.orgel.2017.11.020.

(122) Olthof, S.; Mehraeen, S.; Mohapatra, S. K.; Barlow, S.; Coropceanu, V.; Brédas, J.-L.; Marder, S. R.; Kahn, A. Ultralow Doping in Organic Semiconductors: Evidence of Trap Filling. *Phys. Rev. Lett.* **2012**, *109* (17), 176601. https://doi.org/10.1103/PhysRevLett.109.176601.

(123) Tietze, M. L.; Pahner, P.; Schmidt, K.; Leo, K.; Lüssem, B. Doped Organic Semiconductors: Trap-Filling, Impurity Saturation, and Reserve Regimes. *Adv. Funct. Mater.* **2015**, *25* (18), 2701–2707. https://doi.org/10.1002/adfm.201404549.

(124) Mityashin, A.; Olivier, Y.; Regemorter, T. V.; Rolin, C.; Verlaak, S.; Martinelli, N. G.; Beljonne, D.; Cornil, J.; Genoe, J.; Heremans, P. Unraveling the Mechanism of Molecular Doping in Organic Semiconductors. *Adv. Mater.* **2012**, *24* (12), 1535–1539. https://doi.org/10.1002/adma.201104269.

(125) Tietze, M. L.; Benduhn, J.; Pahner, P.; Nell, B.; Schwarze, M.; Kleemann, H.; Krammer, M.; Zojer, K.; Vandewal, K.; Leo, K. Elementary Steps in Electrical Doping of Organic Semiconductors. *Nat. Commun.* **2018**, *9* (1). https://doi.org/10.1038/s41467-018-03302-z.

(126) Mayer, T.; Hein, C.; Härter, J.; Mankel, E.; Jaegermann, W. A Doping Mechanism for Organic Semiconductors Derived from SXPS Measurements on Co-Evaporated Films of CuPc and TCNQ and on a TCNQ/CuPc Interface. In *Organic Photovoltaics IX*; International Society for Optics and Photonics, 2008; Vol. 7052, p 705204. https://doi.org/10.1117/12.794606.

(127) Higgins, A.; Mohapatra, S. K.; Barlow, S.; Marder, S. R.; Kahn, A. Dopant Controlled Trap-Filling and Conductivity Enhancement in an Electron-Transport Polymer. *Appl. Phys. Lett.* **2015**, *106* (16), 163301. https://doi.org/10.1063/1.4918627.

(128) Pingel, P.; Zhu, L.; Park, K. S.; Vogel, J.-O.; Janietz, S.; Kim, E.-G.; Rabe, J. P.; Brédas, J.-L.; Koch, N. Charge-Transfer Localization in Molecularly Doped Thiophene-Based Donor Polymers. *J. Phys. Chem. Lett.* **2010**, *1* (13), 2037–2041. https://doi.org/10.1021/jz100492c.

(129) Pfeiffer, M.; Beyer, A.; Fritz, T.; Leo, K. Controlled Doping of Phthalocyanine Layers by Cosublimation with Acceptor Molecules: A Systematic Seebeck and Conductivity Study. *Appl. Phys. Lett.* **1998**, *73* (22), 3202–3204. https://doi.org/10.1063/1.122718.

(130) Arkhipov, V. I.; Heremans, P.; Emelianova, E. V.; Adriaenssens, G. J.; Bässler, H. Charge Carrier Mobility in Doped Semiconducting Polymers. *Appl. Phys. Lett.* **2003**, *82* (19), 3245–3247. https://doi.org/10.1063/1.1572965.

(131) Arkhipov, V. I.; Heremans, P.; Emelianova, E. V.; Bässler, H. Effect of Doping on the Density-of-States Distribution and Carrier Hopping in Disordered Organic Semiconductors. *Phys. Rev. B* **2005**, *71* (4), 045214. https://doi.org/10.1103/PhysRevB.71.045214.

(132) Lüssem, B.; Riede, M.; Leo, K. Doping of Organic Semiconductors. *Phys. Status Solidi A* **2013**, *210* (1), 9–43. https://doi.org/10.1002/pssa.201228310.

(133) Lai, T.-H.; Tsang, S.-W.; Manders, J. R.; Chen, S.; So, F. Properties of Interlayer for Organic Photovoltaics. *Mater. Today* **2013**, *16* (11), 424–432. https://doi.org/10.1016/j.mattod.2013.10.001.

(134) Olthof, S.; Tress, W.; Meerheim, R.; Lüssem, B.; Leo, K. Photoelectron Spectroscopy Study of Systematically Varied Doping Concentrations in an Organic Semiconductor Layer Using a Molecular P-Dopant. *J. Appl. Phys.* **2009**, *106* (10), 103711. https://doi.org/10.1063/1.3259436.

(135) Dai, A.; Zhou, Y.; Shu, A. L.; Mohapatra, S. K.; Wang, H.; Fuentes-Hernandez, C.; Zhang, Y.; Barlow, S.; Loo, Y.-L.; Marder, S. R.; Kippelen, B.; Kahn, A. Enhanced Charge-Carrier Injection and Collection Via Lamination of Doped Polymer Layers p-Doped with a Solution-Processible Molybdenum Complex. *Adv. Funct. Mater.* **2014**, *24* (15), 2197–2204. https://doi.org/10.1002/adfm.201303232.

(136) Beretta, D.; Neophytou, N.; Hodges, J. M.; Kanatzidis, M. G.; Narducci, D.; Martin- Gonzalez, M.; Beekman, M.; Balke, B.; Cerretti, G.; Tremel, W.; Zevalkink, A.; Hofmann, A. I.; Müller, C.; Dörling, B.; Campoy-Quiles, M.; Caironi, M. Thermoelectrics: From History, a Window to the Future. *Mater. Sci. Eng. R Rep.* **2019**, *138*, 100501. https://doi.org/10.1016/j.mser.2018.09.001.

(137) Vijayakumar, V.; Zhong, Y.; Untilova, V.; Bahri, M.; Herrmann, L.; Biniek, L.; Leclerc, N.; Brinkmann, M. Bringing Conducting Polymers to High Order: Toward Conductivities beyond 105 S Cm−1 and Thermoelectric Power Factors of 2 MW M−1 K−2. *Adv. Energy Mater.* **2019**, *9* (24), 1900266. https://doi.org/10.1002/aenm.201900266.

(138) Gueye, M. N.; Carella, A.; Faure-Vincent, J.; Demadrille, R.; Simonato, J.-P. Progress in Understanding Structure and Transport Properties of PEDOT-Based Materials: A Critical Review. *Prog. Mater. Sci.* **2020**, *108*, 100616. https://doi.org/10.1016/j.pmatsci.2019.100616.

(139) Jacobs, I. E.; Aasen, E. W.; Nowak, D.; Li, J.; Morrison, W.; Roehling, J. D.; Augustine, M. P.; Moulé, A. J. Direct-Write Optical Patterning of P3HT Films Beyond the Diffraction Limit. *Adv. Mater.* **2018**, *29* (2), 1603221. https://doi.org/10.1002/adma.201603221.

(140) Liu, C.-P.; Wang, W.-B.; Lin, C.-W.; Lin, W.-C.; Liu, C.-Y.; Kuo, C.-H.; Lee, S.-H.; Kao, W.-L.; Yen, G.-J.; You, Y.-W.; Chang, H.-Y.; Jou, J.-H.; Shyue, J.-J. Molecular Migration Behaviors in Organic Light-Emitting Diodes with Different Host Structures. *Org. Electron.* **2011**, *12* (2), 376–382. https://doi.org/10.1016/j.orgel.2010.12.005.

(141) Brédas, J. L.; Wudl, F.; Heeger, A. J. Polarons and Bipolarons in Doped Polythiophene: A Theoretical Investigation. *Solid State Commun.* **1987**, *63* (7), 577–580. https://doi.org/10.1016/0038-1098(87)90856-8.

(142) Li, J.; Rochester, C. W.; Jacobs, I. E.; Aasen, E. W.; Friedrich, S.; Stroeve, P.; Moulé, A. J. The Effect of Thermal Annealing on Dopant Site Choice in Conjugated Polymers. *Org. Electron.* **2016**, *33*, 23–31. https://doi.org/10.1016/j.orgel.2016.02.029.

(143) Hase, H.; O'Neill, K.; Frisch, J.; Opitz, A.; Koch, N.; Salzmann, I. Unraveling the Microstructure of Molecularly Doped Poly(3-Hexylthiophene) by Thermally Induced Dedoping. *J. Phys. Chem. C* **2018**, *122* (45), 25893–25899. https://doi.org/10.1021/acs.jpcc.8b08591.

(144) Fujimoto, R.; Watanabe, S.; Yamashita, Y.; Tsurumi, J.; Matsui, H.; Kushida, T.; Mitsui, C.; Yi, H. T.; Podzorov, V.; Takeya, J. Control of Molecular Doping in Conjugated Polymers by Thermal Annealing. *Org. Electron.* **2017**, *47*, 139–146. https://doi.org/10.1016/j.orgel.2017.05.019.

(145) Yamashita, Y.; Tsurumi, J.; Ohno, M.; Fujimoto, R.; Kumagai, S.; Kurosawa, T.; Okamoto, T.; Takeya, J.; Watanabe, S. Efficient Molecular Doping of Polymeric Semiconductors Driven by Anion Exchange. *Nature* **2019**, *572* (7771), 634–638. https://doi.org/10.1038/s41586-019-1504-9.

(146) Watts, K. E.; Neelamraju, B.; Ratcliff, E. L.; Pemberton, J. E. Stability of Charge Transfer States in F4TCNQ-Doped P3HT. *Chem. Mater.* **2019**, *31* (17), 6986–6994. https://doi.org/10.1021/acs.chemmater.9b01549.

(147) Euvrard, J.; Revaux, A.; Bayle, P.-A.; Bardet, M.; Vuillaume, D.; Kahn, A. The Formation of Polymer-Dopant Aggregates as a Possible Origin of Limited Doping Efficiency at High Dopant Concentration. *Org. Electron.* **2018**, *53*, 135–140. https://doi.org/10.1016/j.orgel.2017.11.020.

(148) Song, M.; You, D. S.; Lim, K.; Park, S.; Jung, S.; Kim, C. S.; Kim, D.-H.; Kim, D.-G.; Kim, J.-K.; Park, J.; Kang, Y.-C.; Heo, J.; Jin, S.-H.; Park, J. H.; Kang, J.-W. Highly Efficient and Bendable Organic Solar Cells with Solution-Processed Silver Nanowire Electrodes. *Adv. Funct. Mater.* **2013**, *23* (34), 4177–4184. https://doi.org/10.1002/adfm.201202646.

(149) Tang, K.; McFarland, F. M.; Travis, S.; Lim, J.; Azoulay, J. D.; Guo, S. Aggregation of P3HT as a Preferred Pathway for Its Chemical Doping with F4-TCNQ. *Chem. Commun.* **2018**, *54* (84), 11925–11928. https://doi.org/10.1039/C8CC05472J.

(150) Mohapatra, S. K.; Zhang, Y.; Sandhu, B.; Fonari, M. S.; Timofeeva, T. V.; Marder, S. R.; Barlow, S. Synthesis, Characterization, and Crystal Structures of Molybdenum Complexes of Unsymmetrical Electron-Poor Dithiolene Ligands. *Polyhedron* **2016**, *116*, 88–95. https://doi.org/10.1016/j.poly.2016.04.025.

2 MOLECULAR DOPING: PROCESSING AND CHARACTERIZATION

Both organic semiconductors and molecular dopants can be either thermally evaporated or solution-processed. This work considers exclusively solution-based doping techniques. Despite the advantage of avoiding ultrahigh vacuum (UHV) related technologies, solution-processed layers also reduce the amount of material that gets wasted during the deposition process (e.g. materials deposited on the chamber walls). Since organic semiconductors and molecular dopants are still expensive materials, doping via solution-based techniques offers a potential solution for reducing costs, not only in terms of equipment but also in terms of materials.

In this context, several research groups have been studying the molecular doping of conjugated polymer by solution-processed techniques[1]. The doping efficiency[2], the quality of the doped layers[3], and even the doping mechanism[4] have shown to be strongly impacted not only by the choice of the polymer:dopant system but also by the processing conditions. Understanding the aggregation process of pristine and doped polymer chains was reported to be important to improve the doping efficiency, but also to overcome problems related to solubility loss for highly doped semi-crystalline polymers[7–10]. Most of the existing literature has focused on polymers with highly ordered morphologies[11,12]. Since this thesis studies disordered polymer hosts, the processing conditions are studied carefully in this chapter, in order to optimize the existing parameters for this specific scenario.

This chapter starts with an overview of important processing aspects controlling the aggregation of conjugated polymer chains and how their conformation may influence the doping process. Besides, this introductory section also presents a detailed description of the solution-processed doping techniques and their actual challenges. The results are divided into three parts: First, we characterize the pristine materials used in this thesis. The second part studies the doping protocol and highlights the important parameters to achieve a controlled and reproducible doping, considering our processing conditions and materials. Finally, with an optimized doping protocol, the last section of this chapter characterizes and discusses the optical, electrical, and morphological properties of the selected doped systems.

CHAPTER CONTENTS

2.1 BACKGROUND

This section starts with an overview of some processing techniques to improve the electrical properties of conjugated polymers chains. In the second part, we describe the solution-processed doping techniques and highlight some critical parameters discussed in the literature. Last, we summarize the important parameters of the doping process that should be studied in the context of this thesis.

2.1.1 Aggregation of conjugated polymer chains

Due to the week nature of the van der Waals interactions between conjugated polymer chains, these macromolecules present various degrees of conformational freedom[1]. In solution, polymer chains can be solubilized or aggregated. The resulting conformation will depend on the strength of polymer-solvent interactions compared to the polymer-polymer interactions. In other words, fully solubilized chains indicate stronger polymer-solvent interaction, whereas aggregated chains result from π-stacking of similarly planarized chains, i.e., strong polymer-polymer interactions (**Figure 2.1**a, b).

In polymer layers, the microstructures can vary from completely amorphous (**Figure 2.1**c) to semi-crystalline, where both disordered (amorphous) and ordered (crystalline) regions coexist (**Figure 2.1**d, e). There are different types of ordered domains: aggregates designate smaller domains with short-range ordering (**Figure 2.1**d) whereas crystallites are larger domains with long-range periodicity (**Figure 2.1**e). Additionally, depending on the intensity of the interchain and/or intrachain interactions, ordered domains may adopt different polymorphisms, i.e. packing motifs like, for example, J and H-aggregates of P3HT[2,3].

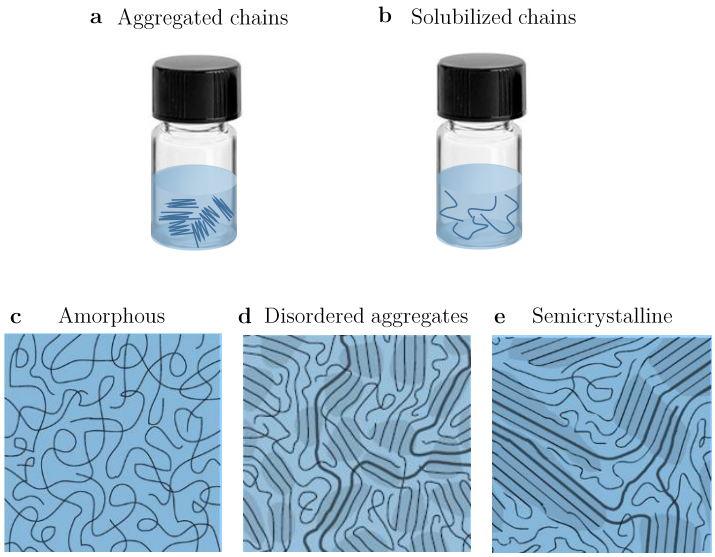

Figure 2.1 – Schematics of ordered and disordered polymer chains. **a-b** different conformation of polymer chains in solution**. c-e** different microstructures of conjugated polymer layers (adapted from [1]). Darker shadowed areas represent ordered domain.

The optoelectronic properties of conjugated polymers will also significantly change depending on the adopted conformation, e.g. if the domains are ordered or disordered. For example, structural disorder induces energetic disorder, and the resulting electronic traps can limit the charge transport in the polymer layer[4,5]. Additionally, the bandgap of semiconducting polymers is also influenced by the conformation of polymer chains, related to the variation in the conjugation length, i.e. length of uninterrupted π-bonds in a conjugated system[6,7]. Note that for OSC, electronic bandgap (E_G) should be distinguished from the optical band gap (E_G^{opt}). The latter corresponds to an excited state (not an ionized state), meaning that electrons remain electrostatically bound to holes (excitons). Due to the low dielectric constant of OSCs, the exciton binding energy in OSCs is in the order of 0.3-0.5 eV[8]. Therefore, the E_G^{opt} is expected to be substantially lower than E_G for OSCs[9].

UV-Vis spectra reveal important morphological aspects related to the organization, i.e. aggregation of polymer chains. A particular advantage of this technique is that the absorption spectra can be measured in solution and solid-state. Disordered domains (amorphous layers or solubilized polymer chains) will display a single broad absorption peak, related to the numerous conformational arrangements of each monomer in the chain (π-π* transitions). Since the conjugation length is shorter in disordered domains than in ordered ones, the absorption spectra will appear at smaller wavelengths, i.e. blue shifted. Ordered domains (semi-crystalline layers or aggregated chains in solution) will display more resolved peaks at higher wavelengths (redshifted), which may be attributed to vibronic transitions of π-π* stacked aggregates[10]. These characteristic features of disordered and ordered conformation can be seen in **Figure 2.2** for different conjugated polymers. Despite morphological aspects, UV-Vis spectra also allow determining the optical band gap (E_G^{opt}) of OSCs, which corresponds to the absorption onset when scanning from low energy photons (high λ) to high energy photons (low λ).

Hence, controlling the morphology of conjugated polymers, i.e. understanding the aggregation processes in solution and thin layers, has proven to be an effective way of tuning and/or optimizing their optoelectronic properties[1,11,12]. Below, we discuss some of the existing processing techniques to manipulate the organization of polymer chains.

Molecular structure

Structure and composition of polymers, i.e. synthesis aspects, highly impact the ordering of polymer chains. For example, the regioregularity of the polymer backbone was reported to influence the packing and therefore the crystallinity of the polymer layer[13]. Ideally, the polymer backbone should be planar to facilitate the π-stacking of polymer chains. Fluorination of polymer backbones has shown to improve the π-stacking by increasing the molecular interaction and therefore the planarity of backbones[14]. One can also mention the choice of alkyl side chains: short alkyl side chains have shown to facilitate the molecular packing, whereas long alkyl side chains were reported to increase the solubility in organic solvents[15]. Regarding the molecular weight (MW) of polymer chains, Noriega *et al.* have shown that disordered aggregates may result in satisfying charge transport if the MW is height enough to ensure a connection between ordered domains (highlighted chains in **Figure 2.1**d)[1].

Solvent choice and solubility

One possible mechanism to drive aggregation is the solubility. Varying the solvent is a direct way of changing the solubility and therefore the interaction of polymer chains in solution (**Figure 2.2**a). A common technique to induce the organization of polymer chains in solution is to modulate the degree of good and poor solvents[4,5]. In a good solvent, the polymer-solvent interactions are strong compared to polymer-polymer interactions, and the individual chains remain fully dissolved, meaning that there is no ordering of the polymer in solution. The addition of a poor solvent results in a driving force for π-stacking and aggregation, as the polymer-polymer interactions become more favorable compared to the polymer-solvent interactions (**Figure 2.2**b). With this technique, highly ordered aggregates such as nanowhiskers, nanowires, or nanoribbons have been reported for P3HT solutions[16,17].

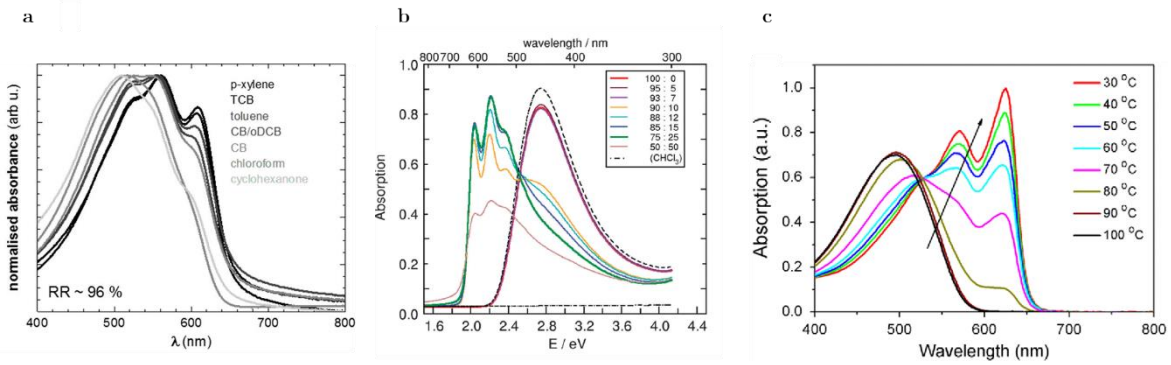

Figure 2.2 - UV-Vis measurement of different techniques controlling the degree of solubilized and aggregated polymer chains in solution: the solvent choice (a)[18], varying the ratio of good and poor solvent chloroform/ethylacetate (b)[7] and varying the temperature of the solution (c)[19]. RR-P3HT is used in (a) and (b), and PffT2-FTAZ (in dichlorobenzene) in (c).

Despite the solvent choice, there are other parameters such as temperature and concentration that influence the solubility of polymer chains. Increasing the polymer concentration favors the aggregation process by increasing the interaction between polymer chains[20]. Regarding the temperature, heating polymer solutions improve their solubility and therefore favor the polymer-solvent interactions[19]. As shown in **Figure 2.2**c, varying the temperature of solutions is an effective strategy to tune between solubilized and aggregated chains.

Solvent evaporation

The solvent evaporation during film formation may also impact the final morphology of polymer layers. Slower drying times result in a more controlled self-assembling of the polymer chains[21]. In this thesis, the polymer layers are processed by spin coating (section 1.1.2, **Figure 1.5**), meaning that the drying process is fast. However, the drying time can be partially controlled by the solvent volatility and also by the airflow, i.e. the spin coating speed.

Post-treatment

The organization of polymer layers can also be improved by post-deposition treatments as, for example, thermal annealing. For semi-crystalline conjugated polymers, thermal annealing was reported to increase the degree of crystallinity and/or to modify the polymorphism of the crystalline phase[22]. Besides, heating up polymer layers may also release residual solvent molecules

not evaporated during the deposition process. Regarding the temperature choice, it depends on the polymer and on the processing solvent, commonly between 100-150°C.

Molecular doping

Molecular doping has also shown to induce aggregation of solubilized polymers chains, resulting in polymer:dopant aggregates[20,23,24,24]. As observed for pristine polymer chains, processing parameters reducing the solubility have been reported to favor doping-induced aggregation[20,25–28]. For example, Albert Salleo's group showed that better doping efficiencies were obtained for layers processed at lower temperatures, presenting a higher concentration of polymer:dopant aggregates[23,27]. They further reported that the doping efficiency of a P3HT:F4TCNQ solutions can be tuned by varying the temperature: heating cycles decreased the doping efficiency and vice-versa[28]. When comparing regioregular and regiorandom P3HT chains, Gao *et al.* propose that regioregular P3HT undergo a more efficient charge-transfer due to a stronger ability to delocalize charge carrier in its aggregated form[24]. In other words, the doping efficiency was correlated with the existence of aggregated polymer chains.

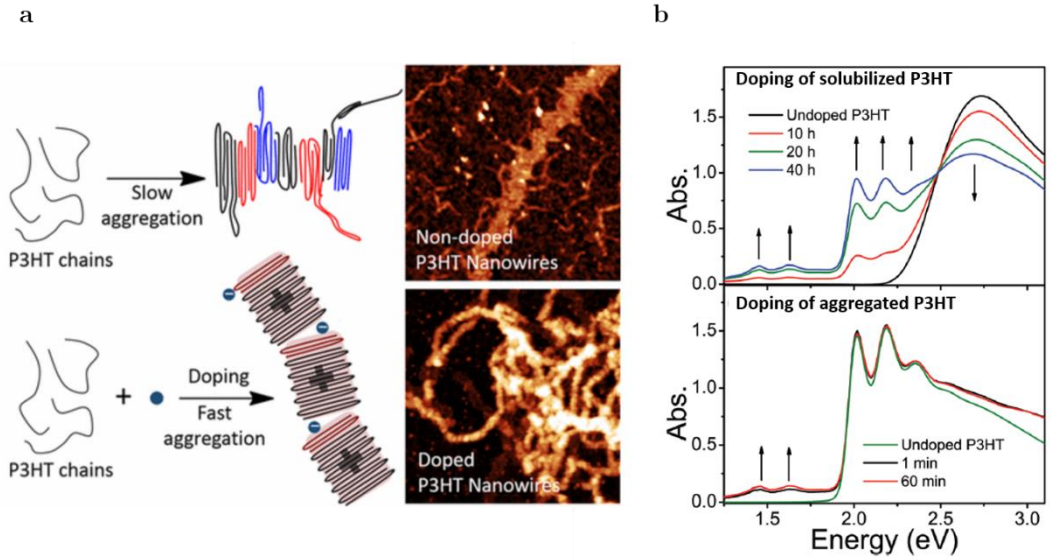

Figure 2.3- a Schematics of the aggregation process of non-doped (above) and doped (below) P3HT chains (from [20]) and b UV-Vis absorption spectra of solubilized (above) and aggregated (below) P3HT solution doped at 5.3 wt% F4TCNQ (adapted from[25]).

In this context, McFarland and coworkers performed several studies to unravel the impact of aggregated polymer chains on the doping process. In a first study, they showed that the doping-induced aggregation is considerably faster compared to the aggregation process of pristine P3HT chains, resulting in more random and disordered P3HT aggregates in the doped state (**Figure 2.3**a). This was explained by the presence of dopant counterions and the complexity of the Coulomb interactions between charged species[20]. Regarding the influence of the conformation of polymer chains on the doping process, they showed that the doping kinetics is considerably faster for aggregated P3HT chains compared to solubilized ones (**Figure 2.3**b)[25]. To explain these results, they propose that the aggregation process of RR-P3HT chains preferentially occurs before the actual charge transfer step takes place with the dopant molecule[26]. Hence, the conformation of polymer chains has shown to strongly impact the chemical doping process.

In conclusion, there are several temperature and solubility-related techniques to manipulate the organization of polymer chains in solution and in thin layers, where one can tune between aggregated or rather amorphous conformations. Chemical doping has also shown to interfere with the conformation of polymer chains, by forming polymer:dopant aggregates that are less ordered than pristine polymer aggregates. Besides, the presence of aggregated polymer chains was reported to be beneficial for the doping efficiency of the system. However, as will be discussed in the following, aggregated polymer chains are not easy to process. Often, one needs to find a trade-off between performance and solubility (or processability) of doped solutions.

2.1.2 Solution-processed doping techniques

There are mainly two methods used in the literature for molecular doping: co-processing and sequential processing. In the further, polymer and dopant are processed simultaneously from the same solution, while in the latter, the polymer layer is processed before incorporating the dopant molecules. Introducing the dopant before or after the solidification of the polymer layer has shown to influence the final morphology and consequently the final properties of doped layers[29]. Below, the main aspects of each technique are discussed and their advantages, as well as their limitations, highlighted.

Co-processing

Co-processing was the first method developed for doping organic semiconductors, where dopant and semiconductor are co-evaporated or co-processed from the same solution[27,30]. Here, we will focus on solution-based processing.

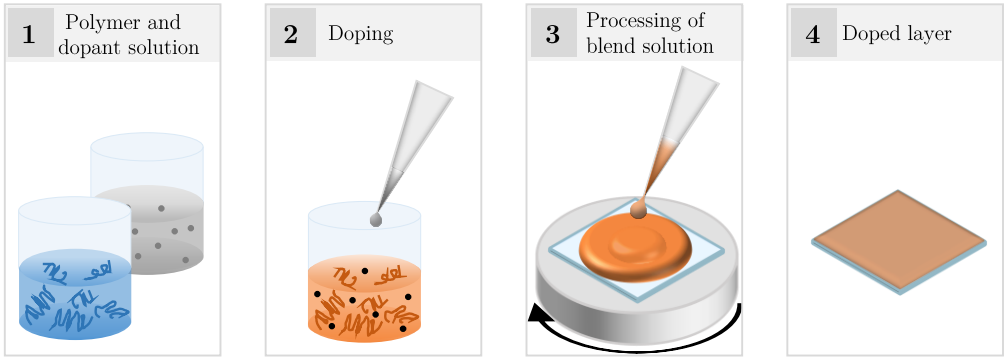

Figure 2.4: Illustration of the co-processing technique, where polymer and dopant solutions are mixed before deposition. Neutral polymer and dopant are represented in blue and gray, respectively, whereas doped polymer chains are represented in orange (and the corresponding ionized dopant molecules in black).

Figure 2.4 illustrates the main processing steps of this doping technique. First, polymer and dopant solutions are prepared separately. This step ensures that both materials are well solubilized and/or dispersed in the chosen solvent before starting the doping process. Then, the volume of the dopant solution corresponding to the desired doping ratio is added to the polymer solution. Finally, the polymer:dopant blend is deposited on a substrate. The schema in **Figure 2.4** illustrates the deposition by spin coating, which was the technique used in this thesis. **Table**

2.1 details the processing parameters of this doping technique. Note that this doping technique normally uses the same solvent or mixture of solvents for both polymer and the dopant solutions.

As mentioned in section 2.1.1, several research groups observed the formation of polymer:dopant aggregates upon the addition of dopant molecules to the polymer solution[23,24,26,27]. Additionally, the doping efficiency presented a correlation with the aggregation process: higher polymer[25] and dopant[27] concentrations, as well as lower stirring temperatures for the blend solution[23,28], favored the formation of polymer:dopant aggregates and at the same time improved the doping efficiency. However, the aggregation process results in a drastic solubility loss, which complicates the processing of doped solutions containing polymer:dopant aggregates[29,31,32]. To avoid inhomogeneous layers with poor electrical properties when using the co-processing technique, polymer solutions are often kept at higher temperatures and processed immediately after mixing the dopant[29]. This strategy consists simply in dissolving the polymer:dopant aggregates or avoiding their formation, ensuring the processability of the solution (and the quality of doped layers) but compromising the doping efficiency[23,28].

Table 2.1 –Parameters for doped layers processed with the co-processing technique.

STEPS	Polymer and dopant solution	Doping (blend solution)	Processing of blend solution
PARAMETERS	Solvent Concentration Stirring temperature Stirring time	Doping ratio Stirring temperature Stirring time	Spin coating conditions Thermal annealing

Hence, the co-processing technique has shown to considerably impact the organization of the polymer chains by the formation of polymer:dopant aggregates already in solution, which may result in processing complications. It is important to highlight that these processing complications related to aggregation and solubility loss have only been reported for semi-crystalline conjugated polymers such as RR-P3HT and PBTTT.

Sequential-processing

As for co-processing, sequential-processing can be performed in solution or via evaporation[18,31]. Here we will only discuss solution-processed layers. The sequential-processing technique is illustrated in **Figure 2.5**. This doping technique consists of two deposition steps: first the polymer and then the dopant molecules, which are incorporated by solid-state diffusion into the polymer layer without disrupting the conjugation[32]. Therefore, doped polymer layers can be processed without significantly impacting the crystallinity of the pristine polymer. This is especially interesting for highly ordered polymers, to preserve the original charge conduction pathways in polymer layers even after the doping process.

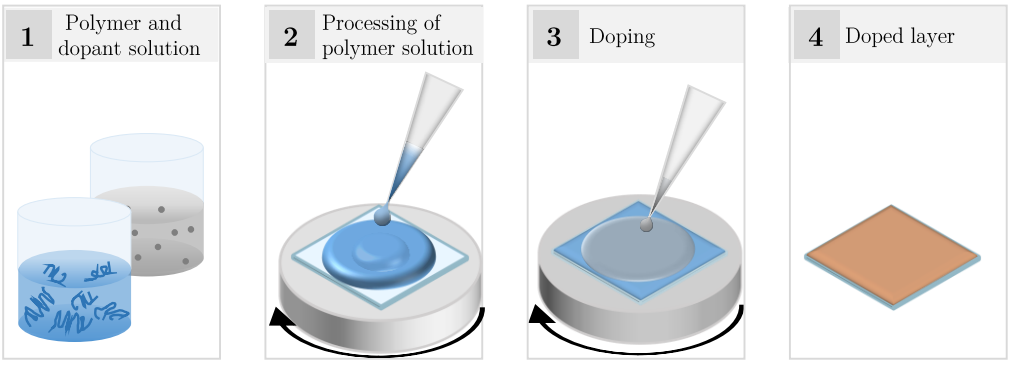

Figure 2.5 - Illustration of the sequential-processing technique. The pristine polymer layer is processed in a first step, followed by the doping with an orthogonal solvent containing the dopant molecules. Neutral polymer and dopant are represented in blue and gray, respectively, whereas the doped polymer layer is represented in orange.

The processing parameters for sequentially-processed layers are summarized in **Table 2.2.** For this two-step deposition technique, the dopant solution is prepared in a solvent orthogonal to the polymer. Jacobs *et al.* emphasized the importance of the choice of the orthogonal solvent, as it may swell the amorphous or the crystalline phase of the polymer layers, controlling the intercalation of dopant molecules[32]. In their study, they observed a higher conductivity at lower doping ratios for dopant anions kept outside the crystalline phase of the polymer layer. The exposure time of the polymer layer to the dopant solution (wetting time) has shown no considerable influence on the doping level of P3HT:F4TCNQ layers, suggesting that a fast equilibrium is reached between neutral F4TCNQ in the solvent and ionized F4TCNQ in the P3HT host[32]. The final doping level for sequentially doped samples was shown to be mainly controlled by the concentration of the dopant solution[29,32].

Table 2.2- Parameters for doped layers processed with the sequential-processing technique.

STEPS	Polymer and dopant solution	Processing of polymer solution	Doping
PARAMETERS	Solvent Concentration Stirring temperature Stirring time	Spin coating conditions Thermal annealing	Wetting time Spin coating conditions Thermal annealing

Finally, this doping technique was reported as a potential solution to overcome the processing issues observed for semi-crystalline polymers doped with the co-processing technique. For RR-P3HT and PBTTT, sequentially-doped layers presented better homogeneity and superior electrical properties compared to co-processed layers[31,32].

Other solution-based doping techniques

To overcome the limited solubility of molecular dopants in organic solvents, Fujimoto *et al.* proposed an adaptation to the sequential doping technique using dopant dispersions, i.e. with dopant molecules that are not necessarily fully dissolved in the solvent[33]. Instead of spin coating the dopant solution from an orthogonal solvent, polymer layers are immersed in an orthogonal solvent with dispersed dopant molecules. The authors highlight that it is important to heat the

system to promote thermal energy for the dopant to migrate to an energetically-favorable location in the polymer layer. Besides, the temperature may also swell polymer layers, allowing the intercalation of dopant molecules.

Strong Lewis acid, such as tris(pentafluorophenyl)borane (BCF), can also be used as *p*-dopant for conjugated polymers[34]. This strategy had been previously identified for tuning the emission color of OSCs used in OLEDs[35,36]. When using the co-processing doping techniques, BCF has the great advantage of being highly soluble in organic solvents, resulting in an improved film quality for higher doping ratios. Oxidative doping was also observed by the immersion of polymer layers into a polyoxometalate solution in nitromethane[37].

Recently, another doping technique was proposed consisting of exchanging the *p*-dopant anion by a second anion provided by an ionic liquid[38]. This technique was called anion exchange and was efficiently demonstrated for PBTTT:F4TCNQ. Spontaneous exchange of the F4TCNQ radical anion with the newly introduce anion (ionic salt) was observed, resulting in increased doping levels (almost one charge per monomer unit) and better thermal stability.

2.1.3 Final considerations

Here, we summarize the positives and negatives aspects highlighted in the literature for the co-processing and sequential-processing technique (**Table 2.3**) and discuss the choice of doping techniques for this work.

Table 2.3– Positive and negative aspects of the co-processing and sequential processing doping techniques. Asterisks (*) indicate aspects that concern semi-crystalline polymer hosts.

	CO-PROCESSING	SEQUENTIAL-PROCESSING
+	• Known dopant concentration • Single deposition step • Single solvent	• Uniform layers even at higher doping levels* • Higher doping efficiencies* • Polymer morphology can be preserved • Better control of the dopant location (amorphous or crystalline domains) in the polymer layer*
-	• Processing complications (polymer:dopant aggregates) at higher doping levels* • Change in polymer morphology • Lower doping efficiencies* • Rougher layers	• Indirect doping level • Two deposition steps • Low solubility of dopant molecules in solvents orthogonal to the polymer

The existing literature investigating the processing conditions of doped conjugated polymers focused mainly on semi-crystalline polymers (PBTTT and RR-P3HT), due to their superior electrical properties. Semi-crystalline polymers present good charge transport properties compared to amorphous polymers, associated with their ability to form aggregates π-π-stacked domains[1,12]. However, in solution, the doping process has shown to interfere in this aggregation process, forming polymer:dopant aggregates with poor solubility in the initial solvent. This doping-induced aggregation process becomes particularly pronounced for higher dopant concentration, limiting the performance and the film quality of doped semi-crystalline hosts. In this context, sequential doping avoids solubility complications related to the doping process and preserves the ordered morphology of semi-crystalline polymer hosts (see section 2.1.2).

When comparing the positive (+) and negative (-) aspects of each doping technique listed in **Table 2.3**, it becomes clear that several advantages and complications were only observed for semi-crystalline polymer hosts (indicated by asterisks). However, only a small fraction of conjugated polymers used for organic devices present semi-crystalline morphologies as PBTTT and RR-P3HT. Therefore, the advantages and complications of each doping technique should also be verified for polymer hosts with less organized morphologies.

In this thesis, we study PBDTTT-c and RRa-P3HT, rather amorphous conjugated polymers. Even though the existence of doping-induced aggregation issues is still to be verified, we chose to work with the co-processing technique. The main reasons for this choice were the direct correlation between the (known) dopant concentration with the conductivity and the fact that the existing literature on PBDTTT-c:Mo(tfd-$COCF_3$)$_3$ employed this technique, which can be used as reference[39–41]. Besides, this technique has also an advantage in terms of simplicity for scalability, since it is a one-step deposition process. To be able to compare both techniques when doping disordered hosts, the sequential-processing technique is briefly tested in 2.4.1, when discussing the maximum conductivities achieved for our doped layers.

2.2 CHARACTERIZATION OF PRISTINE MATERIALS

Independent of the molecular doping technique, the first step consists in preparing pristine polymer and dopant solutions. As indicate in **Table 2.1** and **Table 2.2**, there are several parameters to be chosen, such as solvent, concentration, and stirring conditions. Besides, to infer the impact of the doping process on the optoelectronic properties, it is crucial to characterize the initial state of the involved materials. In this context, this section characterizes pristine polymers, and *p*-dopants studied in this thesis and verifies the impact of process parameters on their initial properties.

The main solvent used in this work is o-Xylene because of its halogen-free composition, an important criterion for the upscaling of organic electronic devices. **Table 2.4** summarizes the characterizations and physical parameters measured for polymer and dopants. For more details on the characterization techniques and measurement setup, see Appendix A.

Table 2.4– Characterization techniques and physical parameters measured in this section.

TECHNIQUE	PHYSICAL PARAMETERS	
	Polymers	Dopants
UV-Vis	• Optical bandgap • π-π* absorption • Aggregation of polymer chains	• Neutral and ionized absorptions
TLM	• Conductivity of pristine polymer layers	-
GIWAXS	• Degree of crystalinity • Lamellar and π-π stacking distance	-
CV	• HOMO and LUMO levels • Electrochemical stability	• LUMO and LUMO-1 levels • Electrochemical stability

This section is organized into three parts. In the first two, we present the characterizations performed on pristine polymers (PBDTTT-c and RRa-P3HT) and *p*-dopants (F4TCNQ and $Mo(tfd\text{-}COCF_3)_3$), respectively. The resulting properties are summarized and discussed in the third and last part.

2.2.1 Pristine Polymers

Several techniques were used to characterize the initial state of PBDTTT-c and RRa-P3HT. First, we present UV-Vis measurements used to determine the π-π* absorption of neutral polymer chains. This characterization is also used to investigate the aggregated state of PBDTTT-c chains that, contrary to RRa-P3HT, do not present completely amorphous signatures. This part is followed by the X-ray scattering measurements (GIWAXS) performed on PBDTTT-c layers, to further characterize their morphology. Then, we present the conductivity of pristine polymer layers, followed by the measurement of the HOMO and LUMO positions by cyclic voltammetry.

UV-Vis absorptions

Contrary to RRa-P3HT, which is known to present amorphous UV-Vis signatures, D–A copolymers as PBDTTT-c were reported to present aggregated chains in solution and thin layers[42]. **Figure 2.6** presents an example of UV-Vis absorption spectra found in the literature for PBDTTT-c and PTB7, the latter being a widely studied D-A polymer. Both spectra are similar, which is in agreement with their similar compositions. For PTB7, the peak at *ca.* 635 nm was attributed to π–π* transitions along the conjugated backbones of the polymer, while the peak at *ca.* 680 nm was attributed to the interchain π–π* transitions due to π–π stacking interactions of adjacent backbones[42,43]. In other words, the peak at higher wavelengths (*ca.* 680 nm) was associated with aggregated PTB7 chains. The same peak assignment was used for π–π* transitions and aggregates in PBDTTT-c chains (**Figure 2.6**).

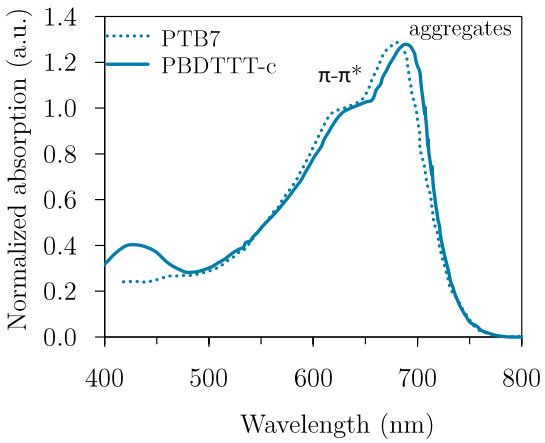

Figure 2.6 –UV-Vis spectra of PBDTTT-c (chloroform)[44] and PTB7 (chlorobenzene) [42] taken from the literature.

Considering the techniques presented in section 2.1.1 to control the aggregation of polymer chains, we verified if the conformation of PBDTTT-c chains could be modulated by changing the polymer concentration, the solvent, and the temperature of PBDTTT-c solutions. The results are presented in **Figure 2.7**. The curves were normalized at 635 nm, to highlight the relative changes with respect to the peak at 680 nm (attributed to aggregated chains in the literature). The concentration of PBDTTT-c solution is limited to ~0.025 $g.L^{-1}$, due to the saturation of the absorbance spectra for higher concentration. The measurements were performed on 1 cm path length quartz cells.

Varying the solution concentration from 0.025 to 0.0025 $g.L^{-1}$ does not change the absorption spectra of PBDTTT-c in o-Xylene (**Figure 2.7**a, dark and light blue line). In other words, the interchain and intrachain interactions are not impacted by the selected concentration range. The inset in **Figure 2.7**a shows a picture of both solutions. Regarding the influence of the solvent, since o-Xylene is not necessarily a good solvent for PBDTTT-c, two halogenated solvents widely used for conjugated polymers were chosen: chlorobenzene and chloroform. The solubility of PBDTTT-c chains showed to be better in chloroform compared to chlorobenzene and o-Xylene (faster dissolution). However, no significant change is observed in the UV-Vis spectrum of

PBDTTT-c in chloroform, only a slight blue shift combined with a decrease in intensity of the 680 nm peak (dotted line, **Figure 2.7**a), which may be associated to the better solubility.

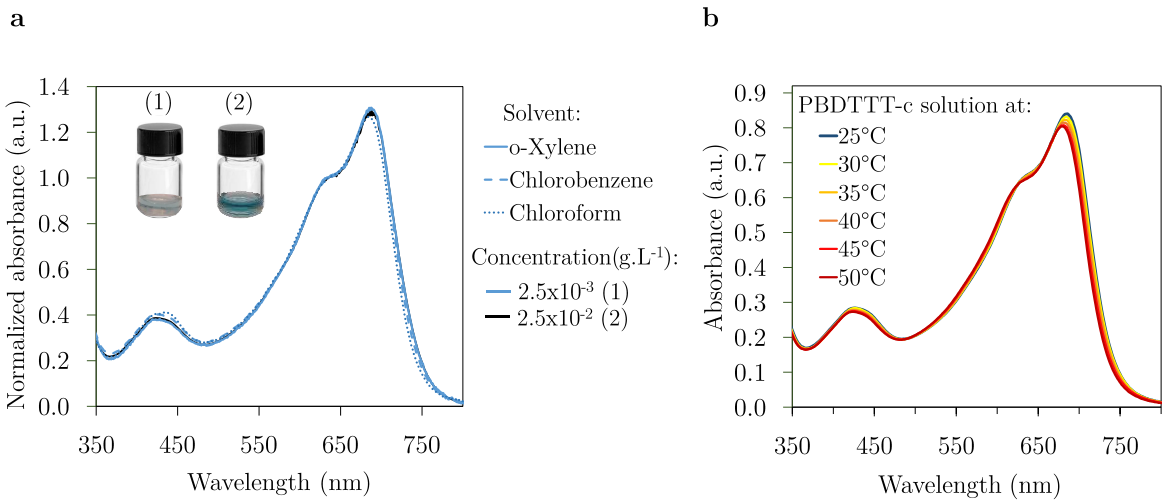

Figure 2.7 – UV-Vis spectra of PBBTTT-c solutions under different conditions: (a) different solvents and concentrations and (b) increasing temperatures. The inset in (a) shows a picture two different concentrations in o-Xylene.

To verify the impact of the temperature, a PBDTTT-c solution in chloroform was heated up to 50 °C and their UV-Vis spectra recorded *in situ*. From **Figure 2.7**b we can see that increasing the temperature of PBDTTT-c solutions results in both an attenuation of the 680 nm peak intensity and a spectral blue shift. This behavior was also observed by Bencheikh *et al.*[42] for PTB7 solutions and was explained by a decrease in the interchain interactions at higher temperatures, resulting in a disorder that breaks the aggregates in solution.

From the results of **Figure 2.7**, we conclude that the conformation of PBDTTT-c chains in solution is only slightly affect by parameters that increase the solubility. For all PBDTTT-c solutions, the UV-Vis spectra presented three peaks with their maximum at 435 nm, 635 nm and 680 nm, in agreement with the literature[44–46].

Table 2.5–Parameters for processing PBDTTT-c and RRa-P3HT layers of different thicknesses.

PBDTTT-c SOLUTION				LAYER DEPOSITION			
Solvent	Concentration	Stirring Conditions		Spin coating			thickness
	[g.L^{-1}]	[h]	[°C]	[rpm]	[s]	[rpm.s^{-1}]	[nm]
o-Xylene	5.0	12	25	1000	60	300	20±5
o-Xylene	10.0	12	50	1000	60	300	45±5
o-Xylene	15.0	12	50	500	60	300	100±5
o-Xylene	19.0	12	50	500	60	300	180±5

For PBDTTT-c layers, only o-Xylene was used as a solvent. We characterized samples with layer thicknesses varying from 15 to 200 nm (PBDTTT-c concentration 5 – 19 g.L^{-1}). The details regarding the processing parameters for each layer are presented in **Table 2.5**. All solutions were stirred overnight before deposition, to ensure complete dissolution of the polymer. For higher

PBDTTT-c concentrations, the stirring temperature overnight was increased to 50°C, but all solutions are processed at room temperature.

Figure 2.8a compares the absorption spectra of PBDTTT-c in solution and as a thin layer (15 nm). Attenuation of the 680 nm peak intensity is observed for the thin layer, indicating a decrease of the aggregated fraction. Otherwise, the resulting spectra are very similar, suggesting no significant differences in the interchain interaction, i.e. no important rearrangement between the solution and the solid-state, as commonly reported for homopolymers like P3HT[7,43]. This result is in agreement with the literature on D-A copolymers and is explained by the rigidity and planarity of the polymer backbones[42,44]. In other words, even in solution, this class of polymers does not lose their conjugation length and their π–π stacking.

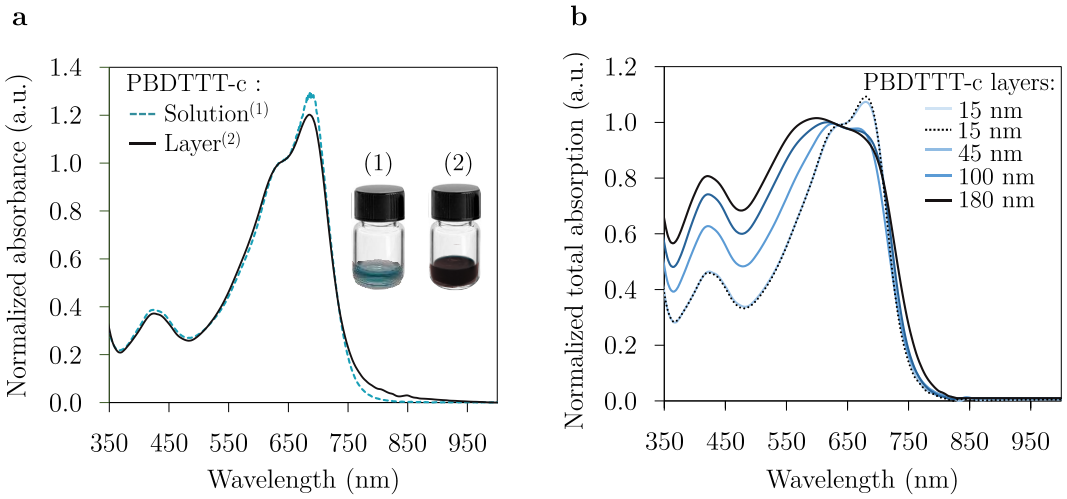

Figure 2.8 – UV-Vis spectra of PBDTTT-c in solution (0.025 g.L^{-1}) and as a thin layer (solution of 5 g.L^{-1}, 15nm-thick layer), in o-Xylene (a). The inset shows a picture of the respective solutions. In (b), we compare the UV-Vis spectra of different layers thicknesses. The dotted line is for a sample that was annealed at 120°C for 15 minutes.

Figure 2.8b compares the absorption spectra for PBDTTT-c films of different layer thicknesses. The dotted curve indicates the spectrum of the 15 nm layer after a post-annealing treatment of 120°C for 15 minutes. We observed no clear changes in the absorption spectra after the thermal treatment. The relatively low sensitivity to thermal annealing might also be explained by the strong intermolecular interaction of PBDTTT-c chains, consistent with the strong aggregation observed already in solution. Regarding the impact of the layer thickness in the UV-Vis spectra: the thicker the PBDTTT-c layer, the more pronounced is the contribution of shorter wavelengths. Besides, the proportion of the peak at 680 nm becomes less pronounced compared to the one at 635 nm, which suggests an increase of disordered regions for thicker samples. Last, the absorption edge measured for PBDTTT-c solutions and thin layers is of *ca.* 770 nm, resulting in an optical bandgap of 1.61 eV. This value is in agreement with the literature[44,47].

For RRa-P3HT, we characterized the UV-Vis spectra in solution (0.025 g.L^{-1}) and as a thin layer processed from o-Xylene, to have a reference spectra in our processing conditions. No aggregation is expected for these polymer chains due to the presence of random side chains, resulting in a nonplanar polymer backbone that prevents ordered structures[48]. As for PBDTTT-c, the

concentration of the RRa-P3HT solution is limited by the saturation of the absorbance spectra at *ca.* 0.025 g.L^{-1}. The 20 nm-thick RRa-P3HT layer is processed from a 5 g.L^{-1} solution in the same conditions indicated in **Table 2.5**. The resulting UV-Vis spectra are plotted in **Figure 2.9** and the inset shows a picture of each solution.

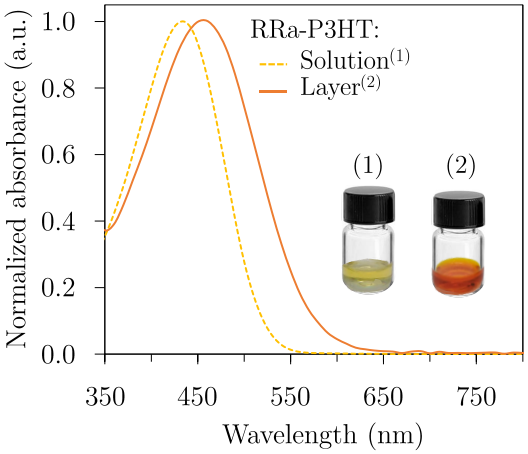

Figure 2.9 - UV-Vis spectra of RRa-P3HT in solution (0.025 g.L^{-1}) and as a thin layers (solution of 5 g.L^{-1}, 20nm-thick layer), in o-Xylene. The inset shows a picture of the respective solutions.

As expected, one broad peak is obtained for the **π-π*** transition of both RRa-P3HT samples, characteristic of solubilized chains (strong polymer-solvent interaction compared to polymer-polymer interactions) and amorphous layers (unaggregated solid)[7]. The red-shift observed for P3HT chains in the solid-state indicated that the chains rearrange after the solvent evaporation (differently from PBDTTT-c). In the literature, this is explained by a longer conjugation length in the solid-state, where the polymer chains have fewer degrees of conformational freedom than in solution[6,7,13]. The optical bandgap extracted from the absorption edge for RRa-P3HT in solution and as a thin layer are of 2.23 eV and 1.98 eV, respectively.

GIWAXS diffractograms

To correlate the aggregation of PBDTTT-c chains, characterized by UV-Vis absorptions, with a molecular arrangement, we used grazing incidence wide angle X-ray scattering (GIWAXS). Considering the amorphous nature of RRa-P3HT, this polymer is not characterized by this technique. The samples were prepared on clean glass substrates.

To distinguish between features related to the glass substrate and those related to polymer layers, we recorded diffractograms of PBDTTT-c layers (spin coated, measured as-cast) for different incident angles (**ω**) and compared them to the signatures obtained for clean glass substrates. From the resulting diffractograms presented in **Figure 2.10**, we conclude that for incident angles below 0.2°, the observed features are mainly related to the PBDTTT-c layer.

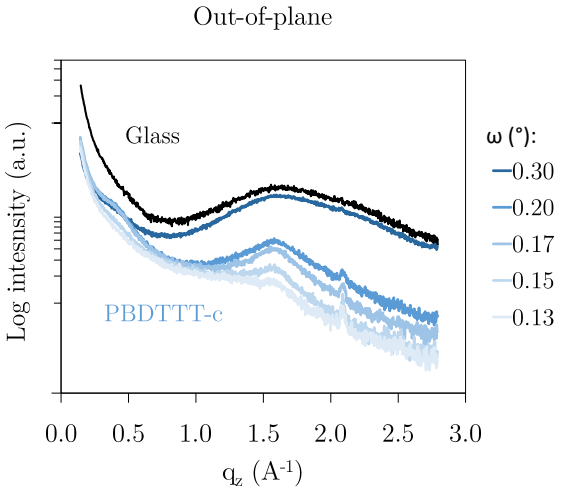

Figure 2.10 - GIWAXS diffractograms of a 30 nm-thick PBDTTT-c layer (blue curves) measured as-cast for different incident angles (ω). The black curve corresponds to the diffractograms of a clean glass substrate (ω: 0.35°).

To investigate the molecular arrangement of PBDTTT-c layers, we measured diffraction patterns for two different thicknesses: 30 nm (spin-coated) and ~1 µm (drop-casted). The thicker sample was chosen to increase the scattering intensity but also to verify if the organization of PBDTTT- c chains are influenced by the layer thickness and/or the deposition technique. Both samples are prepared from the same PBDTTT-c solution of 5 g.L^{-1} in o-Xylene and measured as-cast. The 30 nm thick sample was spin-coated as described in **Table 2.5**, whereas the ~1 µm thick layer was drop-casted and dried slowly overnight inside the glovebox. **Figure 2.11** presents the out-of-plane and in-plane scans for both samples. To allow for a better comparison of the shape and intensity of the resulting peaks, the diffractograms are superposed at higher diffraction angles, where no features were detected.

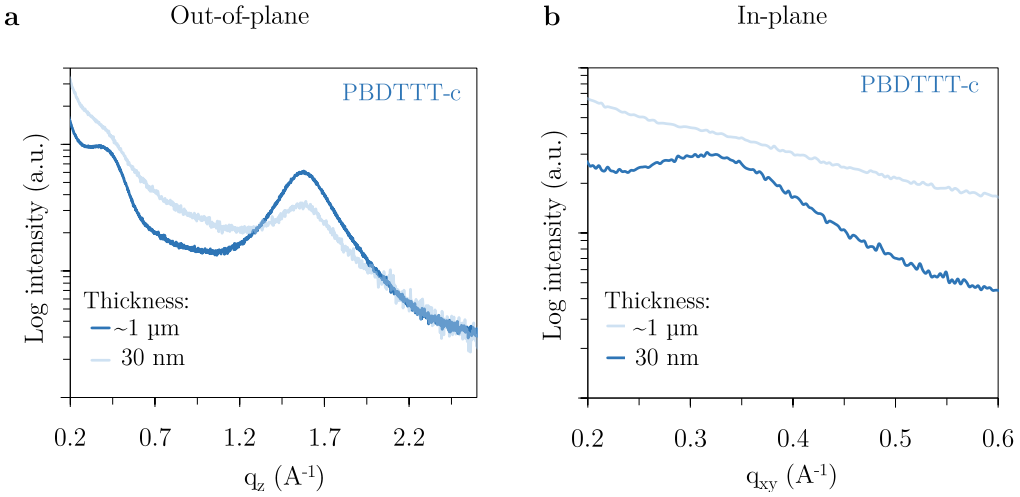

Figure 2.11 – GIWAXS diffractograms of PBDTTT-c layers casted from o-Xylene in out-of-plane scan (a) and in-plane scan (b). Comparison between drop-casted (1 µm-thick) and spin-coated (30 nm-thick) layers.

First of all, the low diffracted intensities and the few broad diffraction peaks indicate an overall disordered morphology. Thus, the presence of aggregated PBDTTT-c chains in the UV-Vis

spectra is not necessarily correlated with an ordered morphology, i.e. with crystallites presenting long-range periodicity. Besides, similar diffractograms are observed for both samples, indicating that the layer thickness and the drying process have no strong influence on the ordering of PBDTTT-c chains. This is consistent with the UV-Vis results, which presented no influence of process parameters (e.g. concentration and temperature) on the aggregation of PBDTTT-c chains. We fitted the peaks using the HighScore software, to allow for a more precise analysis of their position and sharpness. The results are presented in **Table 2.6**. For more details on the fitting process and on the GIWAXS technique, see Appendix A.

By performing out-of-plane and in-plane measurements, it is possible to verify if the polymer layers present preferential orientations parallel or perpendicular to the surface of the sample, respectively. Besides, it allows determining the characteristic distances of lamellar and π-stacking. A diffraction peak at a small angle usually corresponds to lamellar packing distances. Inversely, a diffraction peak at large angles usually corresponds to close intermolecular stacking rising from the interaction of neighboring aromatic rings – commonly called π-stacking[49]. In ordered morphologies, polymer chains present a preferential orientation, i.e. the lamellar-stacking is observed in a different direction than the π- stacking. **Figure 2.12** presents a simplified illustrations of the lamellar and π-stacking distances for ideal cases of face-on and edge-on orientations for visual representation.

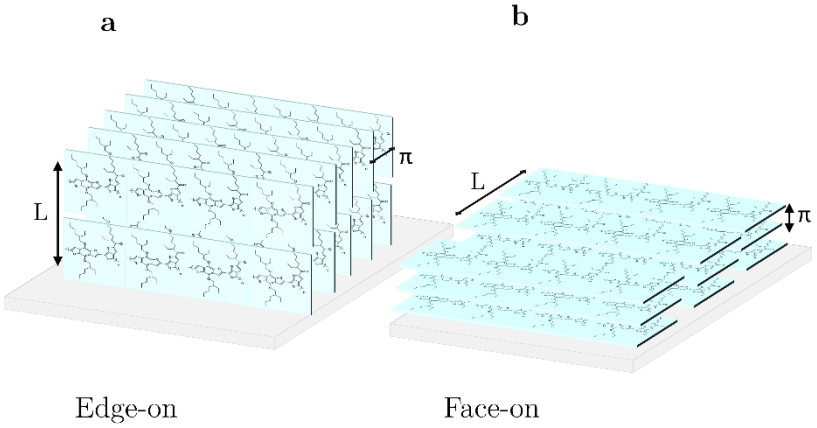

Figure 2.12 – Illustration of lamellar (L) and π-stacking (π) distances for ideal cases of edge-on and face-on orientations.

The out-of-plane scan of PBDTTT-c layers present two peaks, one with an interplanar distance of 3.9 Å, in the order of π-stacking distances in conjugated polymer chains, and a second with a periodicity of 16-17 Å, in the order of lamellar stacking. In the in-plane direction, only one clear diffraction peak was observed with an interplanar distance of 19.5 Å, also in the order of lamellar stacking. This peak was only observed for the thicker sample, which may be related to the lower scattering intensity of the 30 nm sample. Hence, the diffractograms of PBDTTT-c layers presented characteristic lamellar and π-stacking distances in the same scanning direction (**Figure 2.11**a, out-of-plane scan), suggesting a morphology with mixed phases, i.e. some backbones with "edge-on" orientation and others with "face-on" orientation.

Comparing with the literature, a preferential "face-on" orientation was observed for PTB-based polymers (for instance PTB7), with a characteristic π-stacking distance of ~3.9 Å and lamellar stacking with a periodicity of *ca.* 17 Å[50]. These values are very similar to the diffraction peaks found for PBDTTT-c (**Table 2.6**). Therefore, we attribute the peak with interplanar distance of 3.9 Å (out-of-plane scan) to the π-stacking of PBDTTT-c chains with "face-on" orientation. Further analysis should be carried out to allow a more precise determination of the conformation of mixed phases in PBDTTT-c layers.

Table 2.6– Peak fitting of 30 nm and 1 µm PBDTTT-c layers.

Sample	Fitting info.	units	Out-of-plane		In-plane
Spin coated (20 nm)	Peak position	[A^{-1}]	0.37	1.57	-
	Height	[cts]	1255	376	-
	FWHM	[A^{-1}]	0.24	0.36	-
	d spacing	[Å]	17.0	3.9	-
Drop casted (1 µm)	Peak position	[A^{-1}]	0.39	1.57	0.32
	Height	[cts]	1100	744	302
	FWHM	[A^{-1}]	0.21	0.35	0.17
	d spacing	[Å]	16.0	3.9	19.5

Last, these results highlight an interesting interplay between the microstructure and the electrical properties of PBDTTT-c layers: despite the relatively low fraction of organized domains, high-performance OPV devices can be achieved in the literature[51,52]. This may be associated with the presence of aggregates in PBDTTT-c layers (UV-Vis results), even if small and/or relatively disordered (GIWAXS results). As discussed by Noriega *et al.*[1], if the molecular weight of the polymer is high enough, an effective pathway for charge transport is formed by interconnected aggregates, and high carrier mobilities can be expected even for polymers presenting near amorphous diffraction spectra. This reasoning might correlate our experimental results on the aggregation and molecular arrangement of PBDTTT-c chains with the performances reported in the literature.

Conductivity

The conductivity of pristine PBDTTT-c and RRa-P3HT were measured with TLM samples, processed under the conditions presented in **Table 2.5**. For more details on the TLM technique, i.e. measurement and extraction of conductivity values, see Appendix A. Pristine PBDTTT- c layers exhibited a conductivity of around $4x10^{-8}$ S.cm^{-1}. Neither the layer thickness (20-200 nm) nor the thermal annealing (115°C/15 min) showed a significant impact on the measured conductivity. Since the measured values are close to the measurement limits of our system (~$1x10^{-8}$ S cm^{-1}), these results are not further discussed to avoid over-interpretation of data. For pristine RRa-P3HT, the conductivity could not be measured with our setup, meaning that it is below $1x10^{-8}$ S cm^{-1}. These values are consistent with the low carrier density expected from neutral polymers[53].

Energy levels by cycle-voltammetry

The electrochemical bandgap of PBDTTT-c and RRa-P3HT was measured with cyclic voltammetry (CV). The polymers were analyzed as a thin layer and not in solution, due to the poor solubility of conjugated polymers in solvents with a wide electrochemical stability window. For both polymers, 5 g.L^{-1} solutions were stirred overnight in o-Xylene and drop-casted on the working electrode. Once the polymer layer was dry, the working electrode was immersed in freshly distilled acetonitrile with the supporting electrolyte. See Appendix A for more details on the setup and data extraction.

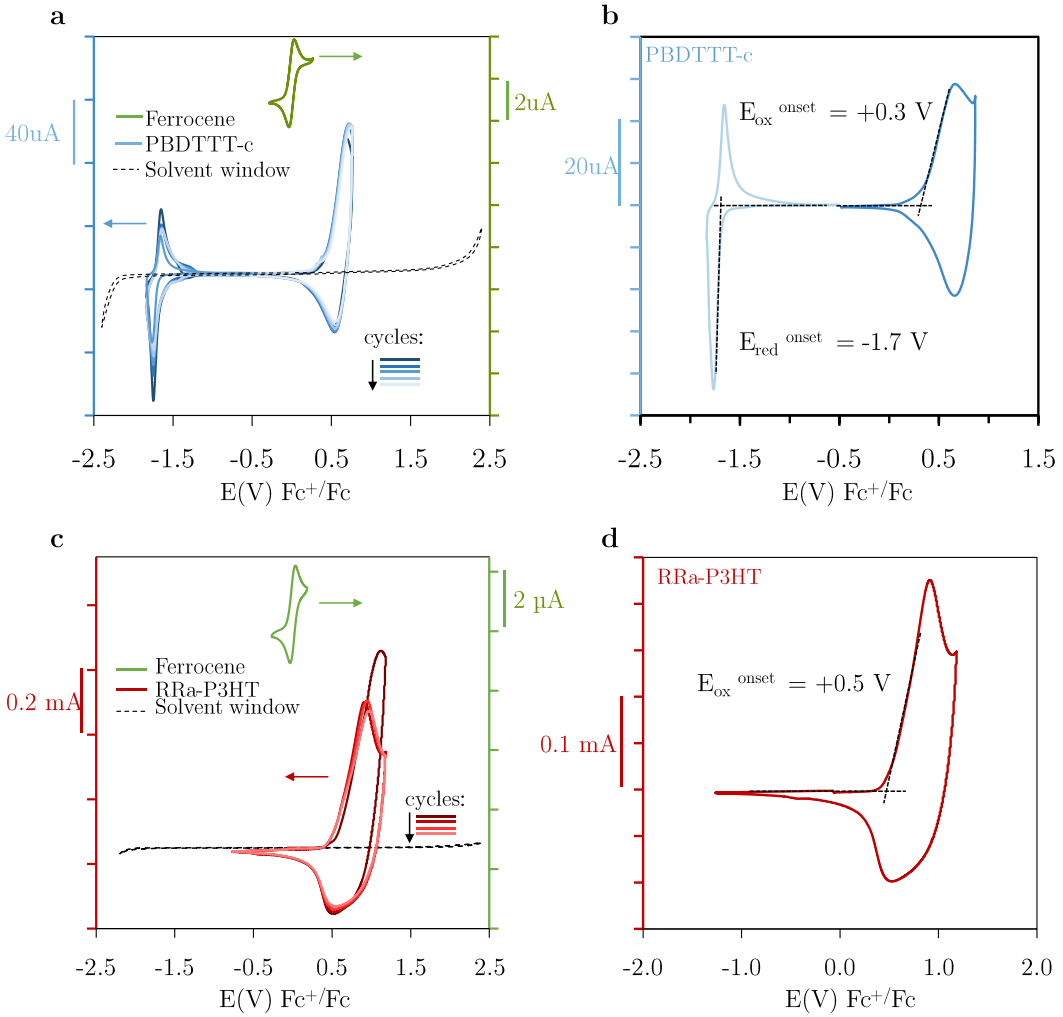

Figure 2.13 - Voltammograms obtained for PBDTTT-c (a, b) and RRa-P3HT (c, d) casted on the working electrode. Experimental conditions: ACN, scan rate 50mV.s^{-1}, 0.1 M [NBu4][PF6], Pt electrode, 0.01 M $Ag/AgNO_3$ calibrated Fc^+/Fc.

The voltammograms reported in **Figure 2.13** were recorded at a scan rate of 50 mV.s^{-1} and calibrated to the half-wave oxidation potential of ferrocene (Fc^+/Fc). **Figure 2.13**a presents the half-wave oxidation potential of Ferrocene, the electrochemical stability window of acetonitrile, and the electrochemical stability of PBDTTT-c over several cycles. All these scans were recorded from the same distilled acetonitrile. The same was performed for RRa-P3HT and is plotted in

Figure 2.13c. Note that the stability window of acetonitrile only allows us to measure the oxidation wave of the RRa-P3HT layer.

When comparing the oxidation waves of both polymers over different cycles, a clear first cycle effect is observed for RRa-P3HT. For PBDTTT-c, only slight changes can be seen. This result is interesting because it shows that even though PBDTTT-c presented characteristics of aggregation, the layers allow better accessibility of ions compared to the amorphous P3HT ones. Otherwise, both polymers presented electrochemically stable and reversible processes.

Figure 2.13b presents the onset potentials extracted from the oxidation (E_{ox}^{onset}) and the reduction (E_{red}^{onset}) waves of PBDTTT-c using the tangential method. The HOMO level measured for PBDTTT-c is of -5.1 ±0.1 eV and the LUMO level of -3.1 ±0.1 eV. Chen *et al.* measured HOMO and LUMO energy levels of -5.12 et -3.35 eV, respectively[45]. Therefore, the electrochemical bandgap measured for PBDTTT-c layers is ca. 2.0 eV and is in agreement with the literature. The difference between the electrochemical and the optical bandgap (measured by UV-Vis) gives us an approximation of the exciton binding energy in organic semiconductors, typically in the range of 0.3-0.5[9,54]. For PBDTTT-c, the exciton binding energy extracted from our measurements is of *ca.* 0.45 eV.

Figure 2.13d presents the E_{ox}^{onset} extracted from the oxidation wave of RRa-P3HT, which resulted in a HOMO level at -5.3 eV. In the literature, the energy levels of P3HT measured by CV have shown to vary considerably with packing order, where larger HOMO energies are obtained with increasing disorder[6]. Therefore, the measured HOMO is consistent with the amorphous nature of the P3HT.

The results presented for pristine polymer solutions and layers are summarized in section 2.2.3. In the following, we present the characterizations performed on pristine dopant molecules.

2.2.2 Pristine dopants

The initial state of F4TCNQ and Mo(tfd-$COCF_3$)$_{3\ a}$ are characterized by UV-Vis measurements, which allows inferring the state of the dopant molecule (neutral, ionized, etc.), and by CV. The latter was carried out to determine the LUMO levels of both molecules and, consequently, their *p*-doping ability towards the selected polymer hosts.

UV-Vis absorption

To be able to analyze the absorption spectra of both *p*-dopants in the conditions chosen for this work, **Figure 2.14**a,b present reference UV-Vis absorptions from the literature of the neutral (solid line), monoanion (dashed line) and dianion (dotted line) F4TCNQ[55,56] and Mo(tfd-$COCF_3$)$_3$[57] molecules.

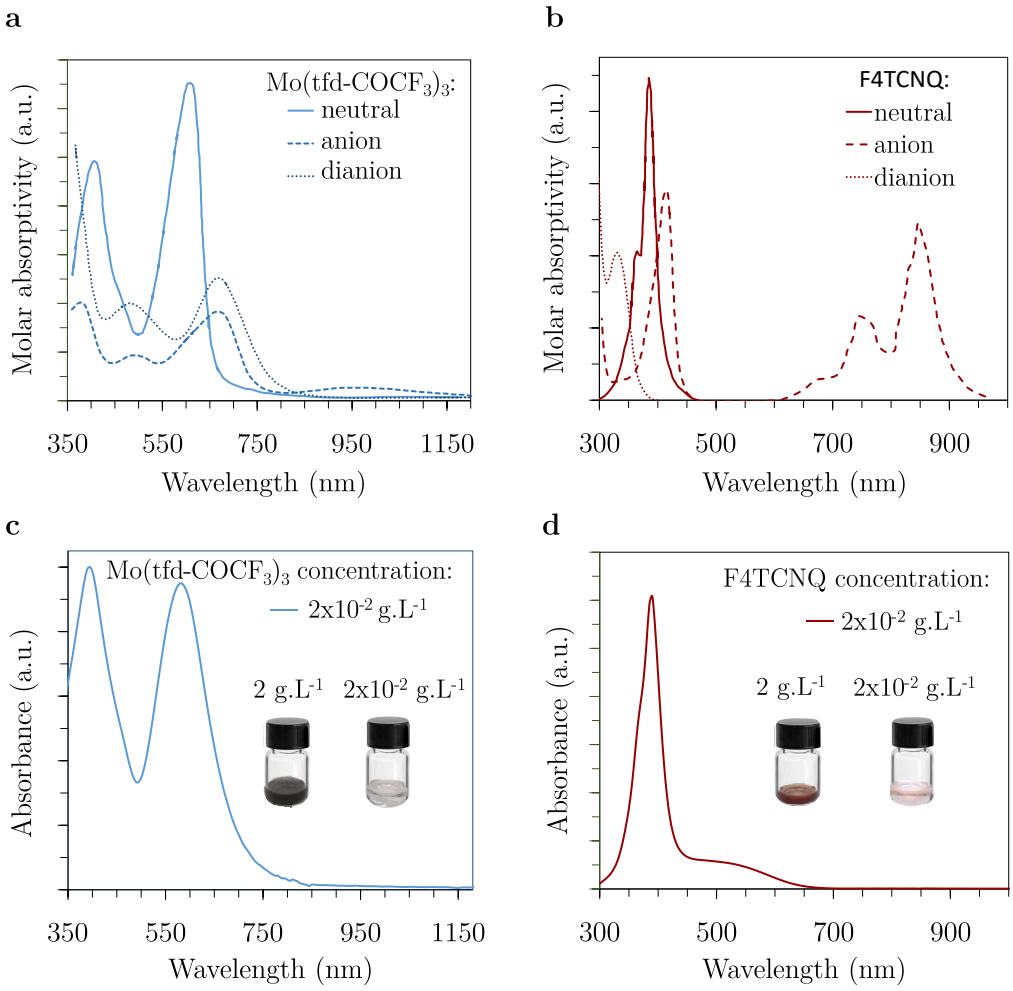

Figure 2.14 – Reference UV-Vis spectra of pristine Mo(tfd-$COCF_3$)$_3$[57] (a) and F4TCNQ[55] (b) compared to the spectra measured in this work for Mo(tfd-$COCF_3$)$_3$ (c) and F4TNCQ (d) dissolved in o-Xylene.

For our experimental UV-Vis spectra, both *p*-dopants were dissolved in o-Xylene and the UV-Vis absorbance was measured only for solutions, as no continuous layers are formed when spin-coating or drop-casting the Mo(tfd-$COCF_3$)$_3$ solutions from o-Xylene. Dopant solutions of $2x10^{-2}$ g.L^{-1} were measured in 1 cm path length quartz cells. The concentration is considerably lower than the one used for processing doped layers (2 g.L^{-1}) due to the saturation of the

absorbance spectra. For sake of comparison, the inset in **Figure 2.14**c,d present images of dopant solutions of both concentrations, for UV-Vis measurements and doping ($2x10^{-2}$ $g.L^{-1}$ and 2 $g.L^{-1}$).

For Mo(tfd-$COCF_3$)$_3$, two defined peaks are observed at 394 nm and 584 nm slightly blue-shifted compared to the neutral reference at 399 nm and 596 nm (**Figure 2.14**c). This might be correlated to a solvatochromic effect as the reference spectra from the literature were measured in dichloromethane[57]. From **Figure 2.14**c, we assume that Mo(tfd-$COCF_3$)$_3$ in o-Xylene is mostly in its neutral state. The impact of different organic solvents on the absorption spectra of Mo(tfd-$COCF_3$)$_3$ is further discussed in section 3.2.4. Note that Mo(tfd-$COCF_3$)$_3$ absorbs in the same spectral range as PBDTTT-c.

For F4TCNQ, one defined peak is observed at approx. 385 nm as for the neutral reference (**Figure 2.14**d), but the additional shoulder at approx. 365 nm is less defined when compared to the literature (**Figure 2.14**b)[55]. Besides, our spectra present an additional broad but less intense peak at higher wavelengths that do not correspond to any feature in **Figure 2.14**b. We assume, however, that the measured F4TCNQ spectrum in o-Xylene is mostly in its neutral state.

Energy levels by cycle-voltammetry

The redox potentials of Mo(tfd-$COCF_3$)$_3$ and F4TCNQ were measured in solution (2.10^{-3} $mol.L^{-1}$) with CV. F4TCNQ was dissolved in acetonitrile and Mo(tfd-$COCF_3$)$_3$ in THF, due to its low solubility in acetonitrile. In **Figure 2.15**a, b, we present the electrochemical stability of Mo(tfd-$COCF_3$)$_3$ and F4TCNQ over several cycles, as well as the ferrocene and solvent references measured under the same conditions. For both dopants, the reduction occurs *via* two, remarkably stable and reversible, one-electron transfers[58]. Such electrochemical stability of the anion and dianion species are valuable for long-lasting operations.

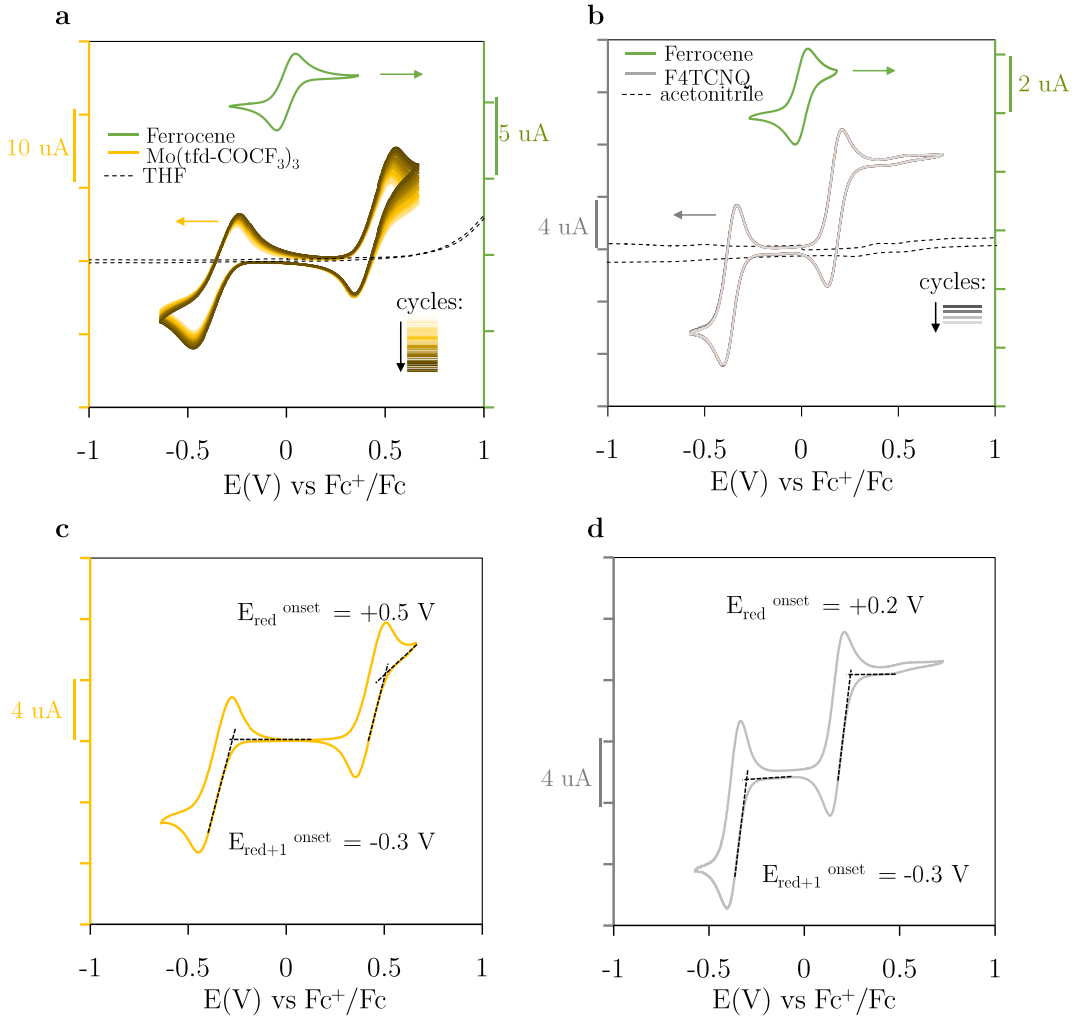

Figure 2.15 - Voltammograms obtained for Mo(tfd-$COCF_3$)$_3$ (a,c) and F4TCNQ (b,d) in THF and acetonitrile respectively. Experimental conditions: scan rate 50mV.s^{-1}, 0.1 M [NBu4][PF6], Pt electrode, 0.01 M Ag/$AgNO_3$ calibrated Fc^+/Fc.

Figure 2.15c,d presents the redox potentials extracted for Mo(tfd-$COCF_3$)$_3$ and F4TCNQ, respectively. The successive reduction waves are assigned to the LUMO and LUMO +1 levels, also referred as EA^0 and EA^-. For Mo(tfd-$COCF_3$)$_3$, we obtained *ca.* -5.3±0.1 eV and -4.5±0.1 eV for the LUMO and LUMO +1 levels, respectively. For F4TCNQ, we obtained *ca.* -5.0±0.1 eV and -4.5±0.1 eV for the LUMO and LUMO +1 levels, respectively. In the literature, -5.2 eV is the reference value for the LUMO level (EA^0) of F4TCNQ, measured by CV[55] and UPS[59]. Regarding Mo(tfd-$COCF_3$)$_3$, the redox waves obtained in this work are in agreement with the electrochemical data measured by Mohapatra et al.[57]. Besides, UPS measurements were also performed in the literature for other molybdenum tris(dithiolene) derivatives, such as Mo(td)$_3$ (-5.6 eV)[30] and Mo(tfd-CO_2Me)$_3$ (-5.0 eV)[39]. In conclusion, the LUMO level of -5.3 eV extracted from our CV measurements for Mo(tfd-$COCF_3$)$_3$ is consistent with the literature, since this dopant has shown to be a stronger oxidizing derivative than Mo(tfd-CO_2Me)$_3$[57].

2.2.3 Final considerations for the doping process

Above, we characterized the initial properties of the selected polymers and *p*-dopants with the processing conditions (solvent, concentrations, layer thickness, etc.) that will be used for the doping process.

Even though both polymers hosts present overall disordered molecular arrangements, the UV- Vis spectra of PBDTTT- c showed characteristics of aggregated chains in solution and thin layers, whereas for RRa-P3HT only amorphous signatures were observed. Interestingly, parameters such as solvent and polymer concentration presented no considerable impact on the aggregated form of PBDTTT-c chains. Note that the aggregation process in solution was reported as beneficial for the doping efficiency[26,28].

Regarding the UV-Vis absorptions of polymers and *p*-dopants, it might be challenging to identify the contribution of *p*-dopants in doped layers, especially when using Mo(tfd-$COCF_3$)$_3$. This dopant presented an extensive overlap of its neutral and ionized absorption signatures with the ground-state absorption of polymer hosts, specially PBDTTT-c.

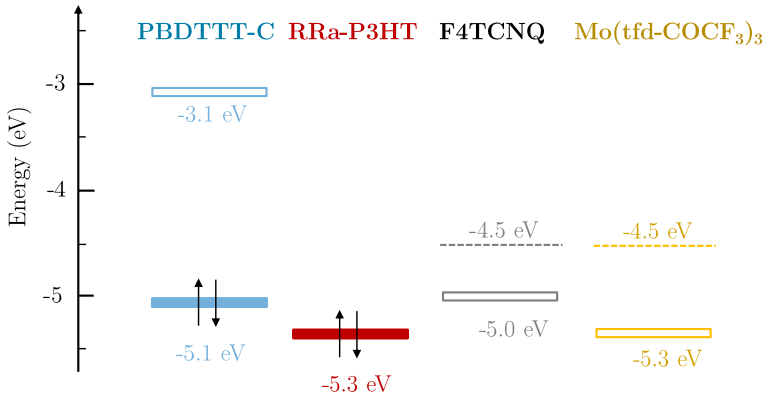

Figure 2.16 – Representation of the energy levels measured by CV for polymers and *p*-dopants. Filled bars indicate HOMO levels (IE); unfilled bars indicate LUMO levels (EA), and dotted lines LUMO-1 levels (EA^-).

The schema in **Figure 2.16** summarizes the energy levels measured for the polymers and the *p*- dopants by CV. Deviations from absolute values reported in the literature are not an issue here, since our goal was to verify their relative positions, e.g. if the HOMO of the polymer is higher or lower than the LUMO of the dopant. Since materials were measured with the same setup, the relative energy differences between the studied materials are comparable.

Assuming the absence of intermolecular electrostatic interactions[60], the LUMO of Mo(tfd-$COCF_3$)$_3$ (≈ -5.3 eV) should favor efficient electrical doping of both polymers, PBDTTT-c and RRa-P3HT. Regarding F4TCNQ, even though the LUMO is a few eV higher than Mo(tfd-$COCF_3$)$_3$, we also expect a *p*-doping effect with this dopant molecules[61]. We should, however, keep in mind that the energetic landscape in doped systems might be considerably different from the energy levels measured for isolated materials.

In the following section, we optimized the doping protocol using the co-processing technique. The doping signatures are discussed in the last section of this chapter (section 2.4.)

2.3 OPTIMIZATION OF THE DOPING PROTOCOL

Achieving homogeneous doped layers with reproducible characteristics has shown to be challenging, especially for higher doping ratios[29]. Molecular doping may induce the formation of polymer:dopant aggregates in solution, which have shown to be beneficial for the doping efficiency but may result in processing complications at higher doping concentrations, related to a solubility loss of doped aggregated chains[31,32]. Consequently, parameters varying the fraction of aggregated and solubilized polymer chains have shown to influence the doping reaction in solution[20,25,27,28]. These parameters include the polymer and dopant concentration, the solvent choice but also the stirring time and temperature of the blend solution. Therefore, the processing conditions can impact considerably the polymer:dopant interactions and should, therefore, be studied carefully to improve the performance and reproducibility of doped layers.

This section aims to identify the important parameters controlling the doping process of PBDTTT-c:Mo(tfd-$COCF_3$)$_3$ in o-Xylene to define the doping protocol to be used in this thesis. The doping is performed with the co-processing technique, which allows a direct correlation between the dopant concentration and the doping signatures. This is a valuable aspect when studying the impact of the dopant concentration of the optoelectronic properties of polymer hosts.

Regarding the calculations of dopant concentration, we chose to express it in molar fraction (mol%) of polymer monomers. In the literature, we can also find the dopant concentration written in weight fraction (wt%). However, molar fractions allow for better control of the ratio between polymer monomer and dopant molecules and avoid, therefore, saturating the blend in dopant molecules (adding more dopant molecules than available polymer monomers). For example for P3HT:F4TCNQ, the system presented signs of saturation for dopant concentrations above *ca.* 16 mol% , which was explained by the absence of free polymer segments (one dopant molecule interacts with approx. 3 thiophene monomers)[27,62].

The following relation is used to prepare doped solution at a given dopant concentration (mol%) with the co-processing technique:

$$\text{Dopant molar ration (mol\%)}: \frac{C_d V_d M_p}{C_p V_p M_d} \qquad \textbf{Equation 2.1}$$

Where C, V and M correspond to the concentration, volume and molecular weight of the polymer (p) and dopant (d), respectively. This equation is demonstrated in Appendix B.

The optimization of the doping protocol is presented in two parts. First, through UV-Vis-NIR absorptions, we verify the impact of the stirring conditions of polymer:dopant blends on the doping process in solution. In the second part, we study the impact of process parameters on the UV-Vis-NIR and conductivity of doped layers, to identify key parameters controlling the doping signatures and to achieve reproducible results. At the end of this section, the final processing protocol is detailed and its reproducibility tested.

2.3.1 Influence of the stirring conditions of blend solutions

This first part analyzes the impact of the stirring conditions and the dopant concentration on the UV-Vis-NIR spectra of PBDTTT-c:Mo(tfd-$COCF_3$)$_3$ solutions. Only o-Xylene was used since this thesis aims to study doped layers with non-halogenated solvents. Note that for pristine PBDTTT-c no considerable influence of the solvent could be observed in the UV-Vis absorption spectra (see **Figure 2.7**).

PBDTTT-c (5 g.L^{-1}) and Mo(tfd-$COCF_3$)$_3$ (2 g.L^{-1}) solutions were stirred separately overnight inside the glovebox. Then, the appropriated volume of dopant solution was added to the polymer solution. The dopant concentrations chosen were 5, 10 and 15 mol%. The PBDTTT-c:Mo(tfd-$COCF_3$)$_3$ solutions were stirred for 5 minutes at room temperature. For the solution with 15 mol% of Mo(tfd-$COCF_3$)$_3$, two stirring times were compared: 5 min and 4 hours. To measure the UV-Vis-NIR spectra of blend solutions, they were diluted to 2.5x10^{-2} g.L^{-1} of PBDTTT-c, as the absorbance saturates for higher concentration using 1 cm path length quartz cells. The resulting spectra for PBDTTT-c:Mo(tfd-$COCF_3$)$_3$ solutions are presented in **Figure 2.17**a.

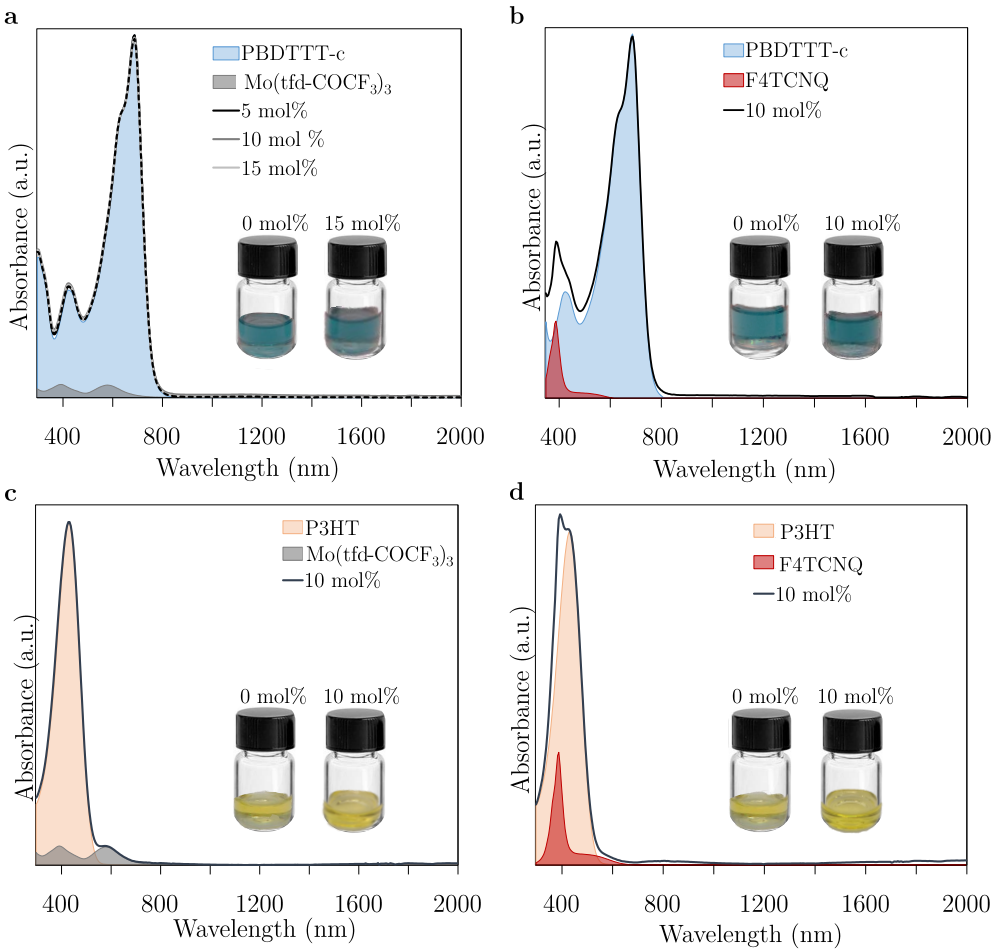

Figure 2.17 –UV-Vis-NIR spectra of different polymer:dopant solutions (lines). Filled areas represent the spectra of pristine polymer and dopants. For PBDTTT-c:Mo(tfd-$COCF_3$)$_3$ solutions, the spectra were recorded for different dopant concentrations (5 mol%, 10mol% and 15 mol%) and stirring times: 5 min (solid line) and 4h (dotted line). The insets present pictures of pristine polymers and polymer:dopant solutions.

Clearly, no difference is observed for the resulting UV-Vis-NIR spectra of PBDTTT-c:Mo(tfd-$COCF_3)_3$ solutions when varying the dopant concentration from 5-15 mol% or the stirring time from 5 min to 4 hours. Neither absorption bands in the NIR nor changes in the spectra of the pristine PBDTTT-c. In other words, no doping signatures can be observed from the absorbance spectra. The inset in Figure 2.17a highlights the absence of visible changes upon doping PBDTTT-c solutions. The neutral spectrum of the dopant is also plotted in the same graph to illustrate its contribution. The fact that the contribution of the neutral $Mo(tfd\text{-}COCF_3)_3$ cannot be clearly distinguished can be explained by the lower molar absorptivity and concentration of the dopant molecule combined with the overlapping of the absorption range.

The other doped systems selected in this thesis present a less intense overlapping of the absorption bands, meaning that one can distinguish if the dopant is in its neutral or ionized state. Therefore, the absorbance spectra of PBDTTT-c:F4TCNQ, P3HT:$Mo(tfd\text{-}COCF_3)_3$ and P3HT:F4TCNQ solutions were also measured and are plotted in Figure 2.17b,c and d, respectively. All three systems were doped at 10 mol%. Polymer (5 $g.L^{-1}$) and dopant (2 $g.L^{-1}$) solutions were stirred separately overnight inside the glovebox. The F4TCNQ solution at 2 $g.L^{-1}$ presented sign of saturation when left without agitation at room temperature. The blend solutions were stirred for 2 hours at RT before dilution for the UV-Vis-NIR measurement ($2.5x10^{-2}$ $g.L^{-1}$ of polymer). All three systems presented neutral spectra of both polymer and dopant. The insets in **Figure 2.17**b, c, d show the respective polymer solutions before and after doping, where no signs of aggregation or colors changes can be observed. This is in agreement with the absorbance spectra of neutral polymers, even after dopant addition.

Finally, these results are different from those published in the literature, where even in solution one could observe doping signatures in the absorbance spectra of P3HT:F4TCNQ[20,27,63]. However, these studies used aggregated RR-P3HT and our study used solubilized RRa-P3HT. This result is in agreement with Farland and coworkers that recently proposed a doping mechanism for P3HT where aggregation preferentially occurs before the charge transfer step takes place.[26] For PBDTTT-c maybe at higher concentration we would observe doping signatures. No higher stirring temperatures were tested because this parameter showed no influence on pristine PBDTTT-c solution (**Figure 2.7**b). Besides, higher temperatures were reported to decrease doping-related signatures[64]. Therefore, we can conclude that at low concentration, the stirring conditions and the dopant concentration have no particular influence on the polymer-dopant interaction of the PBDTTT-c:$Mo(tfd\text{-}COCF_3)_3$ blend solution.

2.3.2 Optimization of the processing protocol of doped layers

To enable a controlled doping process with reproducible optical and electrical properties, this section investigates the impact of some critical process parameters identified in the literature on the final properties of doped layers. Here, the doping signatures of PBDTTT-c:$Mo(tfd\text{-}COCF_3)_3$ layers are characterized in terms of conductivity and UV-Vis-NIR signatures. The dopant concentration is fixed at 5 mol%. Note that the discussion presented in this section will be focused on quantitative variations induced by the selected parameters. The doping signatures as well as

the impact of the dopant concentration on the optical and electrical properties are discussed details in section 2.4, after defining the processing protocol.

First, we present the impact of the stirring conditions as well as the polymer concentration on the final properties of doped layers. In the second part, we investigate the impact of post-annealing treatments, and on the third and last part, we briefly infer the stability of doped layers under argon atmosphere and ambient air. These stability results are particularly relevant for planning experiments, as it allows verifying if samples can be stored before characterization and/or if precaution should be taken for measurements under ambient air.

Impact of stirring conditions and layers thickness

The processing parameters analyzed for doped layers were the stirring conditions of the blend (time and temperature) and the polymer concentration, even though the further presented no impact on the UV-Vis spectra of blend solution. Varying the polymer concentration allows verifying if homogenous doping can be achieved for doped layers of different thicknesses.

Table 2.7 presents the concentrations and processing parameters used for the samples discussed in this section and their respective conductivities. The Mo(tfd-$COCF_3$)$_3$ concentration used for all samples was 2 g.L^{-1}. Two stirring conditions were tested for polymer:dopant solutions prior to spin coating (after dopant addition): 5min/25°C and 300 min/80°C. Regarding the layer thickness, to obtain doped layers in a similar thickness range as measured for pristine PBDTTT-c (15- 200nm), we prepared PBDTTT-c:Mo(tfd-$COCF_3$)$_3$ solutions with the same final PBDTTT-c concentrations (5 g.L^{-1}-19 g.L^{-1}).

The impact of the stirring conditions of PBDTTT-c:Mo(tfd-$COCF_3$)$_3$ blends on the UV-Vis-NIR spectra of doped layers is presented in Figure 2.18a. The resulting spectra are very similar and only a small variation is observed for the conductivity (**Table 2.7**). This is in agreement with the results presented for PBDTTT-c:Mo(tfd-$COCF_3$)$_3$ solutions. However, different from the solution that presented the signatures of neutral polymer and dopant, thin films present clear absorptions bands in the NIR, which are characteristic of an effective doping. The doping signatures will be discussed in details in the following section (section 2.4).

Table 2.7– Table all dopant solution were of 2 g.L^{-1} and were stirred overnight at room temperature, 5% mol.

PBDTTT-c solution			PBDTTT-c:Mo(tfd-$COCF_3$)$_3$ solution (5 mol% dopant)			Layer deposition		Conductivity
Conc. (Cp)	Volume (Vp)	Stirring Conditions	Volume (Vd)	Stirring Conditions	Conc. polymer:dopant	Spin coating	Layer thickness	(x 10^{-2})
[g.L^{-1}]	[µl]	[h]/[°C]	[µl]	[min]/[°C]	[g.L^{-1}]:[g.L^{-1}]	[rpm]/[s]/[rpm.s^{-1}]	[nm]	[S.cm^{-1}]
5,5	900	12/25	150	5/25	4,7:0,28	1000/60/300	17± 2	2.20 ± 0.3
5,5	900	12/25	150	300/80	4,7:0,28	1000/60/300	17± 2	1.30 ± 0.2
14,5	800	12/50	350	5/25	10,1:0,60	1000/60/300	45±5	2.93 ± 0.3
27	600	12/50	500	5/25	15,0:0,9	500/60/300	95±5	2.16 ± 0.1
45	600	12/50	815	5/25	19,1:1,15	500/60/300	135±5	3.70 ± 0.1

Regarding the influence of the layer thickness, **Figure 2.18**b presents the resulting UV-Vis-NIR spectra and **Table 2.7** the respective conductivities. All layer thicknesses presented clear doping signatures in terms of conductivity and NIR absorptions (normalized at 640 nm), where the same doping induced bands are observed for all four thicknesses. The intensity variation observed for the NIR bands corresponds to the variations of the conductivity values, i.e. higher conductivity values present NIR bands of higher intensities. This variation might be related to the different fractions of amorphous and aggregated chains, as observed for pristine PBDTTT-c (**Figure 2.8**). However, no particular trend was observed between the variation in doping signatures and the layer thickness. Thus, we conclude that PBDTTT-c concentrations up to 19 $g.L^{-1}$ can be efficiently doped with this technique.

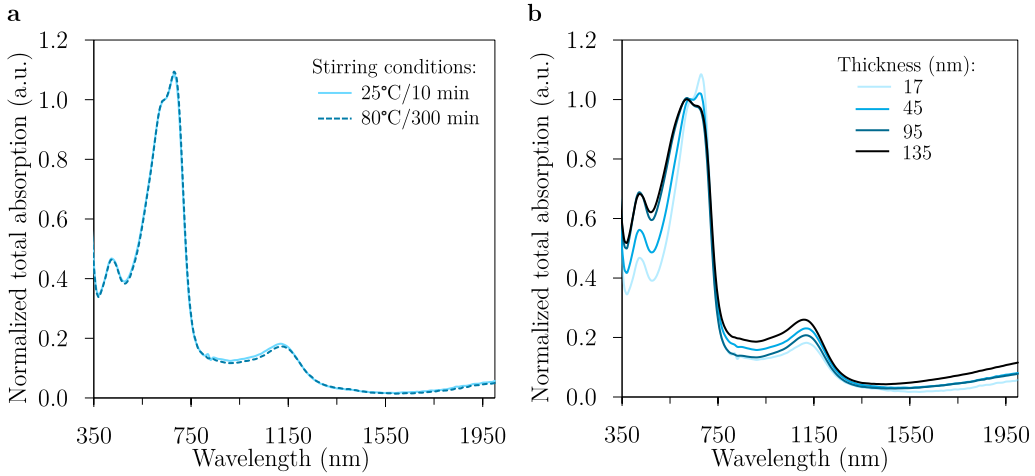

Figure 2.18 –UV-Vis-NIR spectra of PBDTTT-c:Mo(tfd-COCF3)3 layers doped at 5mol%: (a) comparison between two different stirring conditions (before layer deposition) and (b) different layers thicknesses.

It is worth mentioning that no solubility problems were encountered during the processing of PBDTTT-c:Mo(tfd-$COCF_3$)$_3$ solutions, regardless of the stirring conditions and polymer concentration. Comparing to the literature on RR-P3HT:F4TCNQ, the processing issues highlighted by several studies using the co-processing technique were associated with the limited solubility of doped chains in the processing solvent. However, these doped solutions presented UV-Vis-NIR absorption of ionized species[32], contrarily to spectra measured for PBDTTT-c:Mo(tfd-$COCF_3$)$_3$ solutions. Therefore, the absence of solubility issues when processing PBDTTT-c:Mo(tfd-$COCF_3$)$_3$ solutions are in agreement with the fact that, in solution, polymer and dopant presented UV-Vis-NIR spectra of neutral species.

Impact of thermal annealing

The few publications studying the thermal annealing of PBDTTT-c: Mo(tfd-$COCF_3$)$_3$ doped system used 10 min at temperatures varying from 110°C to 150°C[40,41,65]. However, this processing step was identified as critical for F4TCNQ-doped semi-crystalline polymers such as P3HT[66] and PBTTT[67]. This instability was explained by a temperature-induced dedoping process, i.e. a dopant desorption through thermal annealing. Therefore, the impact of thermal annealing on Mo(tfd-$COCF_3$)$_3$-doped conjugated polymers was also verified in this work.

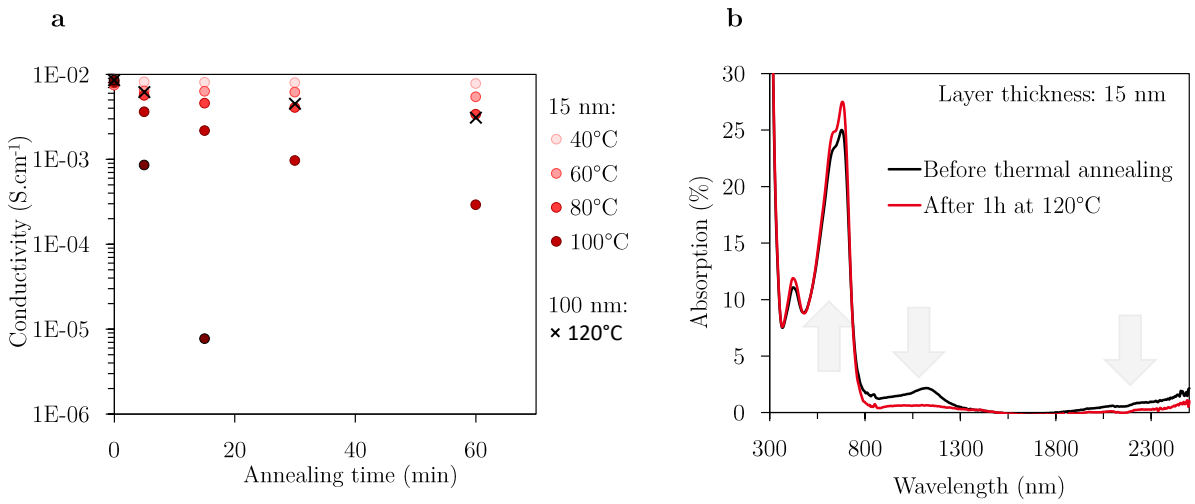

Figure 2.19 – Impact of thermal annealing on the conductivity (a) and UV-Vis-NIR signatures (b) of PBDTTT-c : $Mo(tfd\text{-}COCF_3)_3$ layers doped at 5 mol% $Mo(tfd\text{-}COCF_3)_3$.

In **Figure 2.19**a, we present the impact of different annealing temperature and times on the conductivity of 15 nm-thick PBDTTT-c:$Mo(tfd\text{-}COCF_3)_3$ layers, doped at 5 mol% (processing parameters according to the first sample of **Table 2.7**). For temperatures ≥ 100°C, we observe a strong decrease in the conductivity with the annealing time. This decrease was considerably less intense for thicker layer, as shown for 100nm-thick samples annealed at 120°C (**Figure 2.19**a, X symbol). The impact of thermal annealing on the UV-Vis-NIR spectra is shown in **Figure 2.19**b. The doping-induced NIR absorption vanished completely after this thermal post-treatment, and the absorption signatures of pristine PBDTTT-c are recovered. Therefore, from the conductivity and UV-Vis-NIR results we can conclude that thermal annealing at higher temperatures (≥ 100°C) strongly degrades the doping signatures of PBDTTT-c:$Mo(tfd\text{-}COCF_3)_3$ layers. Besides, even at lower temperatures, this post-treatment showed no conductivity improvement (**Figure 2.19**a, light rose symbols).

As shown in **Figure 2.20**, short thermal annealing treatments decrease the conductivity of all *p*-doped systems studied in this thesis, F4TCNQ-doped layers(**Figure 2.20**a) as well as $Mo(tfd\text{-}COCF_3)_3$-doped layers (**Figure 2.20**b). Note that PBDTTT-c:F4TCNQ layers presented a better stability against short thermal treatments at 120°C (**Figure 2.20**a) compared to the other systems. The UV-Vis-NIR signatures are similar to those observed for PBDTTT-c:$Mo(tfd\text{-}COCF_3)_3$ layers, i.e. recovery of pristine polymer absorptions.

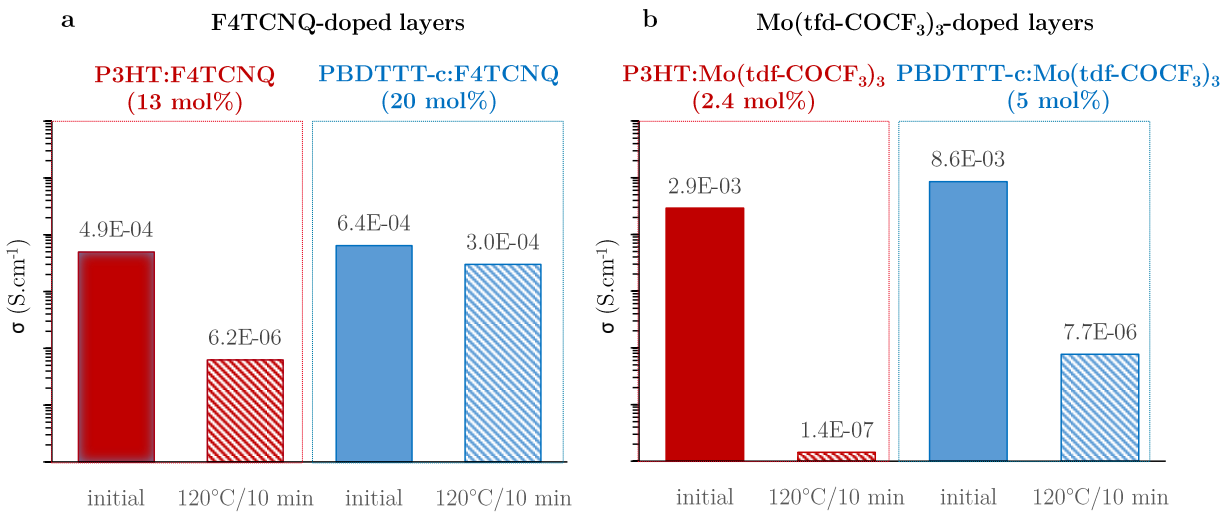

Figure 2.20 –impact of thermal annealing on different *p*-doped systems. All layers are ca. 15 nm thick.

Regardless of the *p*-doped systems and its layers thickness, thermal annealing presented a negative impact on the doping signatures. Besides, our results suggest that thermal dedoping is also the mechanism behind the instability of Mo(tfd-$COCF_3$)$_3$-doped layers at higher temperatures. In the literature, the thermal instability was associated to a low compatibility of polymer hosts with dopant molecules[68,69]. Better thermal stabilities were observed when increasing the interaction of the dopant molecule with the polymer hosts, for example by using polymer hosts with polar side chains when doping with the polar dopant F4TCNQ[68,69] (see section 1.2.7). Hence, our results suggest that no strong interaction occurs between polymer and *p*-dopant in the studied systems.

Finally, no thermal post-treatment step is included in our processing protocol of *p*-doped layers.

Impact of storage conditions

Having information on the stability of freshly prepared samples under ambient air (short exposure) and argon atmosphere is important to:

1. Verify if doped layers can be stored inside the glovebox before characterization or if they should be measure directly after fabrication
2. Verify the possibility of characterizing doped layers under ambient conditions

These are valuable information for the development of a reproducible protocol for processing and characterizing doped layers. It is worth highlighting that several characterization techniques commonly used in the literature for doped OSCs such as UV-Vis, FTIR, and GIWAX are performed under ambient conditions.

Figure 2.21 presents the conductivity values for PBDTTT-c:Mo(tdf-$COCF_3$)$_3$ layers exposed to ambient air (1h) and stored overnight inside an argon-filled glovebox, both under dark conditions. For the sample exposed to ambient air, initial and final conductivity values are measured inside the glovebox. From **Figure 2.21**a we can see that the conductivity is not stable under ambient

air (dark), as a significant decrease is observed after 1h. Regarding the stability under argon atmosphere, the conductivity showed to be stable in the considered timescale (**Figure 2.21**b).

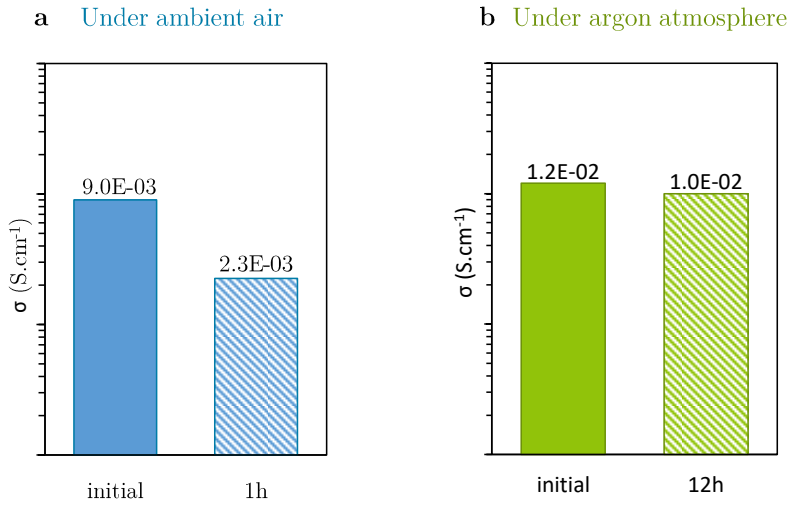

Figure 2.21 – Storage of PBDTTT-c:Mo(tdf-$COCF_3$)$_3$ layers (15nm, 5 mol% Mo(td-$COCF_3$)$_3$) in dark boxes under ambient air (a) and argon atmosphere(b).

Hence, from these results we highlighted that air exposure should be avoided during the fabrication and characterization of doped layers. Therefore, the fabrications as well as the conductivity measurements are performed inside the glovebox. Regarding other characterization techniques that cannot be performed under controlled atmosphere, such as UV-Vis-NIR measurements, the air exposure of the sample was minimized to a few minutes (<30 min). Additionally, even though PBDTTT-c:Mo(tdf-$COCF_3$)$_3$ presented to be relatively stable inside the glovebox (at short timescales), we chose to characterize only freshly prepared samples (unless specified).

The air stability of *p*-doped conjugated polymers is investigated in detail in chapter 3. Nevertheless, this short stability experiment shines a light on possible challenges for the large-scale processing of *p*-doped layers under ambient atmosphere.

2.3.3 Conclusions and final doping protocol

This last part summarizes relevant processing aspects highlighted in this section and presents the final doping protocol used in this thesis.

Differently from the literature on *p*-doped semi-crystalline conjugated polymers, we observed no processing difficulties related to a solubility loss when co-processing rather amorphous polymers with molecular dopants. This might be correlated to the fact that no effective doping signs were observed in polymer:dopant solutions (**Table 2.8**). However, the absence of doping signatures in solution might also be associated to the low concentration used for the analysis. Therefore, another hypothesis is that the aggregated form of PBDTTT-c doped chains is close to the conformation of pristine polymer chains, presenting similar solubility. Or, that the fraction of doped aggregated chains is small compared to pristine polymer chains, resulting in no visible changes in the solubility. Regardless of the reason, our results indicate that the stirring conditions

(time and temperature) of our co-processed doped layers had no influence on the final properties of thin layers.

Table 2.8– Experimental protocol for preparing pristine and blend solutions, and for the layers deposition. The blend solution corresponds to the moment where the dopant volume is added to the polymer solution (co-processing technique).

	PARAMETERS	DOPANT SOLUTION	POLYMER SOLUTION		BLEND SOLUTION	
SOLUTION PREPARATION	Concentration [g.L^{-1}]	2	< 10	≥10	<10	≥10
	Solvent	o-Xylene	o-Xylene		o-Xylene	
	Stirring time	overnight	overnight		5-10 min	
	Stirring temperature [°C]	25	25	50	25	
LAYER DEPOSITION	Rotation speed [rpm]	-	1000	500	1000	500
	Rotation time [s]	-	60		60	
	Acceleration [rpm.s^{-1}]	-	300		300	
	Thickness [nm]	-	15-50	100-200	15-50	100-200

Additionally, we verified that an effective doping can be achieved with the co-processing technique for doped layers with variable thicknesses. This information is valuable for the future application of these layers, but also for planning experiments that employ different characterizations techniques, which may require different layer thicknesses.

Two critical parameters were identified in this section: thermal annealing and air exposure. Regarding the thermal instability, our data suggest a thermal-induced dedoping process and observed in the literature for F4TCNQ-doped conjugated polymers[66–69]. Thus, no thermal annealing is added to the fabrication protocol and the air exposure is avoided as much as possible, i.e. solution fabrication and deposition are performed inside an argon-filled glovebox and characterizations were performed under controlled atmosphere whenever possible.

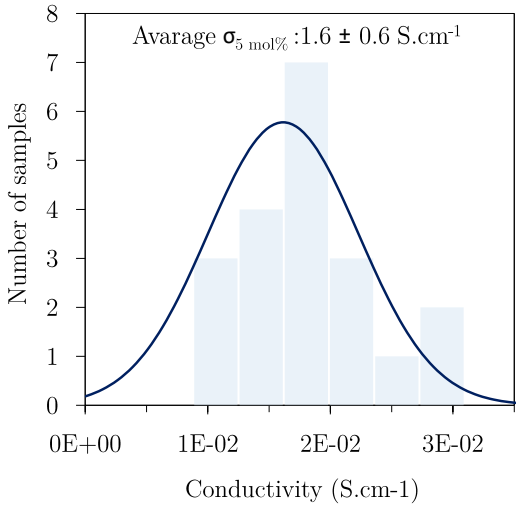

Figure 2.22 – Variation in the conductivity of PBDTTT-c:Mo(tfd-COCF$_3$)$_3$ samples (5mol%, 15 nm) using the final fabrication protocol. Samples are processed and measured inside the glovebox.

Table 2.8 summarizes the final protocol, i.e. the experimental conditions used in this thesis for fabricating pristine and doped polymer layers using the co-processing technique. The

reproducibility of the protocol was tested for 20 PBDTTT-c samples doped at 5 mol% of Mo(tfd-$COCF_3)_3$, prepared from different solutions in different days. The resulting conductivities are presented in **Figure 2.22**, with a mean value of $1.6\pm0.6x10^{-2}$ $S.cm^{-1}$. Thus, from the conductivity distribution presented in **Figure 2.22**, we conclude that our protocol allows for a controlled doping process with reproducible conductivities.

In the following, using the doping protocol presented in **Table 2.8**, we will discuss in more details the evolution of the doping signatures of the four different systems considered in this thesis: PBDTTT-c:Mo(tfd-$COCF_3)_3$, RRa-P3HT: Mo(tfd-$COCF_3)_3$, PBDTTT-c:F4TCNQ and rra-P3HT:F4TCNQ.

2.4 MOLECULAR P-DOPING OF DISORDERED HOSTS

In the previous sections, we characterized the initial properties of polymers and dopants and optimized our doping protocol (with the co-processsing technique), to achieve a controlled doping with reproducible results. It is worth highlighting that these results are crucial for a meaningful study of the doping signatures in polymer hosts, as process parameters can introduce important variations on the final properties of doped layers (see 2.1.2). Here, we discuss the evolution of the electrical, optical and morphological properties of PBDTTT-c and RRa-P3HT upon addition of *p*-dopants (i.e. Mo(tdf-$COCF_3$)$_3$ and F4TCNQ).

This section is organized in two parts. First, we evaluate the doping potential of each polymer:dopant system by means of conductivity and UV-Vis-NIR measurements. Also, to further investigate the conductivity limit of the polymer:dopant systems, the sequential-processing technique is briefly explored. In the second part, we investigate the morphological changes of PBDTTT-c layers upon introduction of dopants molecules by GIWAX.

2.4.1 Conductivity and UV-Vis-NIR spectra

Here, we investigate the evolution of the conductivity and UV-Vis-NIR absorption of PBDTTT-c and RRa-P3HT in the presence of molecular dopants. Conductivity measurements are performed to verify if there is an effective doping of the polymer hosts, i.e. if the selected molecular dopants introduce free holes in the conjugated polymers. Regarding the UV-Vis-NIR measurements, this characterization is used to analyze the doping induced bands and the fraction of doped and neutral species. This information can give insights on the doping mechanism as discussed in 1.2.4.

Evolution of the doping signatures as a function of the dopant concentration

Here, we will present and discuss the evolution of the conductivity and UV-Vis-NIR signatures as a function of the dopant concentration for all four *p*-doped systems: PBDTTT-c:Mo(tfd-$COCF_3$)$_3$, PBDTTT-c:F4TCNQ, RRa-P3HT: Mo(tfd-$COCF_3$)$_3$, and RRa-P3HT:F4TCNQ. Samples were processed with the co-processing technique, using the optimized doping protocol presented in section 2.2.3 (see **Table 2.8**).

The blend solutions prepared for PBDTTT-c:Mo(tfd-$COCF_3$)$_3$, P3HT:Mo(tfd-$COCF_3$)$_3$, PBDTTT-c:F4TCNQ and P3HT:F4TCNQ are summarized in **Table 2.9**. Doped layers were processed with the protocol described in **Table 2.8**. All samples prepared and discussed in this section have thicknesses between 15-20 nm. This was achieved by controlling the final polymer concentration of the blend solution, which was kept constant at 4.7-5 g.L^{-1}.

Table 2.9– Overview of the solutions prepared for different doping ratios using the co-processing doping technique.

System	POLYMER SOLUTION		DOPANT SOLUTION	POLYMER:DOPANT SOLUTION		
	Concentration (Cp)	Volume (Vp)	Volume (Vd)	Doping ratio	Concentration (polymer : dopant)	Layer thickness
[polymer:dopant]	[g.L^{-1}]	[µl]	[µl]	[mol %]	[g.L^{-1}]:[g.L^{-1}]	[nm]
PBDTTT-c: Mo(tfd-COCF$_3$)$_3$	5,3	900	115	4,0	4,7:0,22	15-20
	5,5	900	150	5,0	4,7:0,28	15-20
	6,2	800	240	8,0	4,8:0,46	15-20
	6,7	750	305	10,0	4,8:0,58	15-20
	8,4	600	460	15,0	4,8:0,86	15-20
	11	450	600	20,0	4,8:1,14	15-20
	16	300	725	25,0	4,7:1,41	15-20
	25	200	910	30,0	4,5:1,63	15-20
PBDTTT-c: F4TCNQ	5	1000	10	1,0	4,9:0,02	15-20
	5,2	900	45	5,0	4,9:0,10	15-20
	5,5	900	96	10,0	4,9:0,19	15-20
	6,1	800	190	20,0	4,9:0,38	15-20
	6,5	800	253	25,0	4,9:0,48	15-20
	7	750	306	30,0	4,9:0,58	15-20
P3HT: Mo(tfd-COCF$_3$)$_3$	6,5	800	100	0,7	4,9:019	15-20
	6,5	600	200	2,0	4,8:0,50	15-20
	7,5	550	300	2,8	4,8:0,70	15-20
	8,7	500	400	3,6	4,8:0,88	15-20
	9,6	500	500	4,0	4,8:1,0	15-20
P3HT: F4TCNQ	5,5	900	103	2,5	4,9:0,2	15-20
	6,3	700	183	5,0	4,9:0,4	15-20
	7,5	550	274	8,0	5,0:0,66	15-20
	8,9	500	370	11,0	5,1:0,85	15-20
	9,6	500	479	13,0	5,1:0,97	15-20

The conductivity and UV-Vis-NIR absorption spectra of freshly prepared samples are presented in **Figure 2.23** as function of the dopant concentration. The UV-Vis-NIR spectra are normalized at the π-π* absorption band of the polymer host, to better observe the changes related to the doped state. Besides, to help identifying signatures of dopant molecules, their neutral and ionized absorptions are plotted below the UV-Vis-NIR spectra of doped layers. To facilitate the comparison of the conductivity changes with the appearance of NIR absorptions of doped polymer chains, the evolution of the 2300 nm band is plotted together with conductivity results (black signs **Figure 2.23**a, c, e). This band was chosen due to its relative isolation from other spectral features such as aggregated polymer chains or neutral and/or ionized dopant molecules.

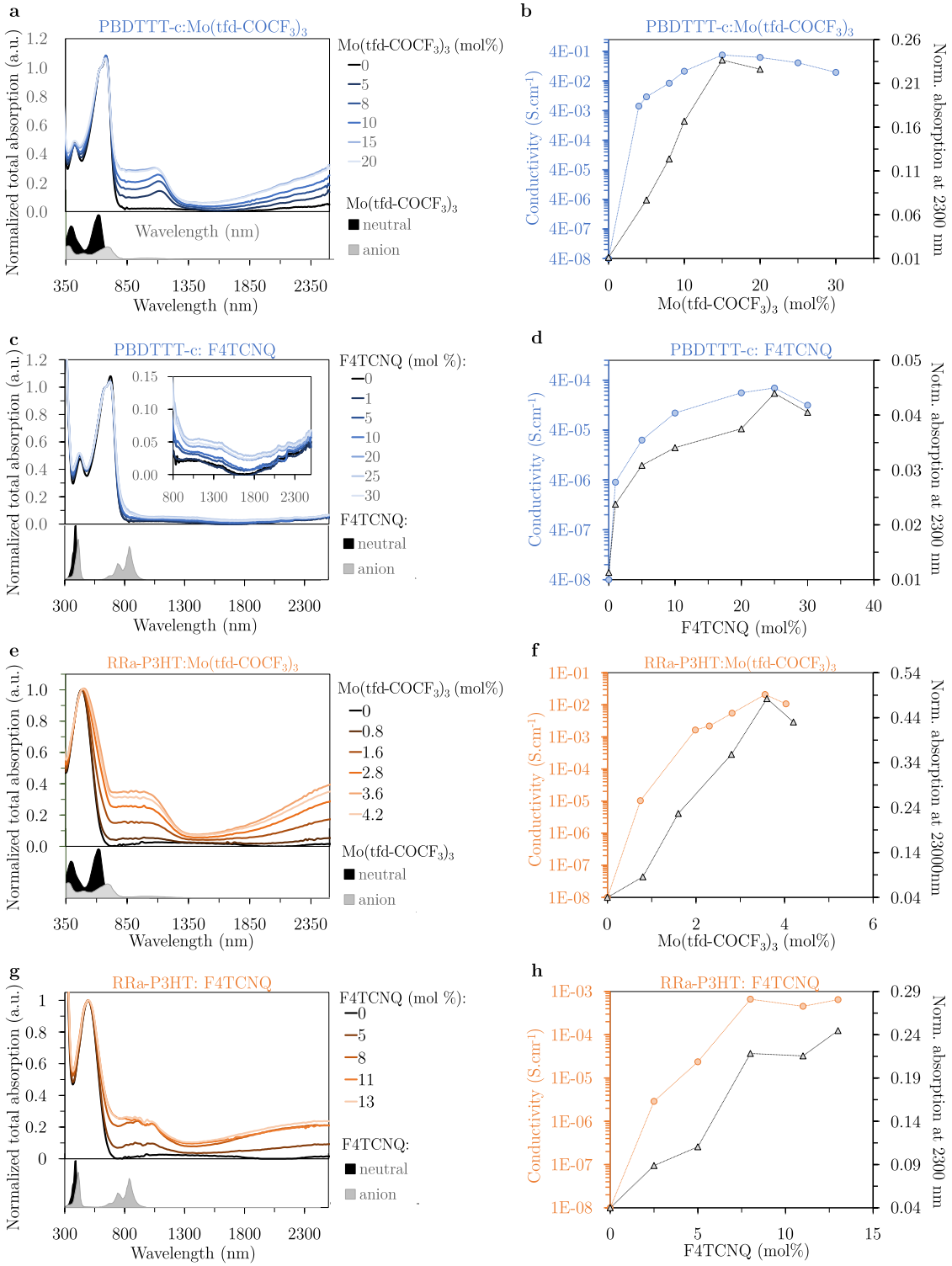

Figure 2.23 – UV-Vis-NIR spectra (a,c,e,g) and conductivity evolution (circles in b,d,f,h) of *p*-doped layers as a function of the dopant concentration. For comparison, the evolution of the absorption at 2300 nm are plotted together with the conductivity evolution (triangles in b,d,f,h). All layers presented approximately 15 nm.

For PBDTTT-c: $Mo(tfd\text{-}COCF_3)_3$ layers, clear bleaching of the **π-π*** transition is observed as the dopant molar ratio is increased (**Figure 2.23**a). This variation is concomitant with the growing of new sub-gap absorption bands in the NIR located at ≈1100 nm and beyond 2000 nm. These

bands are similar to those found by Cobet and coworkers for PBDTTT-c polarons by iodine-doping (peak maxima at ≈1033 nm and ≈3180 nm)[70]. The absorption signatures of Mo(tfd-$COCF_3)_3$ are masked by the **π-π*** absorption of neutral PBDTTT-c. Thus, it is not possible to verify the presence of ionized dopant molecules even at 20 mol% of Mo(tfd-$COCF_3)_3$. The conductivity of this doped system increases seven orders of magnitude, with a maximum of 0.3 $S.cm^{-1}$ at 15 mol% Mo(tfd-$COCF_3)_3$ (**Figure 2.23**b). Compared to previous studies on the same polymer:dopant system, our samples presented exceptionally high conductivities.[39–41] The main difference between our processing conditions and those reported previously for PBDTTT-c:Mo(tfd-$COCF_3)_3$ layers relies on the absence of the thermal annealing post-treatment.

For F4TCNQ-doped PBDTTT-c, only slight changes are observed in the UV-Vis-NIR spectra upon doping, even at high doping ratios up to 30 mol% (**Figure 2.23**c). A broad band at 1200 nm and a second one beyond 2000 nm grow slightly with increasing the F4TCNQ concentration. No clear absorption neither of neutral nor ionized F4TCNQ can be observed. Besides, the conductivity increase is considerably lower than for PBDTTT-c: Mo(tfd-$COCF_3)_3$, reaching a maximum of approx. $2x10^{-4}$ $S.cm^{-1}$ (**Figure 2.23**d).

Regarding P3HT doped layers, the introduction of both F4TCNQ and Mo(tfd-$COCF_3)_3$ presented clear NIR sub-gap absorptions located at *ca.* 850 nm and beyond 2000 (**Figure 2.23**e, g). This bands were also reported for RR-P3HT:F4TCNQ in the literature and correlated to P3HT polaron absorptions[28,32]. Additionally, in **Figure 2.23**g we also identify the absorption band of F4TCNQ anion at approx. 865 nm and 775 nm[56]. A maximum conductivity of approx. $2x10^{-4}$ $S.cm^{-1}$ was achieved (**Figure 2.23**h). This value is considerably lower than the ones reported in the literature for RR-P3HT:F4TCNQ, but is consistent with the amorphous character of our P3HT host.

For P3HT: Mo(tfd-$COCF_3)_3$, the fact that we observe clear P3HT polaron bands tells us that we also have ionized dopants in the samples. However, the absorption of the dopant anion is masked by the neutral and polaron absorption of P3HT and cannot be discerned in the doped spectra. The maximum conductivity obtained for Mo(tfd-$COCF_3)_3$ – doped P3HT is 1.2 x 10^{-2} $S.cm^{-1}$, approx. two orders of magnitude higher than for F4TCNQ – doped P3HT. This is consistent with the higher polaron band observed when doping with Mo(tfd-$COCF_3)_3$. The low dopant concentration used here compared to other systems is related to the difference in the molar weight of Mo(tfd-$COCF_3)_3$ and RRa-P3HT and consequently the solubility limits of the dopant.

For all doped systems, the conductivity and the in the NIR absorption follow the same trend with the dopant addition (**Figure 2.23**a, c, e, f): up to a given dopant concentration, a steep increase in conductivity and in NIR absorption bands is observed, what can be correlated to the formation of doped polymer chains. At higher doping levels, both doping signatures stop increasing, indicating that no more doped polymer segments are formed. The saturation beyond a certain dopant concentration was already reported for other doped OSCs and correlated to the limited number of dopant anions that can be accommodated in the host material, depending on the nature of the polymer-dopant interactions[27,62,71]. Therefore, the slight conductivity decrease observed for our samples suggests an increase of molecular disorder due to an excess of dopant[72].

Note that all the systems still present a considerable amount of neutral polymer, differently from rr-P3HT:F4TCNQ that presents a complete bleaching of the P3HT π-π* band at 17 mol%[27,32].

Regarding the doping mechanism, one can highlight some interesting facts from the UV-Vis-NIR spectra presented in **Figure 2.23**. As discussed in section 1.2.4, this technique allows extracting valuable information on the state of the materials, i.e. if they are neutral, ionized or if hybridization of orbitals occurred. Both mechanism were reported to present NIR features growing with the dopant concentration[71]. Therefore, this analysis requires a knowledge of the neutral and ionized signatures of the involved materials. In this context, the two new absorption bands observed for RRa-P3HT-doped samples have been assigned to the presence of positive polarons in P3HT backbones[28,70,73,74]. Besides, for F4TCNQ-doped RRa-P3HT, we also see optical signatures of F4TCNQ anions (slightly shifted compared to the reference spectra taken from[55]). Even though we do not observed the absorption of ionized Mo(tfd-$COCF_3$)$_3$ (probably related to the lower concentration in the sample combined with a lower molar absorptivity[57]), our results suggest that ion-pairs formation is the mechanism governing the doping of RRa-P3HT:F4TCNQ and RRa-P3HT: Mo(tfd-$COCF_3$)$_3$.

Regarding PBDTTT-c-doped hosts, the doping-induced NIR absorption are considerably different. When doping with Mo(tfd-$COCF_3$)$_3$, we also observed polaron-like absorption bands close to the value found in the literature[70]. The absence of clear absorption signatures of dopant anions can be justified by the overlapping of the absorption spectra, combined with the fact that the polymer presents a higher concentration and molar absorptivity. Thus, our results also suggest that ion-pair formation is the doping mechanism for PBDTTT-c: Mo(tfd-$COCF_3$)$_3$. Note that this conclusion diverge from recent articles studying the same system[40], which observed however different doping-induced absorption peaks. These different results highlight the influence of the processing conditions on the doping process, as reported by Jacobs *et al.* for P3HT:F4TCNQ[75].

The doping-induced absorption for PBDTTT-c:F4TCNQ are less pronounced. No band below 2000 nm seems to grow in this system even at higher dopant concentration. Besides, we do not distinguish absorption of neither neutral nor ionized F4TCNQ, which may be hidden by the polymer absorption. One may argue that lower NIR absorption are due to the lower LUMO level of F4TCNQ compared to Mo(tfd-$COCF_3$)$_3$. However, if we compare with our results for RRa-P3HT, we observed nearly the same polaron-like absorption for both dopants, which were however more pronounced for Mo(tfd-$COCF_3$)$_3$ doped layers, in agreement with the higher reduction potential of this *p*-dopant. Interestingly, RRa-P3HT:F4TCNQ presented higher conductivities than PBDTTT-c:F4TCNQ. From the energy levels measured by CV, we would expect an inverse trend (See **Figure 2.16**). Note that from all four studied *p*-doped systems, PBDTTT-c:F4TCNQ is the only one where polymer and dopant present relatively planar structures. Planarity was reported as a parameter that favor the hybridization of molecular orbitals involved in the doping process, creation charge transfer complexes[61,71].

Finally, an effective doping process was observed for all four systems. Higher conductivities and NIR absorption were obtained when doping with Mo(tfd-$COCF_3$)$_3$. This result is consistent with

the higher LUMO level of Mo(tfd-$COCF_3$)$_3$ (5.3 eV) compared to F4TCNQ (5.1 eV). Nevertheless, our results also highlighted that the doping process is not only dependent on the offset between the HOMO of the polymer and the LUMO of the *p*-dopant. The doping signatures obtained for PBDTTT-c:F4TCNQ suggest that the geometry, for instance the planarity, is also an important parameter controlling the doping mechanism and, consequently, generation of free holes in polymer hosts. This observation is agreement with the literature[61].

Sequential-processing of Mo(tfd-$COCF_3$)$_3$-doped PBDTTT-c

Here, we compare the conductivity and UV-Vis-NIR absorption obtained for co-processed and sequentially-processed layers, to evaluate the potential of this two-steps doping technique when processing nearly amorphous polymer hosts with bulky dopant molecules. The study is performed with Mo(tfd-$COCF_3$)$_3$-doped PBDTTT-c. Besides presenting the highest conductivities, this system was chosen to investigate the impact of the doping technique on the aggregation process of PBDTTT-c chains, and to verify if bulky dopants such as Mo(tfd-$COCF_3$)$_3$ can be effectively used for the sequential-processing technique, where dopants are introduced by solid state diffusion.

When doping semi-crystalline polymer hosts, sequentially-processed layers presented better overall properties than co-processed layers, which showed homogeneity issues due to a doping-induced aggregation process (see 2.1.2)[31]. Even though we do not observe any kind of processing issues when co-processing PBDTTT-c: Mo(tfd-$COCF_3$)$_3$ samples, this section aims to compare both doping techniques in the context of overall disordered hosts. As far as we know, this comparison was not yet performed in the literature.

For the sequential-processing technique, the doping is realized in a second deposition step, where the dopant solution is processed from a solvent orthogonal to the polymer layer (as illustrated in **Figure 2.5**). First, we tested the reproducibility of the doping signatures with a protocol taken from the literature[32]. Afterwards, we verified the influence of the wetting time (i.e. the time at which the polymer layers are exposed to the dopant solution) on the doping signatures. For RR- P3HT:F4TCNQ, the doping signatures have shown to be independent of the wetting time, leading the authors to the conclusion that the equilibrium between neutral dopant molecules (in the solvent) and the ionized dopant molecules (in the polymer host) is reached extremely fast[32]. Since Mo(tfd-$COCF_3$)$_3$ is bulkier than F4TCNQ, we chose to verify if this conclusion is also valid for different systems. Last, this doping technique was tested for different layers thicknesses, as performed for co-processed layers in section 2.3.2 (see **Table 2.7**).

We chose acetonitrile as orthogonal solvent to PBDTTT-c. The polymer layers were processed as described in **Table 2.8**. To test the reproducibility of the processing protocol, the concentration of the dopant solution and the wetting time were fixed at 0.2 $g.L^{-1}$ and 20 seconds. Thin polymer layers were prepared by spin coating PBDTTT-c (5 $g.L^{-1}$, o-Xylene) to form approximately 20 nm thick layers. Doping was performed by wetting the PBDTTT-c layer with Mo(tfd-$COCF_3$)$_3$, waiting 20 seconds, then spinning off the excess solution at 1000 rpm. This process was adapted from [32]. The reproducibility of this protocol was tested over five samples prepared in different days and from different solution. The obtained conductivities are presented

in **Table 2.10**, with a median value of 1.2 ±0.4x10^{-1} S.cm^{-1} (sample 1-5). Hence, we conclude that reproducible conductivities are obtained with the selected protocol.

Table 2.10– Parameters varied for sequentially doped PBDTTT-c:Mo(tfd-COCF$_3$)$_3$ layers. Layer thickness was measured for the pristine PBDTTT-c layer (before doping).

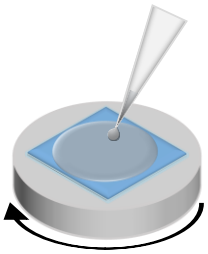

Sample	Wetting time (s)	Layer Thickness (nm)	Conductivity (S.cm^{-1})
1	20	17±3	1.22E-01
2	20	17±3	8.35E-02
3	20	17±3	1.07E-01
4	20	17±3	1.15E-01
5	20	17±3	1.81E-01
6	**300**	17±3	1.38E-01
7	20	**45±5**	1.46E-01
8	20	**125±5**	1.19E-01

No significant conductivity variation was observed for a wetting time of 300 seconds (sample 6, **Table 2.10**) and for thicker PBDTTT-c layers (samples 7 and 8, **Table 2.10**). In other words, for a fixed dopant solution of 0.2 g.L^{-1}, we obtained approximatively the same conductivities for all samples, regardless of the wetting time or the polymer layer thickness. We note that further analysis are required to verify if Mo(tfd-COCF$_3$)$_3$ molecules are homogeneously incorporated in thicker PBDTTT-c layers (e.g. 125 nm) after a doping process of 20 seconds. Nevertheless, this experimental study suggests that sequential processing can also be used to doped polymer layers of several thicknesses with 3D dopant molecules. We were not able to test higher dopant concentration as the solubility of Mo(tfd-COCF$_3$)$_3$ in acetonitrile was limited to *ca.* 0.2 g.L^{-1}.

To be able to compare both doping techniques, the doping level of sequentially doped samples was estimated. This was performed as described by Jacobs and coworkers at[32]. Basically, as the doping level of the co-processed samples is known, we used their UV-Vis-NIR spectra to estimate the doping level of the sequentially processed samples. In **Figure 2.23**b, we presented the evolution of the 2300 nm band with the dopant concentration for co-processed samples (taken after normalizing the spectra to absorption maximum of the π-π* band). Here, we use the linear region from 0-15 mol% of Mo(tfd-COCF$_3$)$_3$ to convert the NIR absorption of sequentially doped layers to doping levels. **Figure 2.24**a presents the linear fit as well as the conductivity results for both techniques. The estimated doping level of our sequentially doped samples is of *ca.* 10 mol%. **Figure 2.24**b compares the UV-Vis-NIR spectra of a co-processed sample at 10 mol% with a sequentially processed, where one can verify an identical fraction of pristine and doped absorptions.

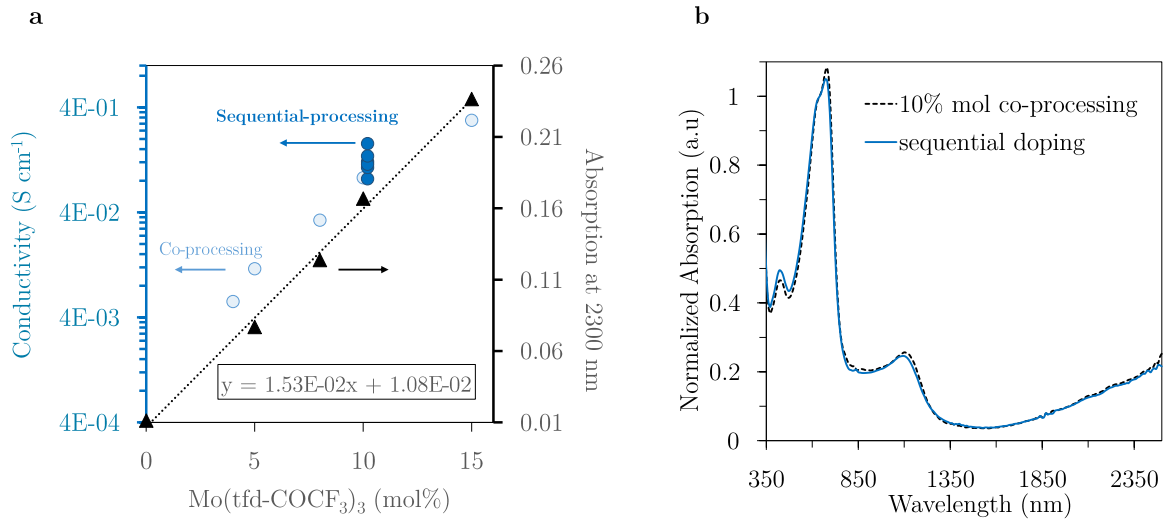

Figure 2.24 – Comparison between sequentially process and co-processed PBDTTT-c:Mo(tfd-$COCF_3)_3$ layers. (a) linear relation between NIR signatures of co-processed samples at 2300 nm as a function of the dopant concentration (black triangles) used to extract the dopant concentration of sequentially doped samples and comparison between conductivities obtained with both techniques (blue circles). (b) Comparison of UV-Vis- NIR absorption of sequentially and co-processed layers.

The maximum conductivity (σ_{max}) reached with the sequential doping technique was 0.2 S cm^{-1} for an estimated doping level of 10.5 mol%, higher than co-processed samples with the similar doping level (8.5 x10^{-2} S cm^{-1} at 10 mol% of Mo(tfd-$COCF_3)_3$), as shown in **Figure 2.24**a. Nevertheless, the maximum conductivity value obtained for PBDTTT-c: Mo(tfd-$COCF_3)_3$ was 0.3 S.cm^{-1} for co-processed samples (15 mol%). Since this values are very close, we conclude that σ_{max} achieved with both technique are identical. Note that improving the solubility of Mo(tfd-$COCF_3)_3$ in a solvent orthogonal to PBDTTT-c may result in higher conductivities for sequentially doped layers. Here, we were limited to a solubility of *ca.* 0.2 g.L^{-1} in acetonitrile.

Finally, we can conclude that sequential processing is also a viable technique for doping PBDTTT-c layers of different thicknesses with Mo(tfd-$COCF_3)_3$, despite the bulky nature of this dopant molecule. The σ_{max} achieved with co-processed and sequentially processed layers are identical.

2.4.2 Impact of molecular dopants in the morphology of PBDTTT-c

The diffraction pattern of pristine and doped PBDTTT-c layers were measured to verify the influence of a planar (F4TCNQ) and a 3D ($Mo(tfd\text{-}COCF_3)_3$) molecular dopant on the arrangements of these polymer chains. The measurements were performed with PBDTTT-c layers doped at 20 mol% via co-processing. Samples were spin coated and drop casted from the same solution on glass substrates, to prepared ~20 nm and ~1 µm thick layers, respectively (see **Table 2.9** for details on the concentrations). The influence of the glass substrate on the measurement was verified in section 2.2.1 (See **Figure 2.10**). To avoid exposing doped layers several hours to ambient air, these measurements were performed under argon atmosphere inside a graphite dome. Hence, the doped layers were only exposed a few minutes to ambient atmosphere before installing the samples in the X-ray diffractometer.

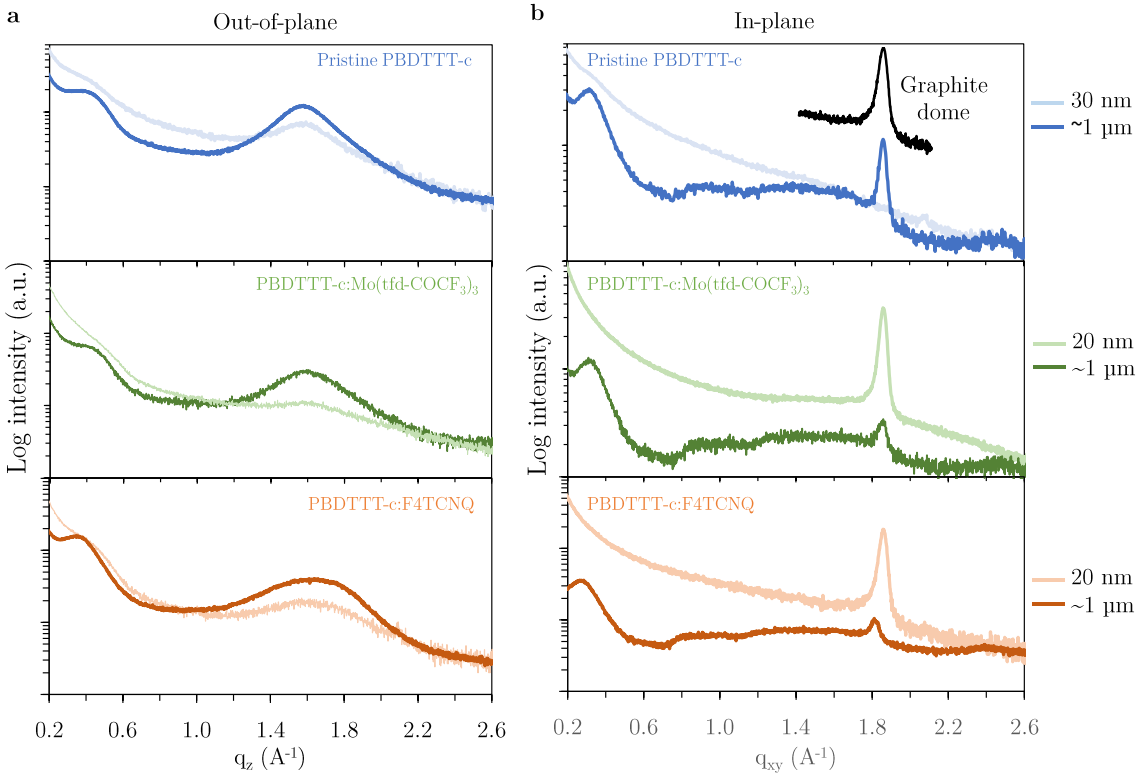

Figure 2.25 - GIWAXS diffractograms of pristine and doped PBDTTT-c layers casted from o-Xylene in out-of-plane scan (a) and in-plane scan (b). Comparison between drop-casted (1 µm-thick) and spin-coated (30 nm-thick) layers.

Figure 2.25 presents the out-of-plane and in-plane scans for pristine and doped PBDTTT-c layers. To allow for a better comparison of the shape and intensity of the resulting peaks of ~20 nm and ~1 µm samples, the diffractograms are superposed at higher diffraction angles, where no features were detected. From the out of plane scans (**Figure 2.25**a), we observe no particular difference between thin and thick doped layers. Regarding the in-plane scans (**Figure 2.25**b), despite the features related to polymer layers, we also observed a diffraction peak of the graphite dome. A similar peak is observed for both thicknesses at low diffraction angles, but thicker

samples presented additional broad diffraction features at higher angles. Since these features are also observed for pristine polymer layers of ~1 µm, they are not related to the doping process, but to the layers thickness. Here, we are interested in discussing the changes related to the dopant addition. From the diffractograms presented in **Figure 2.25** we conclude that the layers thickness and the drying process (fast for spin coating and slow for drop casted layers) have particular influence on the ordering of pristine and doped PBDTTT-c chains.

To allow for a quantitative analysis of the changes related to the dopant addition, the diffraction peaks were fitted with HighScore software. The thicker samples were used for this purpose, due to the higher intensities of the peaks. Since no considerable difference was observed for thin and thick doped layers, the conclusion from the fits are extended for both thicknesses. **Figure 2.26** presents the out of plane scans of pristine and doped ~1 µm samples superposed at higher diffraction angles and the resulting fits. The values extracted from the fits are presented in **Table 2.11**. For more details on the fitting process, see Appendix A.

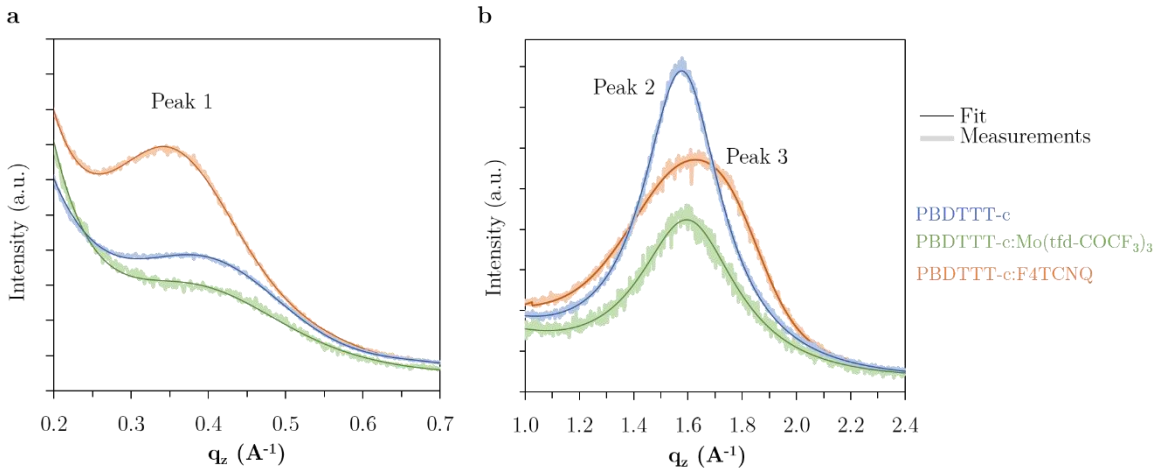

Figure 2.26 – Comparison of GIWAXS diffractograms of pristine and doped PBDTTT-c (20 mol% dopant) layers casted from o-Xylene in out-of-plane.

Before commenting the quantitative results from the fits, one can already conclude from **Figure 2.26** that the peaks of PBDTTT-c layers doped with F4TCNQ present different shapes and/or positions compared to pristine and Mo(tfd-COCF$_3$)$_3$ doped layers, which are very similar. These observations are confirmed by the fits. When comparing the fits for pristine PBDTT-c and PBDTTT-c:Mo(tfd-COCF$_3$)$_3$, the peak positions are very similar but higher FWMH are obtained for the doped sample, indicating an increase in disorder upon dopant addition. This is consistent with the quantity (20 mol%) and size of Mo(tfd-COCF$_3$)$_3$. Regarding PBDTTT-c:F4TCNQ doped layers, despite the shift of the Peak 1 (**Figure 2.26a**), the broader peak observed at higher diffraction angles (Figure 2.26b) suggest the presence of a second peak. Thus, this broad peak was fitted with two peaks, Peak2 and Peak 3 (**Table 2.11**). Interestingly, Peak 2 presented similar values than for pristine and Mo(tfd-COCF$_3$)$_3$-doped PBDTTT-c. When considering only one peak (Peak 2), it was not possible to correctly fit this broad peak.

Table 2.11– Peak fitting for in-plane and out-of-plane GIWAXS diffractograms of pristine and doped PBDTTT-c layers (20 mol% dopant).

Out-of-plane

Layers	PBDTTT-c		:Mo(tfd-$COCF_3$)$_3$		:F4TCNQ		
	Peak 1	Peak 2	Peak 1	Peak 2	Peak 1	Peak 2	Peak 3
q (A^{-1})	0.40	1.58	0.38	1.60	0.34	1.57	1.76
Peak position (2theta)	5.6	22.3	5.3	22.6	4.9	22.2	24.9
d spacing	15.7	4.0	16.7	3.9	17.9	4.0	3.6
Height (cts)	848	744.33	685	389	1291	378	141
FWHM(2theta)	3.0	4.92	3.4	6.33	2.5	6,7	4,2

As discussed in section 2.2.1 for the diffractograms of pristine PBDTTT-c, our results suggest a morphology with mixed phases, i.e. some backbones with "edge-on" orientation and others with "face-on" orientation, as in-plane and out-of-plane scans presented characteristics distances of lamellar stacking. If we assume that our PBDTTT-c samples have a preferential "face-on" orientation and Peak 2 corresponds to their π-stacking distance, the existence of Peak 3 for PBDTTT-c:F4TCNQ doped samples indicates that the F4TCNQ interacts with π-stacked PBDTTT-c chains. This results are consistent with the planarity of both dopant and polymer chains, which would allow a stacking of F4TCNQ molecules between π-stacked polymer chains. This observation could also be related to the doping signatures of PBDTTT-c:F4TCNQ samples, which suggested a CPX formation for this system and consequently a strong interaction between π orbitals of polymer and dopant molecules.

Due to the limited information obtained for higher diffraction angles in the in-plane direction, we will avoid extrapolating possible explanations for the shift in Peak 1 observed for PBDTTT- c:F4TCNQ samples.

Finally, the presented results indicate that bulky dopants such as Mo(tfd-$COCF_3$)$_3$ increase the disorder of PBDTTT-c chains and planar dopants such as F4TNCQ change the conformation of polymer chains, possibly by a packing of F4TCNQ molecules between π-stacked PBDTTT-c chains.

2.5 CONCLUSION

In this chapter, we characterized the pristine materials, optimized the doping process in the conditions selected for this work and studied the initial state of *p*-doped layers. Characterizing the pristine materials was important for the interpretation of the results obtained doped solutions and layers. Below, the main conclusion of this chapter are summarized.

When doping PBDTTT-c and RRa-P3HT with molecular *p*-dopants using the co-processing technique, we observed no processing difficulties related to a solubility loss, regardless of the stirring conditions (time and temperature) of the polymer:dopant blend or the concentration of the solutions (or layer thickness). No rigorous control of the doping conditions is needed for the *p*-doped layers studied in this work. This flexibility is an advantage for large scale productions.

Two critical parameters were identified in this section: thermal annealing and air exposure. Regarding the thermal instability, our data suggest a thermal-induced dedoping process for F4TCNQ and Mo(tfd-$COCF_3$)$_3$ doped layers, possibly related to the weak interaction of polymer and dopant molecules combined with the volatility of the latter. When avoiding these critical parameters, the optimized doping protocol presented reproducible results.

We showed that sequential processing is also a viable technique for doping PBDTTT-c layer of different thicknesses with Mo(tfd-$COCF_3$)$_3$, despite the bulky nature of this dopant molecule. The σ_{max} achieved with co-processed and sequentially processed layers are identical.

An effective doping process was observed for all four systems. Higher conductivities and NIR absorption were obtained when doping with Mo(tfd-$COCF_3$)$_3$. This result is consistent with the higher LUMO level of Mo(tfd-$COCF_3$)$_3$ (5.3 eV) compared to F4TCNQ (5.1 eV). Nevertheless, our results also highlighted planar polymer:dopant systems, such as PBDTTT-c:F4TCNQ, might be an disadvantage for achieving higher conductivities, as it favors the hybridization of frontier orbitals and consequently the formation of CPX.

Finally, the GIWAX diffractograms of doped layers suggested that Mo(tfd-$COCF_3$)$_3$ increase the disorder of PBDTTT-c chains, whereas F4TNCQ changes the conformation of polymer chains, possibly by a packing of F4TCNQ molecules between π-stacked PBDTTT-c chains. This can be explained by the bulky and planar geometry of the respective dopant molecules.

Now that we characterized and discussed the initial state of the *p*-doped layers studied in this work, the next chapter investigates the stability of the *p*-doped state under ambient air, i.e. in the presence of oxygen and humidity.

2.6 REFERENCES

(1) Noriega, R.; Rivnay, J.; Vandewal, K.; Koch, F. P. V.; Stingelin, N.; Smith, P.; Toney, M. F.; Salleo, A. A General Relationship between Disorder, Aggregation and Charge Transport in Conjugated Polymers. *Nat. Mater.* **2013**, *12* (11), 1038–1044. https://doi.org/10.1038/nmat3722.

(2) Yamagata, H.; Spano, F. C. Interplay between Intrachain and Interchain Interactions in Semiconducting Polymer Assemblies: The HJ-Aggregate Model. *J. Chem. Phys.* **2012**, *136* (18), 184901. https://doi.org/10.1063/1.4705272.

(3) Spano, F. C.; Silva, C. H- and J-Aggregate Behavior in Polymeric Semiconductors. *Annu. Rev. Phys. Chem.* **2014**, *65* (1), 477–500. https://doi.org/10.1146/annurev-physchem-040513-103639.

(4) Newbloom, G. M.; Iglesia, P. de la; Pozzo, L. D. Controlled Gelation of Poly(3-Alkylthiophene)s in Bulk and in Thin-Films Using Low Volatility Solvent/Poor-Solvent Mixtures. *Soft Matter* **2014**, *10* (44), 8945–8954. https://doi.org/10.1039/C4SM00960F.

(5) Xu, W.; Li, L.; Tang, H.; Li, H.; Zhao, X.; Yang, X. Solvent-Induced Crystallization of Poly(3-Dodecylthiophene): Morphology and Kinetics. *J. Phys. Chem. B* **2011**, *115* (20), 6412–6420. https://doi.org/10.1021/jp201044b.

(6) Ko, S.; Hoke, E. T.; Pandey, L.; Hong, S.; Mondal, R.; Risko, C.; Yi, Y.; Noriega, R.; McGehee, M. D.; Brédas, J.-L.; Salleo, A.; Bao, Z. Controlled Conjugated Backbone Twisting for an Increased Open-Circuit Voltage While Having a High Short-Circuit Current in Poly(Hexylthiophene) Derivatives. *J. Am. Chem. Soc.* **2012**, *134* (11), 5222–5232. https://doi.org/10.1021/ja210954r.

(7) Böckmann, M.; Schemme, T.; Jong, D. H. de; Denz, C.; Heuer, A.; Doltsinis, N. L. Structure of P3HT Crystals, Thin Films, and Solutions by UV/Vis Spectral Analysis. *Phys. Chem. Chem. Phys.* **2015**, *17* (43), 28616–28625. https://doi.org/10.1039/C5CP03665H.

(8) Mikhnenko, O. V.; Blom, P. W. M.; Nguyen, T.-Q. Exciton Diffusion in Organic Semiconductors. *Energy Environ. Sci.* **2015**, *8* (7), 1867–1888. https://doi.org/10.1039/C5EE00925A.

(9) Bredas, J.-L. Mind the Gap! *Mater. Horiz.* **2013**, *1* (1), 17–19. https://doi.org/10.1039/C3MH00098B.

(10) Clark, J.; Silva, C.; Friend, R. H.; Spano, F. C. Role of Intermolecular Coupling in the Photophysics of Disordered Organic Semiconductors: Aggregate Emission in Regioregular Polythiophene. *Phys. Rev. Lett.* **2007**, *98* (20), 206406. https://doi.org/10.1103/PhysRevLett.98.206406.

(11) Virkar, A. A.; Mannsfeld, S.; Bao, Z.; Stingelin, N. Organic Semiconductor Growth and Morphology Considerations for Organic Thin-Film Transistors. *Adv. Mater.* **2010**, *22* (34), 3857–3875. https://doi.org/10.1002/adma.200903193.

(12) Brinkmann, M. Structure and Morphology Control in Thin Films of Regioregular Poly(3-Hexylthiophene). *J. Polym. Sci. Part B Polym. Phys.* **2011**, *49* (17), 1218–1233. https://doi.org/10.1002/polb.22310.

(13) Urquhart, S. G.; Martinson, M.; Eger, S.; Murcia, V.; Ade, H.; Collins, B. A. Connecting Molecular Conformation to Aggregation in P3HT Using Near Edge X-Ray Absorption Fine Structure Spectroscopy. *J. Phys. Chem. C* **2017**, *121* (39), 21720–21728. https://doi.org/10.1021/acs.jpcc.7b07143.

(14) Leclerc, N.; Chávez, P.; Ibraikulov, O. A.; Heiser, T.; Lévêque, P. Impact of Backbone Fluorination on π-Conjugated Polymers in Organic Photovoltaic Devices: A Review. *Polymers* **2016**, *8* (1). https://doi.org/10.3390/polym8010011.

(15) Welford, A.; Maniam, S.; Gann, E.; Jiao, X.; Thomsen, L.; Langford, S. J.; McNeill, C. R. Influence of Alkyl Side-Chain Type and Length on the Thin Film Microstructure and OFET Performance of Naphthalene Diimide-Based Organic Semiconductors. *Org. Electron.* **2019**, *75*, 105378. https://doi.org/10.1016/j.orgel.2019.105378.

(16) Guo, Y.; Jiang, L.; Ma, X.; Hu, W.; Su, Z. Poly(3-Hexylthiophene) Monolayer Nanowhiskers. *Polym. Chem.* **2013**, *4* (16), 4308–4311. https://doi.org/10.1039/C3PY00728F.

(17) McFarland, F. M.; Ellis, C. M.; Guo, S. The Aggregation of Poly(3-Hexylthiophene) into Nanowires: With and without Chemical Doping. *J. Phys. Chem. C* **2017**, *121* (8), 4740–4746. https://doi.org/10.1021/acs.jpcc.7b00816.

(18) Hynynen, J.; Kiefer, D.; Yu, L.; Kroon, R.; Munir, R.; Amassian, A.; Kemerink, M.; Müller, C. Enhanced Electrical Conductivity of Molecularly P-Doped Poly(3-Hexylthiophene) through Understanding the Correlation with Solid-State Order. *Macromolecules* **2017**, *50* (20), 8140–8148. https://doi.org/10.1021/acs.macromol.7b00968.

(19) Li, Z.; Lin, H.; Jiang, K.; Carpenter, J.; Li, Y.; Liu, Y.; Hu, H.; Zhao, J.; Ma, W.; Ade, H.; Yan, H. Dramatic Performance Enhancement for Large Bandgap Thick-Film Polymer Solar Cells Introduced by a Difluorinated Donor Unit. *Nano Energy* **2015**, *15*, 607–615. https://doi.org/10.1016/j.nanoen.2015.05.016.

(20) McFarland, F. M.; Ellis, C. M.; Guo, S. The Aggregation of Poly(3-Hexylthiophene) into Nanowires: With and without Chemical Doping. *J. Phys. Chem. C* **2017**, *121* (8), 4740–4746. https://doi.org/10.1021/acs.jpcc.7b00816.

(21) Yuan, Y.; Zhang, J.; Sun, J.; Hu, J.; Zhang, T.; Duan, Y. Polymorphism and Structural Transition around 54 °C in Regioregular Poly(3-Hexylthiophene) with High Crystallinity As Revealed by Infrared Spectroscopy. *Macromolecules* **2011**, *44* (23), 9341–9350. https://doi.org/10.1021/ma2017106.

(22) Prosa, T. J.; Winokur, M. J.; McCullough, R. D. Evidence of a Novel Side Chain Structure in Regioregular Poly(3-Alkylthiophenes). *Macromolecules* **1996**, *29* (10), 3654–3656. https://doi.org/10.1021/ma951510u.

(23) Duong, D. T.; Phan, H.; Hanifi, D.; Jo, P. S.; Nguyen, T.-Q.; Salleo, A. Direct Observation of Doping Sites in Temperature-Controlled, p-Doped P3HT Thin Films by Conducting Atomic Force Microscopy. *Adv. Mater. Deerfield Beach Fla* **2014**, *26* (35), 6069–6073. https://doi.org/10.1002/adma.201402015.

(24) Gao, J.; Niles, E. T.; Grey, J. K. Aggregates Promote Efficient Charge Transfer Doping of Poly(3-Hexylthiophene). *J. Phys. Chem. Lett.* **2013**, *4* (17), 2953–2957. https://doi.org/10.1021/jz401555x.

(25) McFarland, F. M.; Bonnette, L. R.; Acres, E. A.; Guo, S. The Impact of Aggregation on the P-Doping Kinetics of Poly(3-Hexylthiophene). *J. Mater. Chem. C* **2017**, *5* (23), 5764–5771. https://doi.org/10.1039/C7TC00189D.

(26) Tang, K.; McFarland, F. M.; Travis, S.; Lim, J.; Azoulay, J. D.; Guo, S. Aggregation of P3HT as a Preferred Pathway for Its Chemical Doping with F4-TCNQ. *Chem. Commun.* **2018**, *54* (84), 11925–11928. https://doi.org/10.1039/C8CC05472J.

(27) Duong, D. T.; Wang, C.; Antono, E.; Toney, M. F.; Salleo, A. The Chemical and Structural Origin of Efficient P-Type Doping in P3HT. *Org. Electron.* **2013**, *14* (5), 1330–1336. https://doi.org/10.1016/j.orgel.2013.02.028.

(28) Wang, C.; Duong, D. T.; Vandewal, K.; Rivnay, J.; Salleo, A. Optical Measurement of Doping Efficiency in Poly(3-Hexylthiophene) Solutions and Thin Films. *Phys. Rev. B* **2015**, *91* (8), 085205. https://doi.org/10.1103/PhysRevB.91.085205.

(29) Jacobs, I. E.; Moulé, A. J. Controlling Molecular Doping in Organic Semiconductors. *Adv. Mater.* **2018**, *29* (42), 1703063. https://doi.org/10.1002/adma.201703063.

(30) Qi, Y.; Sajoto, T.; Kröger, M.; Kandabarow, A. M.; Park, W.; Barlow, S.; Kim, E.-G.; Wielunski, L.; Feldman, L. C.; Bartynski, R. A.; Brédas, J.-L.; Marder, S. R.; Kahn, A. A Molybdenum Dithiolene Complex as P-Dopant for Hole-Transport Materials: A Multitechnique Experimental and Theoretical Investigation. *Chem. Mater.* **2010**, *22* (2), 524–531. https://doi.org/10.1021/cm9031623.

(31) Scholes, D. T.; Hawks, S. A.; Yee, P. Y.; Wu, H.; Lindemuth, J. R.; Tolbert, S. H.; Schwartz, B. J. Overcoming Film Quality Issues for Conjugated Polymers Doped with F4TCNQ by Solution Sequential Processing: Hall Effect, Structural, and Optical Measurements. *J. Phys. Chem. Lett.* **2015**, *6* (23), 4786–4793. https://doi.org/10.1021/acs.jpclett.5b02332.

(32) Jacobs, I. E.; Aasen, E. W.; Oliveira, J. L.; Fonseca, T. N.; Roehling, J. D.; Li, J.; Zhang, G.; Augustine, M. P.; Mascal, M.; Moulé, A. J. Comparison of Solution-Mixed and Sequentially Processed P3HT:F4TCNQ Films: Effect of Doping-Induced Aggregation on Film Morphology. *J. Mater. Chem. C* **2016**, *4* (16), 3454–3466. https://doi.org/10.1039/C5TC04207K.

(33) Fujimoto, R.; Yamashita, Y.; Kumagai, S.; Tsurumi, J.; Hinderhofer, A.; Broch, K.; Schreiber, F.; Watanabe, S.; Takeya, J. Molecular Doping in Organic Semiconductors: Fully Solution-Processed, Vacuum-Free Doping with Metal–Organic Complexes in an Orthogonal Solvent. *J. Mater. Chem. C* **2017**, *5* (46), 12023–12030. https://doi.org/10.1039/C7TC03905K.

(34) Pingel, P.; Arvind, M.; Kölln, L.; Steyrleuthner, R.; Kraffert, F.; Behrends, J.; Janietz, S.; Neher, D. P-Type Doping of Poly(3-Hexylthiophene) with the Strong Lewis Acid Tris(Pentafluorophenyl)Borane. *Adv. Electron. Mater.* **2016**, *2* (10), 1600204. https://doi.org/10.1002/aelm.201600204.

(35) Welch, G. C.; Coffin, R.; Peet, J.; Bazan, G. C. Band Gap Control in Conjugated Oligomers via Lewis Acids. *J. Am. Chem. Soc.* **2009**, *131* (31), 10802–10803. https://doi.org/10.1021/ja902789w.

(36) Zalar, P.; Henson, Z. B.; Welch, G. C.; Bazan, G. C.; Nguyen, T.-Q. Color Tuning in Polymer Light-Emitting Diodes with Lewis Acids. *Angew. Chem. Int. Ed.* **2012**, *51* (30), 7495–7498. https://doi.org/10.1002/anie.201202570.

(37) Kolesov, V. A.; Fuentes-Hernandez, C.; Chou, W.-F.; Aizawa, N.; Larrain, F. A.; Wang, M.; Perrotta, A.; Choi, S.; Graham, S.; Bazan, G. C.; Nguyen, T.-Q.; Marder, S. R.; Kippelen, B. Solution-Based Electrical Doping of Semiconducting Polymer Films over a Limited Depth. *Nat. Mater.* **2017**, *16* (4), 474–480. https://doi.org/10.1038/nmat4818.

(38) Yamashita, Y.; Tsurumi, J.; Ohno, M.; Fujimoto, R.; Kumagai, S.; Kurosawa, T.; Okamoto, T.; Takeya, J.; Watanabe, S. Efficient Molecular Doping of Polymeric Semiconductors Driven by Anion Exchange. *Nature* **2019**, *572* (7771), 634–638. https://doi.org/10.1038/s41586-019-1504-9.

(39) A. Dai. Creating Highly Efficient Carrier Injection or Collection Contacts via Soft Contact Transfer Lamination of P-Doped Interlayers. Princeton University 2015.

(40) Euvrard, J.; Revaux, A.; Bayle, P.-A.; Bardet, M.; Vuillaume, D.; Kahn, A. The Formation of Polymer-Dopant Aggregates as a Possible Origin of Limited Doping Efficiency at High Dopant Concentration. *Org. Electron.* **2018**, *53*, 135–140. https://doi.org/10.1016/j.orgel.2017.11.020.

(41) Euvrard, J.; Revaux, A.; Nobre, S. S.; Kahn, A.; Vuillaume, D. Toward a Better Understanding of the Doping Mechanism Involved in Mo(Tfd-COCF3)3 Doped PBDTTT-c. *J. Appl. Phys.* **2018**, *123* (22), 225501. https://doi.org/10.1063/1.5029810.

(42) Bencheikh, F.; Duché, D.; Ruiz, C. M.; Simon, J.-J.; Escoubas, L. Study of Optical Properties and Molecular Aggregation of Conjugated Low Band Gap Copolymers: PTB7 and PTB7-Th. *J. Phys. Chem. C* **2015**, *119* (43), 24643–24648. https://doi.org/10.1021/acs.jpcc.5b07803.

(43) Qian, D.; Ye, L.; Zhang, M.; Liang, Y.; Li, L.; Huang, Y.; Guo, X.; Zhang, S.; Tan, Z.; Hou, J. Design, Application, and Morphology Study of a New Photovoltaic Polymer with Strong Aggregation in Solution State. *Macromolecules* **2012**, *45* (24), 9611–9617. https://doi.org/10.1021/ma301900h.

(44) Hou, J.; Chen, H.-Y.; Zhang, S.; Chen, R. I.; Yang, Y.; Wu, Y.; Li, G. Synthesis of a Low Band Gap Polymer and Its Application in Highly Efficient Polymer Solar Cells. *J. Am. Chem. Soc.* **2009**, *131* (43), 15586–15587. https://doi.org/10.1021/ja9064975.

(45) Chen, H.-Y.; Hou, J.; Zhang, S.; Liang, Y.; Yang, G.; Yang, Y.; Yu, L.; Wu, Y.; Li, G. Polymer Solar Cells with Enhanced Open-Circuit Voltage and Efficiency. *Nat. Photonics* **2009**, *3* (11), 649–653. https://doi.org/10.1038/nphoton.2009.192.

(46) Dong, B. X.; Huang, B.; Tan, A.; Green, P. F. Nanoscale Orientation Effects on Carrier Transport in a Low-Band-Gap Polymer. *J. Phys. Chem. C* **2014**, *118* (31), 17490–17498. https://doi.org/10.1021/jp506374m.

(47) Liang, Y.; Yu, L. A New Class of Semiconducting Polymers for Bulk Heterojunction Solar Cells with Exceptionally High Performance. *Acc. Chem. Res.* **2010**, *43* (9), 1227–1236. https://doi.org/10.1021/ar1000296.

(48) Khlaifia, D.; Ewels, C. P.; Massuyeau, F.; Chemek, M.; Faulques, E.; Duvail, J.-L.; Alimi, K. Unraveling the Real Structures of Solution-Based and Surface-Bound Poly(3-Hexylthiophene) (P3HT) Oligomers: A Combined Theoretical and Experimental Study. *RSC Adv.* **2016**, *6* (61), 56174–56182. https://doi.org/10.1039/C6RA03903K.

(49) Martinez, C. R.; Iverson, B. L. Rethinking the Term "Pi-Stacking." *Chem. Sci.* **2012**, *3* (7), 2191–2201. https://doi.org/10.1039/C2SC20045G.

(50) Hammond, M. R.; Kline, R. J.; Herzing, A. A.; Richter, L. J.; Germack, D. S.; Ro, H.-W.; Soles, C. L.; Fischer, D. A.; Xu, T.; Yu, L.; Toney, M. F.; DeLongchamp, D. M. Molecular Order in High-Efficiency Polymer/Fullerene Bulk Heterojunction Solar Cells. *ACS Nano* **2011**, *5* (10), 8248–8257. https://doi.org/10.1021/nn202951e.

(51) Chen, H.-Y.; Hou, J.; Zhang, S.; Liang, Y.; Yang, G.; Yang, Y.; Yu, L.; Wu, Y.; Li, G. Polymer Solar Cells with Enhanced Open-Circuit Voltage and Efficiency. *Nat. Photonics* **2009**, *3* (11), 649–653. https://doi.org/10.1038/nphoton.2009.192.

(52) Li, G.; Chang, W.-H.; Yang, Y. Low-Bandgap Conjugated Polymers Enabling Solution-Processable Tandem Solar Cells. *Nat. Rev. Mater.* **2017**, *2* (8), 1–13. https://doi.org/10.1038/natrevmats.2017.43.

(53) Wang, Y.; Nakano, M.; Michinobu, T.; Kiyota, Y.; Mori, T.; Takimiya, K. Naphthodithiophenediimide–Benzobisthiadiazole-Based Polymers: Versatile n-Type Materials for Field-Effect Transistors and Thermoelectric Devices. *Macromolecules* **2017**, *50* (3), 857–864. https://doi.org/10.1021/acs.macromol.6b02313.

(54) Brédas, J.-L.; Beljonne, D.; Coropceanu, V.; Cornil, J. Charge-Transfer and Energy-Transfer Processes in Pi-Conjugated Oligomers and Polymers: A Molecular Picture. *Chem. Rev.* **2004**, *104* (11), 4971–5004. https://doi.org/10.1021/cr040084k.

(55) Kiefer, D.; Kroon, R.; Hofmann, A. I.; Sun, H.; Liu, X.; Giovannitti, A.; Stegerer, D.; Cano, A.; Hynynen, J.; Yu, L.; Zhang, Y.; Nai, D.; Harrelson, T. F.; Sommer, M.; Moulé, A. J.; Kemerink, M.; Marder, S. R.; McCulloch, I.; Fahlman, M.; Fabiano, S.; Müller, C. Double Doping of Conjugated Polymers with Monomer Molecular Dopants. *Nat. Mater.* **2019**, 1. https://doi.org/10.1038/s41563-018-0263-6.

(56) Dixon, D. A.; Calabrese, J. C.; Miller, J. S. Crystal and Molecular Structure of the 2:1 Charge-Transfer Salt of Decamethylferrocene and Perfluoro-7,7,8,8-Tetracyano-p-Quinodimethane: [[Fe(C5Me5)2]+.Cntdot.]2[TCNQF4]2-. The Electronic Structure of [TCNQF4]n (n = 0, 1-, 2-). *J. Phys. Chem.* **1989**, *93* (6), 2284–2291. https://doi.org/10.1021/j100343a019.

(57) Mohapatra, S. K.; Zhang, Y.; Sandhu, B.; Fonari, M. S.; Timofeeva, T. V.; Marder, S. R.; Barlow, S. Synthesis, Characterization, and Crystal Structures of Molybdenum Complexes of Unsymmetrical Electron-Poor Dithiolene Ligands. *Polyhedron* **2016**, *116*, 88–95. https://doi.org/10.1016/j.poly.2016.04.025.

(58) Lee, S. K.; Zu, Y.; Herrmann, A.; Geerts, Y.; Müllen, K.; Bard, A. J. Electrochemistry, Spectroscopy and Electrogenerated Chemiluminescence of Perylene, Terrylene, and Quaterrylene Diimides in Aprotic Solution. *J. Am. Chem. Soc.* **1999**, *121* (14), 3513–3520. https://doi.org/10.1021/ja984188m.

(59) Gao, W.; Kahn, A. Controlled P-Doping of Zinc Phthalocyanine by Coevaporation with Tetrafluorotetracyanoquinodimethane: A Direct and Inverse Photoemission Study. *Appl. Phys. Lett.* **2001**, *79* (24), 4040–4042. https://doi.org/10.1063/1.1424067.

(60) Li, J.; Duchemin, I.; Roscioni, O. M.; Friederich, P.; Anderson, M.; Da Como, E.; Kociok-Köhn, G.; Wenzel, W.; Zannoni, C.; Beljonne, D.; Blase, X.; D'Avino, G. Host Dependence of the Electron Affinity of Molecular Dopants. *Mater. Horiz.* **2019**, *6* (1), 107–114. https://doi.org/10.1039/C8MH00921J.

(61) Salzmann, I.; Heimel, G.; Oehzelt, M.; Winkler, S.; Koch, N. Molecular Electrical Doping of Organic Semiconductors: Fundamental Mechanisms and Emerging Dopant Design Rules. *Acc. Chem. Res.* **2016**, *49* (3), 370–378. https://doi.org/10.1021/acs.accounts.5b00438.

(62) Pingel, P.; Zhu, L.; Park, K. S.; Vogel, J.-O.; Janietz, S.; Kim, E.-G.; Rabe, J. P.; Brédas, J.-L.; Koch, N. Charge-Transfer Localization in Molecularly Doped Thiophene-Based Donor Polymers. *J. Phys. Chem. Lett.* **2010**, *1* (13), 2037–2041. https://doi.org/10.1021/jz100492c.

(63) Gao, J.; Stein, B. W.; Thomas, A. K.; Garcia, J. A.; Yang, J.; Kirk, M. L.; Grey, J. K. Enhanced Charge Transfer Doping Efficiency in J-Aggregate Poly(3-Hexylthiophene) Nanofibers. *J. Phys. Chem. C* **2015**, *119* (28), 16396–16402. https://doi.org/10.1021/acs.jpcc.5b05191.

(64) Wang, C.; Duong, D. T.; Vandewal, K.; Rivnay, J.; Salleo, A. Optical Measurement of Doping Efficiency in Poly(3-Hexylthiophene) Solutions and Thin Films. *Phys. Rev. B* **2015**, *91*, 085205. https://doi.org/10.1103/PhysRevB.91.085205.

(65) Dai, A. Creating Highly Efficient Carrier Injection or Collection Contacts via Soft-Contact Lamination of p-Doped Interlayers, Princeton University, 2015.

(66) Hase, H.; O'Neill, K.; Frisch, J.; Opitz, A.; Koch, N.; Salzmann, I. Unraveling the Microstructure of Molecularly Doped Poly(3-Hexylthiophene) by Thermally Induced Dedoping. *J. Phys. Chem. C* **2018**. https://doi.org/10.1021/acs.jpcc.8b08591.

(67) Fujimoto, R.; Watanabe, S.; Yamashita, Y.; Tsurumi, J.; Matsui, H.; Kushida, T.; Mitsui, C.; Yi, H. T.; Podzorov, V.; Takeya, J. Control of Molecular Doping in Conjugated Polymers by Thermal Annealing. *Org. Electron.* **2017**, *47*, 139–146. https://doi.org/10.1016/j.orgel.2017.05.019.

(68) Li, J.; Rochester, C. W.; Jacobs, I. E.; Aasen, E. W.; Friedrich, S.; Stroeve, P.; Moulé, A. J. The Effect of Thermal Annealing on Dopant Site Choice in Conjugated Polymers. *Org. Electron.* **2016**, *33*, 23–31. https://doi.org/10.1016/j.orgel.2016.02.029.

(69) Kroon, R.; Kiefer, D.; Stegerer, D.; Yu, L.; Sommer, M.; Müller, C. Polar Side Chains Enhance Processability, Electrical Conductivity, and Thermal Stability of a Molecularly p-Doped Polythiophene. *Adv. Mater.* **2017**, *29* (24), n/a-n/a. https://doi.org/10.1002/adma.201700930.

(70) Cobet, C.; Gasiorowski, J.; Menon, R.; Hingerl, K.; Schlager, S.; White, M. S.; Neugebauer, H.; Sariciftci, N. S.; Stadler, P. Influence of Molecular Designs on Polaronic and Vibrational Transitions in a Conjugated Push-Pull Copolymer. *Sci. Rep.* **2016**, *6*, 35096. https://doi.org/10.1038/srep35096.

(71) Méndez, H.; Heimel, G.; Winkler, S.; Frisch, J.; Opitz, A.; Sauer, K.; Wegner, B.; Oehzelt, M.; Röthel, C.; Duhm, S.; Többens, D.; Koch, N.; Salzmann, I. Charge-Transfer Crystallites as Molecular Electrical Dopants. *Nat. Commun.* **2015**, *6*, 8560. https://doi.org/10.1038/ncomms9560.

(72) Huang, D.; Yao, H.; Cui, Y.; Zou, Y.; Zhang, F.; Wang, C.; Shen, H.; Jin, W.; Zhu, J.; Diao, Y.; Xu, W.; Di, C.; Zhu, D. Conjugated-Backbone Effect of Organic Small Molecules for n-Type Thermoelectric Materials with ZT over 0.2. *J. Am. Chem. Soc.* **2017**, *139* (37), 13013–13023. https://doi.org/10.1021/jacs.7b05344.

(73) Yee, P. Y.; Scholes, D. T.; Schwartz, B. J.; Tolbert, S. H. Dopant-Induced Ordering of Amorphous Regions in Regiorandom P3HT. *J. Phys. Chem. Lett.* **2019**, *10* (17), 4929–4934. https://doi.org/10.1021/acs.jpclett.9b02070.

(74) Brown, P. J.; Thomas, D. S.; Köhler, A.; Wilson, J. S.; Kim, J.-S.; Ramsdale, C. M.; Sirringhaus, H.; Friend, R. H. Effect of Interchain Interactions on the Absorption and Emission of Poly(3-Hexylthiophene). *Phys. Rev. B* **2003**, *67* (6), 064203. https://doi.org/10.1103/PhysRevB.67.064203.

(75) E. Jacobs, I.; Cendra, C.; F. Harrelson, T.; Valdez, Z. I. B.; Faller, R.; Salleo, A.; J. Moulé, A. Polymorphism Controls the Degree of Charge Transfer in a Molecularly Doped Semiconducting Polymer. *Mater. Horiz.* **2018**, *5* (4), 655–660. https://doi.org/10.1039/C8MH00223A.

3 AIR STABILITY OF P-DOPED CONJUGATED POLYMERS

Molecular *p*-type doping of OSCs has shown to be a promising technique to control the charge carriers in organic layers and consequently tune their electrical properties. However, the potential of *p*-doped layers depends not only on their performance but also on their stability. In this context, the air stability of *p*-doped OSCs has received very little attention, although it is a crucial aspect for the future integration of *p*-doped layers into printed devices. This is not only important for scalable fabrication of devices, where air processes should be favored, but also for their long-term stability, since O_2 and H_2O may be present even in encapsulated devices.

In this chapter, we investigate the stability of *p*-doped conjugated polymers exposed to ambient air, i.e. in the presence of O_2 and H_2O related species. First, we present an overview of existing literature on O_2 and H_2O related charge carrier traps and their impact on the stability of doped OSCs. The second part presents a throughout investigation on the air stability of *p*-doped PBDTTT-c:Mo(tfd-$COCF_3$)$_3$. The stability study is extended to other *p*-doped systems in the third part, to have a broader view on the stability of *p*-doped conjugated polymers under ambient air. Finally, the last part reinforces the main conclusions of this chapter through simulations and presents a diffusion model to further explain our experimental results.

CHAPTER CONTENTS

3.1 BACKGROUND

This section starts with an overview of hole and electron traps introduced in OSCs by O_2 and H_2O and discusses the position of HOMO and LUMO levels proposed in the literature for stable, trap-free charge transport. In the second part, these stability limits regarding the hole and electron traps present in the air are used to discuss the air stability of n and *p*-type doped OSCs. Finally, the last part discusses the expected air-stability of the materials studied in this thesis regarding the literature on air-traps highlighted throughout this background section. Hence, these theoretical part presents valuable information to understand the motivations of studying the air stability of *p*-type conjugated polymers as well as for the interpretation of experimental results.

3.1.1 Air related traps in OSCs

This section aims to present an overview of the advances in the field of air-related traps, which compromise the performance of pristine and doped conjugated polymers[1,2]. Water and oxygen present in ambient air were suggested to introduce traps in conjugated polymers[3,4]. Water is considered to be omnipresent in OSCs, originating from synthesis and/or from device preparation[2–4]. More precisely, water molecules were reported to fill nanometre-sized voids present in polymer layers, which generally present a strong driving force to be filled[2,3]. Even under a controlled atmosphere (H_2O <1 ppm), there are sufficient water molecules to fill up voids in organic layers. Hence, water-related traps are also observed in devices that were not directly exposed to ambient air[1,4] highlighting the importance of understanding these traps for the development of stable organic devices, even without air exposure.

Over the last years, electron traps (acceptor traps) have received more attention than hole traps (donor traps) due to the critical performance degradation observed for *n*-type OSCs exposed to ambient air, as well as the limited electron mobility compared to hole mobility[1,5]. Consequently, air instability is commonly associated with *n*-type OSCs. However, as will be shown in the following, hole traps are also present in conjugated polymers and have recently received more attention in the literature.

Traps can be seen as localized states in the semiconductor bandgap that capture free charge carriers. Acceptor levels will capture electrons and analogically donor levels will capture holes. Charge carriers (electrons or holes) are present in semiconductors under operation (photoexcitation, injection/extraction, etc.) or introduced through doping. Hence, to ensure a trap-free hole (electron) transport of a *p*-type (*n*-type) pristine polymer, the HOMO (LUMO) level should be protected from donor (acceptor) traps. Consequently, for a stable *p*-type (*n*-type) doping, the positive (negative) polarons should also be protected from donor (acceptor) traps. Depending on their position, traps can also act like dopants, as for example oxygen doping (see section 1.1.3). However, additional free charges are not always an advantage. For example, if the electronic semiconductor properties are desired (for example 'on–off' characteristics of organic field-effect transistors or the dark current of organic solar cells), unintentional doping will negatively affect the device's performance. These trapping processes are illustrated in **Figure 3.1** for pristine and doped conjugated polymers. Note that the trapping process is represented in

Figure 3.1 by an electron transfer from/to donor or acceptor levels, but other mechanisms are also possible as discussed below.

In this context, to avoid traps, several studies were carried out to identify their origin, position, and the underlying mechanism. Below, we present some important advances in the understanding of air and water-related traps in OSCs.

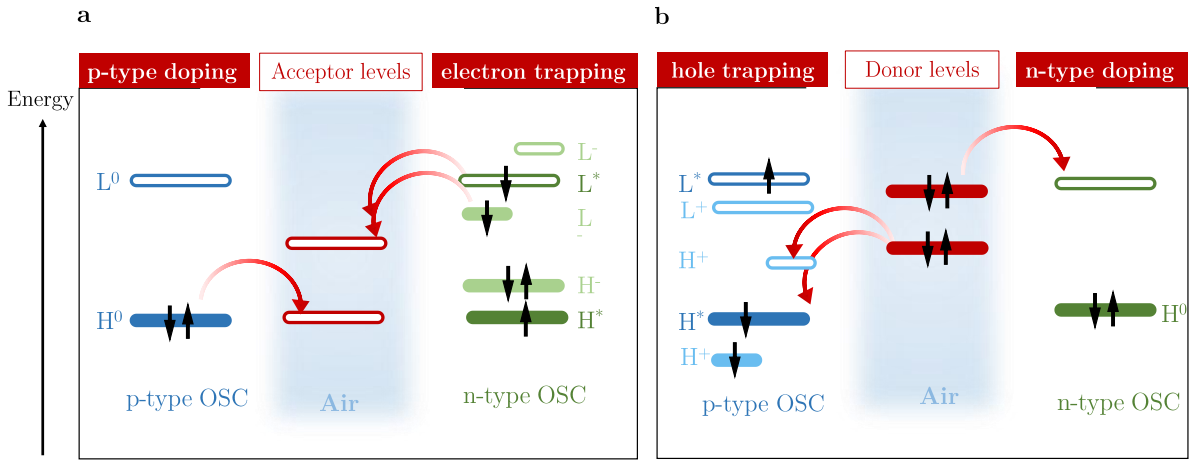

Figure 3.1 - Trapping processes for pristine and doped OSCs in the presence of acceptor (a) and donor (b) traps. For pristine OSCs, ground state (0) and excited states (*) are considered.

Leeuw and coworkers performed one of the first air stability studies for pristine and doped conjugated polymers[6]. Their approach consisted in evaluating the redox potentials for reactions involving conjugated polymers and air species (mainly oxygen and water). Consequently, the trapping processes illustrated in **Figure 3.1** were seen as a redox reaction by Leeuw *et al.*, where the trapping of electrons (loss of electrons) corresponds to an oxidation process, whereas the trapping of a hole (gain of electrons) corresponds to a reduction process. To prevent a reaction from taking place, the standard change in free energy (ΔG^0) of redox reactions involving conjugated polymers and ambient species should be positive, that is:

$$\Delta G^0 = -nF\Delta E^0 \geq 0 \qquad \textbf{Equation 3.1}$$

where n corresponds to the mol of electrons, F is the Faraday's constant (magnitude of charge carried by one mole of electrons) and ΔE^0 the change in potential involving the redox reaction.

Table 3.1 presents an overview of redox reactions involving directly H_2O and O_2 discussed by Leeuw *et al.*[6]. Reactions with hydrogen peroxide and ozone are not included here, as these species are present in lower concentration under ambient conditions (see[6] for all reactions with species present in ambient air). The redox potentials are approximated to IE/EA by adding 4.4 eV[6,7]. Note that these energy levels are approximations as the redox potentials are PH dependent and do not consider eventual activation energies (overpotentials) required for a reaction to proceed. With this in mind, **Table 3.1** summarizes the donor and acceptor traps proposed by Leeuw *et al.* for OSCs in the presence of H_2O and air (H_2O + O_2). Note that to be stable against acceptor traps, electrons should occupy levels higher in energy than the acceptor level (**Figure 3.1**a). For instance, to be stable against H_2O and air (H_2O + O_2), electrons should occupy energies higher than 3.7 eV and 4.9 eV, respectively[6]. Analogically, holes should occupy levels lower in energy compared to the donor level to be stable against donor traps (see **Figure 3.1**b). According to

Leeuw *et al.*, the stability of holes is dictated by the oxidation of H_2O. Thus, holes should have energies below 4.9 eV o be stable against H_2O[6].

Table 3.1 - Acceptor and donor traps derived from redox reactions involving H_2O and air (H_2O + O_2). The potentials (and consequently the energies) are pH dependent and may present additional overpotentials. Adapted from[6].

Reaction	$E_{pH=7}$ (V vs. SCE)	E (eV)	trap
$2H_2O + 2e^- \leftrightarrow H_2 + 2OH^-$ E^0=- 0.244 - 0.05912 x pH	-0.658	3.7	acceptor
$O_2 + 2H_2O + 2e^- \leftrightarrow HO_2^- + OH^-$ E^0=- 0.438 - 0.05912 x pH	0.024	4.4	acceptor
$O_2 + 2H_2O + 4e^- \leftrightarrow 4OH^-$ E^0=0.985 - 0.05912 x pH	0.571	4.9	acceptor
$2H_2O + 4h^+ \leftrightarrow O_2 + 4H^+$ E^0=0.985 - 0.05912 x pH	0.571	4.9	donor
$2H_2O + 2h^+ \leftrightarrow H_2O_2 + 2H^+$ E^0=1.532 - 0.05912 x pH	1.118	5.5	donor
$O_2 + H_2O + 2h^+ \leftrightarrow O_3 + 2H^+$ E^0=1.826 - 0.05912 x pH	1.412	5.8	donor

Besides this electrochemical stability approach, different authors performed systematic investigations to determine, experimentally, the position of traps in OSCs[1,3,4]. In terms of electron traps, several studies reported on an acceptor level at ~3.6 eV[1,4,5,8]. Regarding their origin, Zhou *et al.* showed that water dissolved in the polymer matrix plays a significant role in this electron trap, which was related to hydrated oxygen complexes ($O_2(H_2O)_n$)[8]. Hence, the following publications identifying the electron trap at ~3.6 eV also referred to $O_2(H_2O)_n$ clusters as a possible origin for these traps[1,4,5]. Note that Leeuw *et al.* also observed an acceptor level at ~3.7 eV, which was associated with the reduction of water (**Table 3.1**)[6]. Most importantly, trap-free charge transport was observed for electrons populating levels higher in energy than 3.6 eV [1,4]. Therefore, for air-stable *n*-type devices (i.e. trap-free electron transport in the presence of ambient species), the literature commonly refers to LUMO levels below 3.6 eV (or even 4 eV).

Regarding the experimental investigations on hole traps, they were often associated with the presence of water in polymer voids[2–4,9]. However, the trapping mechanisms proposed in the literature vary considerably. Nikolka *et al.* explained the trapping process by the impact of water molecules on the torsional potential energy profile of polymer bonds[2]. Thus, shallow traps arise due to disorder, i.e. energetic broadening of occupied states in the presence of water molecules. In terms of electrochemical reactions involving holes, their calculations did not indicate a possible electron transfer from H_2O or H_2O-O_2 complexes to positive polarons (holes) as proposed by Leeuw et al[6,9]. However, they argue that hydroxyl anions (OH^-) have sufficiently low IP to transfer an electron to a positive polaron (hole trapping).

Kotadiya *et al.* also performed calculations to verify if H_2O itself could be responsible for hole trapping by electrochemical reactions[4]. They discuss that even though the IE of water in the gas phase (12.65 eV) is too high to cause hole trapping (via electron transfer from H_2O to an OSCs), the scenario changes completely when clusters of water are considered. Their calculations showed that the IE of a water molecule can drastically decrease when surrounded by an H_2O shell, whose dipole moments stabilize the charge on the water molecule, reducing the gas phase IE from

~12 eV to ~6eV. Besides, this study showed that the voids in organic materials are large enough to allow this electrostatic stabilization in water molecules.

Another trapping mechanism related to the presence of water in OSCs was proposed by Zuo *et al*[3]. Interestingly, this study did not observe electron traps at ~3.6 eV[1,4,8] and hole traps at ~6 eV[4] associated with oxidative or reductive reactions with specific compounds. Instead, they reported on generic traps sitting ~0.3-0.4 eV above the HOMO level (for holes) or below the LUMO level (for electrons), which arise from electrostatic interactions with water clusters present in nanovoids of polymer layers (**Figure 3.2**).

Therefore, the proposed trapping mechanism consists in the stabilization of polarons by water molecules sitting in its vicinity. This dielectric effect was reported to be independent of the energy level and the polarity of the charge.

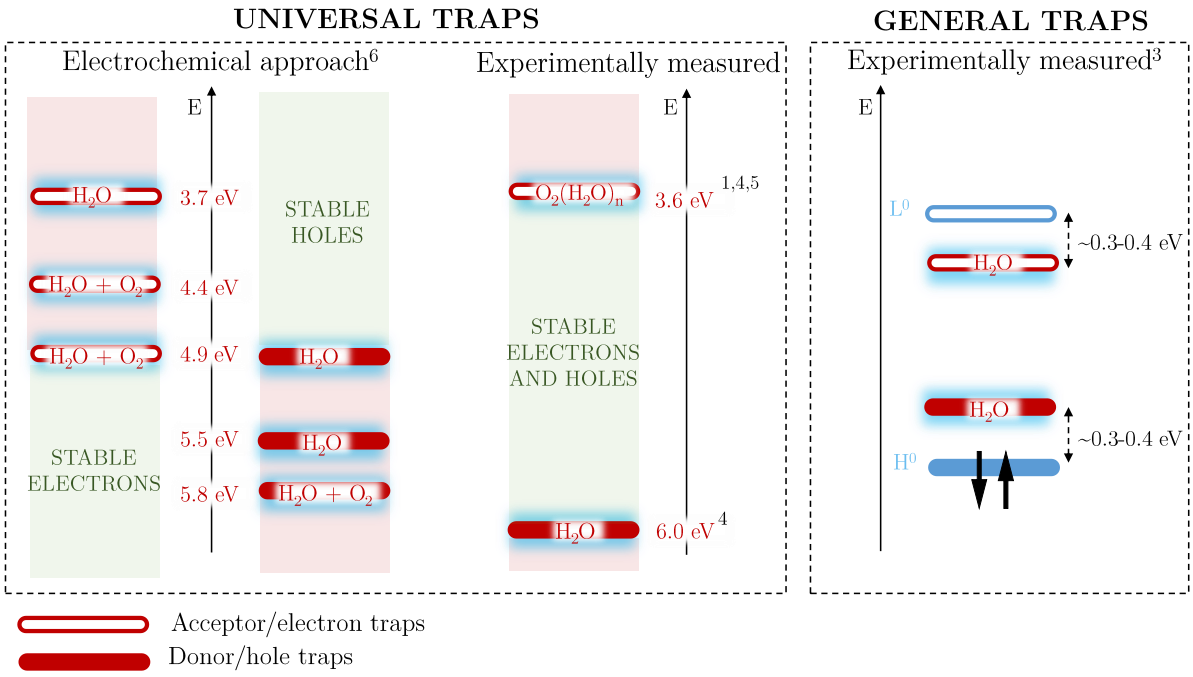

Figure 3.2 – Overview on the water and air-related traps highlighted in the literature. The energies illustrated for the electrochemical approach are approximations, which may varied according to the pH and overpotentials[6].

Some techniques have been discussed to remove water-related traps in OSCs, such as thermal annealing (above 100°C) or solvent annealing[3,4]. Solvent annealing may also promote a morphological rearrangement that removes the nanovoids, preventing therefore the reuptake of water. Consequently, this technique showed better effectiveness in removing water traps from OSCs than thermal annealing[3]. Additionally, molecular additives that do not act as charge transfer dopants have also shown to be beneficial to remove water traps in OSCs[2]. The authors suggested two mechanisms to explain this result: either the additive interacts strongly with water molecules such as to perturb the polymer-water interaction, or additive-polymer interactions are more favorable than water-polymer interactions. Thus, different techniques may be employed to avoid water-related traps.

Finally, **Figure 3.2** presents an overview of the air-related electron and hole traps discussed in this section. Traps found in different materials at the same position, or related to a redox reaction

requiring a specific energy (potential), are called "universal traps". General traps correspond therefore to traps with no specific position, as observed by Zuo et al[3]. To study the stability of *p*-doped conjugated polymers in the presence of air species, we are mainly interested in hole traps that could interfere with the stability of positive polarons (see **Figure 3.1**b). Even though the articles discussed in this section seem to agree on the origin of hole traps in OSCs, for instance water filling nanometre-sized voids in polymer layers, the underlying physics and their position are still under debate. These results highlight however the importance of controlling the preparation, storage, and measurement conditions also for *p*-type conjugated polymers, as the presence of water molecules may compromise their performance. Besides, when integrated into devices, good encapsulations might be required to avoid additional water-related hole traps from the air.

In the following, we discuss the impact of H_2O and O_2 related traps in the stability of p and *n*-doped OSCs.

3.1.2 Stability of doped OSCs in the presence of H_2O and O_2 related traps

In this section, we present some existing studies on the ambient stability of molecular doped OSCs. As mentioned above, ambient stability is often associated with electron trapping and oxidation of materials with low IE. Not surprisingly, the existing studies on the stability of molecular doped OSCs consider mainly *n*-doped OSCs, particularly the development of air stable *n*-dopant compounds. Before discussing separately some stability studies on *n* and *p*-type doped OSCs, some important considerations on dedoping processes in the presence of donor or acceptor levels are presented. If one considers a doped OSC, a dedoping process refers to the recovery of the optical and electrical properties of the pristine OSC, i.e., a vanishing of the doping characteristics. In this context, exposing *p*-doped (*n*-doped) OSCs to donor (acceptor) traps may result in a dedoping process, as the trapping of free holes (electrons) implies a recovery of the electrical properties of neutral OSCs.

In a recent publication, Jacobs *et al.* highlighted two dedoping routes: competitive and reactive dedoping[10]. If we consider the case of a *p*-doped conjugated polymer, both dedoping routes start with a charge transfer from a donor trap to the polymer (**Figure 3.3**a). For this process to happen, the donor should present an IE low enough to allow a charge transfer to the unoccupied midgap state of the polymer (positive polaron), reducing the latter to its neutral state (**Figure 3.3**a**,** left). In this scenario, the positive charge of ionized donors balances the negative charge of ionized dopants. Reactive dedoping still presents an additional step, where the ionized donor reacts with the ionized dopant and forms a non-doping product. Hence, for a reactive dedoping the selected donor should be reactive toward the dopant but nonreactive toward the polymer (Figure **3.3**a, right). This mechanism is therefore non-reversible, contrary to the competitive dedoping where the dopant molecule is not degraded. Analogically, for *n*-doped conjugated polymers, the dodoping process may occur in the presence of an acceptor trap, as illustrated in **Figure 3.3**b**.**

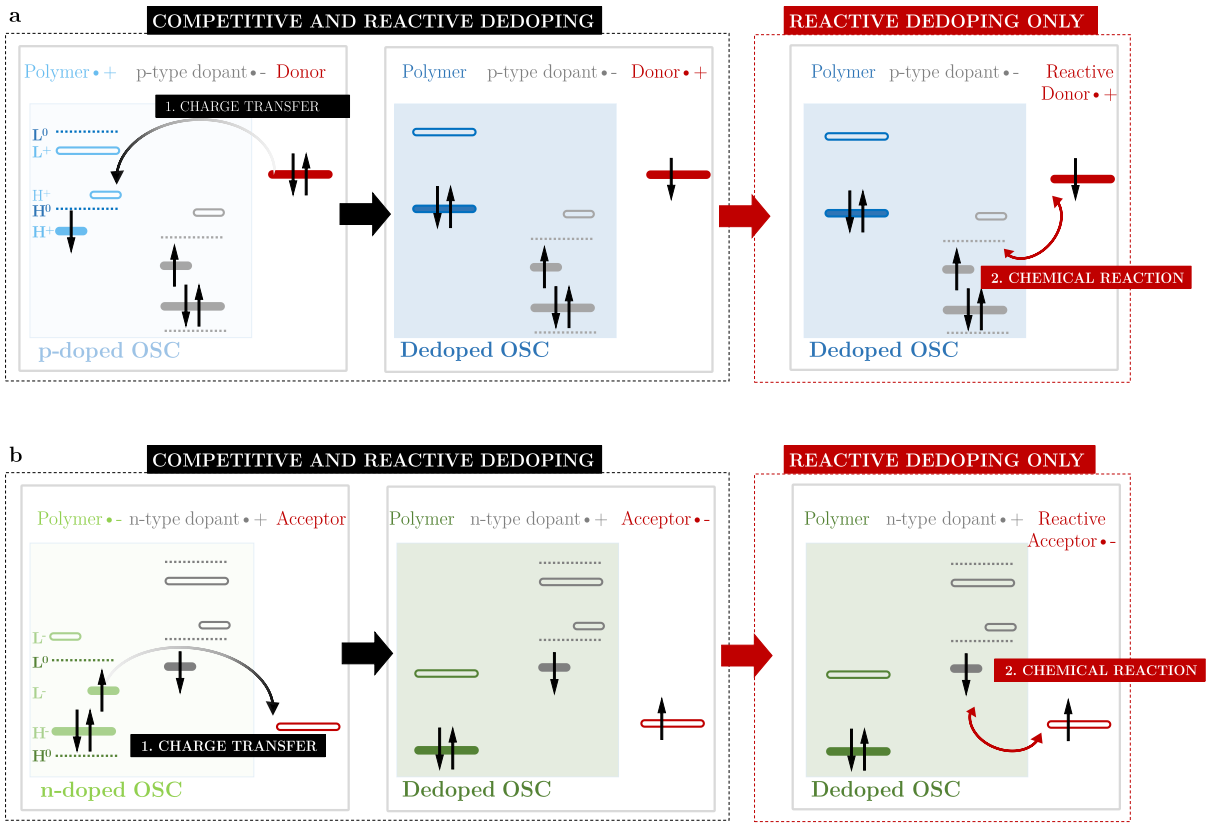

Figure 3.3 – Schematic representation of competitive and reactive dedoping mechanism for *p*-doped OSCs (a) and *n*-doped OSCs (b).

These dedoping routes were demonstrated by Jacobs et al for P3HT:F4TCNQ films, using amines as donor molecules[10]. Hence, from **Figure 3.3** one can conclude that depending on the position of water and/or air-related traps, they may induce dedoping processes in doped OSCs.

N-doped OSCs

Molecular *n*-type dopants are sensitive to immediate oxidation in ambient air due to their low IE, which is however a requirement for an efficient electron transfer to *n*-type OSCs. For example $W_2(hpp)_4$ is known as an efficient *n*-type dopant and presents an IE of 2.4 eV[5]. However, according to the stability window presented in **Figure 3.2** (universal traps, middle panel), this molecule is prone to interact with air-related acceptor traps, as electrons occupy levels lower in energy than 3.6 eV. Indeed, this *n*-dopant is known to be unstable in air. The degradation route suggested for this molecule starts with an electron transfer to $O_2(H_2O)$ (EA 2.9 eV) and/or $O_2(H_2O)_2$ (EA 3.6 eV) complexes[8], and the reactive products were reported to decompose the dopant molecule by cleavage at their W-W and/or W-N bonds[11]. Thus, air-stable molecular *n*-dopants is still a challenge for synthetic chemists. One solution proposed to overcome this problem is photo-assisted doping[12].

The second challenge of air-stable *n*-doped OSCs is related to the stability of the anion hosts. Depending on their energy, the negative polarons may also interact with acceptor traps and result in a dedoping process, as illustrated in **Figure 3.3**b (left panel). Tietze *et al.* showed that the *n*-doping effect remained partially active after short periods of air exposure in organic host

molecules with EA higher than -3.6 eV[11,13]. These experimental results agree with the stability window presented in **Figure 3.2** (middle panel, experimentally measured traps), were electrons populating energies higher than 3.6 eV experience a trap-free transport. Consequently, the *n*-doping effect vanished in the air for host molecules with EA < 3.6 eV. The dedoping after air exposure was explained by a charge transfer to $O_2(H_2O)_2$ complexes (acceptor traps at 3.6 eV), which is only possible for organic hosts with EA<3.6 eV. The charged $O_2(H_2O)_2\bullet-$ radicals were reported to further react with the charged dopant molecules $W_2(hpp)_4\bullet+$, leading to their decomposition[11,13]. Note that the explanation proposed by the authors corresponds to the dedoping route illustrated in **Figure 3.3**b**.** It is worth mentioning that for *n*-doped organic hosts with EA>3.6 eV this study observed reversible electron traps, which were removed by post-annealing in vacuum[11]. No recovery of the *n*-doping effect was observed for organic hosts with EA<3.6 eV[11].

Hence, the general electron traps at 3.6 eV, associated with $O_2(H_2O)_2$ complexes, were also observed in *n*-doped OSCs, reinforcing the importance of studying air related traps to improve the stability limits of doped systems.

P-doped OSCs

Contrary to *n*-type dopants, molecular *p*-dopants are usually considered as air-stable materials since their electrons occupy energy levels far below the universal acceptor traps at 3.6 eV. Besides, these electrons traps should not interfere with the stability of free holes in *p*-doped OSCs. However, as presented in 3.1.1, hole traps have been experimentally observed and associated with the presence of water, which is assumed to be omnipresent in OSCs even under controlled atmosphere[2–4,14]. To the best of our knowledge, there are no studies that verified if water and/or air related traps induce dedoping processes in *p*-doped OSCs. Besides, these layers are mostly processed under inert atmosphere (or vacuum), which obviously tends to minimize the risk of air-related degradation mechanisms. Since air-processability is an important requirement for the compatibility of *p*-doped OSCs with printed electronics, it seems therefore crucial to verify the stability of the *p*-doping effect in the presence of air related species.

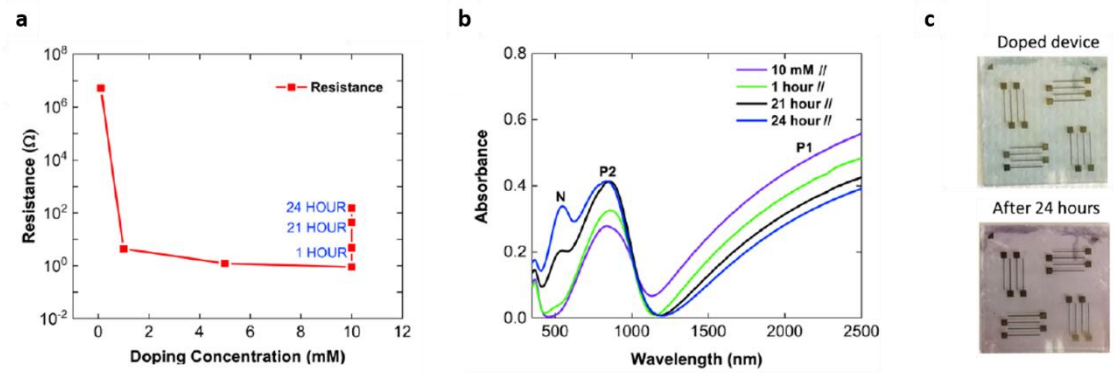

Figure 3.4 - Evolution of the sheet resistance (a) UV–vis–NIR absorption spectrum (b) and changes in color (c) of PBTTT:$FeCl_3$ layers (10mM doping concentration) exposed to ambient atmosphere for 24h. Adapted from[15].

However, two recent papers have highlighted signs of doping instability under ambient conditions [15,16]. Vijayakumar *et al.* observed unstable *p*-doping characteristics for thin PBTTT:$FeCl_3$ layers exposed to ambient conditions[15]. The samples presented an increase in resistance (**Figure 3.4**a, for doping concentration of 10 mM), a decrease in the polaronic absorptions (P1 and P2) combined with a recover of pristine absorption (N) (**Figure 3.4**b), and consequently a color change from doped to pristine layers (**Figure 3.4**c). Nevertheless, the authors do not further discuss this instability since it is beyond the scope of the study.

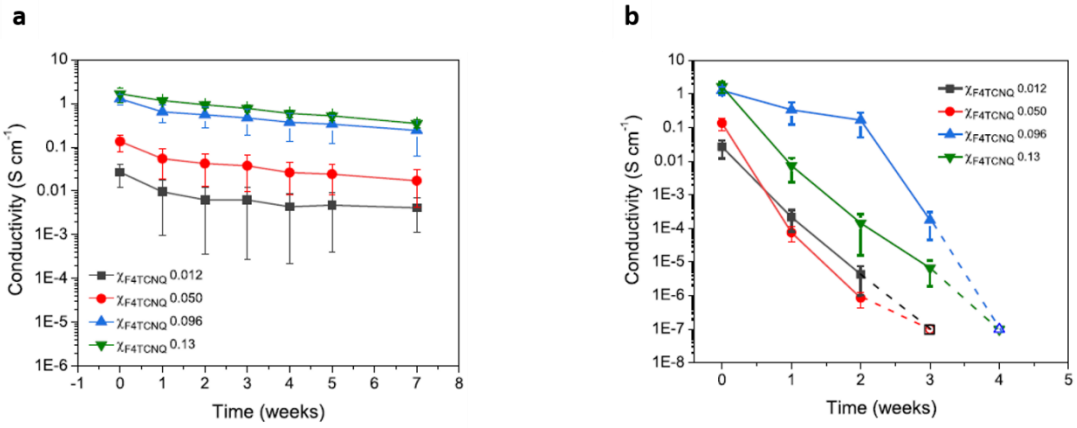

Figure 3.5 – Stability of P3HT:F4TCNQ doped layers under argon atmosphere (a) and ambient air (b). Adapted from[16].

The second article verified the stability of the charge transfer state in P3HT:F4TCNQ layers[16]. The authors observed that under argon atmosphere and dark conditions, the conductivity of doped layers decreased slowly over time (**Figure 3.5**a). After characterizing the samples in terms of XPS, UV-Vis, and FTIR they correlated this observation to a conversion of IPA to CPX states. Consequently, the conductivity loss was associated with the trapping of free charge carriers in CPX states (see 1.2.4). Additionally, the so-called ICT-to-CPX conversion showed to be impacted by changes in the electronic environment such as doping concentration, P3HT molecular weight, and ambient exposure. In particular, the conductivity presented a drastic decrease under ambient conditions relative to the results under a controlled atmosphere (**Figure 3.5**b), where the effect of light was reported to be minimal. Therefore, the authors concluded that the ambient storage facilitates the CPX formation, associated with the presence of ambient gases, primarily oxygen.

Hence, this first evidence of unstable *p*-doping under ambient air and also under an argon atmosphere, further highlights the need of investigating the stability of *p*-doped systems (i.e. positive polarons and dopant anions, or CPX states) towards ambient species.

3.1.3 Considerations for the studied p-doped systems

In this section, we compare the energy levels experimentally measured for our polymer hosts and *p*-dopants with the trap levels reported in the literature to draw some first conclusions regarding their expected air-stability. Ideally, neutral and ionized states of *p*-dopants and polymer hosts should be stable towards water and air-related traps.

Figure 3.6 illustrates the energy levels for PBDTTT-c, RRa-P3HT, F4TCNQ, and Mo(tfd- $COCF_3)_3$ in the presence of the so-called universal traps[4,8,17] and general traps[3] experimentally found in the literature. Thus, this schema does not include the electrochemical donor and acceptor levels derived by Leeuw *et al.* from the standard redox potential of ambient species (see section 3.1.1). The polaron levels for the polymer hosts were taken from the literature and are therefore approximations[18]. Note that the P1 and P2 optical transitions measured for PBDTTT-c and P3HT at[18] are represented in **Figure 3.6** according to the revised polaron model[19] (see section 1.2.2), were both transitions start at the HOMO level (H^0) towards an unoccupied intragap state (H^+ and L^+). Last, the splitting of the half occupied H^+ levels (for polymers) and L^- levels (for dopants) were arbitrary drawn as no information was found concerning the Hubbard U interaction in the studied materials.

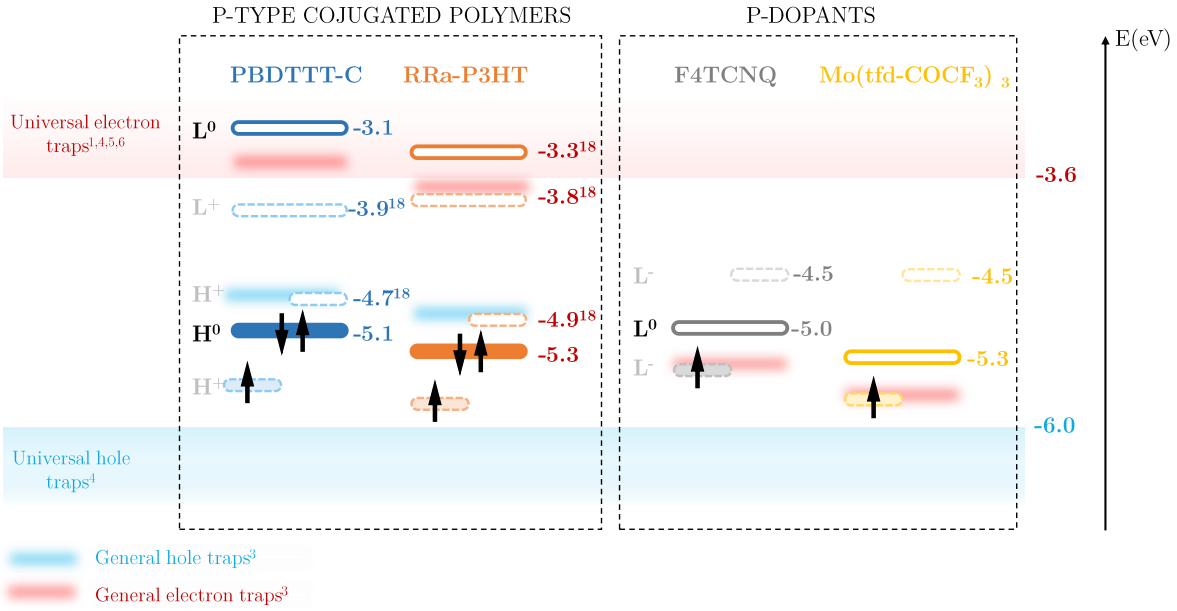

Figure 3.6 – Representation of the hole traps (blue) and electron traps (red) experimentally measured for organic materials as well as the energy levels of the conjugated polymers and *p*-dopants studied in this work. Both universal and general traps are represented. Note that the values for the doping induced absorptions (positive polarons P1 and P2) of the polymers are taken from the literature[18] and are therefore approximations. Besides, the schema above uses the revisited polaron model[19].

For stable *p*-doped conjugated polymers, the unoccupied H^+ level should be far from hole traps, which could transfer an electron back to the polymer chain and consequently dedope it (see **Figure 3.3**a). Regarding the universal hole traps (> 6 eV), both PBDTT-c and RRa-P3HT present unoccupied intragap states (H^+ levels) inside the stability window proposed in the literature[4], i.e. above -6 eV (**Figure 3.6**, left panel). However, the presence of general water-related hole traps at +/- 0.3 eV above the HOMO (H^0) could act as hole traps for both *p*-doped polymers. Even though these polymers are not used to conduct electrons in this work, we note that the LUMO level (L^0) of both polymers are above -3.7 eV and therefore prone to electron trapping by universal and general acceptor traps (+/- 0.3 eV below LUMO).

Regarding the *p*-dopants, the energy levels involved in the doping process (L^0 and L^-) of both molecules are below -3.7 eV and therefore inside the stability window for universal electron traps.

Besides, L^0 of both dopants is above the universal hole traps (donor traps), meaning that the dopant molecule should not get ionized according to this stability diagram. Nevertheless, general water-related electron traps lying +/- 0.3 eV below the LUMO (L^0) might act as electrons traps for the single occupied L^- levels of dopant anions. The HOMO levels of F4TCNQ and Mo(tfd-$COCF_3)_3$ are not represented but lye far below 6 eV.

Finally, it is hard to infer on the air and water stability of the *p*-doped systems studied in this work from **Figure 3.6**, as the universal and general traps result in considerably different scenarios. For *n*-doped polymers, the stability of negative polarons against electron traps has shown to be critical for the overall stability of the *n*-doped state[13]. In analogy, the stability of positive polarons against hole traps should also be a critical parameter for the stability of *p*-doped layers. Additionally, the stability of dopant anions against electron traps might also be an important parameter for the overall stability of the *p*-doped state.

In the following section, we present a thorough investigation of the stability of PBDTTT-c: Mo(tfd-$COCF_3)_3$ layers under different atmospheres. We chose to focus on this system due to the highest conductivities (see **Figure 2.23**) and because we are interested in verifying the stability of Mo(tfd-$COCF_3)_3$ – doped layers, to infer about the potential of this promising *p*-dopant molecule. In section 3.3, we present an overview of the stability results obtained for all four *p*-doped systems considered in this thesis under different atmospheres. This comparison allows verifying if the conclusions obtained for PBDTTT-c: Mo(tfd-$COCF_3)_3$ are unique to this system or if they can be extended to other *p*-doped systems.

3.2 AIR STABILITY OF PBDTTT-C:MO(TFD-$COCF_3)_3$

Air stability is an important aspect defining the potential of molecular doping for electronic devices. As presented in section 3.1 hole traps present under ambient conditions may affect the stability of free holes in *p*-doped OSCs in a similar way than reported for free electrons in *n*-doped OSCs[3,4]. These hole traps were mainly attributed to the presence of water in nanovoids of polymer layers. Note that water is believed to be omnipresent in OSCs, highlighting the importance of studying these hole traps not only for inferring on the air-stability of *p*-doped conjugated polymer but also on their stability under controlled atmosphere. In this context, this section deeply investigates the stability of *p*-doped PBDTTT-c:Mo(tfd-$COCF_3)_3$ layers under different atmospheres.

All samples were prepared following the protocol presented in section 2.3.2. Note that reproducible initial properties does not necessarily mean reproducible aging behavior, as some parameters may not be important for the initial doping performances, but have a considerable impact on long-term stability. As will be discussed in the following, we observed variations on the degradations kinetics for samples prepared on different days, with identical initial conductivities. One may list several possible reasons, such as variations in the polymer and dopant batch (batch-to-batch variation, aging history, contamination, etc.), in the solvent bottle (contamination, residual water, etc.), or even in the aging conditions (relative humidity, temperature, glovebox contamination, etc.). Therefore, to avoid introducing hidden variables that lead to erroneous conclusions, we will only compare quantitatively the degradation kinetic of samples prepared from the same materials (same batch of polymer and dopant, same solvent bottle) and aged under the same conditions (unless specified). In other words, the samples presented in the same graph throughout this chapter were prepared and aged at the same time, from the same materials (unless specified).

This section is divided into five parts. The first two parts verify the stability of the doping signature of PBDTTT-c:Mo(tfd-$COCF_3)_3$ layers under an argon atmosphere (glovebox), to verify the intrinsic stability of the doped system, and during air exposure (ambient air and anhydrous air). Particular attention was given to the impact of the layer thickness on the stability of *p*-doped layers, as this parameter may vary considerably depending on the application. Besides, the layer thickness can have an important impact on the permeability and consequently on the diffusion of oxygen and water-related species[20]. The third part presents XPS analysis on PBDTTT-c:Mo(tfd-$COCF_3)_3$ layers after air exposure, to infer on the chemical changes of the doped system in the presence of O_2 and H_2O related species. The stability of the dopant molecule towards water and ambient species is further investigated in the last experimental part, before presenting an overview of the main conclusion of this section.

3.2.1 P-doping stability under controlled atmosphere

Here, the conductivity of freshly prepared PBDTTT-c:Mo(tfd-$COCF_3)_3$ samples were measured directly after fabrication and remeasured over time at intervals of several days. Samples were

prepared, stored, and measured in the same argon-filled glovebox (<5 ppm O_2 and H_2O). Between the measurements, samples were stored in black boxes inside the glovebox to limit light exposure. As mentioned above, samples presented in the same graph were prepared on the same day, from the same solution, and have seen the same glovebox conditions. We did not perform UV-vis-NIR measurements on these samples since it would imply exposing them to ambient conditions. Thus, it would be hard to separate the potential changes related to the short air exposure from the ones associated with the glovebox aging.

In **Figure 3.7**, we present the conductivity variations under a controlled atmosphere for different layers thickness (varying approximatively from 15 to 140 nm) at a fixed dopant concentration of 5 mol% Mo(tfd-$COCF_3$)$_3$. For all samples, the conductivity decreased over time, especially during the first month. When considering the normalized loss over time (**Figure 3.7** relative to the initial conductivity σ_0), a trend can be observed: the conductivity loss of thicker samples appears to be slower than for thinner ones (**Figure 3.7**b). A conductivity loss over 90 % of σ_0 is observed for the 15 nm sample after 4 months under a controlled atmosphere compared to a loss of around 70% for the 140 nm sample.

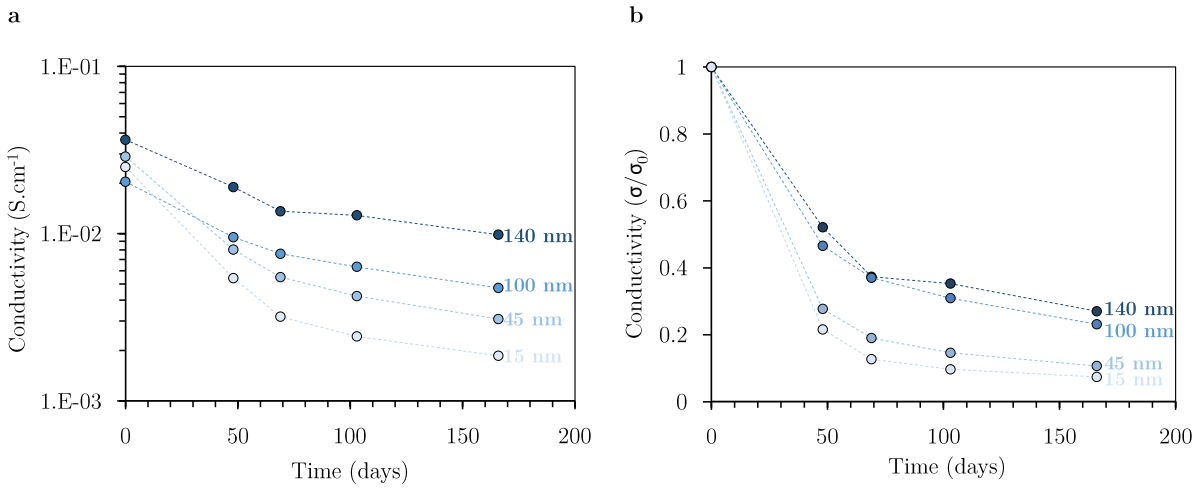

Figure 3.7 – Conductivity evolution over time under an argon atmosphere (glovebox conditions) for PBDTTT-c: Mo(tfd-$COCF_3$)$_3$ layers with different thicknesses, at a fixed dopant concentration of 5 mol%. Samples were stored in the dark between measurements. Absolute (a) and normalized (b) values.

Figure 3.8 presents the evolution of the conductivity inside the glovebox for different dopant concentrations (from 5 mol% to 20 mol%). All samples were around 15nm-thick. Whatever the dopant concentration, the conductivity decreases over time (**Figure 3.8**). As observed for different layer thicknesses (**Figure 3.7**), the conductivity loss seems more accentuated in the first month. No particular trend is observed when considering the normalized conductivity loss over time (**Figure 3.8**b). The sample at 5 mol% presented the fastest decrease of *ca.* 95% after 3 months compared to 87 % for the slowest decrease (10 mol% of dopant).

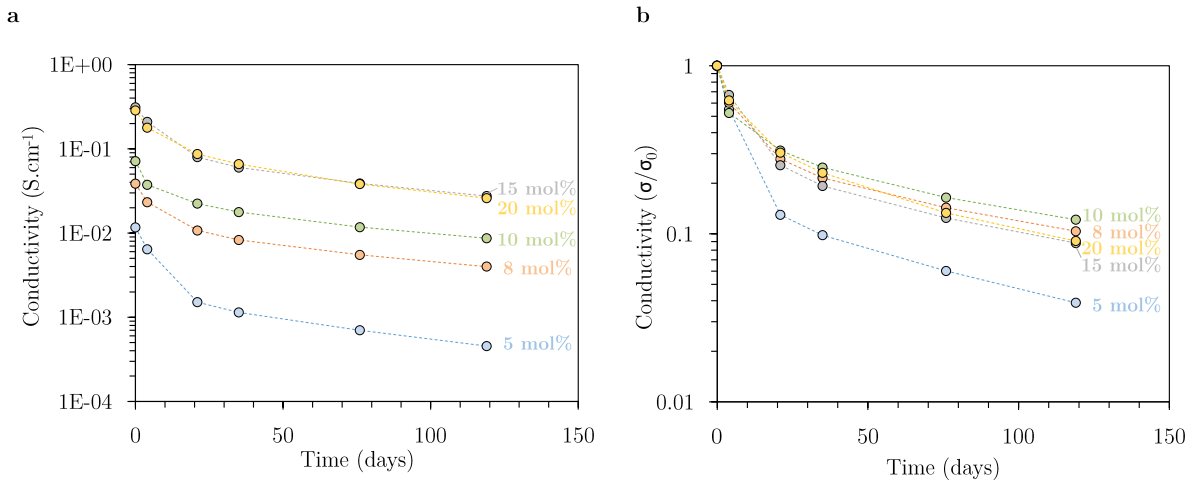

Figure 3.8 - Conductivity evolution over time under argon atmosphere for PBDTTT-c: $Mo(tfd\text{-}COCF_3)_3$ layers with different dopant concentrations, at a fixed layer thickness of approx. 15 nm. Samples were stored in the dark between measurements. Absolute (a) and normalized (b) values.

Hence, whatever the dopant concentration or layer thickness, we observed a decrease in the conductivity of PBDTTT-c: $Mo(tfd\text{-}COCF_3)_3$ over time inside the glovebox (dark conditions). Interestingly, the conductivity decrease observed for 15 nm PBDTTT-c: $Mo(tfd\text{-}COCF_3)_3$ layers under argon atmosphere is in the same order of magnitude as observed by Watts *et al.* for ~10-15 nm P3HT:F4TCNQ samples[16] (**Figure 3.5**a). Besides, a similar fractional decrease in conductivity was observed for different dopant concentrations. The authors suggested that this conductivity decrease is related to changes in the charge transfer state within the doped film, i.e. conversion of ICT to CPX states, which can also be seen as a trapping mechanism for free charge carriers. This conversion is proposed to be thermodynamically driven. However, both charge transfer states have been experimentally observed for P3HT: F4TCNQ layer[21]. Regarding the PBDTTT-c: $Mo(tfd\text{-}COCF_3)_3$ system, the hypothesis of ICT-to-CPX conversion is less probable if one considers the steric bulk of $Mo(tfd\text{-}COCF_3)_3$ molecules compared to the flat F4TNCQ molecules and their exposed π-orbitals. As discussed in section 1.2.4, the formation of CPX is due to the hybridization of frontier molecular orbitals of polymer and dopant molecules, mainly observed for planar polymer: *p*-dopant systems.

Another possible explanation for this conductivity decrease may be the presence of water in PBDTTT-c: $Mo(tfd\text{-}COCF_3)_3$ layers (e.g. in nanovoids), which may interact with the positive polarons and/or dopant anions, or introduce as hole traps[2,3]. Thermal annealing was highlighted as a technique to remove water from polymer voids[3,4]. However, this post-treatment presented a negative impact on the doping properties of several *p*-doped systems[22,23], including PBDTTT-c: $Mo(tfd\text{-}COCF_3)_3$ (see section 2.3.2). Therefore, solvent annealing could be considered as a post-treatment to verify the impact of water on the conductivity decrease observed under a controlled atmosphere.

Finally, the conductivity measurements presented in **Figure 3.7** and **Figure 3.8** do not allow to conclude on the mechanism behind the conductivity decrease under a controlled atmosphere. However, they highlighted the importance of considering the stability of *p*-doped systems. Besides, these results are particularly important when planning experiments and

characterizations, since they reveal that internal processes occur in PBDTTT-c:Mo(tfd-$COCF_3)_3$ layers and that one cannot assume that samples stored in a glovebox are the same as freshly prepared ones. In the following, we present results on the stability of PBDTTT-c:Mo(tfd-$COCF_3)_3$ layers under ambient air, to infer on the effect of ambient species, such as oxygen and water, in the *p*-doping stability.

3.2.2 P-doping stability under ambient atmosphere

In this section, we investigate the evolution of the conductivity and UV-vis absorption of PBDTTT-c: Mo(tfd-$COCF_3)_3$ layers exposed to ambient air. For the UV-vis measurements, samples are stored in a dark box under ambient air between measurements. For the conductivity evolution, TLM samples were installed in a measurement bench under dark conditions and I(V) curves were recorded with a semi-automated program. This avoids opening the measurement bench (light exposure) and allows obtaining a more precise curve in case of a fast current decrease. Thus, instead of conductivity versus time, we plot the current evolution at 1V (chosen arbitrarily). Note that under argon atmosphere all channels of TLM samples were manually measured to extract the conductivity.

This section is organized into three parts. First, we briefly discuss the impact of air exposure on pristine materials. The second part investigates the impact of air exposure on the doping signatures, i.e. conductivity, polaronic absorptions, and spin density. Finally, we explore the impact of humidity (H_2O vapor present in air) on the stability of PBDTTT-c: Mo(tfd-$COCF_3)_3$ layers by comparing the doping stability under anhydrous air and ambient air.

Pristine PBDTTT-c and Mo(tfd-$COCF_3)_3$ under ambient conditions

For comparison purposes, we verified the impact of ambient atmosphere on pristine PBDTTT-c and Mo(tdf-$COCF_3)_3$. For PBDTTT-c, these measurements are performed on thin layers of ca. 20 nm that are characterized in terms of UV-Vis-NIR absorptions and conductivity. As for doped layers, the evolution of the conductivity is analyzed by measuring the current of a TLM channel over time, to avoid photo-oxidation processes by exposing samples to light and oxygen (see section 1.1.3 for more information on photo-oxidation of conjugated polymers). Regarding Mo(tdf-$COCF_3)_3$, we were not able to prepare homogeneous layers of pristine dopant. Therefore, dopant molecules are stored under different conditions (glovebox and ambient air) and air-stability is inferred through the UV-vis spectra of dopant solutions.

Figure 3.9a presents the current evolution over approx. 4 days for PBDTTT-c layers under ambient air. We observe a significant current increase over time, especially during the first 20h. This current increase may be attributed to oxygen doping as observed for different *p*-type conjugated polymers (see section 1.1.3 for more information on oxygen doping)[24]. As shown in the inset (**Figure 3.9**a), the current increase does not take place immediately. Regarding the UV-vis-NIR absorption, no visible changes can be observed for PBDTTT-c layers stored 4 days in air (dark), neither bleaching of the π-π* absorption nor an increase in the NIR absorption (**Figure 3.9**b). The same result was obtained for different thicknesses, indicating that PBDTTT-c is stable in air under dark conditions (in the considered timescale). Note that for the NIR

absorptions have a slight polaronic aspect. However, since the UV-vis-NIR measurements are performed under ambient conditions, we are not able to tell if the NIR absorptions are already present after fabrication (glovebox), or if they arise between the time the sample left the glovebox and the measurement (below 30 min). Independently, the NIR absorptions do not increase after the first measurement even though the current increased during the measured interval.

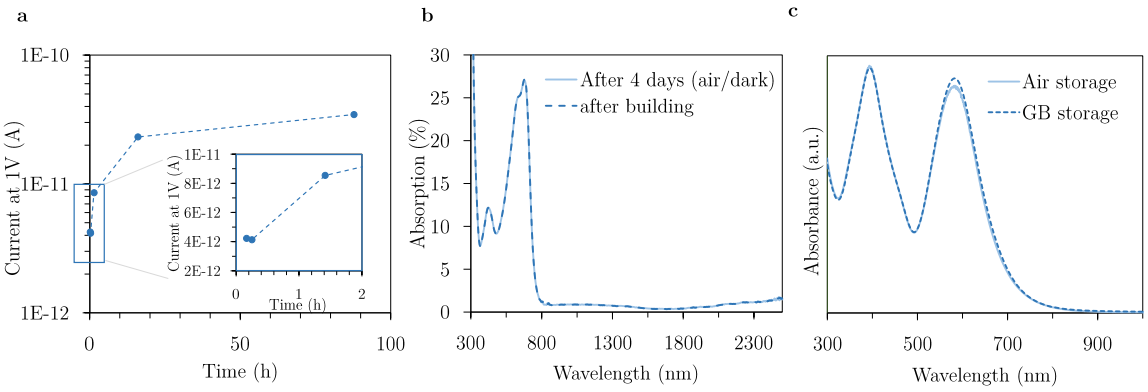

Figure 3.9 – Impact of ambient air (dark) on the optical and electrical characteristics of pristine PBDTTT-c (20 nm layers) and Mo(tdf-$COCF_3$)$_3$ (solutions): current evolution (a) and UV-Vis-NIR spectra (b) of PBDTTT-c layers exposed to ambient air during 4 days, and UV-vis spectra of Mo(tdf-$COCF_3$)$_3$ solution for dopant flasks (solid) stored under different atmospheres (normalized).

For the *p*-dopant, we compare the UV-vis spectra of Mo(tdf-$COCF_3$)$_3$ solutions prepared from different flasks: one stored several months inside the glovebox and a second stored several months under ambient air (brown flask). The solutions are measured under ambient conditions, but prepared in the respective storage environments. As presented in **Figure 3.9**c, no significant difference can be observed in the UV-vis spectra. Therefore, we assume that Mo(tdf-$COCF_3$)$_3$ molecules are stable in air.

PBDTTT-c:Mo(tfd-$COCF_3$)$_3$ layers under ambient conditions

The results presented in this part were mainly performed with a dopant concentration of 5 mol%. This dopant concentration allows fabricating homogeneous layers of different thicknesses with the mixed solution technique without saturating the initial polymer solution (note that the dopant concentration is limited at 2 g.L^{-1}). Besides, PBDTTT-c layers doped at 5 mol% of Mo(tfd-$COCF_3$)$_3$ present a conductivity increase of ca. 6 orders of magnitude compared to pristine PBDTTT-c without being saturated of dopant molecules (see **Figure 2.23**b). Four layer thicknesses are prepared: 15 nm, 45 nm, 120 nm, and 200 nm. The initial conductivity of all freshly-prepared PBDTTT-c:Mo(tfd-$COCF_3$)$_3$ layers doped at 5 mol% was *ca.* 1.5×10^{-2} S cm^{-1}. **Figure 3.10**a presents the current evolution during 15h under ambient air (dark) for two samples (different channels lengths) of each layer thickness. Thanks to a customized printed circuit board, all the samples were measured at the same time and therefore exposed to the same ambient conditions.

Contrary to pristine PBDTTT-c (**Figure 3.9**a), all PBDTTT-c:Mo(tfd-$COCF_3$)$_3$ layers presented a current decrease over time. Besides, the current loss upon air exposure is clearly faster for thinner layers, as also observed in **Figure 3.7.** For samples of 15 nm, we observed a

current loss of approx. 4 orders of magnitude in less than 5 hours, whereas for samples of 200 nm, the current decreased only by a factor of 2 (after 5h). Consequently, these results show that considering samples with similar thickness is crucial for relevant comparative degradation studies.

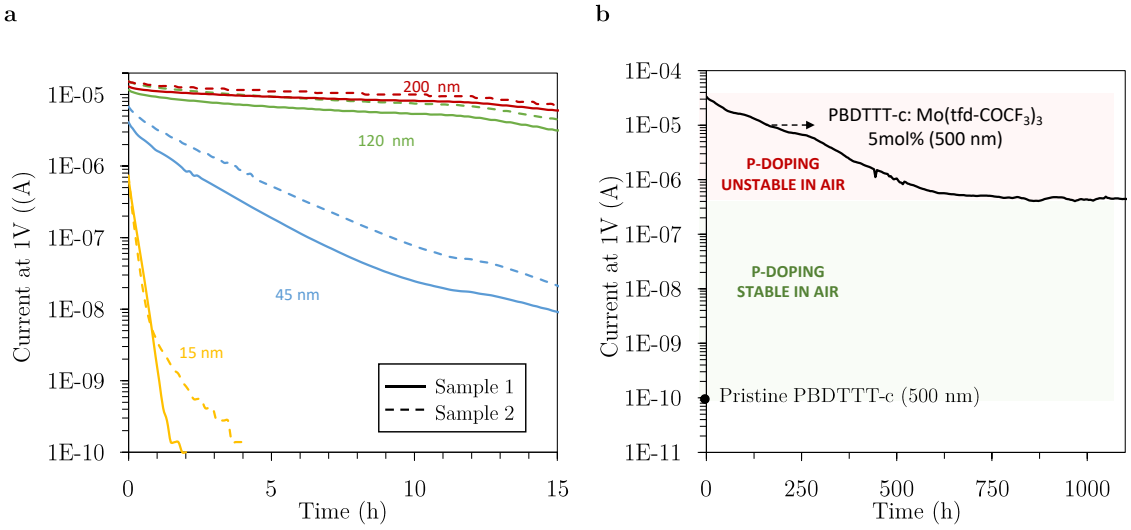

Figure 3.10 - Impact of air exposure on the current of PBDTTT-c:Mo(tfd-$COCF_3$)$_3$ layers of different thicknesses.

Figure 3.10b presents the current evolution for a 500 nm PBDTTT-c: Mo(tfd-$COCF_3$)$_3$ sample over 1000h under ambient air (dark). This graph is interesting because it shows that for thicker samples, the current decrease observed under ambient conditions may reach a plateau. Even though the sample presented current decreased of ca. 2 orders of magnitude, it is still over 3 orders of magnitude higher than a pristine PBDTTT-c layer of 500 nm (**Figure 3.10**b). In other words, there is a considerable fraction of the *p*-doping that remains active under ambient conditions. This is not the case for samples of 15 nm and 45 nm, where all the samples aged in this thesis reached the current value of pristine PBDTTT-c samples. These results highlight the impact of the layer thickness on the stability of PBDTTT-c: Mo(tfd-$COCF_3$)$_3$ samples exposed to air.

We briefly considered the reversibility of the current decrease under ambient air. The literature on air-induced dedoping of *n*-type OSCs verified that doping signatures could be recovered by removing ambient species responsible for electron traps[5,11,25]. This was performed by thermal annealing (T>100°C), secondary vacuum, and/or returning samples to a controlled atmosphere. Considering the instability of PBDTTT-c:Mo(tfd-$COCF_3$)$_3$ layers to thermal annealing above 100 °C (see **Figure 2.19**), we only verified the impact of a controlled atmosphere (argon) and secondary vacuum (2×10^{-7} mbar). However, no recovery of the doping characteristics was observed for PBDTTT-c:Mo(tfd-$COCF_3$)$_3$ layers left overnight in the aforementioned conditions.

Regarding the UV-vis-NIR spectra, **Figure 3.11**a shows the evolution under ambient conditions for a PBDTTT-c:Mo(tfd-$COCF_3$)$_3$ layer of ~15 nm. We observe a clear decrease of the NIR absorption bands associated with the doped chains combined with a recovery of the pristine PBDTTT-c $\pi\pi^*$ absorption band. After 8h30 air exposure, the UV-vis-NIR spectra of the doped layers is identical to the spectra of pristine PBDTTT-c (**Figure 3.11**b). No additional features

can be verified in the spectra, not even signatures of the dopant molecule. Note that the dopant absorption may be masked by the PBDTTT-c absorption (despite presenting a higher concentration, the polymer also presents a higher molar absorptivity). Thus, the absence of dopant signatures does not allow inferring on the state of the dopant molecule (ionized, neutral, degraded, etc.). For PBDTTT-c:Mo(tfd-$COCF_3$)$_3$ layers exposed to ambient air for several days, we observed degradation signatures on the UV-vis spectra, characterized by bleaching of the π-π*absorption of PBDTTT-c (dashed and dotted curves in **Figure 3.11**a). Therefore, even though the samples were stored in the dark, short periods of light exposure during UV-vis-NIR measurements seem to be sufficient to initiate a photo-oxidation of the PBDTTT-c, and consequently its degradation[26,27].

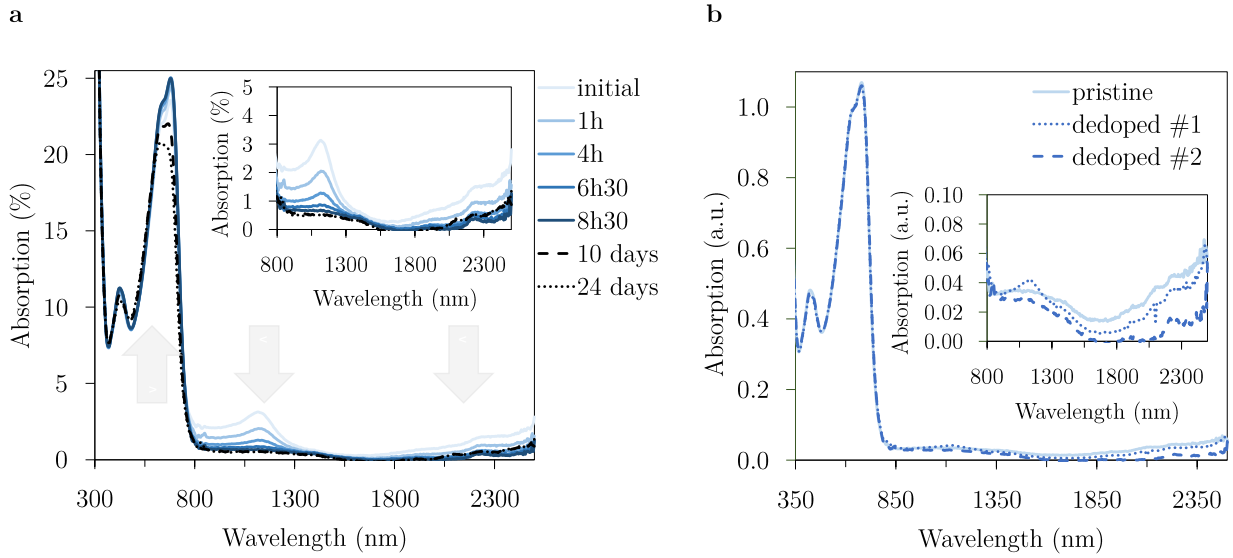

Figure 3.11 – UV-vis-NIR spectra of PBDTTT-c:Mo(tfd-COCF3)3 layers (5 mol% dopant, 15nm-thick). Evolution under ambient air and dark conditions (a) and comparison of aged samples (dedoped) with pristine polymer layers (b).

Hence, two different degradations are observed in **Figure 3.11** for the PBDTTT-c:Mo(tfd-$COCF_3$)$_3$ layer. First, the bleaching of the doping related spectroscopic signatures suggests a dedoping mechanism upon air exposure (**Figure 3.11**a, b). Then, after several days under ambient conditions (dark), we observed an intrinsic degradation of the polymer (**Figure 3.11**a, dotted and dashed lines). Here, we are particularly interested in the first degradation, where the doping signatures vanish.

Both conductivity and UV-vis-NIR measurements point to a dedoping of PBDTTT-c: Mo(tfd-$COCF_3$)$_3$ layers in the presence of ambient species. To further reinforce the hypothesis of a dedoping process under ambient air, we performed electron paramagnetic resonance (EPR) measurements. This characterization was chosen to verify if air exposure also changes the concentration of unpaired electrons in doped layers. Unpaired electrons are assumed to be present in doped layers with polaronic signatures, since the formation of polarons is associated to a charge transfer between polymer and dopant, resulting in an unpaired electron in the polymer matrix, which can be detected by EPR. Note that bipolarons, as diamagnetic species, cannot be probed by EPR measurement.

Figure 3.12a shows the EPR spectrum of a 100 nm thick sample measured after 1 h and 67 h air exposure (for more details on the measurement conditions see Appendix A). The strong signal measured at room temperature is characteristic of organic radicals (g ≈ 2.0) and reflects an efficient charge generation upon doping. After 67h under ambient atmosphere (dark), the intensity of the signal is significantly decreased. The relative loss of unpaired electrons is estimated to be 83 %, as calculated from the double integration of the signals (**Figure 3.12**b). This result is in accordance with the conductivity loss and the bleaching of the UV–vis-NIR doping signatures observed upon air exposure.

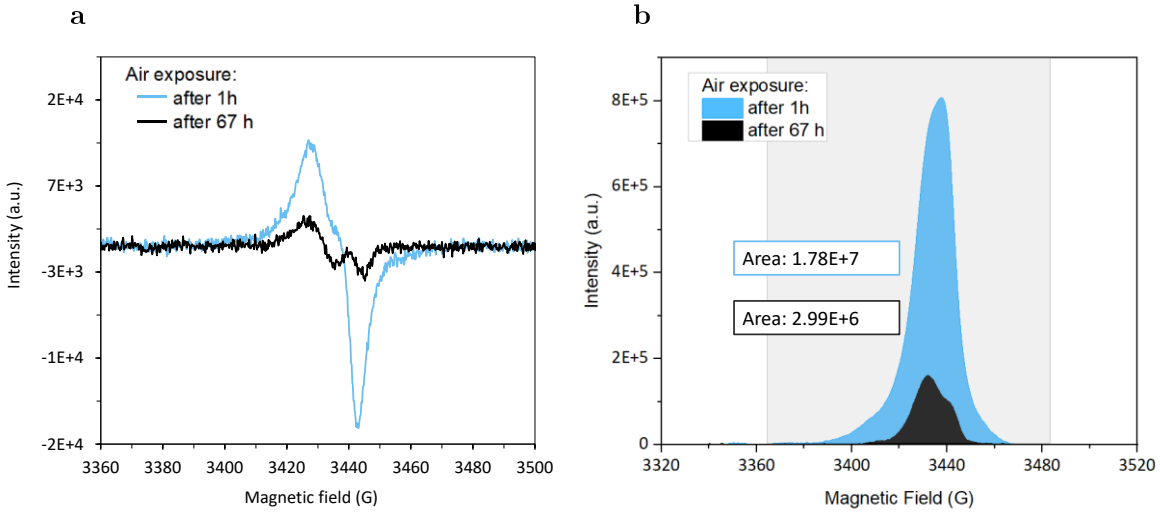

Figure 3.12 – Evolution of the EPR spectrum of a PBDTTT-c:Mo(tfd-$COCF_3$)$_3$ layer (5 mol% dopant, 100 nm) exposed to ambient air (a) and the respective double integration of the signals (b).

Morphological changes could also impact the stability of *p*-doped layers[28,29]. However, GIWAX measurements on thin PBDTTT-c: Mo(tfd-$COCF_3$)$_3$ layers showed no clear changes in the diffraction spectra compared to pristine PBDTTT-c, i.e. no doping signatures could be identified in 20 nm layers, even at higher doping ratios (see **Figure 2.25**). Thus, the GIWAX setup used in this work is not adapted to identify morphological changes on thin doped layers. Note that we observed morphological changes related to the doping process on drop casted layers (thickness of *ca.* 1µm). Nevertheless, as the layer thickness presented a strong impact on the doping instability, we did not consider the scenario of drop-casted layers comparable with the thin spin-coated ones studied in this chapter.

In summary, our results suggest that a dedoping process takes place when exposing PBDTTT-c:Mo(tfd-$COCF_3$)$_3$ layers to ambient conditions. In other words, doped PBDTTT-c chain returned to the neutral state:

$$PBDTTT-c^{\bullet+}:Mo(tfd-COCF_3)_3^{\bullet-} \xrightarrow{AIR} PBDTTT-c^{0}:Mo(tfd-COCF_3)_3?$$

As highlighted in the equation above, the results presented in this section do not allow inferring on the state of the dopant molecule (neutral, ionized, or degraded). Nevertheless, if we consider the dedoping mechanism presented in section 3.1.2 (**Figure 3.3**), this equation should present a

donor species (hole trap), responsible for transferring an electron back to $PBDTTT-c^{\bullet+}$, dedoping it:

$$PBDTTT-c^{\bullet+}:Mo(tfd-COCF_3)_3^{\bullet-} \xrightarrow{AIR} PBDTTT-c^{\bullet+}:Mo(tfd-COCF_3)_3^{\bullet-} + donor$$

$$\xrightarrow{COMPETITIVE\ DEDOPING} PBDTTT-c^{0}:Mo(tfd-COCF_3)_3^{\bullet-} + donor^{\bullet+} \xrightarrow{REACTIVE\ DEDOPING} ?$$

In the case of a competitive dedoping, the radical donor cations would eventually counterbalance the charges of the dopant anion[10]. Or, if the ionized donor is reactive towards the dopant, it may result in a degradation of the dopant molecule and in this case in a reactive dedoping. In both cases, the *p*-doping signatures of the polymer host are expected to vanish. To be able to distinguish between both mechanism (reactive or competitive), we need information on the state of the dopant molecule after the dedoping process. Therefore, XPS analyses are performed in section 3.2.3 to infer the changes in the chemical environment of PBDTTT-c:Mo(tfd-$COCF_3$)$_3$ layers exposed to ambient air. In the following, we investigate the origin of ambient species (i.e. donor molecules) that introduce hole traps in $PBDTTT-c^{\bullet+}$.

Investigating the dedoping process under different atmospheres

To gain deeper insights into the impact of water (ambient humidity) and oxygen on the dedoping process observed for PBDTTT-c:Mo(tfd-$COCF_3$)$_3$ layers under ambient conditions, we compared the current evolution under different atmospheres: ambient air, anhydrous air (< 200 ppm H_2O) and argon (< 5 ppm H_2O and O_2). For the aging under anhydrous atmosphere, samples were transported from the glovebox in a metal transfer module, which was opened inside the anhydrous room, i.e. a clean room with controlled temperature and very low relative humidity (< 200 ppm H_2O). An identical measurement bench is used for the samples aged in anhydrous and ambient air. This experiment was performed on 15 nm-thick doped layers (5 mol% of Mo(tfd-$COCF_3$)$_3$), to rapidly highlight the degradation process since faster degradation rates observed for thinner samples (see **Figure 3.10**).

The current evolution under controlled atmosphere (glovebox) was already presented in 3.2.1. We also observed a current decrease over time, but on a time scale of days instead of hours. To allow for a quantitative comparison between the current decrease under argon atmosphere, anhydrous air and ambient air, samples presented in **Figure 3.13** were fabricated from the same solution, and aged in the same day. The initial conductivity of all samples was 1.5±0.1 S.cm^{-1}. Clearly, the current decrease under argon atmosphere is slower than under ambient air. Under argon atmosphere, the current exhibited only a slight decrease in the considered timescale (only a few hours, differently from the time scale of several moths presented in **Figure 3.7** and **Figure 3.8**).

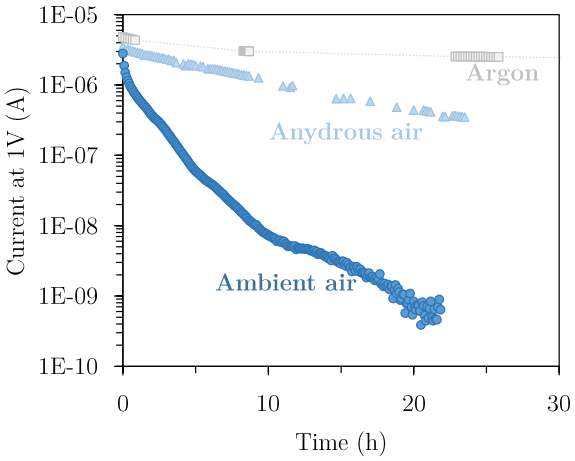

Figure 3.13 – Current evolution for PBDTTT-c:Mo(tfd-$COCF_3$)$_3$ layers (5 mol% dopant, 15 nm-thick) exposed to different atmospheres.

To allow for more statistical analysis, **Figure 3.14** presents the current decrease for three different samples aged under argon, anhydrous air, and ambient air. Here, we compare samples prepared on different days and from different solutions. However, the same fabrication protocol was used and the initial conductivities are identical. **Figure 3.14**a and **Figure 3.14**b compare the absolute and normalized current decrease under anhydrous and ambient air, respectively. Since the time scale is considerably different for samples aged under argon atmosphere, the results are plotted separately in **Figure 3.14**c.

Regarding the stability under ambient air (**Figure 3.14**a, b dark blue), a significant variation can be observed among the three samples, but all presented faster degradations compared to anhydrous air. For the samples expose to anhydrous air, a similar rate is observed for the current decrease. Indeed, external parameters such as humidity and temperature are less controlled under ambient air than inside the anhydrous room. In our experiments under ambient air, the relative humidity (RH) fluctuated between 40-60% and the temperature between 20-25°C. In other words, the stronger variation in the current degradation of samples exposed to ambient air may be associated with variations in ambient conditions. Since the initial conductivities are identical, the hypothesis of contamination during fabrications is less likely. We note that different polymer and dopant batches were used in these samples. Even though batch-to-batch variations are often reported in the literature[30], we observed no particular trend related to the change in polymer and/or dopant batch.

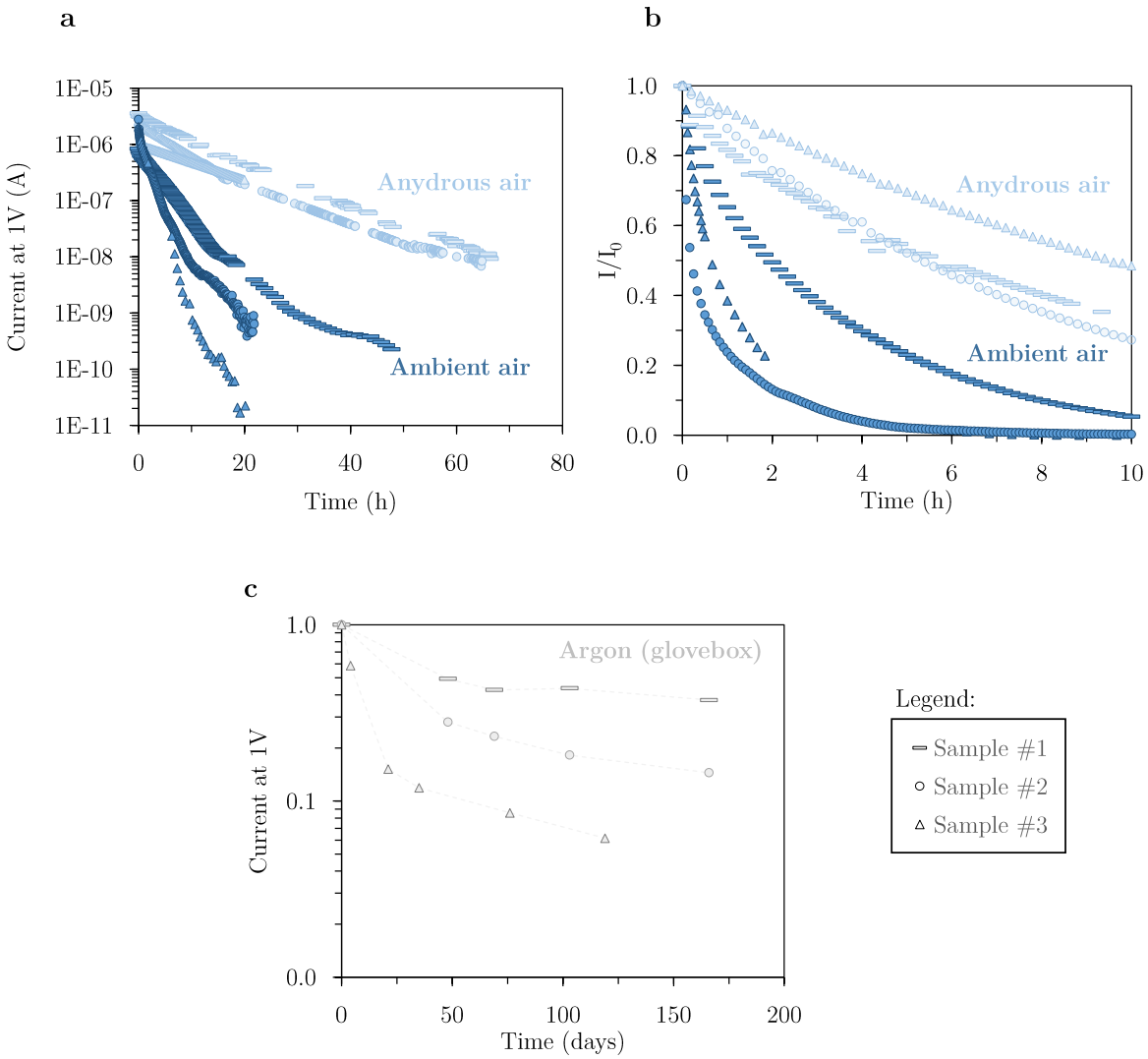

Figure 3.14 – Current evolution under different atmospheres for PBDTTT-c:Mo(tfd-$COCF_3$)$_3$ samples (5 mol% dopant, 15 nm-thick). Comparison between anhydrous and ambient air in absolute (a) and normalized values (b). The normalized current decrease under argon atmosphere is plotted separately(c).

Under argon atmosphere (**Figure 3.14**c), a considerable variation can be observed among the different samples. Considering the small concentration of ambient species inside the glovebox, these samples may be sensible to parameters such as residuals water in solvents or from synthesis (that may vary between batches). Besides, we cannot rule out the possibility of glovebox contamination on a time scale of 200 days.

Hence, from the results presented in **Figure 3.13** and **Figure 3.14**, we can conclude that ambient humidity accelerates the dedoping rate of PBDTTT-c:Mo(tfd-$COCF_3$)$_3$ layers. Besides, controlling the external conditions (temperature and humidity) resulted in a more reproducible dedoping process (light blue curves vs. dark blue curve, **Figure 3.14**). Therefore, to have better control of the dedoping process under ambient air and to further investigate the impact of ambient humidity, we developed a more sophisticated measurement bench, where the I(V) curves were measure in a climatic chamber. In this new measurement bench, the current evolution under ambient air can be monitored for several samples at the same time (customized printed circuit

board), under controlled conditions (temperature and relative humidity). Thus, this bench allows performing statistical analysis on the dedoping process of *p*-doped layers under controlled ambient conditions, where the role of humidity (and also temperature) can be further explored.

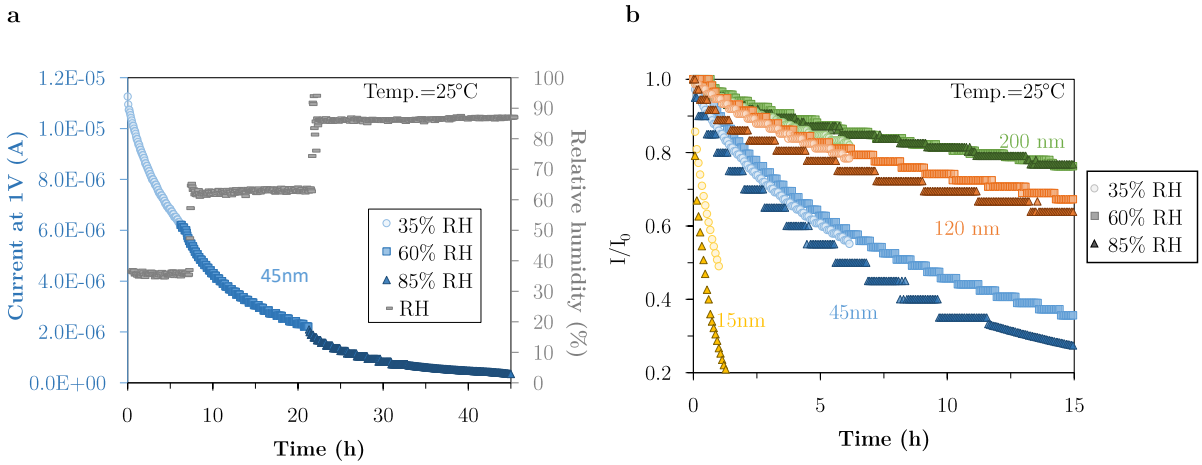

Figure 3.15 – Current evolution for PBDTTT-c:Mo(tfd-$COCF_3$)$_3$ layers (5 mol%, 15 nm-thick) performed inside a climatic chamber. Impact of RH level on the current decrease for 45 nm sample (a) and for different thicknesses (b).

Figure 3.15a presents the impact of relative humidity (RH) on the current decrease of a PBDTTT-c:Mo(tfd-$COCF_3$)$_3$ layer (45 nm, 5 mol % dopant). We observe local accelerations at the moment where the humidity changes, highlighting the sensibility of this *p*-doped system to changes in RH. Indeed, variations in RH may explain the shape of the curves presented in **Figure 3.14**a, where a stepwise decrease is observed for samples exposed to ambient air (dark blue). **Figure 3.15**b presents the same experiment for layers of different thicknesses. To verify the impact of RH on the dedoping rate of different thicknesses, the samples are normalized (to I_0) and the time is set to T_0 for each RH level(35%, 60% and 85%).Thus, **Figure 3.15**b compares the dedoping rate for different thicknesses at three different RH levels.

The first conclusion that can be drawn from **Figure 3.15**b is the clear effect of the layer thickness on the dedoping rate, as observed previously in this chapter (**Figure 3.10**a). Thinner layers present faster dedoping rates than thicker ones. Regarding the impact of RH, even though local accelerations are observed when changing the RH (**Figure 3.15**a), a similar dedoping rate is observed for the three RH levels, regardless of the layer thickness (**Figure 3.15**b). Slightly faster dedoping rates can be observed for thinner layers (15 nm, 45nm, and 120 nm) at 85% RH compared to lower RH.

The impact of the RH in the dedoping rate is not evident from this experiment. Note that the RH was changed during the aging process for the same sample and that the current evolution of PBDTTT-c:Mo(tfd-$COCF_3$)$_3$ layers exposed to ambient air (not in the climatic chamber) presented an exponential-like decay, i.e. faster current loss during the first hours. Thus, when changing the RH level during the aging experiment, the impact of RH may be hidden in the exponential-like degradation of doped samples. To further investigate the impact of RH on the dedoping rate, one should compare samples exposed to different RH during the whole dedoping

process. Since this aging bench was developed at the end of this thesis, and we were not able to fully explore the role of RH on the dedoping rate of PBDTTT-c:Mo(tfd-$COCF_3$)$_3$ layers. Still, we verified the potential of this aging bench and we consider it a valuable tool for studying air stability, i.e. the air-induced dedoping process of *p*-doped OSCs.

In conclusion, the results presented in this section highlighted the role of ambient humidity on the dedoping process of PBDTTT-c:Mo(tfd-$COCF_3$)$_3$ layers: the air-induced dedoping process is faster for higher RH. In other words, water-related species have an important role in the *p*-doping instability under ambient air. This result is consistent with[2,3], which argue that water can introduce hole traps in organic semiconductors. However, we cannot exclude the impact of oxygen on this dedoping process, since we did not consider the *p*-doping stability under wet nitrogen. In other words, this water-related donor could be in the form of hydrated oxygen complexes ($O_2(H_2O)_n$), as observed in the literature for electron traps[5,8,17]. Or, O_2 may facilitate the intercalation of H_2O in polymer layers by interacting with the polymer backbone, as observed by Zhou *et al.* for RR-P3HT[8]. Nevertheless, regardless of the role of O_2, humidity has shown an important impact on the dedoping process of PBDTTT-c:Mo(tfd-$COCF_3$)$_3$ layers under ambient air. Therefore, we suggest that the donor responsible for the dedoping process under ambient conditions is a water-related species.

In the next section, we verify the chemical state of PBDTTT-c:Mo(tfd-$COCF_3$)$_3$ samples after dedoping under ambient conditions, to have some information on the state of the dopant molecule.

3.2.3 XPS analyses on dedoped layers

XPS analyses are performed to infer the changes in the chemical environment of PBDTTT-c:Mo(tfd-$COCF_3$)$_3$ layers exposed to ambient air and, consequently, to better understand the dedoping mechanism. Here, we are mainly interested in verifying what happens to the dopant molecule after the dedoping process under ambient air. From the results presented throughout this chapter, we were only able to probe the changes in the polymer matrix upon air exposure, which presented no clear signs of degradation (see section 3.2.2). Therefore, XPS measurements allow verifying the chemical state of Mo(tfd-$COCF_3$)$_3$ molecules after the dedoping process under ambient conditions. With these results, we will be able to distinguish between reactive or competitive dedoping mechanisms (see **Figure 3.3**).

To obtain information about the initial state of the pristine materials and to properly assign the peaks of the doped layers, this section also measures the XPS spectra of pure Mo(tfd-$COCF_3$)$_3$ and PBDTTT-c. Regarding the doped layers, to infer on the impact of air exposure on the chemical state of PBDTTT-c:Mo(tfd-$COCF_3$)$_3$ layers, two samples were analyzed: one exposed to glovebox conditions and another to ambient air (dark). The samples were 15 nm-thick. This thickness was chosen considering that XPS is a surface analysis and therefore probes only the first 10 nm of the sample (see Appendix A on XPS technique). Besides, the faster dedoping rate of 15 nm samples allows analyzing strongly dedoped samples in short periods of air exposure, avoiding other air-related degradations processes such as photo-oxidation of PBDTTT-c (see

Figure 3.11a). The dopant concentration used was 25 mol% of Mo(tfd-$COCF_3$)$_3$. This higher molar ratio was chosen to better distinguish between the polymer and dopant signatures. For 5 mol%, the intensity of the dopant features was considerably low and, consequently, difficult to attribute the chemical state.

Since this chapter did not consider the dedoping process of higher dopant concentration under ambient air (only for 5 mol%), **Figure 3.16** presents the current evolution for both doped samples analyzed in this section, before entering the XPS chamber. The samples were freshly prepared from the same solution and monitored overnight under different atmospheres (argon and air, under dark conditions). Both samples presented an initial conductivity of approximatively 7.1 10^{-2} S cm^{-1}. After 20h, the conductivity of the sample exposed to air dropped to 7.5 10^{-5} S cm^{-1} whereas the one stored under argon atmosphere presented a decrease of about 60% (**Figure 3.16**b), resulting in a conductivity of approx. 4.3 10^{-2} S.cm^{-1}. These results are consistent with the previous aging test presented in section 3.2.1 and 3.2.2.

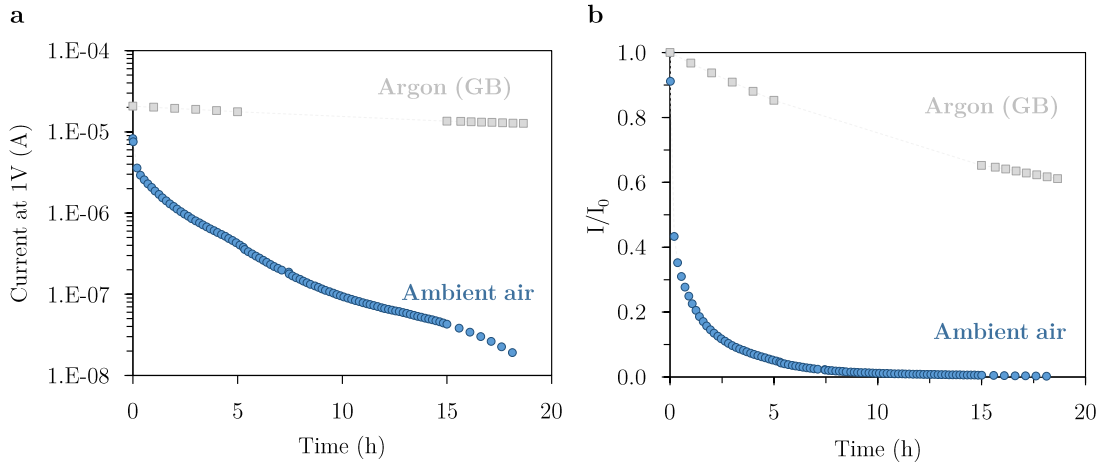

Figure 3.16 – Current evolution of PBDTTT-c:Mo(tfd-$COCF_3$)$_3$ layers (25 mol%, 15 nm) under argon atmosphere and ambient air before XPS measurements. Absolute (a) and normalized (b) values.

Since *p*-dopants can be volatile and XPS analyses are performed under Ultra High Vacuum (UHV) conditions, we verified the stability of 15nm PBDTTT-c:Mo(tfd-$COCF_3$)$_3$ samples at 10^{-9} mbar. Using a sophisticated sample holder (**Figure 3.17**a), the current evolution was monitored inside the XPS UHV chamber. Only a slight decrease in conductivity was observed after 12h under UHV (**Figure 3.17**b). Thus, we assumed that our doped samples are stable in the XPS measurement conditions.

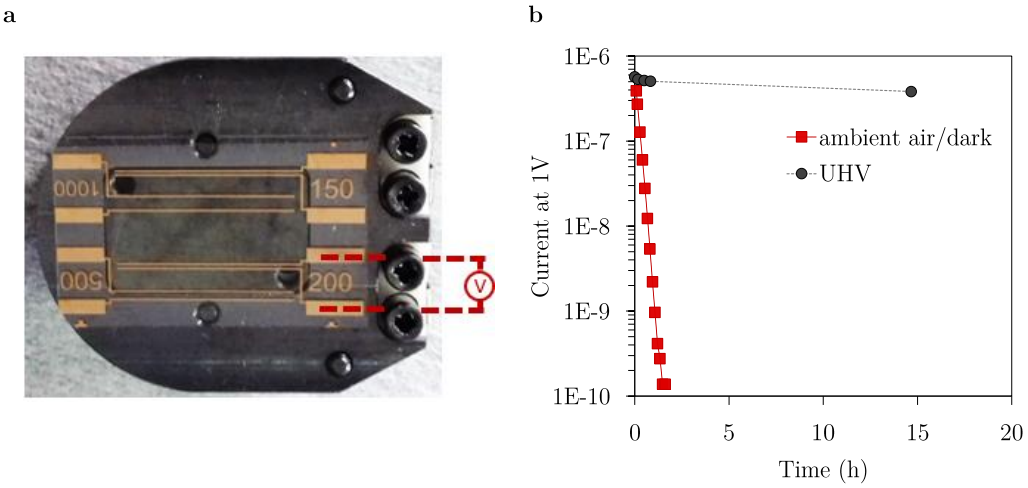

Figure 3.17 – Stability of PBDTTT-c:Mo(tfd-$COCF_3$)$_3$ samples (5 mol% dopant, 15 nm-thick) under UHV conditions. Sample holder used for I(V) measurements of TLM samples inside the XPS chamber (a). Stability of the current under UHV conditions compared to ambient air (b).

Last, this section focuses on the S2p and Mo3d core level peak regions, where polymer and dopant signatures are present and can be clearly distinguished (see Appendix C for C1s, O1s, and F1s peak regions). Besides, these spectral regions presented clear changes after air exposure, as will be discussed in the following. The XPS spectra discussed in this section for pristine and doped layers are presented in **Figure 3.18** and their respective binding energies summarized in **Table 3.2**. Details of peak fitting are given in Appendix C.

The results will be presented in three parts. First, we discuss the chemical state of pristine polymer and dopant. Then, we show the results obtained for doped layers stored overnight under an argon atmosphere, to characterize the initial chemical state of PBDTTT-c:Mo(tfd-$COCF_3$)$_3$ layers, before the dedoping process under air. This sample was transported from the glovebox to the XPS machine in a transfer module, which was opened directly inside the XPS antechamber to avoid air exposure. Last, we present the spectra obtained for dedoped samples exposed to ambient air overnight and summarize the main results.

Pristine PBDTTT-c and Mo(tfd-$COCF_3$)$_3$

The XPS spectra of pristine PBDTTT-c and Mo(tfd-$COCF_3$)$_3$ were measured for the bulk materials.

For PBDTTT-c, the S2p core level spectrum presented a splitting into two doublets (associated to spin-orbit coupling) at a binding energy of 163.7 eV ($2p_{3/2}$) and 164.9 eV ($2p_{1/2}$), attributed to the C-S environment (**Figure 3.18**a). The lower intensity S2p doublet at higher binding energies was assigned to SOx groups.

Regarding the dopant molecule, the S2p core level spectrum presented doublets at 162.3 eV ($2p_{3/2}$) and 163.5 eV ($2p_{1/2}$), which were attributed to the sulfur present in the Mo-S-C environment (**Figure 3.18**b). A small fraction of S2p doublets were found at higher oxidation states assigned to $(S_n)^{2-}$ and (SO_2)-like species, which are possibly related to residual impurities from synthesis present in the material.

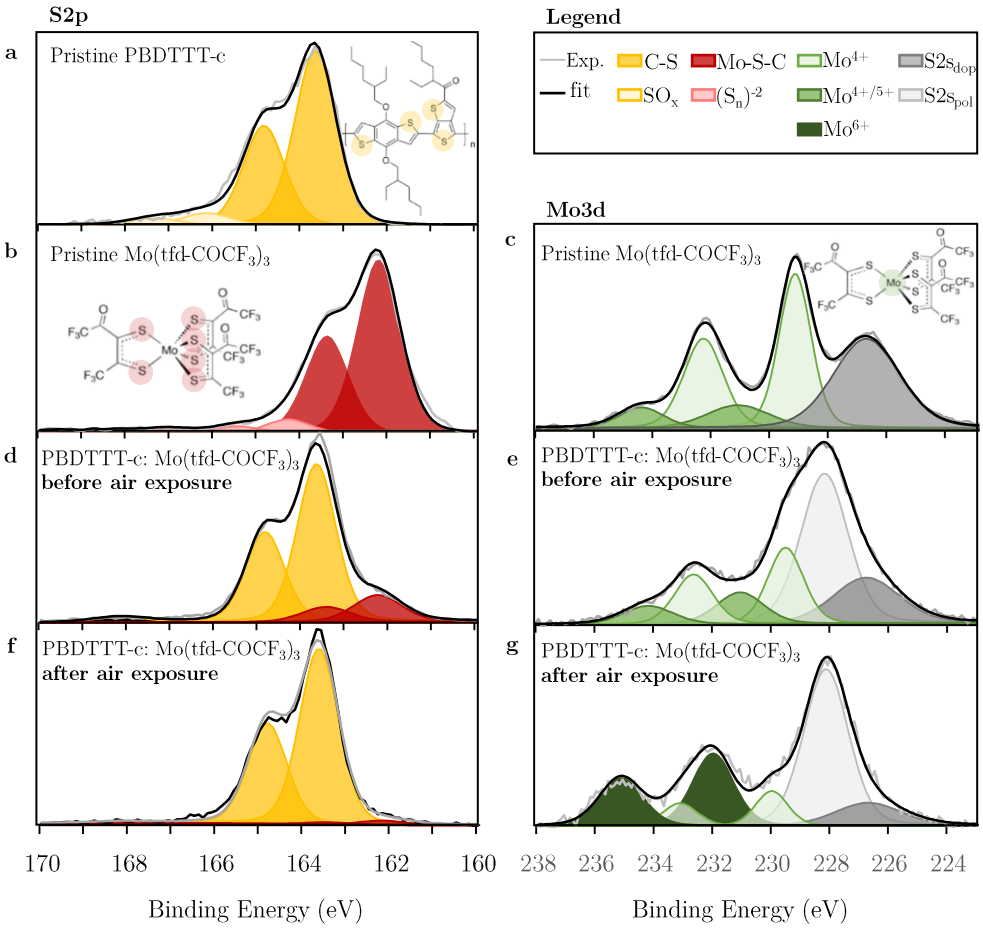

Figure 3.18 - Mo3d and S2p levels measured by XPS: pristine PBDTTT-c (a), pristine Mo(tfd-$COCF_3$)$_3$ (b, c), and Mo(tfd-$COCF_3$)$_3$-doped PBDTTT-c layers (15 nm-thick, 25 mol% dopant) after 20h under argon (d, e) and air (f, g).

Regarding the 3d spectral region of Mo in the pure dopant molecule, spin-orbit coupling also induces a splitting of the Mo3d core levels into two doublets (**Figure 3.18**c, green area): a higher intensity doublet at 229.1 eV ($3d_{5/2}$) and 232.3 eV ($3d_{3/2}$), and a lower intensity one at 231.3 eV ($3d_{5/2}$) and 234.4 eV ($3d_{3/2}$). Thus, Mo atoms in the dopant molecule are present in two different oxidation states. Besides, the additional peak at 226.7 eV was assigned to the S2s core level of the dopant ($S2s_{dop}$). Comparing with the literature, the Mo3d binding energies reported for Mo(tfd)$_3$ and Mo(tfd-CO_2Me)$_3$ are similar to those measured for the higher intensity doublet of Mo(tfd-$COCF_3$)$_3$[31,32]. The authors suggested an oxidation state of 4+ for the Mo coordinated with tris(dithiolene) ligands, as the binding energies are similar to those measured for MoS_2[33]. Therefore, we attributed the doublet at 229.1 eV ($3d_{5/2}$) and 232.3 eV ($3d_{3/2}$) to the Mo^{4+} oxidation state and the doublet at 231.3 eV ($3d_{5/2}$) and 234.4 eV ($3d_{3/2}$) to a Mo fraction at higher oxidation state, between 4+ and 5+. The latter was not observed in the aforementioned publications.

PBDTTT-c:Mo(tfd-COCF3)3 before air exposure

For the PBDTTT-c: Mo(tfd-$COCF_3$)$_3$ layer kept under argon atmosphere, the S2p spectral region presented the C-S environment of the polymer and the Mo-S-C environment of the dopant at

the same binding energies as measured for the pristine materials (**Figure 3.18**d). Regarding the Mo3d spectra region (**Figure 3.18**e), we observed the same two doublets of the pure dopant, attributed to the Mo^{4+} and $Mo^{4+/5+}$ oxidation state. In addition to the $S2s_{dop}$, we also observed the S2s core level of the polymer at 228.1 eV ($S2s_{pol}$). Note that no Mo doublets are observed in lower oxidation states, as one could expect for dopant molecules in its reduced state (after electron transfer from PBDTTT-c). Qi *et al.* presented DFT calculations for the $Mo(tfd)_3$ anion showing that the extra electron is mainly accommodated by the ligands and that Mo is only slightly influenced by the reduction[31]. This behavior was observed in different molybdenum sulfide complexes, such as Chevrel phases (Mo_6S_8), used as electrode material for Mg batteries[34]. The charge transfer during the reduction process in Mo_6S_8 involves both metal and ligands, inducing structural rearrangements rather than a formal Mo reduction. Additionally, electronic structure calculations of metal dithiolene complexes revealed an extensive ligand-metal mixing of the frontier orbitals with redox-active ligands[35]. Therefore, conventional oxidation-state descriptions are not suitable in these metal complexes. This might explain why we observed the same Mo core levels for pure $Mo(tfd\text{-}COCF_3)_3$ and PBDTTT-c:$Mo(tfd\text{-}COCF_3)_3$ layers.

Table 3.2 - XPS binding energies (eV) of Mo and S levels for pristine bulk materials (PBDTTT-c and $Mo(tfd\text{-}COCF_3)_3$) and for $Mo(tfd\text{-}COCF_3)_3$-doped PBDTTT-c layers (25 mol%, 15 nm) before and after air exposure.

Material	$S2s_{dop}$	$S2s_{pol}$	C-S		Mo-S-C		Mo^{4+}		$Mo^{4+/5+}$		Mo^{6+}	
			$S2p_{3/2}$	$S2p_{1/2}$	$S2p_{3/2}$	$S2p_{1/2}$	$Mo3d_{5/2}$	$Mo3d_{3/2}$	$Mo3d_{5/2}$	$Mo3d_{3/2}$	$Mo3d_{5/2}$	$Mo3d_{3/2}$
Pristine PBDTTT-c	–	–	163.7	164.9	–	–	–	–	–	–	–	–
Pristine $Mo(tfd\text{-}COCF_3)_3$	226.7	–	–	–	162.3	163.5	229.1	232.3	231.3	234.4	–	–
PBDTTT-c: $Mo(tfd\text{-}COCF_3)_3$ **before air exposure**	226.7	228.1	163.7	164.9	162.3	163.5	229.4	232.6	231.0	234.1	–	–
PBDTTT-c: $Mo(tfd\text{-}COCF_3)_3$ **after air exposure**	226.7	228.1	163.7	164.9	162.3 **(vanished)**	163.5	230.0	233.1	–	–	232.0	235.1

PBDTTT-c:Mo(tfd-COCF3)3 after air exposure

For the PBDTTT-c:$Mo(tfd\text{-}COCF_3)_3$ sample exposed to ambient air (20h), significant changes in the dopant molecule were detected (**Figure 3.18**f,g). In the Mo3d spectral region, a higher intensity doublet appeared at 231.9 eV ($3d_{5/2}$) and 235.1 eV ($3d_{3/2}$) that can be assigned to a Mo^{6+} oxidation state[36,37]. Besides, we observed a smaller fraction of the Mo^{4+} oxidation state at slightly higher binding energies: 229.9 eV ($3d_{5/2}$) and 233.0 eV ($3d_{3/2}$). No intermediate oxidations state ($Mo^{4+/5+}$) was observed in this sample. Hence, upon air exposure the *d* character of the Mo atom changes from a d^2 (Mo^{4+}) to a d^0 (Mo^{6+}), *i.e.* from a conducting to an isolating electronic structure.

Regarding the S2p spectral region, the peaks corresponding to Mo-S-C environment of the dopant molecule vanished after air exposure (red area, **Figure 3.18**f). In contrast, no changes were observed in the peaks assigned to the C-S environment of the polymer (yellow area, **Figure 3.18**f). This is in agreement with the UV-Vis-NIR measurements of dedoped layers, which showed no significant changes in the π-π* absorption of PBDTTT-c after air exposure (**Figure**

3.11b). Lastly, the total atomic concentration of F in the doped layers presented a significant reduction after air exposure (from 3.6 to 1.4 at%).

Summing up, exposing PBDTTT-c:Mo(tfd-$COCF_3)_3$ layers to ambient air (dark) presented no change in the polymer core levels, contrary to the dopant molecule, which presented an oxidation of the Mo3d core levels and signs of intrinsic degradation. These results indicate that Mo(tfd-$COCF_3)_3$ interacts with species present in ambient air, even though its EA of -5.3 eV. Interestingly, this degradation cannot be simply associated with traps identified in the literature. As presented in **Figure 3.6**, the energy levels of neutral and ionized Mo(tfd-$COCF_3)_3$ are located inside the air-stability window for universal traps[4,8,13]. Besides, the presence of general electron traps at approx. 0.3 eV below the LUMO level[3] would oxidize the ionized dopant back to its neutral state, but not necessarily result in a degradation of the dopant molecule.

One possible explanation would be a reactive dedoping process (see section 3.1.2), where the charged donor $\bullet^+$ radicals, resulting from the dedoping process of PBDTTT-c $\bullet^+$ to PBDTTT-c ^{0}, further react with Mo(tfd-$COCF_3)_3$ $\bullet^-$ radicals. In this scenario, ionized donor species are reactive towards ionized dopant molecules. According to this hypothesis, the dopant degradation would be associated with the presence of ionized donor species. Degradation of molecular *p*-dopants by ionized donor species present in ambient air was not yet evidenced in the literature. Hence, in the next section, we further verify the hypothesis of reactive dedoping by investigating the stability of Mo(tfd-$COCF_3)_3$ molecules towards water and ambient species.

3.2.4 Stability of Mo(tfd-$COCF_3)_3$ against H_2O and O_2

In this section, we aim to verify the hypothesis of reactive dedoping as the origin of the degradation of Mo(tfd-$COCF_3)_3$ molecules (see 3.1.2). To verify this hypothesis, we investigated the stability of pristine dopant molecules in the presence of H_2O and O_2. A stable behavior would further support our hypothesis of reactive dedoping, meaning that the degradation only takes place in the presence of charged donor radicals, which are formed during the dedoping process of PBDTTT-c:Mo(tfd-$COCF_3)_3$ layers to ambient air.

In section 3.2, we briefly discussed the stability of neutral Mo(tfd-$COCF_3)_3$ stored under ambient conditions. The results indicated that neutral molecules are stable under ambient air. Here, we further investigate the stability Mo(tfd-$COCF_3)_3$ molecules in the presence of H_2O. As this *p*-dopant does not form homogeneous layers when processed from solutions, this study is performed with Mo(tfd-$COCF_3)_3$ solutions, and UV-vis is used as the main characterization technique. This technique allows inferring the state of the dopant molecule (neutral, ionized, or degraded).

To investigate the stability of dopant molecules towards H_2O, small quantities of H_2O were added to the solutions. Therefore, we chose to work with THF (water-miscible) instead of o-Xylene (non-miscible with water). Note that THF was also used for the CV measurements of Mo(tfd-$COCF_3)_3$. The solutions were prepared inside the glovebox with freshly distilled and degassed THF. We also removed the stabilizer (BHT), to avoid unwanted reactions with the dopant molecule. Three solutions were prepared: one reference, one for the stability in the presence of

H_2O, and a third for the stability in air. The quartz cuvettes were filled and sealed with parafilm before leaving the glovebox. The reference remained sealed during the experiment. For the stability in the presence of H_2O, 3µl H_2O were added to the dopant solution just after the first UV-vis measurement (**Figure 3.19**a). The stability $Mo(tfd\text{-}COCF_3)_3$ in air was investigated by leaving the third cuvette open, under ambient air, to verify if the uptake of O_2 and H_2O by the solvent impacts the stability of the dopant molecule (**Figure 3.19**b). All the solutions were protected from ambient light with an aluminum foil and kept at 25°C.

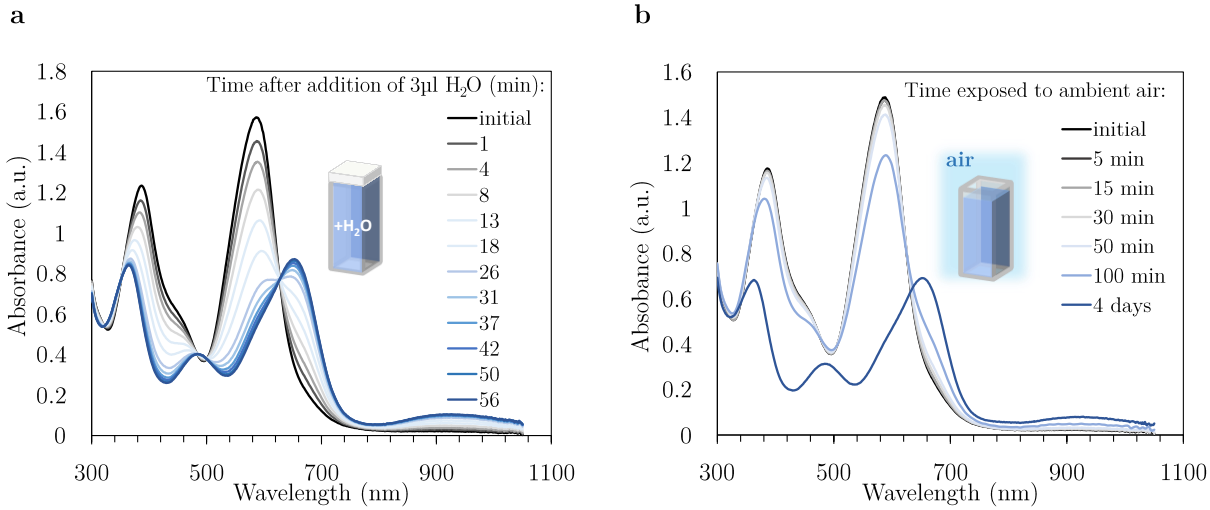

Figure 3.19 –Impact of water addition (a) and air exposure (b) on the UV-vis spectra of $Mo(tfd\text{-}COCF_3)_3$ solutions in THF.

There are several interesting points to discuss from the results presented in **Figure 3.19**. First, $Mo(tfd\text{-}COCF_3)_3$ molecules interact with H_2O (**Figure 3.19**a) and with O_2 and H_2O-related species present in air (**Figure 3.19**b). Since THF is a hygroscopic solvent, it absorbs moisture and/or other water-related species when exposed to air. Therefore, the changes in the UV-vis spectra in the case of air exposure may also be related to water molecules. Both scenarios presented a transition from the spectra of neutral $Mo(tfd\text{-}COCF_3)_3$ molecules (initial state) to monoanionic ones (see **Figure 2.14**)[38]. In other words, the UV-vis spectra of **Figure 3.19** suggest that the dopant molecule gets ionized in the presence of H_2O, and potentially O_2 and H_2O-related species present in air. The slower kinetics observed in **Figure 3.19**b may be associated with the kinetics of O_2 and H_2O uptake of THF. For $Mo(tfd\text{-}COCF_3)_3$ solution prepared from THF stored under ambient conditions (neither distilled nor degassed), the resulting UV-vis spectra corresponded directly to the monoanion (**Figure 3.20**a, green curve).

Regarding the stability of $Mo(tfd\text{-}COCF_3)_3$ solutions with monoanionic character in the presence of water and ambient species (**Figure 3.19**), no signs of degradation are observed when protected from ambient light. Besides, the interaction with water showed a completely reversible behavior: after solvent evaporation and a drying process under argon flow, the dopant presented the initial neutral signatures. In other words, our results show that no covalent bond is formed between $Mo(tfd\text{-}COCF_3)_3$ and water.

These observations suggest that the degradations observed with XPS analysis for Mo(tfd-$COCF_3$)$_3$ molecules, after the dedoping process in air, are not simply associated with the presence of O_2 and H_2O related species. To further explore the stability of dopant anion in the presence of water and ambient species, this experiment should be repeated with chemically reduced Mo(tfd-$COCF_3$)$_3$ molecules, to ensure that we are analyzing the ionized state of the dopant molecule (as found in PBDTTT-c: Mo(tfd-$COCF_3$)$_3$ layers). For example, it could be interesting to perform this experiment with a UV–Vis spectrometer coupled to an electrochemical cell, where the dopant solution could be electrochemically ionized, and the evolution of the UV-vis spectra upon addition of water and/or absorption of ambient species verified in situ.

Interestingly, the transition from neutral to ionized UV-vis spectra was also observed for other solvents as shown in **Figure 3.20**a. All solutions were prepared in air (on the same day), from the same dopant batch (the solvents used for this experiment are stored in a chemistry laboratory, under ambient air). A clear trend can be observed between the water miscibility of the solvent and the ionized character of the UV-vis spectra. Similar behavior is also observed for F4TCNQ (**Figure 3.20**b).

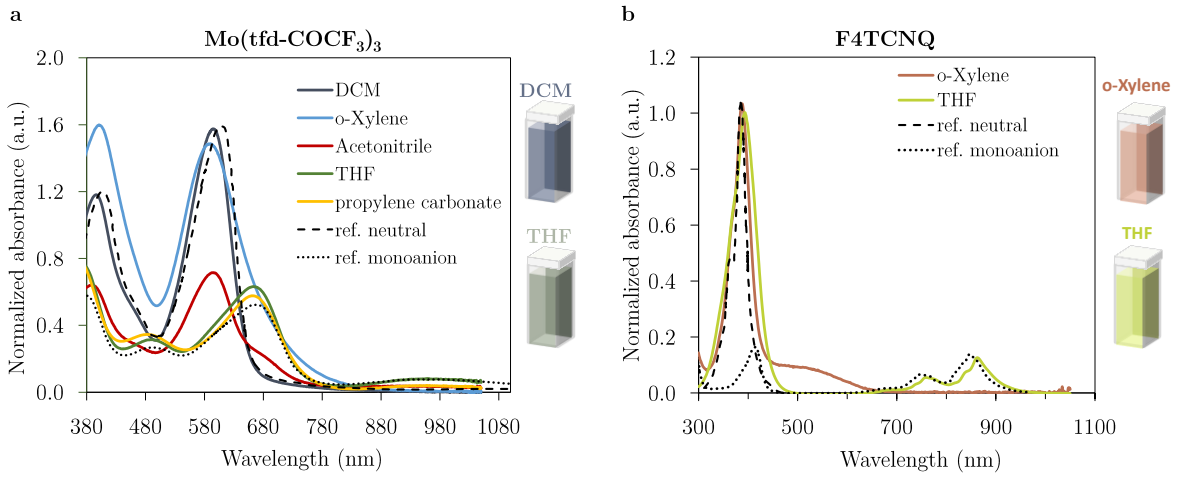

Figure 3.20 – UV-vis spectra of Mo(tfd-$COCF_3$)$_3$ (a) and F4TCNQ (b) solutions in different solvents. Comparison with reference spectra of neutral and ionized species.

No literature was found on changes in the state of Mo(tfd-$COCF_3$)$_3$ molecules in the presence of H_2O or when solubilized in different organic solvents. This *p*-dopant was only recently synthesized by Seth Marder's group[38], which might explain the lack in literature. However, this dopant was referred to be unstable in polar solvents[39], but no additional information was found on the mechanism. Regarding F4TCNQ molecules, Nikolka *et al.* also reported on the formation of F4TCNQ anions for dopant molecules exposed to ambient air, suggesting that F4TCNQ molecule also interacts with environmental species and undergoes charge transfer[2]. Interestingly, the authors did not observe such interaction for TCNQ molecules. If we analyze these results in terms of redox reactions, one could hypothesize that the EA of TCNQ is not low enough to receive an electron from ambient species (EA of -4.8 eV compared to -5.2 eV for F4TCNQ). For example, Leeuw *et al.* proposed water related donor levels at approx. -4.9 eV (this value is pH-dependent and may present additional activation energy) that could be related to the observed

charge transfer[14] (see **Table 3.1**). This water-related donor level may also explain the interaction between water and Mo(tfd-$COCF_3$)$_3$ molecules (**Figure 3.19**)

However, there are also acid/basic reactions that may be involved in these processes. F4TCNQ radical anions (F4TCNQ$\bullet^-$) were reported to react with strong acids forming protonated species (such as H_2F4TCNQ)[40,41]. In this context, to avoid changing the chemical state of F4TNCQ anions in organic hosts, Watts et al highlighted the importance of considering their stability against acid-base reaction with ambient gases[41]. However, no water interactions with neutral F4TNCQ were mentioned in these studies[40,41].

In conclusion, no degradation of Mo(tfd-$COCF_3$)$_3$ molecules was observed in the presence of water and ambient species (dark conditions), only reversible interactions. These results support the hypothesis of reactive dedoping, meaning that the dopant degradation observed by XPS takes place in the presence of positively charged donor radicals (donor$\bullet^+$). However, further investigations with chemically reduced Mo(tfd-$COCF_3$)$_3$ are required to confirm this hypothesis.

Last, the results presented in this section highlighted that studying the stability of neutral and ionized *p*-dopants in the presence of O_2 and H_2O related species might also be important for the stability of the *p*-doped state in conjugated polymers.

3.2.5 Final considerations on the dedoping process

Here, we summarize the main results presented in this section to drawn some final conclusions on the air-stability of PBDTTT-c: Mo(tfd-$COCF_3$)$_3$ system.

Regardless of the atmosphere, PBDTTT-c: Mo(tfd-$COCF_3$)$_3$ samples presented unstable doping signatures. Even under a controlled atmosphere, the conductivity is not stable over time (**Figure 3.7** and **Figure 3.8**). Optical and electrical characterizations suggest a dedoping process since the degradation of the *p*-doping characteristics is concomitant with the recovery of the properties of pristine PBDTTT-c (section 3.2.2). By performing stability studies under different atmospheres, we highlighted the impact of ambient humidity on the dedoping rate. Thus, the *p*-doping instability is associated with the presence of water-related species acting as hole traps. These results agree with recent studies suggesting that water introduce hole traps in OSCs [2–4]. Besides, water-related hole traps can also explain the instability observed under a controlled atmosphere, as water was reported to be omnipresent in polymer layers.

Regarding the dopant, Mo(tfd-$COCF_3$)$_3$ molecules presented signs of degradation after the dedoping process under ambient conditions (**Figure 3.18**e, f). However, no signs of instability are observed for pristine dopant molecules in the presence of water and ambient species (**Figure 3.19**).

The layer thickness presented an important impact on the dedoping rate, which was considerably faster for thinner layers (section 3.2.2). In section 3.4.2, we propose a diffusion model to explain these results.

Finally, we suggest that *p*-doping instability of PBDTTT-c: $Mo(tfd\text{-}COCF_3)_3$ layers is due to reactive dedoping processes, which happens in two steps (**Figure 3.21**):

1. Recovery of pristine PBDTTT-c properties: water-related species introduce hole traps (donor levels) in the doped layers, resulting in a dedoping process
2. Degradation of $Mo(tfd\text{-}COCF_3)_3$: ionized donor traps are reactive towards ionized dopant molecules, resulting in a degradation of $Mo(tfd\text{-}COCF_3)_3$.

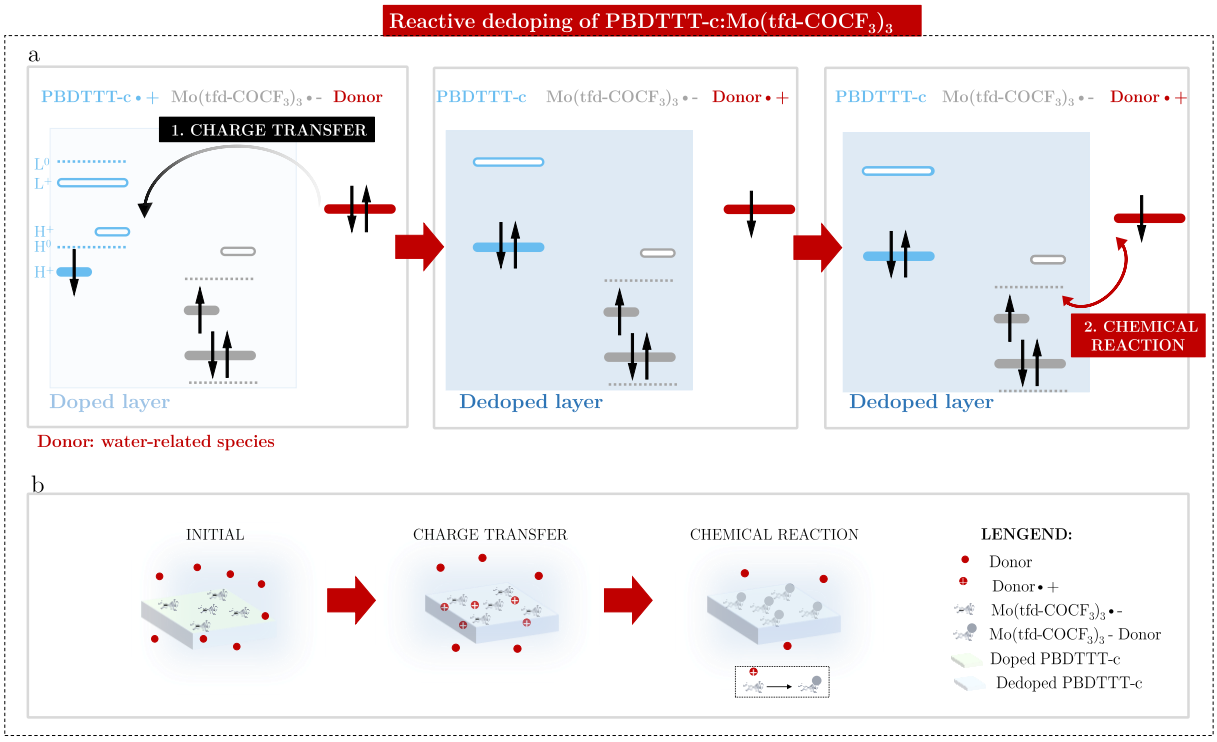

Figure 3.21 – Reactive dedoping process proposed for PBDTTT-c:$Mo(tfd\text{-}COCF_3)_3$ layers exposed to water-related species. Energetic (a) and schematic (b) representation.

Hence, water-related hole traps may be an important issue for the stability of *p*-doped systems under ambient conditions, and even under controlled atmosphere. However, we also highlighted the instability of $Mo(tfd\text{-}COCF_3)_3$ ions, which is also a critical aspect for the stability of the *p*-doped state. In the next section, we verify the air stability of the different *p*-doped systems studied in this thesis, to further investigate the impact of hole traps in the *p*-doping stability of conjugated polymers.

3.3 AIR-STABILITY OF OTHER P-DOPED SYSTEMS

In the previous section, we deeply investigated the stability of the PBDTTT-c:Mo(tfd-$COCF_3$)$_3$ system under different atmospheres and proposed a reactive dedoping mechanism to explain the *p*-doping instability of these layers. Our results suggested that the donor responsible for the dedoping process is a water-related species present in ambient air. To have a broader idea on the impact of this dedoping mechanism on the stability of *p*-doped systems (i.e. free holes), this section investigates the *p*-doping stability of P3HT:F4TCNQ, PBTTT-c:F4TCNQ and P3HT: Mo(tfd-$COCF_3$)$_3$ under controlled atmosphere, anhydrous air, and ambient air.

The samples were prepared as described in **Table 2.8** and **Table 2.9**. Here, we focused on thin (15 nm) layers, aiming to verify the stability of the selected systems in critical conditions. For PBDTTT-c:Mo(tfd-$COCF_3$)$_3$, thinner layers presented stronger instability signatures compared to thicker ones (see **Figure 3.10**). The *p*-doping stability is investigated in terms of conductivity and UV-Vis-NIR absorptions. The measurements are performed in the same conditions as for PBDTTT-c: Mo(tfd-c$OCOF_3$)$_3$ samples. For more details see section 3.2.1.

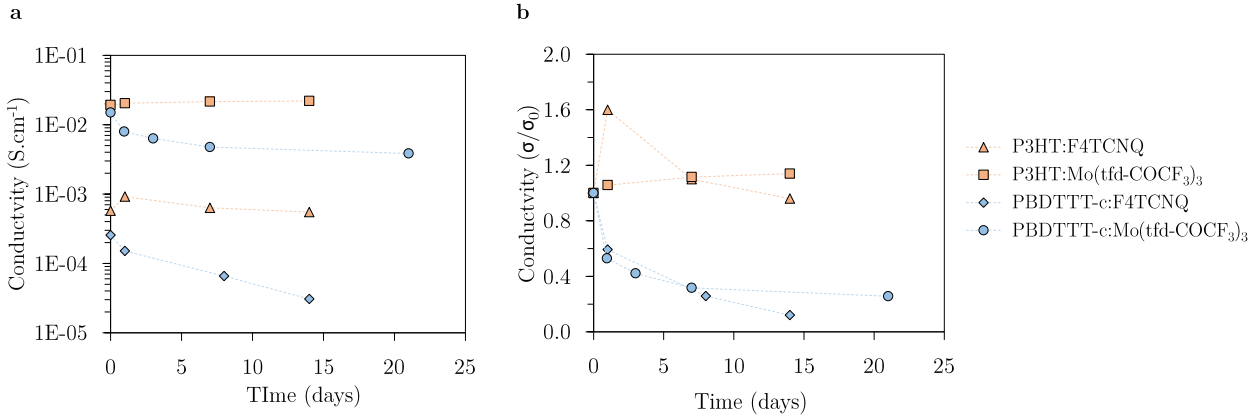

Figure 3.22 - Conductivity evolution over time for inside the glovebox (argon atmosphere). Absolute (a) and normalized (b) values. All layers are approximately 15 nm-thick. Different dopant concentrations: 5 mol% for PBDTTT:Mo(tfd-$COCF_3$)$_3$, 3.6 mol% for RRa-P3HT:Mo(tfd-$COCF_3$)$_3$, 20 mol% for PBDTTT-c:F4TCNQ, and 11 mol% for RRa-P3HT:F4TCNQ.

Figure 3.22 presents the conductivity evolution over 15 days under a controlled atmosphere (argon-filled glovebox) for all four *p*-doped systems. These graphs aim to illustrate a general trend observed on the conductivity evolution under a controlled atmosphere. We note that these samples were prepared and aged in different days and present different dopant concentrations. Thus, quantitative comparisons should be performed with caution.

The main conclusion that can be drawn from **Figure 3.22** is that the conductivity of *p*-doped P3HT (red symbols) presented better stability compared to PBDTTT-c (blue symbols), as highlighted in **Figure 3.22**b. P3HT:Mo(tdf-$COCF_3$)$_3$ presented to be particularly stable. No conductivity decrease was observed for this system, even for samples stored over two months under a controlled atmosphere. Regarding PBDTTT-c-doped systems, all samples measured inside the glovebox (independent of the dopant nature, its concentration, and layer thickness)

presented an immediate conductivity decrease. Hence, the matrix appears to have a strong influence on the stability of the doped systems under a controlled atmosphere.

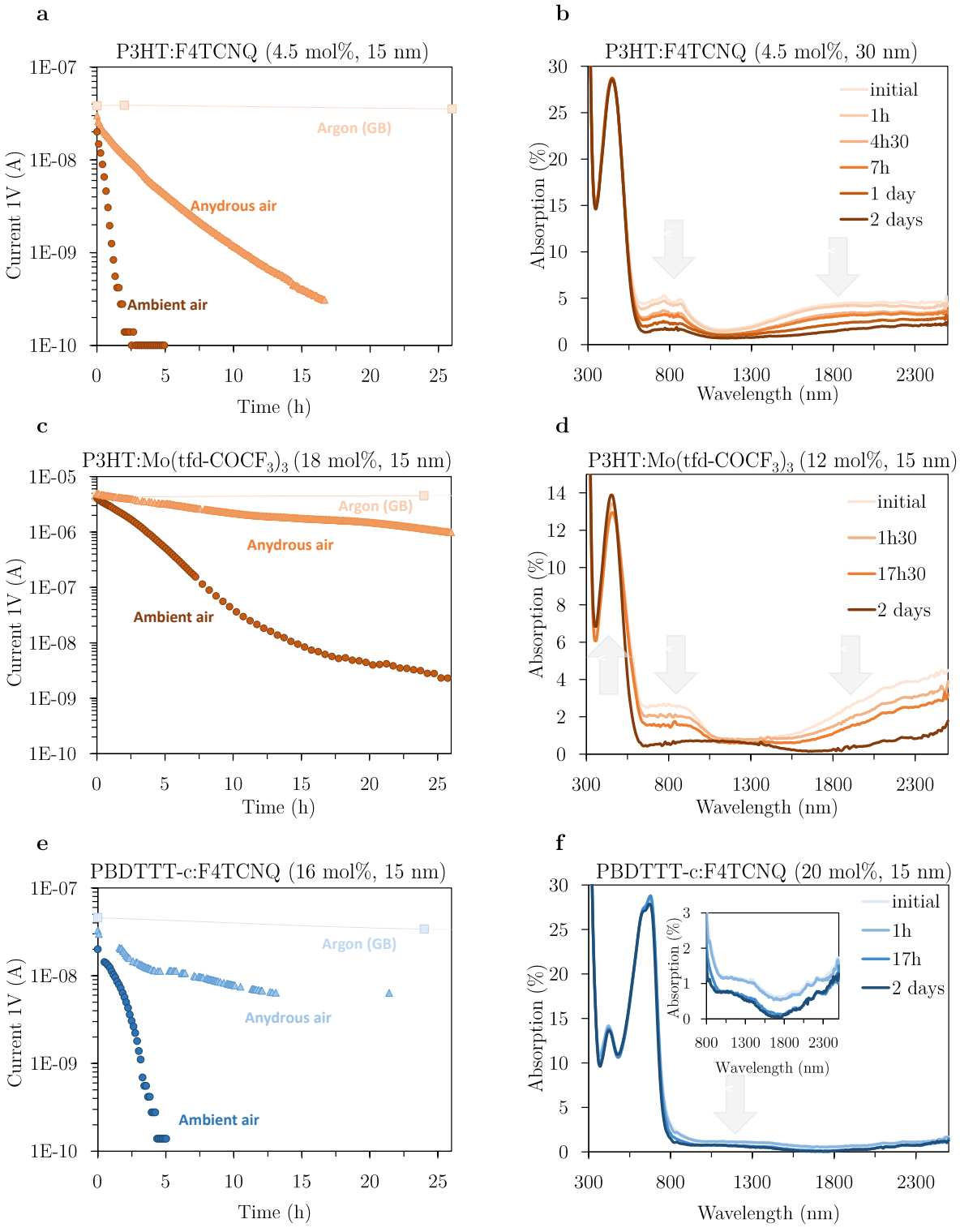

Figure 3.23 –Current evolution of different *p*-doped systems under argon, anhydrous air and ambient air (dark conditions) and stability of the UV-vis-NIR absorptions under ambient air.

The stability of P3HT:F4TCNQ, PBTTT-c:F4TCNQ and P3HT: Mo(tfd-$COCF_3$)$_3$ under ambient air and anhydrous air are presented in **Figure 3.23**. To allow for a quantitative

comparison of the current evolution in different atmospheres, samples plotted in the same graph were prepared from the same solution and aged in the same day (**Figure 3.23**a, c, e). The evolution of UV-vis-NIR signatures under ambient air is presented in **Figure 3.23**b, d, f.

The first conclusion from **Figure 3.23** is that all *p*-doped systems present unstable *p*-doping signatures under ambient air. Besides, a similar trend is observed for the current evolution under different atmospheres: the three *p*-doped systems presented a faster decrease under ambient air compared to anhydrous air. Hence, we can affirm that humidity, i.e. water vapor present in air, has a negative impact on the conductivity of all *p* -doped systems considered in this thesis. The existing data do not allow a meaningful comparison of the current decrease (rate) between different *p*-doped systems, as we do not know the impact of the dopant concentration on the degradation rate, and no statistical analyses were performed. Note that for PBDTTT-c:Mo(tfd-$COCF_3)_3$, an important variation on the dedoping rate was observed between different experiments (see **Figure 3.13** and **Figure 3.14**).

Regarding the UV-vis spectra, the doping induced absorptions vanish under air exposure for all systems. If we take a closer look, for P3HT:F4TCNQ (**Figure 3.23**b) both polaronic signatures of P3HT and F4TCNQ anions vanish. Note that this is the only system studied in this thesis where we can clearly distinguish the signatures of the dopant anion on the UV-Vis-NIR spectrum. However, we do not observe a clear recovery of the π-π* absorption of pristine P3HT. This could be related to absorption of neutral F4TCNQ molecules (peak at ca. 390 nm), if one considers a transition from $F4TCNQ^{\bullet -}$ to $FT4TCNQ^0$. Nevertheless, the bleaching of the F4TCNQ anion does not necessarily mean that the dopant becomes neutral. It could also react with ambient species. Nevertheless, **Figure 3.23**b does not allow inferring on the final state of F4TCNQ molecules. For P3HT: Mo(tdf-$COCF_3)_3$, the polymer host presents clear dedoping signatures: bleaching of polaronic absorptions and recovery of pristine π-π* absorption (**Figure 3.23**d). As for PBDTTT-c: Mo(tdf-$COCF_3)_3$, it is not possible to infer on the state of the dopant molecule as their spectra cannot be distinguished when mixed with the polymer host (see **Figure 3.11**). Finally, the PBDTTT-c: F4TCNQ systems also presented a decrease of the NIR doping features, but no information on the dopant state can be extracted from this spectra either (**Figure 3.23**e).

In **Figure 3.24** we compared the spectra of pristine polymer layers with doped layers after air exposure. For both RRa-P3HT (**Figure 3.24**a) and PBDTTT-c (**Figure 3.24**b), no significant difference can be observed. In other words, the optical properties for doped layers after air exposure are very close to the pristine absorption of the polymer host.

The presence of general hole traps may be the origin of the *p*-doping instability observed for all four systems. However, we should keep in mind that unstable dopant ions could also lead to a dedoping process, to keep the charge neutrality in the system. Anyway, all *p*-doped systems considered in this thesis presented unstable doping signatures under ambient conditions, accelerated in the presence of humidity.

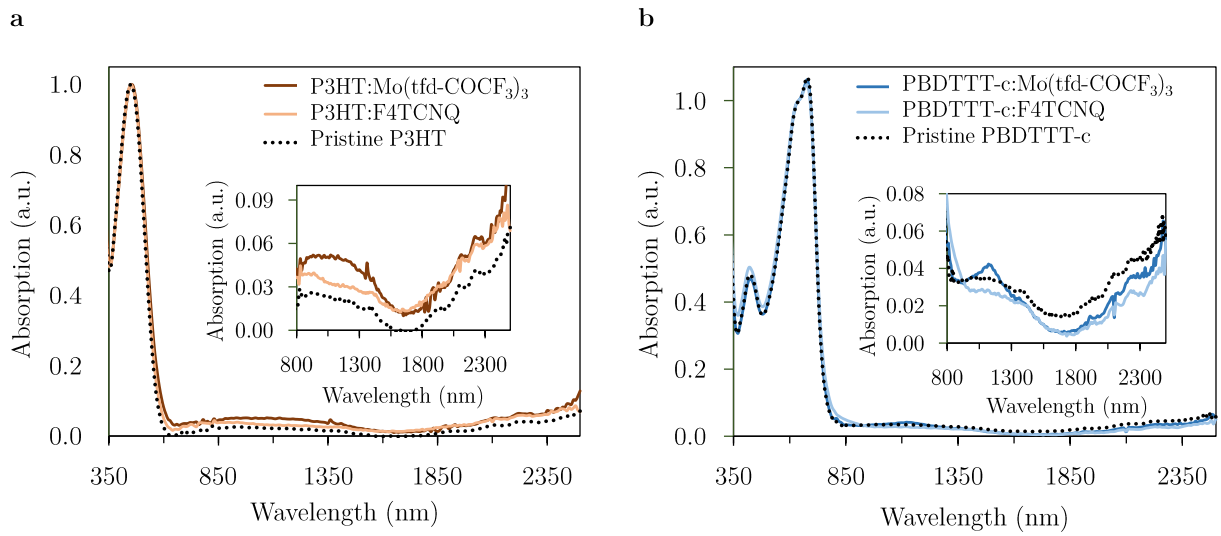

Figure 3.24 – Comparison between pristine and dedoped UV-vis-NIR absorptions for RRa-P3HT (a) and PBDTTT-c (b).

The existence of hole traps under ambient conditions could also explain the few studies in the literature reporting on unstable *p*-doped layers under ambient air, for instance PBTTT:$FeCl_3$[15] and RR-P3HT:F4TCNQ[16]. The hypothesis of water-related hole traps lying ±0.3 eV above the HOMO level of OSCs, as proposed by Zuo *et al.*[3], might induce dedoping processes in several *p*-doped systems. Further analysis are required to verify this hypothesis.

In the last section of this chapter we verify through simulations the impact of hole traps on the stability of *p*-doped semiconductors. Besides, we present a diffusion model to explain the impact of the layer thickness of the dedoping rate observed for PBDTTT-c: Mo(tfd-$COCF_3$)$_3$.

3.4 SIMULATIONS OF DEDOPING BY COMPENSATION

In this section, a model is proposed to explain the conductivity degradation observed for *p*-doped polymers over time.

The model relies on the assumption that some elements contained in the atmosphere, probably water-related species, diffuse into the semiconductor layer, and act as donor dopants (i.e. donor traps). As demonstrated below, a significant amount of donor dopants can induce a mechanism of compensation, i.e. dedoping of the layer, and thus degrade the conductivity.

This section is divided into two parts. First, we investigated the impact of donor traps on the stability of *p*-doped semiconductors. In the second part, we develop a diffusion model to explain the impact of the layer thickness on the dedoping rate observed in section 3.2.2. (**Figure 3.10** and **Figure 3.15**)

3.4.1 Dedoping by compensation

In semiconductors, the electron and hole concentrations at thermal equilibrium result from a trade-off with ionized impurities to maintain charge neutrality.

Consequently, we have :

$$p + {N_d}^+ = {N_a}^- + n$$

p (resp. n) is the free hole (resp. electron) concentration, and Na^- (resp. Nd^+) the fraction of ionized acceptor (resp. donor) concentration. All these quantities depend on the Fermi level E_F at equilibrium, according to :

$$p(E_F) = \int_{-\infty}^{+\infty} g_{HOMO}(E)\left(1 - f(E, E_F)\right) dE$$

$$n(E_F) = \int_{-\infty}^{+\infty} g_{LUMO}(E)\, f(E, E_F)\, dE$$

$${N_a}^-(E_F) = \int_{-\infty}^{+\infty} g_{acceptor}(E)\, f(E, E_F)\, dE$$

$${N_d}^+(E_F) = \int_{-\infty}^{+\infty} g_{donor}(E)\left(1 - f(E, E_F)\right) dE$$

$$f(E, E_F) = \frac{1}{1 + \exp(\frac{E - E_F}{kT})}$$

where g refers to the corresponding density of state.

The modeling of the impact of doping (acceptors and donors) on the free carrier concentration n and p consists in finding the value of the Fermi level solution of the charge neutrality equation.

In the following discussion, and in order to limit the number of unknown parameters, we will make to following simplifying assumptions :

- The Fermi level E_F lies within the gap (Boltzmann statistics).

- Acceptor and Donor are represented by a single energy level E_A and E_D accouting for polaron effects.
- States for electrons within the gap are neglected (although it is known that it is not exactly the case for polymer semiconductor).

Note that a more accurate model accounting for the exact density of states would not significantly modify the final conclusion.

In the case of *p*-type doping, the electron concentration remains negligible, and we have :

$$p = N_a^-$$

If the acceptor level of the dopant (E_A) is lower than the HOMO level of the polymer (or eventually only a few meV higher), almost all the dopant are ionized at room temperature, and the doping process is effective :

$$p = N_a^- \approx N_a$$

Now let's examine the impact of additional donor levels, i.e. a hole traps, in the doping process. Throughout this chapter, the *p*-doped state presented to be unstable in the presence of water-related species. Recently, Zuo *et al.* have reported that water (introduced by air contamination) can introduce hole trap levels in OSCs, located approximately 0.3 – 0.4 eV above the HOMO level[3]. These values will be considered to investigate the impact of additional donor levels on the *p*-doping stability. Indeed, the presence of donor species (N_d) will perturb the equilibrium of charges in *p*-doped OSCs, as in the case of ionized donors (N_d^+) and consequently trapped holes, the charge neutrality becomes :

$$p + N_d^+ = N_a^-$$

To verify the impact of additional donor levels (hole traps) in the *p*-doping process, i.e. in the concentration of free holes (p) and ionized dopant molecules (N_a^-), the solution of this equation is plotted in **Figure 3.25** as a function of the donor concentration (more precisely the ratio between donor and acceptors N_d/N_a). Here, the acceptor level (E_A) has been arbitrary set at -5.05 eV (representing the LUMO of the *p*-dopant), the HOMO of the OSCs ($OSCs_{HOMO}$) was fixed at - 5.1 eV and the donor level (E_D) was 0.3 eV above $OSCs_{HOMO}$.

Regarding the ratio of ionized donors (green curve in **Figure 3.25**), when $N_d < N_a$, i.e. when the concentration of donors is below the concentration of acceptors, all donors are ionized. The presence of positively charged donors is in agreement with the decrease in the concentration of free holes (p). The decrease in the ratio of ionized donors when $N_d > N_a$ can be explained by an excess of donor molecules.

Last, the ratio of ionized acceptors (blue curve in **Figure 3.25**) is not affected by the presence of additional donors at lower N_d, meaning that the positively charged donors (N_d^+) balance the negative charge of ionized dopants (N_a^-). At higher N_d, we observe an increase in ionized dopants (N_a^-), suggesting that the excess of donors can also ionize dopant molecules that do not participate in the doping process because of the saturation regime (highly doped samples). This is in agreement with the observation of Jacobs *et al.* on the dedoping process of *p*-doped OSCs

with additional donor molecules (amines)[10]. Note that the compensation of *p*-dopants by *n*-dopants (donors) strongly impacts the free hole concentration in the semiconductor (p), while the acceptor dopants remain ionized.

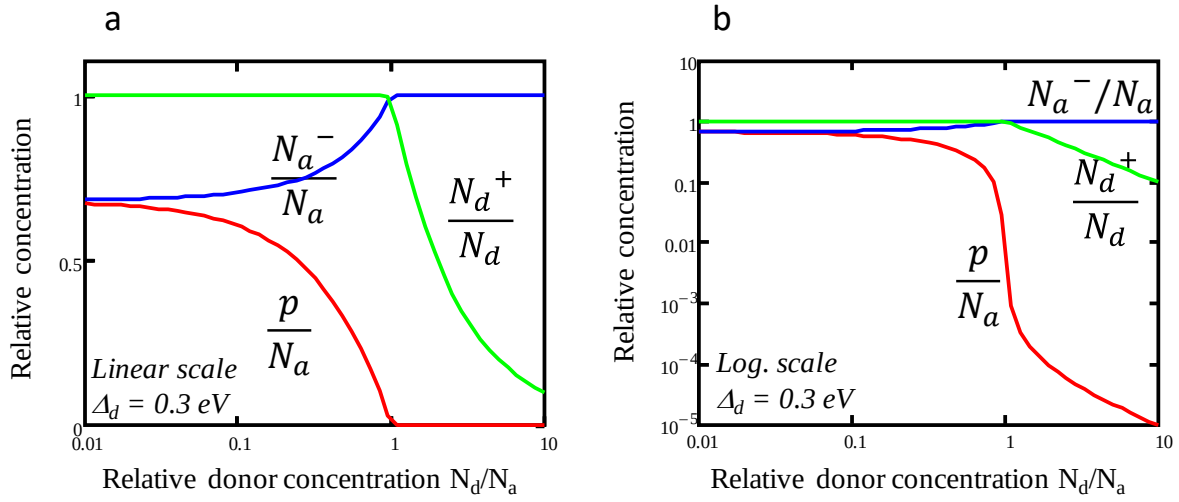

Figure 3.25 – Concentration of free holes (p), ionized donors (N_d^+) and ionized acceptors (N_a^-) for a *p*-doped semiconductor in the presence of additional donors. Linear (a) and log (b) scale. Parameters: E_A=-5.05 eV, OSC_{HOMO}=5.1 eV and E_D=4.8 eV (0.3 eV above OSC_{HOMO}, i.e. Δ_d=0.3 eV) $N_a = 10^{19}$ cm^{-3}, $N_v = 10^{20}$ cm^{-3}.

Using the same parameters, **Figure 3.26** shows the impact of donor and acceptor levels on the Fermi level (E_F) of an OSC. In the presence of an acceptor level (E_A) close to the OSC_{HOMO}, the resulting E_F is only a few meV above OSC_{HOMO} (dotted blue line, acceptor only), characteristic of a highly *p*-doped semiconductor. When only donor levels are present, the E_F is identical to an intrinsic semiconductor, i.e. in the middle of the bandgap (dotted green line, donor only). Last, when donor and acceptor levels are present in the semiconductor (dotted red line, donor + acceptor), the position of E_F depends on the donor N_d/N_a ratio. For lower N_d, the E_F is characteristic of a highly *p*-doped semiconductor, and for higher N_d, E_F moves away from the OSC_{HOMO}, indicating a dedoping process. Interestingly, even with excess in N_d (N_d/N_a>1), the Fermi level does not reach the value of an intrinsic semiconductor, meaning that positively charged donors (N_d^+) also influence the E_F of the semiconductor.

Hence, the hole traps proposed by Zuo *et al.* at approximately 0.3 – 0.4 eV above the $OSCs_{HOMO}$ can explain the dedoping process observed in this work for *p*-doped layers in the presence of water-related species. The ionized donors (N_d^+) have shown to balance the charge of the ionized acceptors (N_a^-). Additionally, if the ionized state of the *p*-dopant is stable under ambient conditions and in the presence of ionized donors, the dedoping process may occur without changes in the state of the dopant molecule.

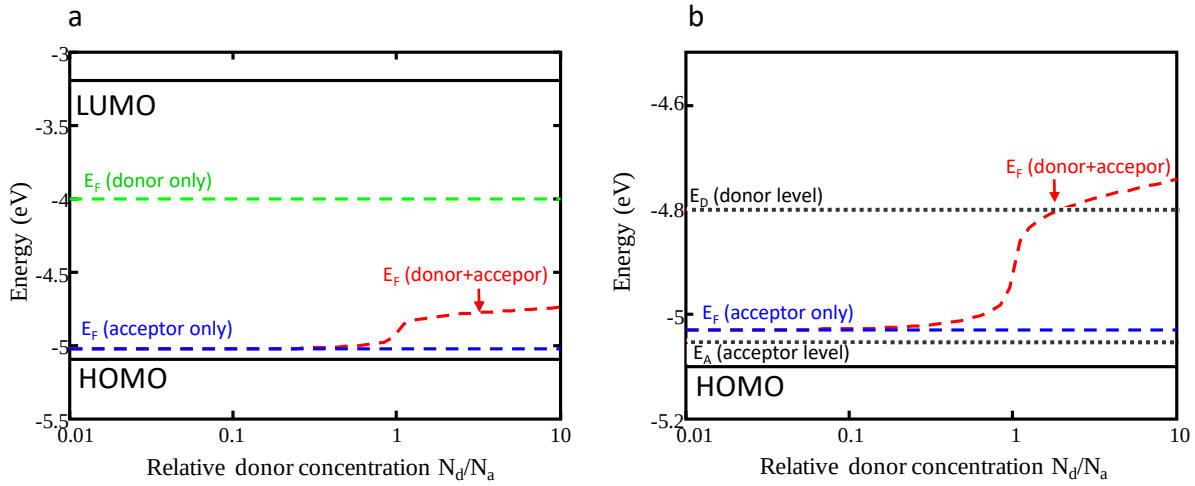

Figure 3.26 – Changes in the Fermi level of a semiconductor in the presence of a donor level (E_D), an acceptor level (E_A) and both (E_D+E_A). Other parameters are the same than in Figure 3.25.

Since we observed a strong effect of the layers thickness on the dedoping rate of PBDTTT-c:Mo(tfd-$COCF_3$)$_3$ samples (**Figure 3.10** and **Figure 3.15**), in the following section we verify if this behavior can be explained by the diffusion of donor species in *p*-doped OSCs.

3.4.2 Diffusion model for donor species

Diffusion model

This section aims to propose a diffusion model that describes the dedoping rate as a function of the layer thickness. The proposed model considers the diffusion of donors in homogeneous layers (**Figure 3.27**).

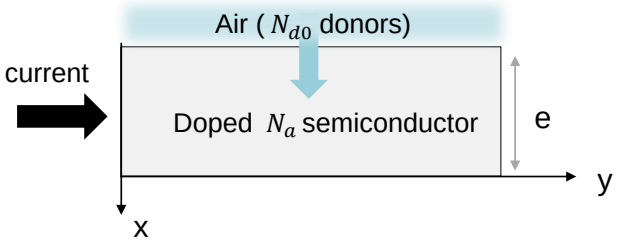

Figure 3.27 – Schematic representation of the diffusion of donors present in air (N_{d0}) in *p*-doped semiconductors with the parameters used for the diffusion model.

The donor concentration is assumed to follow the time dependent diffusion equation :

$$\frac{\partial \Delta N_d}{\partial t} = D \frac{\partial^2 \Delta N_d}{\partial x^2}$$

D is the diffusion coefficient ($m^2.s^{-1}$), where

$$\Delta N_d(x,t) = N_d(x,t) - N_{d0}$$

N_{d0} being the equilibrium donor concentration in the doped OSCs-air interface.

The following boundary conditions are used:

$$N_d(x, t < 0) = 0$$

$$\Delta N_d(x = 0, t) = 0$$

$$\frac{\partial \Delta N_d}{\partial x}(x = e, t) = 0$$

To find the solution, we apply the separation variable method. Therefore, we look for solutions satisfying the diffusion equation and the corresponding boundary conditions:

$$\Delta N_d(x, t) = X(x)\, T(t)$$

We thus have :

$$X\, T' = DTX''$$

$$\frac{1}{D}\frac{T'}{T}(t) = \frac{X''}{X}(x) = Cst = -\omega^2$$

Hence, we obtain two ordinary equations:

$$\frac{1}{D}\frac{T'}{T}(t) = \frac{X''}{X}(x) = Cst = -\omega^2$$

$$T' = -D\,\omega^2 T$$

$$X'' + \omega^2 X = 0$$

The time solution T(t) is :

$$T(t) \propto \exp(-\omega^2 D\, t)$$

(the constant $-\omega^2$ is taken negative, in order to avoid the divergence of T versus time).

The spatial solution X(x) is :

$$X(x) = A\, cos(\omega\, x) + B\, \sin(\omega\, x)$$

The boundary conditions:

$$\Delta N_d(x = 0, t) = 0$$

$$\frac{\partial \Delta N_d}{\partial x}(x = e, t) = 0$$

lead to :

$$X(0) = 0 = A$$

And :

$$X'(x) = B\, \omega \cos(\omega\, x)$$

$$X'(L) = 0 = B\, \omega \cos(\omega\, e)$$

In order to avoid the non physical solution B=0, the unkown constant has to take the following discrete value

$$\omega_n = \left(n + \frac{1}{2}\right)\frac{\pi}{e}$$

And the most general solution is thus :

$$\Delta N_d(x,t) = \sum_{n=0}^{\infty} B_n \sin\left(\left(n+\frac{1}{2}\right)\pi\frac{x}{e}\right) \exp\left[-\left(n+\frac{1}{2}\right)^2\frac{\pi^2}{e^2}D\,t\right]$$

To find the B_n constant, we use the boundary condition at t = 0 :

$$\Delta N_d(x, t=0) = -N_{d0}$$

And the fact that $\sin(\omega_n x)$ functions are orthogonal :

$$B_n = -N_{d0}\frac{2}{e}\int_0^e \sin\left(\left(n+\frac{1}{2}\right)\pi\frac{x}{e}\right)dx = \frac{-4N_{d0}}{\pi\,(2n+1)}$$

Leading to :

$$N_d(x,t) = N_{d0}\left(1 - \sum_{n=0}^{\infty}\frac{4}{\pi\,(2n+1)}\sin\left(\left(n+\frac{1}{2}\right)\pi\frac{x}{e}\right)\exp\left[-\left(n+\frac{1}{2}\right)^2\frac{\pi^2}{e^2}D\,t\right]\right)$$

In the following, this diffusion model will be used to describe the dedoping rate over different layer thickness, observed experimentally, by the diffusion of donor species in polymer layers.

Comparison between experimental and simulated dedoping

Here, we aim to verify if diffusion of water-related species into polymer layers can explain the considerable differences in dedoping rates observed when varying the layer thickness of PBDTTT-c:Mo(tfd-$COCF_3$)$_3$, where faster rates were observed for thinner layers (see **Figure 3.10**). The diffusion model developed above describes the diffusion of external donor molecules N_d (representing water-related donor traps) in polymer layers. Further work is required to correlate N_d with the external humidity and/or H_2O concentration varied in our aging experiments. Besides, since we have no information on the initial concentration of water-related trap inside the polymer layers, this parameter was not considered in our model. Nevertheless, the developed model allows investigating if a diffusion like behavior could be the origin of the slower dedoping rates for thicker samples.

Table 3.3 – Parameters used for the simulations.

PARAMETERS	VALUE
Effective density of state Nv in the HOMO band	Nv = 10^{20} cm^{-3}
Acceptor level	- 0.05 eV below HOMO level
Acceptor doping level	N_a = 10^{20} cm^{-3}
Donor level	0.3 eV above LUMO level
Donor doping level at the sample entrance (fitting parameter)	N_{d0} = 2.5 10^{20} cm^{-3}
Diffusion Coefficient (fitting parameter)	D = 5.7 10^{-21} m^2s^{-1}

We chose to teste our model on the results obtained inside a climatic chamber (current decrease over time) since they were performed under controlled conditions (40% RH, 25°C). Four different layer thicknesses were fitted with our diffusion model, which present two free parameters: the initial concentration of external donors N_{d0} in the polymer-air interface and the diffusion coefficient D. The *p*-dopant concentration was estimated to Na ~ 10^{20} cm^{-3}, based on the

conductivity of PBDTTT-c:Mo(tfd-$COCF_3$)$_3$ layers doped at 5 mol% (~1 x 10^{-2} S.cm^{-1}), and taking the hole mobility for PBDTTT-c from the literature (2 x 10^{-4} cm^2.V^{-1}.s^{-1}[142]).

For each x, knowing the Nd(x,t) donor concentration, the hole concentration is computed according to the procedure explained earlier. As the debye length L_d is, for highly doped semiconductor, much lower than the semiconductor thickness, the Fermi level can be defined locally. Since we aim to fit our results presenting the current decrease over time, the conductance G is computed by summing all layer contribution :

$$G = \frac{A}{L} q\,\mu \int_0^e p(x)dx$$

Where A is the section, q the elementary charge, μ the hole mobility, $p(x)$ the free hole concentration, and e the thickness. The parameters used for the simulations are listed in **Table 3.3**.

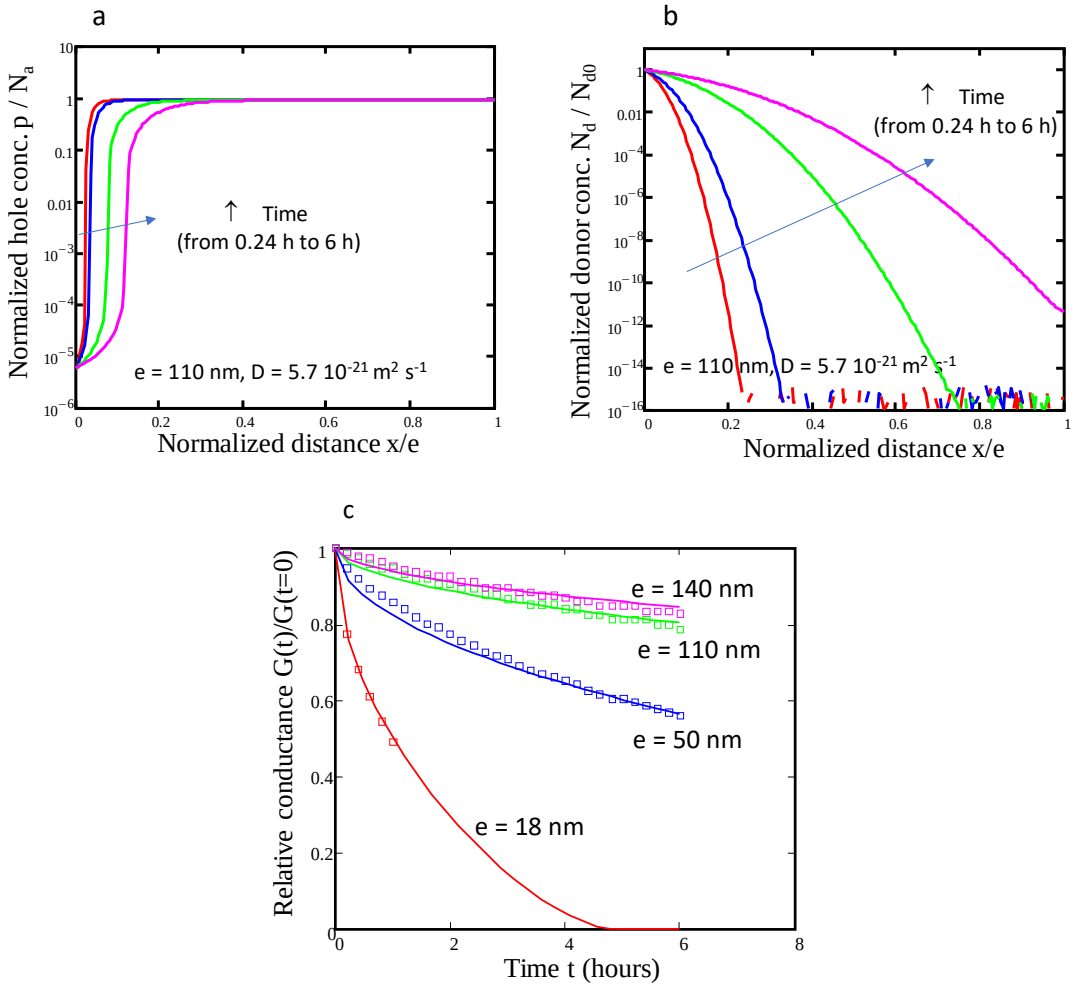

Figure 3.28 – Experimental values compared to the model. Fitting parameters: $N_a = 10^{20}$ cm^{-3}, $N_{d0} = 2.5\ 10^{20}$ cm^{-3}, D = 5.7 10^{-21} m^{2}s^{-1}. The fitted thicknesses are indicated in the Figures. Nominal thicknesses were 15, 45, 120, and 180 nm.

In **Figure 3.28**a, we present the doping efficiency as a function of the position within the layer using the diffusion model proposed above, for a given Nd(x,t) donor concentration. In this example, the dedoping process takes 1.2h for the first nanometers in contact with air (red curve),

whereas the bulk is still doped. After 6h (fuchsia curve), the diffusion of donor species and consequently the dedoping process reaches ca. 20 nm a doped layer of 110 nm. **Figure 3.28**b illustrates the diffusion of donor species within the polymer layer as a function of position and time.

In **Figure 3.28**c, we compare the experimental values of relative conductance to our model. This model fits correctly the experimental results. The fitted thicknesses extracted from the fit (indicated in **Figure 3.28**c) are very close to the nominal ones (15, 45, 120, 180 nm).

In conclusion, our results of conductivity degradation after air exposure versus time of exposition of P doped layers are consistent with the hypothesis of dedoping by donors.

The degradation kinetics follows quite well a donor diffusion model, for all the thicknesses tested here, suggesting that donor diffusion would be the limiting mechanism for dedoping evolution over time (and not, for instance, the time needed for donors to reach thermal equilibrium with the polymer:dopant system, i.e. the kinetics of dedoping process).

Of course, additional experiments such as concentration-depth profiles of donors by SIMS measurements, conductivity versus temperature, and the impact of humidity would help to confirm the validity of our analysis.

3.5 CONCLUSION

The stability study presented in this chapter focused on the PBDTTT-c: $Mo(tfd\text{-}COCF_3)_3$ system. This choice was mainly driven by the higher conductivities obtained for this system, and also to investigate the potential of this promising *p*-dopant. The stability of the doped state was investigated under different atmospheres: argon (glovebox), anhydrous air, and ambient air. Regardless of the atmosphere, PBDTTT-c: $Mo(tfd\text{-}COCF_3)_3$ samples presented a surprising unstable doping characteristic, verified through a conductivity loss and a decrease in the doping related NIR absorptions. Hence, optical and electrical characterizations suggested the existence of a dedoping process, faster in the presence of humidity. Thus, *p*-doping instability seems linked to the presence of water-related species.

Through XPS analysis we showed that the dedoping process does not change the chemical state of PBDTTT-c, but clear signs of degradation are observed for $Mo(tfd\text{-}COCF_3)_3$. Interestingly, no signs of degradation were observed when exposing pure $Mo(tfd\text{-}COCF_3)_3$ molecules to water and air. Hence, we conclude that the mechanism behind the *p*-doping instability of PBDTTT-c: $Mo(tfd\text{-}COCF_3)_3$ involves a reactive dedoping process, where water-related species introduce donor levels in the *p*-doped layers that act as hole traps. The dopant degradation was therefore associated with a reactivity of the ionized donor towards the dopant anion.

All *p*-doped systems considered in this thesis presented unstable doping characteristics under ambient conditions, indicated by a conductivity loss and a decrease in the doping related NIR absorptions. For all four systems, the dedoping process was found to be faster in the presence of humidity.

Through simulations, following an argument given by Zuo *et al.*, we showed that donor levels lying at 0.3 – 0.4 eV above the HOMO of an OSC can act as hole traps and induce a dedoping process in the presence of water-related species. The influence of the layer thickness in the dedoping rate observed for PBDTTT-c:$Mo(tfd\text{-}COCF_3)_3$ can be explained by a diffusion model.

In conclusion, our results highlighted two important instability issues for *p*-doped conjugated polymers exposed to air: the dedoping of *p*-doped polymer hosts, associated with the presence of water-related hole traps, and the instability of ionized dopant molecules (verified for $Mo(tfd\text{-}COCF_3)_3$). In the reactive dedoping process proposed for PBDTTT-c:$Mo(tdf\text{-}COCF_3)_3$, the degradation of the dopant molecule is a consequence of the compensation process (ionized donors are reactive to ionized dopant). However, further analyses are required to clarify the impact of each mechanism, i.e. hole trapping and instability of dopant ions, on the degradation of the *p*-doped state.

3.6 REFERENCES

(1) Nicolai, H. T.; Kuik, M.; Wetzelaer, G. a. H.; Boer, B. de; Campbell, C.; Risko, C.; Brédas, J. L.; Blom, P. W. M. Unification of Trap-Limited Electron Transport in Semiconducting Polymers. *Nat. Mater.* **2012**, *11* (10), 882–887. https://doi.org/10.1038/nmat3384.

(2) Nikolka, M.; Nasrallah, I.; Rose, B.; Ravva, M. K.; Broch, K.; Sadhanala, A.; Harkin, D.; Charmet, J.; Hurhangee, M.; Brown, A.; Illig, S.; Too, P.; Jongman, J.; McCulloch, I.; Bredas, J.-L.; Sirringhaus, H. High Operational and Environmental Stability of High-Mobility Conjugated Polymer Field-Effect Transistors through the Use of Molecular Additives. *Nat. Mater.* **2017**, *16* (3), 356–362. https://doi.org/10.1038/nmat4785.

(3) Zuo, G.; Linares, M.; Upreti, T.; Kemerink, M. General Rule for the Energy of Water-Induced Traps in Organic Semiconductors. *Nat. Mater.* **2019**, *18* (6), 588–593. https://doi.org/10.1038/s41563-019-0347-y.

(4) Kotadiya, N. B.; Mondal, A.; Blom, P. W. M.; Andrienko, D.; Wetzelaer, G.-J. A. H. A Window to Trap-Free Charge Transport in Organic Semiconducting Thin Films. *Nat. Mater.* **2019**, *18* (11), 1182–1186. https://doi.org/10.1038/s41563-019-0473-6.

(5) Tietze, M. L.; Rose, B. D.; Schwarze, M.; Fischer, A.; Runge, S.; Blochwitz-Nimoth, J.; Lüssem, B.; Leo, K.; Brédas, J.-L. Passivation of Molecular N-Doping: Exploring the Limits of Air Stability. *Adv. Funct. Mater.* **2016**, *26* (21), 3730–3737. https://doi.org/10.1002/adfm.201505092.

(6) de Leeuw, D. M.; Simenon, M. M. J.; Brown, A. R.; Einerhand, R. E. F. Stability of N-Type Doped Conducting Polymers and Consequences for Polymeric Microelectronic Devices. *Synth. Met.* **1997**, *87* (1), 53–59. https://doi.org/10.1016/S0379-6779(97)80097-5.

(7) Cardona, C. M.; Li, W.; Kaifer, A. E.; Stockdale, D.; Bazan, G. C. Electrochemical Considerations for Determining Absolute Frontier Orbital Energy Levels of Conjugated Polymers for Solar Cell Applications. *Adv. Mater.* **2011**, *23* (20), 2367–2371. https://doi.org/10.1002/adma.201004554.

(8) Zhuo, J.-M.; Zhao, L.-H.; Png, R.-Q.; Wong, L.-Y.; Chia, P.-J.; Tang, J.-C.; Sivaramakrishnan, S.; Zhou, M.; Ou, E. C.-W.; Chua, S.-J.; Sim, W.-S.; Chua, L.-L.; Ho, P. K.-H. Direct Spectroscopic Evidence for a Photodoping Mechanism in Polythiophene and Poly(Bithiophene-Alt-Thienothiophene) Organic Semiconductor Thin Films Involving Oxygen and Sorbed Moisture. *Adv. Mater.* **2009**, *21* (46), 4747–4752. https://doi.org/10.1002/adma.200901120.

(9) Bobbert, P. A.; Sharma, A.; Mathijssen, S. G. J.; Kemerink, M.; Leeuw, D. M. de. Operational Stability of Organic Field-Effect Transistors. *Adv. Mater.* **2012**, *24* (9), 1146–1158. https://doi.org/10.1002/adma.201104580.

(10) Jacobs, I. E.; Wang, F.; Hafezi, N.; Medina-Plaza, C.; Harrelson, T. F.; Li, J.; Augustine, M. P.; Mascal, M.; Moulé, A. J. Quantitative Dedoping of Conductive Polymers. *Chem. Mater.* **2017**, *29* (2), 832–841. https://doi.org/10.1021/acs.chemmater.6b04880.

(11) Tietze, M. L.; Wölzl, F.; Menke, T.; Fischer, A.; Riede, M.; Leo, K.; Lüssem, B. Self-Passivation of Molecular n-Type Doping during Air Exposure Using a Highly Efficient Air-Instable Dopant. *Phys. Status Solidi A* **2013**, *210* (10), 2188–2198. https://doi.org/10.1002/pssa.201330049.

(12) Lin, X.; Wegner, B.; Lee, K. M.; Fusella, M. A.; Zhang, F.; Moudgil, K.; Rand, B. P.; Barlow, S.; Marder, S. R.; Koch, N.; Kahn, A. Beating the Thermodynamic Limit with Photo-Activation of n-Doping in Organic Semiconductors. *Nat. Mater.* **2017**, *16* (12), 1209–1215. https://doi.org/10.1038/nmat5027.

(13) Tietze, M. L.; Rose, B. D.; Schwarze, M.; Fischer, A.; Runge, S.; Blochwitz-Nimoth, J.; Lüssem, B.; Leo, K.; Brédas, J.-L. Passivation of Molecular N-Doping: Exploring the Limits of Air Stability. *Adv. Funct. Mater.* **2016**, *26* (21), 3730–3737. https://doi.org/10.1002/adfm.201505092.

(14) de Leeuw, D. M.; Simenon, M. M. J.; Brown, A. R.; Einerhand, R. E. F. Stability of N-Type Doped Conducting Polymers and Consequences for Polymeric Microelectronic Devices. *Synth. Met.* **1997**, *87* (1), 53–59. https://doi.org/10.1016/S0379-6779(97)80097-5.

(15) Vijayakumar, V.; Zhong, Y.; Untilova, V.; Bahri, M.; Herrmann, L.; Biniek, L.; Leclerc, N.; Brinkmann, M. Bringing Conducting Polymers to High Order: Toward Conductivities beyond 105 S Cm−1 and Thermoelectric Power Factors of 2 MW M−1 K−2. *Adv. Energy Mater.* **2019**, *9* (24), 1900266. https://doi.org/10.1002/aenm.201900266.

(16) Watts, K. E.; Neelamraju, B.; Ratcliff, E. L.; Pemberton, J. E. Stability of Charge Transfer States in F4TCNQ-Doped P3HT. *Chem. Mater.* **2019**, *31* (17), 6986–6994. https://doi.org/10.1021/acs.chemmater.9b01549.

(17) Nicolai, H. T.; Kuik, M.; Wetzelaer, G. a. H.; Boer, B. de; Campbell, C.; Risko, C.; Brédas, J. L.; Blom, P. W. M. Unification of Trap-Limited Electron Transport in Semiconducting Polymers. *Nat. Mater.* **2012**, *11* (10), 882–887. https://doi.org/10.1038/nmat3384.

(18) Cobet, C.; Gasiorowski, J.; Menon, R.; Hingerl, K.; Schlager, S.; White, M. S.; Neugebauer, H.; Sariciftci, N. S.; Stadler, P. Influence of Molecular Designs on Polaronic and Vibrational Transitions in a Conjugated Push-Pull Copolymer. *Sci. Rep.* **2016**, *6*, 35096. https://doi.org/10.1038/srep35096.

(19) Heimel, G. The Optical Signature of Charges in Conjugated Polymers. *ACS Cent. Sci.* **2016**, *2* (5), 309–315. https://doi.org/10.1021/acscentsci.6b00073.

(20) Oh, J. H.; Sun, Y.-S.; Schmidt, R.; Toney, M. F.; Nordlund, D.; Könemann, M.; Würthner, F.; Bao, Z. Interplay between Energetic and Kinetic Factors on the Ambient Stability of N-Channel Organic Transistors Based on Perylene Diimide Derivatives. *Chem. Mater.* **2009**, *21* (22), 5508–5518. https://doi.org/10.1021/cm902531d.

(21) E. Jacobs, I.; Cendra, C.; F. Harrelson, T.; Valdez, Z. I. B.; Faller, R.; Salleo, A.; J. Moulé, A. Polymorphism Controls the Degree of Charge Transfer in a Molecularly Doped Semiconducting Polymer. *Mater. Horiz.* **2018**, *5* (4), 655–660. https://doi.org/10.1039/C8MH00223A.

(22) Fujimoto, R.; Watanabe, S.; Yamashita, Y.; Tsurumi, J.; Matsui, H.; Kushida, T.; Mitsui, C.; Yi, H. T.; Podzorov, V.; Takeya, J. Control of Molecular Doping in Conjugated Polymers by Thermal Annealing. *Org. Electron.* **2017**, *47*, 139–146. https://doi.org/10.1016/j.orgel.2017.05.019.

(23) Hase, H.; O'Neill, K.; Frisch, J.; Opitz, A.; Koch, N.; Salzmann, I. Unraveling the Microstructure of Molecularly Doped Poly(3-Hexylthiophene) by Thermally Induced Dedoping. *J. Phys. Chem. C* **2018**. https://doi.org/10.1021/acs.jpcc.8b08591.

(24) Liao, H.-H.; Yang, C.-M.; Liu, C.-C.; Horng, S.-F.; Meng, H.-F.; Shy, J.-T. Dynamics and Reversibility of Oxygen Doping and De-Doping for Conjugated Polymer. *J. Appl. Phys.* **2008**, *103* (10), 104506. https://doi.org/10.1063/1.2917419.

(25) Kiefer, D.; Giovannitti, A.; Sun, H.; Biskup, T.; Hofmann, A.; Koopmans, M.; Cendra, C.; Weber, S.; Anton Koster, L. J.; Olsson, E.; Rivnay, J.; Fabiano, S.; McCulloch, I.; Müller, C. Enhanced N-Doping Efficiency of a Naphthalenediimide-Based Copolymer through Polar Side Chains for Organic Thermoelectrics. *ACS Energy Lett.* **2018**, *3* (2), 278–285. https://doi.org/10.1021/acsenergylett.7b01146.

(26) Soon, Y. W.; Cho, H.; Low, J.; Bronstein, H.; McCulloch, I.; Durrant, J. R. Correlating Triplet Yield, Singlet Oxygen Generation and Photochemical Stability in Polymer/Fullerene Blend Films. *Chem. Commun.* **2013**, *49* (13), 1291–1293. https://doi.org/10.1039/C2CC38243A.

(27) Perthué, A.; Fraga Domínguez, I.; Verstappen, P.; Maes, W.; Dautel, O. J.; Wantz, G.; Rivaton, A. An Efficient and Simple Tool for Assessing Singlet Oxygen Involvement in the Photo-Oxidation of Conjugated Materials. *Sol. Energy Mater. Sol. Cells* **2018**, *176*, 336–339. https://doi.org/10.1016/j.solmat.2017.10.019.

(28) Tang, K.; McFarland, F. M.; Travis, S.; Lim, J.; Azoulay, J. D.; Guo, S. Aggregation of P3HT as a Preferred Pathway for Its Chemical Doping with F4-TCNQ. *Chem. Commun.* **2018**, *54* (84), 11925–11928. https://doi.org/10.1039/C8CC05472J.

(29) Neelamraju, B.; Watts, K. E.; Pemberton, J. E.; Ratcliff, E. L. Correlation of Coexistent Charge Transfer States in F4TCNQ-Doped P3HT with Microstructure. *J. Phys. Chem. Lett.* **2018**, *9* (23), 6871–6877. https://doi.org/10.1021/acs.jpclett.8b03104.

(30) Wantz, G.; Szymanski, R.; Vongsaysy, U.; Hirsch, L.; Chambon, S. Organic Photovoltaics, from Lab to Fab. In *MRS Fall Meeting 2019*; Boston, United States, 2019.

(31) Qi, Y.; Sajoto, T.; Kröger, M.; Kandabarow, A. M.; Park, W.; Barlow, S.; Kim, E.-G.; Wielunski, L.; Feldman, L. C.; Bartynski, R. A.; Brédas, J.-L.; Marder, S. R.; Kahn, A. A Molybdenum Dithiolene Complex as P-Dopant for Hole-Transport Materials: A Multitechnique Experimental and Theoretical Investigation. *Chem. Mater.* **2010**, *22* (2), 524–531. https://doi.org/10.1021/cm9031623.

(32) A. Dai. Creating Highly Efficient Carrier Injection or Collection Contacts via Soft Contact Transfer Lamination of P-Doped Interlayers. Princeton University 2015.

(33) Turner, N. H.; Single, A. M. Determination of Peak Positions and Areas from Wide-Scan XPS Spectra. *Surf. Interface Anal.* **1990**, *15* (3), 215–222. https://doi.org/10.1002/sia.740150305.

(34) Richard, J.; Benayad, A.; Colin, J.-F.; Martinet, S. Charge Transfer Mechanism into the Chevrel Phase Mo6S8 during Mg Intercalation. *J. Phys. Chem. C* **2017**, *121* (32), 17096–17103. https://doi.org/10.1021/acs.jpcc.7b03979.

(35) Eisenberg, R.; Gray, H. B. Noninnocence in Metal Complexes: A Dithiolene Dawn. *Inorg. Chem.* **2011**, *50* (20), 9741–9751. https://doi.org/10.1021/ic2011748.

(36) Wagner, C. D.; Riggs, W. M.; Davis, L. E.; Moulder, J. F.; Muilenburg, G. E. *Handbook of X-Ray Photoelectron Spectroscopy*; Perkin-Elmer: Eden Prairie, MN, 1979.

(37) Fleisch, T. H.; Mains, G. J. An XPS Study of the UV Reduction and Photochromism of MoO3 and WO3. *J. Chem. Phys.* **1982**, *76* (2), 780–786. https://doi.org/10.1063/1.443047.

(38) Mohapatra, S. K.; Zhang, Y.; Sandhu, B.; Fonari, M. S.; Timofeeva, T. V.; Marder, S. R.; Barlow, S. Synthesis, Characterization, and Crystal Structures of Molybdenum Complexes of Unsymmetrical Electron-Poor Dithiolene Ligands. *Polyhedron* **2016**, *116*, 88–95. https://doi.org/10.1016/j.poly.2016.04.025.

(39) Fujimoto, R.; Yamashita, Y.; Kumagai, S.; Tsurumi, J.; Hinderhofer, A.; Broch, K.; Schreiber, F.; Watanabe, S.; Takeya, J. Molecular Doping in Organic Semiconductors: Fully Solution-Processed, Vacuum-Free Doping with Metal–Organic Complexes in an Orthogonal Solvent. *J. Mater. Chem. C* **2017**, *5* (46), 12023–12030. https://doi.org/10.1039/C7TC03905K.

(40) Le, T. H.; Nafady, A.; Qu, X.; Martin, L. L.; Bond, A. M. Detailed Electrochemical Analysis of the Redox Chemistry of Tetrafluorotetracyanoquinodimethane TCNQF4, the Radical Anion [TCNQF4] •−, and the Dianion [TCNQF4]2– in the Presence of Trifluoroacetic Acid. *Anal. Chem.* **2011**, *83* (17), 6731–6737. https://doi.org/10.1021/ac201373d.

(41) Watts, K. E.; Clary, K. E.; Lichtenberger, D. L.; Pemberton, J. E. FTIR Spectroelectrochemistry of F4TCNQ Reduction Products and Their Protonated Forms. *Anal. Chem.* **2020**, *92* (10), 7154–7161. https://doi.org/10.1021/acs.analchem.0c00615.

(42) Hou, J.; Chen, H.-Y.; Zhang, S.; Chen, R. I.; Yang, Y.; Wu, Y.; Li, G. Synthesis of a Low Band Gap Polymer and Its Application in Highly Efficient Polymer Solar Cells. *J. Am. Chem. Soc.* **2009**, *131* (43), 15586–15587. https://doi.org/10.1021/ja9064975.

GENERAL CONCLUSIONS AND OUTLOOKS

In this thesis, we investigated the molecular doping of overall disordered polymer semiconductors and the stability of the doped state under different atmospheres, i.e. in the presence of oxygen and water-related species. The main motivation of this thesis was to infer the compatibility of *p*-doped semiconducting polymers with the industrial development of flexible electronic devices, where performance, stability, and scalability are essential aspects.

In terms of materials, we have chosen PBDTTT-c and RRa-P3HT as host polymers. The former belongs to a class of donor:acceptor polymers with promising performances in organic solar cells and photodetectors. RRa-P3HT was selected as a reference polymer. Regarding the *p*-dopant, two molecules were chosen: the planar reference *p*-dopant, F4TCNQ, and the bulky soluble derivative of $Mo(tfd)_3$, $Mo(tfd\text{-}COCF_3)_3$, which presented better stability against dopant diffusion. Thus, this thesis studied four polymer:dopant systems: PBDTTT-c: $Mo(tfd\text{-}COCF_3)_3$, RRa-P3HT: $Mo(tfd\text{-}COCF_3)_3$, PBDTTT-c:F4TCNQ, and RRa-P3HT:F4TCNQ.

In the **first chapter**, we presented an extensive literature overview of the potential and challenges of OSCs and the interest of the doping process. A special focus was given to the fundamental differences between the commercialized doping process of inorganic semiconductor, and the actual understanding of the doping process in OSCs.

In the **second chapter**, we studied the initial state of pristine materials and doped layers. To allow for a better understanding of the changes induced by the doping process, we characterized the optical, electrical, electrochemical, and structural properties of pristine materials. The doping protocol was optimized with the aim of identifying critical parameters and limitations of the studied materials, but also to achieve a controlled doping process. We compared two doping techniques used for solution-processed conjugated polymers. In the doped state, we investigated the evolution of the optical, electrical and structural properties upon the introduction of molecular *p*-dopants, aiming to understand the doping signatures of each polymer:dopant system before investigating their stability under different atmospheres.

No difficulties related to a solubility loss or film quality were observed when doping with the co-processing technique. Regarding the process parameters, only the dopant concentration presented a visible influence on the final properties of doped layers. The stirring conditions (time and temperature) of doped solutions presented no clear impact. In other words, our results showed that no rigorous control of the doping conditions is needed when doping disordered polymer host with the co-processing technique, which is an advantage in terms of industrialization. We showed that sequential processing is also a viable technique for doping PBDTTT-c layer of different thicknesses with $Mo(tfd\text{-}COCF_3)_3$, despite the bulky nature of this dopant molecule. For the materials used in this thesis, we conclude that both technique are adapted and similar maximum conductivities were obtained.

Thermal annealing presented to be a critical processing step for all *p*-doped systems studied in this thesis. F4TCNQ and $Mo(tfd\text{-}COCF_3)_3$-doped layers presented unstable doping signatures

after short thermal treatments above 100°C. Thermal dedoping might be the mechanism behind the thermal instability of our *p*-doped layers.

The maximum conductivity (σ_{max}) reached in this thesis was 0.3 S.cm^{-1} for PBDTTT-c: Mo(tfd-$COCF_3)_3$ (15 mol% dopant). The σ_{max} achieved with co-processed and sequentially processed layers were very close. The UV-Vis-NIR spectra showed no complete bleaching of the neutral polymers (π-π* absorption), indicating that there is still a considerable fraction of undoped polymer chains and, consequently, potential for improvement. All four *p*-doped systems presented a saturation of conductivity and NIR absorptions beyond a certain dopant concentration, and even slight conductivity decreases, which were associated with an increase of molecular disorder due to an excess of dopant.

Higher conductivities and NIR absorption were obtained when doping with Mo(tfd-$COCF_3)_3$ compared to F4TCNQ, in agreement with a stronger oxidizing potential measured by CV (-5.3 eV vs. -5.1 eV). Nevertheless, our results showed that the planarity of the polymer:dopant system is also an important parameter controlling the doping process. From optical and electrical characterizations, we suggest that ion-pairs formation is the mechanism governing the doping of PBDTTT-c: Mo(tfd-$COCF_3)_3$, RRa-P3HT:F4TCNQ, and RRa-P3HT: Mo(tfd-$COCF_3)_3$.

The stability of the *p*-doped state is investigated in **the third chapter**. First, we presented a state-of-art overview of the presence of traps in OSCS, with a special focus on hole traps. The stability of the doped state was verified by monitoring the optical and electrical doping signatures under argon, anhydrous air, and ambient air. This chapter focused on PBDTTT-c:Mo(tfd-$COCF_3)_3$, which has shown the highest conductivities. XPS analyses were performed to analyze the chemical state of doped layers before and after air exposure. Simulations were carried out to verify the impact of donor species on the stability of the *p*-doped state. Last, a diffusion model was developed to explain the impact of the layer thickness on the stability of doped layers.

Regardless of the atmosphere, PBDTTT-c: Mo(tfd-$COCF_3)_3$ samples presented unstable doping signatures, evidenced by a conductivity decrease and a recovery of pristine UV-vis-NIR absorption signatures (π-π* absorption). Even under a controlled atmosphere (argon), the conductivity was not stable over time. Optical and electrical characterizations suggest the existence of a dedoping process, accelerated in the presence of ambient humidity. The layer thickness presented an important impact on the dedoping rate, considerably faster for thinner layers. XPS results presented signatures of degradation of the dopant molecule, whereas the polymer showed no evident changes in the chemical state after the dedoping process. Thus, we suggested that the *p*-doping instability of PBDTTT-c:Mo(tfd-$COCF_3)_3$ layers is due to reactive dedoping processes.

The stability study was extended to RRa-P3HT: Mo(tfd-$COCF_3)_3$, RRa-P3HT:F4TCNQ and PBDTTT-c:F4TCNQ. All *p*-doped systems presented unstable doping signatures under ambient conditions, with accelerated degradation in the presence of humidity. Therefore, our experimental results suggested that water-related hole traps are a common cause of unstable *p*-doping under different atmospheres.

Hence, two important instability issues have been highlighted for *p*-doped conjugated polymers exposed to air: the dedoping of *p*-doped polymer hosts, associated with the presence of water-related hole traps, and the instability of ionized dopant molecules. Further analyses are required to clarify the impact of each mechanism, i.e. hole trapping and instability of dopant ions, on the degradation of the *p*-doped sate. Nevertheless, to obtain stable *p*-doped layers, our results underlined the importance of verifying not only the air stability of pristine but also ionized polymer and *p*-dopants.

Simulations showed that the presence of donor (hole) traps above the HOMO level of the polymer host can explain the dedoping process experimentally observed, where the positive charge of ionized donor traps balance the negative charge of ionized *p*-dopants. The water traps recently reported by Zuo *et al.* for several semiconducting polymers can explain the instability of the *p*-doped state observed in this thesis. The proposed diffusion model offers a possible explanation for the impact of the layer thickness on the dedoping rate of *p*-doped polymers.

Finally, the existing literature on the stability of p–doped OSCs focused mainly on dopant molecules, where the diffusion and the thermal stability were highlighted as critical issues. Here, we highlighted an instability related to the presence of hole traps in polymer hosts, where the dopant itself might not directly influence the dedoping process. However, our results showed that the stability of dopant ions might also be a critical aspect controlling the stability of the *p*-doped state. These main conclusions are particularly important for the future application of *p*-doped layer in organic devices. The instability of the *p*-doping effect in the presence of water-related species would introduce several complications for the fabrication, such as controlling the atmosphere during the whole process as well as ensuring the quality of the encapsulation of the final device.

However, complementary stability studies are necessary to build a global picture of the instability of free holes in OSCs, their origins, position, trapping mechanism, etc. The existing systematic investigations on the presence of hole traps in pristine conjugated polymers lead to divergent conclusions regarding their positions and the trapping mechanism. Besides, the stability of dopant ions under working conditions is also an important aspect to ensure a stable doping effect that should be considered when synthesizing molecular *p*-dopants.

Finally, only single doped layers were investigated during this study. The impact of underlined degradation mechanisms in the performance of encapsulated devices, where doped layers are used as hole transport layers or for thermoelectric generators, is still to be verified.

APPENDIX A: EXPERIMENTAL SECTION

Several characterization techniques have been used when studying doped OSCs, in terms of electrical, structural, and chemical properties. This section presents the main characterization techniques used in this thesis: UV-vis, CV, XPS, TLM, and GIWAXS. The basic principles of each technique are briefly recalled before presenting the characterization setup, the instrumentation, and the data interpretation. For EPR, which was only used punctually, the instrumentation is given at the end of this section.

UV–Vis-NIR spectroscopy

Atoms and molecules exist in several defined energy states or levels in a material. From Planck-Einstein's equation we know that an electron can be transferred from one energy level to another by the absorption or emission of quantized amounts of energy, i.e. photons[1]:

$$E = h\nu = h\frac{c}{\lambda} \qquad \textbf{Equation A.1}$$

where h is the Planck constant and ν is the frequency of the photon, which is defined by the ratio between the speed of light in vacuum (c) and the wavelength of the photon (λ). If the incident photon has an energy equal or higher than a given electronic transition in the material, it may be absorbed and consequently excite an electron. Ultraviolet-visible-near infrared (UV-Vis-NIR) spectroscopy is a technique that measures the light absorption of materials in the ultraviolet (100 nm - 400 nm), visible (400 nm - 750 nm) and near-infrared (750 nm – 2,500 nm) range.

In this work, All UV-Vis and UV-Vis-NIR measurements were performed under ambient atmospheres. Regarding the instrumentation, the UV-Vis measurements (from 250 to 1050 nm) were carried out on an Agilent Cary 60 spectrophotometer. The UV-Vis-NIR (from 250 to 2500 nm) measurements were carried out on a PerkinElmer Lambda 950 spectrophotometer with an integrating sphere.

The solution samples were measured in quartz cuvettes (175−2700 nm) with path lengths of 1 mm. The sample cuvette holder temperature was fixed at 25°C using an Agilent Peltier temperature controller. The UV-Vis spectra of solutions are presented in absorbance vs. wavelength, which is more convenient than transmittance since it is directly proportional to the concentration of the solution (Beer-Lambert Law):

$$Absorbance = log\frac{1}{Tranmittance} = \varepsilon lc \qquad \textbf{Equation A.2}$$

where ε is the absorptivity of the material, l is the optical path length and c the concentration. The transmittance corresponds to the ratio between the incident and the transmitted radiation. Note that when measuring UV-Vis spectra of solutions, the reflection is kept at a minimum and therefore overlooked.

When measuring the UV-Vis-NIR of thin layers, the reflection is taken into account since the latter increases significantly with the layer thickness, and this parameter is intentionally varied in this thesis. Therefore, when characterizing thin layers, we measure the total transmission(T) and the total reflection (R) of the samples with the help of an integrating sphere to calculate the total absorption (A) using the following relation:

$$A\ (\%) = 100 - T - R \qquad \textbf{Equation A.3}$$

The thin layers were prepared on glass substrates, inside the glovebox, as described in the respective sections. Last, since UV-Vis-NIR spectra are recoded under ambient atmosphere, the samples were measured directly after leaving the glovebox, limiting the air exposure to a few minutes.

Cyclic voltammetry

Determining the HOMO and LUMO levels is an important step governing the choice of potential polymer:dopant systems. There are mainly two techniques used to characterize experimentally HOMO and LUMO levels of OSCs: cyclic voltammetry (CV) and a combination of photoemission and inverse photoemission spectroscopy (PES, IPES). There is a permanent discussion on which techniques is more suitable for determining HOMO and LUMO levels of OSCs[2,3]. Generally speaking, each of these technique is susceptible to experimental difficulties and can be more or less suitable depending on the system of interest.

In this thesis, we chose the CV technique, as the measurement conditions are closer to the real conditions (doping is performed in solution). Most importantly, all measurements are performed under the same conditions, with the same references and using the same extraction technique to estimate the energy levels. In other words, the obtained values are comparable. Note that the deviation from the exact absolute values is not an issue here, since our goal is to verify their relative positions, e.g. if the HOMO of the polymer is higher or lower than the LUMO of the dopant.

The CV technique consists of oxidizing and reducing the materials electrochemically, not chemically as for the doping process of OSCs. Nevertheless, both redox processes use the energy difference between two materials as the driving force for the redox reactions. In chemical redox reactions, molecules are used as reductant and oxidant whereas in electrochemical redox reaction an external power source (potentiostat) is used to modulate the energy of electrons in the working electrode. In other words, electrochemical redox processes allow increasing the driving force until an electron transfer becomes favorable[4], whereas for chemical redox processes, increasing the driving force requires changing the molecules.

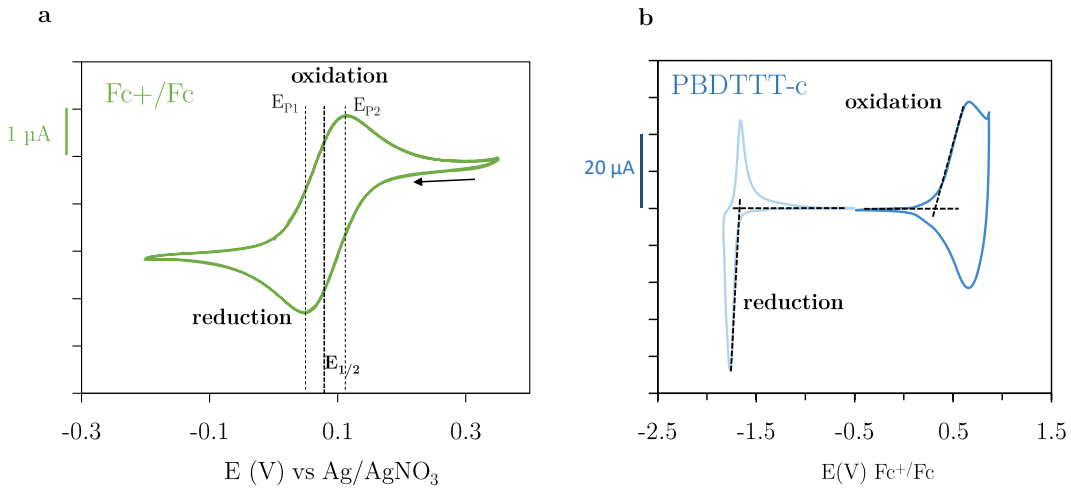

Figure A.1 - Example of redox waves measured for Ferrocene (a) with half wave potential ($E_{1/2}$) as extraction technique and PBDTTT-c (b) with tangent extraction technique.

Figure A.1 presents examples of voltamograms with the resulting redox waves that are used to extracted redox potentials, i.e. the potential at which oxidation or reduction processes occur. To convert the redox potentials (V) into energy values relative to the vacuum level (eV) a reference material is used, which presents a known redox potential in eV. In this thesis, we used Ferrocenium/Ferrocene (Fc^+/Fc), one of the redox couples recommended by the International Union of Pure and Applied Chemistry (IUPAC) for reporting energy levels in nonaqueous solvents[5]. The reversible redox waves of Ferrocenium/Ferrocene (Fc^+/Fc) measured in this work are presented in **Figure A.1**a. For completely reversible redox waves, the redox potential can be extracted by the half-wave technique ($E_{1/2}$) that consists in extracting the halfway potential between the anodic and cathodic peak as represented in **Figure A.1**a[4]. The obtained value is then used to calibrate the voltammogram with respect to Fc^+/Fc, i.e. the $E_{1/2}$ of Fc^+/Fc is set as zero.

Figure A.1b presents the oxidation and reduction waves of PBDTTT-c with respect to Fc^+/Fc. Note that the waves are only partially reversible. In this case, the extraction of the redox potentials is done with the tangent technique that consists in estimating the onset potential, defined as the potential at which the injection of holes to the HOMO or electrons to the LUMO initiates. With the onset potential, the following relations were used to calculate the electron affinities (E_{EA}) and ionization energies (E_{IE}):

$$E_{EA}\,(eV) \approx 4.8 + E_{red}^{onset}(V \text{ vs } Fc^+/Fc). \qquad \textbf{Equation A.4}$$

$$E_{IE}\,(eV) \approx 4.8 + E_{ox}^{onset}\,(V \text{ vs } Fc^+/Fc). \qquad \textbf{Equation A.5}$$

where 4.8 eV refers to the vacuum energy level of Fc^+/Fc [6]. As highlighted by Cardona *et. al* there is, however, little consensus about the correct vacuum energy level of the Fc^+/Fc redox couple, where values varying from 4.4 to 5.4 eV can be found in the literature[6].

Regarding the characterization setup, cyclic voltammetry (CV) measurements were performed with a three-electrode setup, consisting of a platinum electrode as the working electrode (ALS, diameter 1 mm), a platinum wire as the counter electrode, and a non-aqueous $Ag/AgNO_3$ electrode as pseudo-reference. PBDTTT-c, RRa-P3HT, and F4TCNQ measurements were performed in freshly distilled acetonitrile and $Mo(tfd\text{-}COCF_3)_3$ in freshly distilled THF (better solubility). Tetrabutylammonium hexafluorophosphate is used as supporting electrolyte (NBu_4PF_6, Electrochemical grade, Sigma Aldrich, 0.1 M), dried under primary vacuum at room temperature. The dopants were analyzed in solution (2 mM) and the polymers were drop-casted on the working electrode (from 4.7 $g.L^{-1}$ solutions in o-Xylene) and analyzed as a film. The voltammograms were recorded at a scan rate of 50 $mV.s^{-1}$ and calibrated with respect to the half-wave oxidation potential of ferrocene (Fc^+/Fc),.

Grazing incidence wide angle X-ray scattering

Grazing incidence wide angle X-ray scattering (GIWAXS) refers to an x-ray diffraction method, where the incident X-ray beam makes a small angle (typically $\omega < 1°$) with the surface of the sample. This is particularly advantageous when characterizing thin films since it limits the penetration depth of the X-rays into the sample and, consequently, avoids and/or reduces the contribution of the substrate. Additionally, using small angle increases the surface sensitivity since the beam irradiates a large area of the film's surface. By varying the incidence angle, one can change the penetration depth of the X-rays. This is also useful for discriminating if an observed peak originates from the substrate or from the sample.

Regarding the detection, *wide-angles* (2Θ from 3° to 60°) are commonly used, corresponding to small distances (from approximately 3.0 Å (30°) to 29 Å (3°)). The penetration depth depends on the electronic density of the material and, therefore will vary for each material.

The measurements were performed using a laboratory Rigaku Smartlab diffractometer (Cu, $\lambda_{K\alpha}$ = 1.54184 Å, 8 kV). The interplanar distances were extracted using Bragg's law with $\lambda_{Cu(K\alpha)}$ = 1,54184 Å:

$$\lambda = 2d\sin(\Theta) \qquad \textbf{Equation A.6}$$

Diffractograms are represented as a function of the scattering vector (q):

$$q = 4\pi \sin(\Theta)/\lambda \qquad \textbf{Equation A.7}$$

where 2Θ is the angle between the incident beam and the detector measuring the scattered intensity. The direction of the scattering vector defines the orientation probed, where q_{xy} represents in-plane scans and q_z out-of-plane scans (**FigureA.2**a). In both cases, a precise alignment of the sample with respect to the primary and secondary optical paths has to be performed prior to each measurement. The sample is placed parallel to the ground. In the out-of-plane scan, the detector rotates vertically, probing the distances more or less perpendicular to the sample's surface, as illustrated in **FigureA.2**a (left). In the in-plane scan, the detector rotates horizontally, probing the planes perpendicular to the surface (**FigureA.2**a, right).

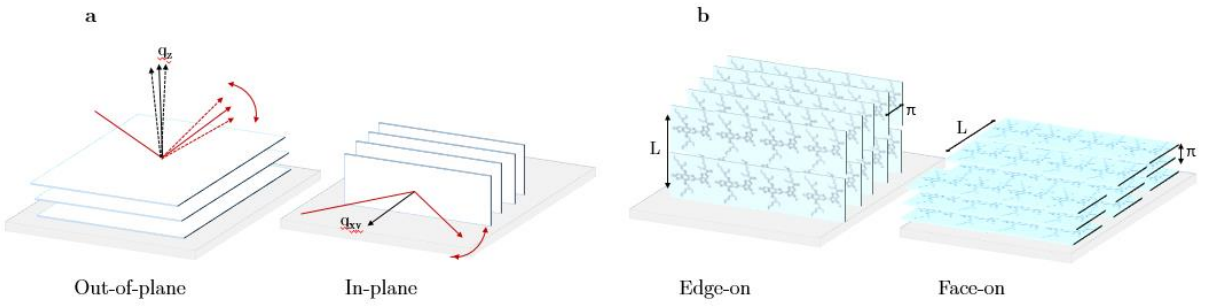

Figure A.2 - Out-of-plane and in-plane GIWAXS measurements. Illustration of the orientations probed depending on the scattering geometry (a) and representation of face-on and edge on orientations (b).

For organic semiconductors, GIWAXS diffractograms reveal the organization of polymer chains in thin films. Ordered regions are characterized by the interactions between polymer chains that result in π-stacks and side chain lamellar stacks. Depending on the orientation of the ordered domains, two terms are currently used in the literature: "face-on" and "edge-on". In edge-on orientation, the conjugated backbone axis and π-stacking axis are parallel to the substrate, and the alkyl side chains (lamellar stacking) are perpendicular to the substrate plane (**Figure A.2**b**,** left). Contrary, in the face-on orientation, the conjugated backbone axis and alkyl-stacking axis are parallel to the substrate, and consequently the π-stacking axis is perpendicular to the substrate (**Figure A.2**b, right). Thus, if the π-π stacking characteristics distance is observed in the out-of-plan scan and the lamellar stacking in the in-plane scan, the orientation will be face-on. Inversely, the orientation will be edge-on. This example is for completely anisotropic films. Isotropy (amorphous) and preferential orientation are also possible.

GIWAXS measurements are carried out under an ambient atmosphere for pristine PBDTTT-c and under argon atmosphere (inside a graphite dome) for doped samples. All sample preparations were carried out inside the glovebox with the conditions described in the respective sections.

The diffractograms were fitted using the HighScore software. Pseudo Voigt functions were used to fit the peaks. Different background functions were used according to the peak region, as illustrated in **Figure A.3**. For the out-of-plane peak at smaller diffraction angles (**Figure A.3**a), the polynomial background consisted in a reciprocal function (1/x) with one coefficient and three constants. The shape factor of this peak was fixed to zero. For the in-plane peak at smaller diffraction angles and the π-stacking peak (out-of-plane, **Figure A.3**b), the polynomial background consisted in a reciprocal function (1/x) with one coefficient and one constant. The shape factor of these peaks was fixed at 1.

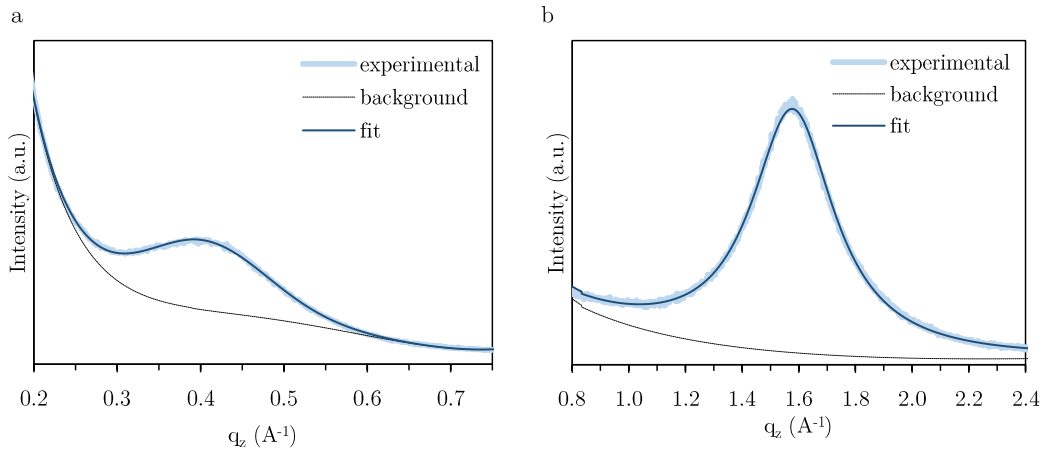

Figure A.3 – Representation of the fitting procedure for the GIWAXS peaks at lower (a) and higher (b) diffraction angles.

These measurements were possible thanks to Dr. Stéphanie Pouget, to whom I am very grateful.

Transmission Length measurements (TLM)

Different techniques are used in the literature to measure the conductivity of OSCs. This characteristic is a direct way of verifying the improvement in the transport properties upon doping. The most commonly used technique is the four-point-probe. This technique consists of passing a current through two outer probes, whilst simultaneously measuring the potential produced across two inner probes. Thus, the sheet resistance (R_s) of the sample can be deduced while minimizing the effects of contact resistance. The sheet resistance is a measure of the resistance of thin films that are nominally uniform in thickness (**Equation A.8**). The advantage of using the four-point probe method is that it ignores the contact resistance between the probe and material. For more details see Van der Pauw method[7].

$$R_{sheet} = \frac{\rho}{d} \qquad \textbf{Equation A.8}$$

However, when measuring thin semiconducting polymer layers (10-100nm) at low doping ratios or pristine, the R_s is often out of the measurement range (high resistivity combined to the small thicknesses). Hence, the four-point-probe technique is not adapted for our study.

Transmission Line or Transfer Length Measurements (TLM) was used in this work. This technique is commonly employed to determine the contact resistance between metal and semiconductors in electronic devices[8]. Nevertheless, it also allows extracting the conductivity. Basically, this technique consists of applying a voltage between two contacts and measure the current that flows from one contact to another through a semiconductor. The metal/semiconductor interface should form an ohmic contact. In terms of materials and setup, TLM has also the advantage of being a simple technique that only requires current-voltage measurements, i.e. a source meter and probe tips.

When plotting the current as a function of the voltage (which should be a straight line), the inverse of the slope will give us the total resistance (R_{total}) of de measured sample (Ohm's law).

R_{total} is a linear combination of the contact resistance of both metal/semiconductor interfaces ($R_{contact}$) and the resistance of the semiconductor ($R_{semiconductor}$) in-between the contacts:

$$R_{total} = R_{semiconductor} + 2R_{contact} \qquad \textbf{Equation A.9}$$

The resistance of the metal (R_{metal}) was ignored in **Equation A.9** since in most situations $R_{contact} \gg R_{metal}$. The semiconductor resistance is defined as:

$$R_{semiconductor} = R_{sheet}\frac{L}{W} \qquad \textbf{Equation A.10}$$

Where, L corresponds to the channel length and W to the contact width. Thus, R_{total} can be written as:

$$R_{total} = R_{sheet}\frac{L}{W} + 2R_{contact} \qquad \textbf{Equation A.11}$$

Equation A.11 corresponds to a straight line equation. Hence, TLM measurements consist in measuring the R_{total} of different L/W ratios (by varying the length and/or width of the area between the contact). When plotting R_{total} versus L/W a straight line should be obtained, with the slope of the line being R_{sheet} and the intercept of the line y-axis being $2R_{contact}$ (**Figure A.4**a). Hence, R_{sheet} as well as $R_{contact}$ can be determined from this technique. Finally, the conductivity (σ) of the semiconductor is calculated with the following expression:

$$\sigma = \frac{1}{R_{sheet}\,d} \qquad \textbf{Equation A.12}$$

Note that the contacts can be adapted in this technique. To allow measuring the conductivity of resistive and thin materials, large contact width compared to the channel length are commonly used.

a **b**

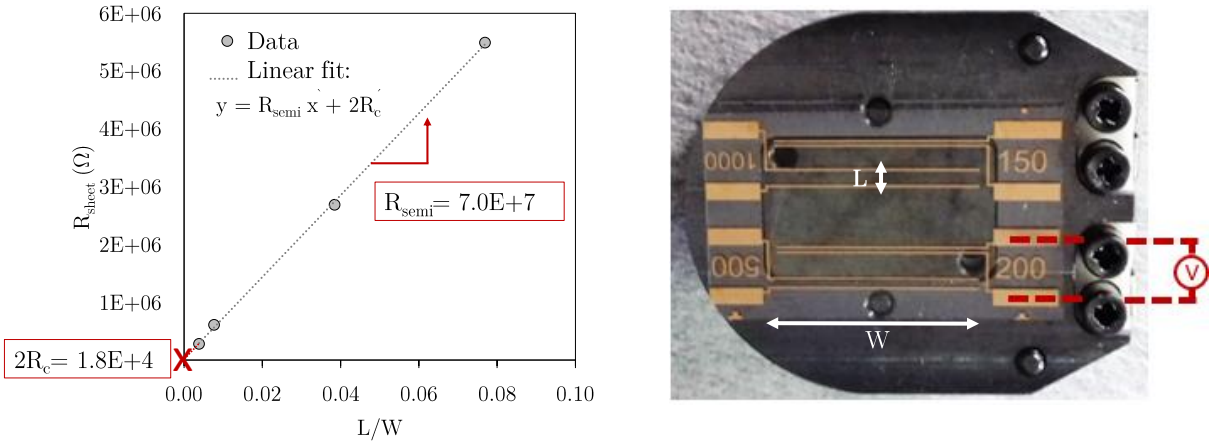

Figure A.4 – Picture of a TLM sample with four channels with a same contact width (W) and different channel length (L), for instance 150, 200, 500, and 1000µm (a). Representation of the extraction technique used for TLM samples (b).

When comparing TLM to the four-point-probe technique, instead of measuring the R_{sheet} with probes presenting an extremely small contact area, TLM measures R_{total} where the L/W ratio (the contact area) can be optimized to increase the current that passes through the semiconducting layer. Hence, TLM allows measuring the conductivity of resistive and thin materials that cannot be measured with the four-point-probe technique. Both techniques measure in-plane conductivities.

TLM samples were prepared on patterned flexible PEN (12 µm) /gold (30 nm) substrates, presenting a channel width of ca. 14,500 µm and four different channel lengths, varying from 50 to 1000 µm (**Figure A.4**b). Gold contacts were chosen due to their WF of ca. -5 eV, to allow ohmic contact with PBDTTT-c (HOMO -5.1 eV) and RRa-P3HT (HOMO -5.3 eV). Pristine and doped polymer layers were prepared by spin coating inside the glovebox with the conditions given in the respective sections. Current-voltage (I-V) measurements were performed in the dark and inside the argon-filled glovebox with a Keithley 2400 SourceMeter. An identical setup was used for the measurement under ambient air.

To characterize the stability of the electrical conductivity under ambient air, freshly prepared samples were exposed to air (dark) and the I-V curve of a selected contact was automatically collected over time. The results are plotted in current at 1V (arbitrarily chosen) versus time.

X-ray photoelectron spectroscopy

X-ray Photoelectron Spectroscopy (XPS) is one of the most established methods for determining the elemental composition and the chemical state of solid surfaces and thin films. Therefore, it is a powerful tool for studying degradation mechanisms[9,10]. For this reason, we chose XPS analysis for our stability study of doped conjugated polymers, to help to correlate chemical changes with degradation paths. Below, the principles of this technique are briefly reviewed and the instrumentation details are given.

XPS analysis consists in irradiating samples with X-ray photons and collecting the generated photoelectrons, which will carry valuable information concerning the chemical environment of the electron. Photoelectrons can be generated if the energy of the incident X-ray photon is higher than the binding energies (E_{bin}) of electrons in an atom. In this case, a photoelectron is ejected/emitted from the sample into vacuum and another electron from the outer shell will recombine to take the lower energetic state of the ejected electron. The photoelectrons are collected/captured by a detector and their kinetic energy is recorded. From the following basic XPS equation, the Ebin of the photoelectron can be calculated[11].

$$E_{bin} = h\nu - E_{kin} - \Phi \qquad \textbf{Equation A.13}$$

where Φa is the spectrometer work function, E_{kin} the measured kinetic energy and hν the energy of the X-ray photons, where φa and hν are known.

A schematic representation of the fundamental processes occurring during XPS analyses is illustrated in **Figure A.5**. Note that the sample is electrically connected to the spectrometer

and properly grounded so that the sample and spectrometer Fermi levels align. Therefore, the knowledge of the sample work function is not necessary.

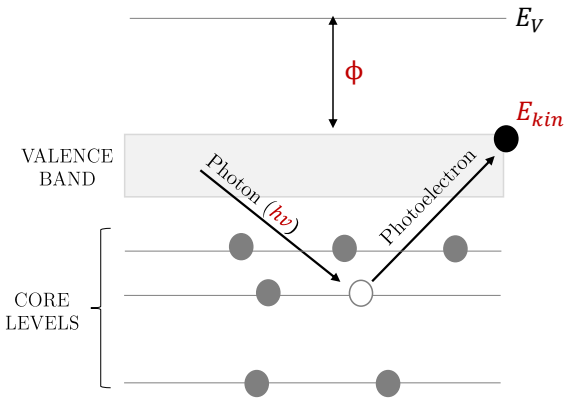

Figure A.5 - Representation of the fundamental processes occurring during XPS analyses.

Since the kinetic energy of the photoelectrons (E_{kin}) carry the elemental information of interest, it is important to assure that photoelectrons will reach the detector unaltered. Therefore, UHV is needed for precise analysis. Besides, it is important to have a monochromatic X-ray source, to avoid energy variation of the incident photons (variation of hν). Note that XPS analyses are surface sensitive, meaning that even though the X-ray penetrates several micrometers of the sample, the measured information corresponds to photoelectrons emitted from the first few nanometers. This is correlated to the mean free path available for electrons to leave the sample before losing the available kinetic energy to the environment. This value is dependent on the materials but is globally around 10 nm[11].

Assigning elements from binding energy is possible because the electron shell structure of each element is known, and consequently the binding energy of each electron. Differences in core level binding energies for different elements arise from the interaction of the electrons with the nucleus. Higher atomic number results in higher attraction with the nucleus and therefore higher binding energies. Thus, the measured binding energy corresponds to a specific electron, in a specific orbital of a specific element.

XPS spectra present sharp peaks corresponding to specific electrons from particular levels of particular atoms. The spectra are represented in signal versus binding energy, from the higher to lower binding energy and the detected photoelectrons are named after the orbital that they originate from (1s, 2s, 2p …). Several other artifacts may be present in XPS spectra. In the following, we briefly describe those observed in our measurements: chemical shift, spin-orbit splitting, and satellite peaks. For more information see[12].

Chemical shifts allow assigning peaks not only to elements but also to chemical bonds, as slight shift in E_{bin} are observed depending on the chemical environment. Generally, atoms losing electrons or having a smaller electrons density due to chemical interaction will shift to higher binding energies and vice versa.

Spin-orbit splitting is an artifact observed for electrons originating from orbitals with quantum number $l > 0$, i.e. all orbitals except the *s*, characterized by a splitting of the photoelectron peak

in a doublet. This is explained by the interaction of two angular momentum in a single electron: one arising from the intrinsic electron spin and a second angular momenta arising because the electrons orbit around the nucleus[11]. The total angular momentum (j) in this case is the sum of both vectors and is added to the notation of the XPS peak to differentiate the doublet. In this works, spin-orbit splitting is observed for p orbitals of Sulfur, $2p_{1/2}$ and $2p_{3/2}$, and d orbitals of Molybdenum, $3d_{3/2}$ and $3d_{5/2}$ doublets

Another effect that can be observed in XPS spectra are **satellite** peaks. These peaks with relatively low intensity have their origin in different electron energy losses that occur during the photoelectron generation process.

Since we are dealing with electrons, if the sample is not conductive enough it might get positively charged. **Charging effects** are usually corrected by using a known reference peak to recalibrate the spectra**.** As carbon is present in all our samples, the C 1s peak at 284.6 eV was used to calibrate the spectra

Analysis of the spectral peak energies, intensities, and fine structure are used to deduce the composition and often the chemical state of the sample surface species. By fitting the XPS spectra, a precise understanding of the surface "chemistry" can be achieved. However, the fitting procedure requires a good understanding of the chemical structure at the surface sample, to avoid overseen the contribution of different chemical states during the fitting procedure.

For the instrumentations, XPS analyses were performed with a ULVAC PHI 5000 VersaProbe II spectrometer using AlKα X-ray radiation (1,486.6 eV). The residual pressure inside the analysis chamber was of 7×10^{-8} Pa. A fixed analyzer pass energy of 23 eV was used for core level scans, leading to an overall energy resolution of 0.6 eV. Survey spectra were captured at pass energy of 117 eV. All spectra were referenced against an internal signal, typically by adjusting the C 1s level peak at a binding energy of 284.6 eV. A specific four contacts sample holder manufactured by ULVAC-PHI was used to probe the stability of thin doped layers under Ultra High Vacuum condition. The XPS spectra were fitted using the Multipak software in which a Shirly background is assumed and the fitting peaks of the experimental spectra are defined by a combination of Gaussian (80%) and Lorentzian (20%) distribution. The measurements were performed on bulk materials for pristine PBDTTT-c and Mo(tfd-COCF3)3 and on TLM samples for doped layers before and after aging.

These measurements were possible thanks to Dr. Anass Benayad, to whom I am very grateful.

EPR measurements

Electron paramagnetic resonance (EPR) spectra were recorded with a Bruker EMX spectrometer operating at X-band frequency with an ER-4116 dual mode cavity. The measurements were done at room temperature and obtained with the following parameters: 9.655 GHz frequency, 31.65 mW power, and 3.0 G modulation amplitude. To allow direct comparison and avoid morphology variation due to the substrate, the EPR sample is a cutout part of TLM flexible devices inserted in a 3 mm internal diameter quartz EPR tube. The film is deposited by spin-coating. PEN does not give any EPR signal in the given conditions.

APPENDIX B: CALCULATION OF DOPANT MOLAR RATIO

Here, we demonstrate the equation used to calculate the dopant concentration in mol%.

The dopant concentration indicates the number of dopant molecules n_d per monomer of polymer n_p:

$$\frac{n_d}{n_p} \qquad \textbf{Equation B.1}$$

where n_d and n_p depend on the dopant and polymer weight (m_d and m_p) and their respective molecular weight (M_d and M_p) as follows:

$$n_d = \frac{m_d}{M_d} \qquad \textbf{Equation B.2}$$

$$n_p = \frac{m_p}{M_p} \qquad \textbf{Equation B.3}$$

Since the doping is performed in solution, we write m_d and m_p as a function of the polymer and dopant concentration (C_p and C_d) as well as their respective volumes (V_p and V_d):

$$m_d = C_d V_d \qquad \textbf{Equation B.4}$$

$$m_p = C_p V_p \qquad \textbf{Equation B.5}$$

Finally, the dopant concentration in mol% was calculated with the following relation:

$$\text{Dopant molar ratio (mol\%)}: \frac{C_d V_d M_p}{C_p V_p M_d} \qquad \textbf{Equation B.6}$$

APPENDIX C: ADDITIONAL XPS DATA

Pristine PBDTTT-c

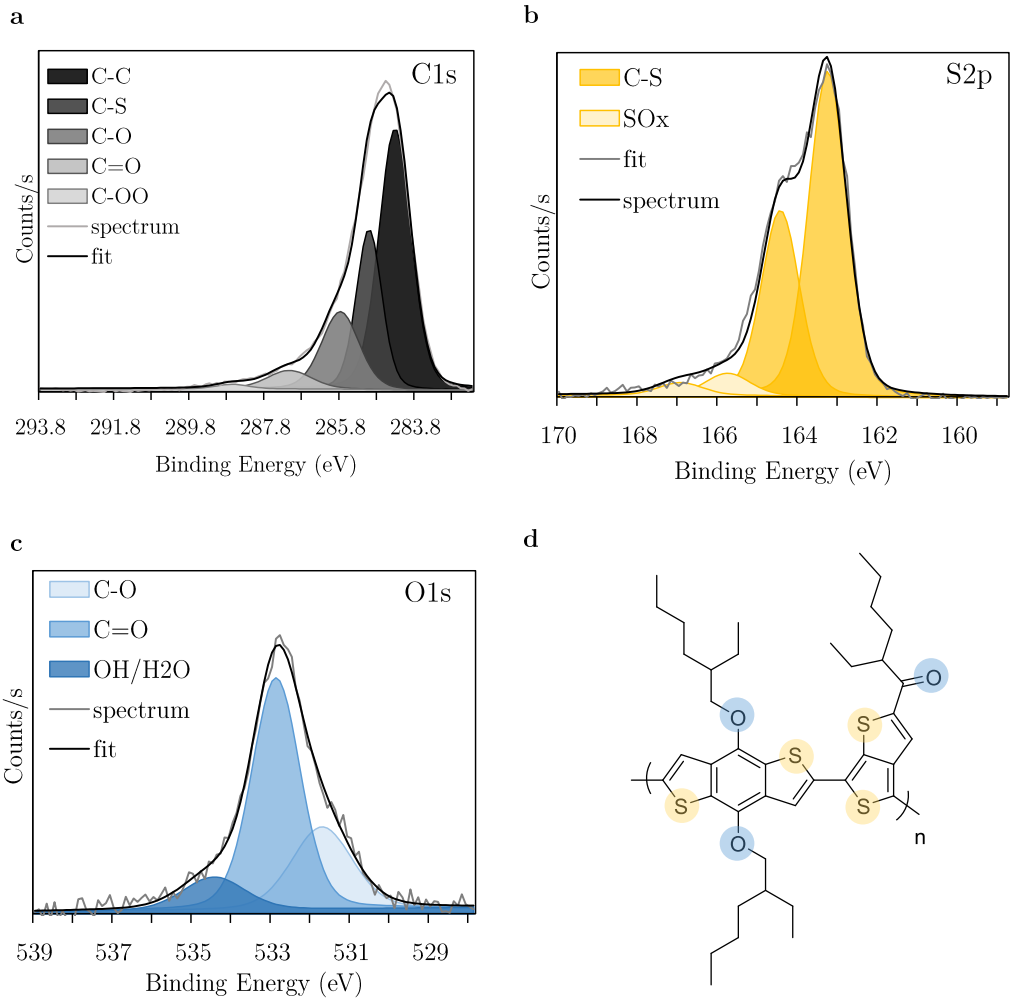

Figure C.1 – XPS spectra of pristine PBDTTT-c: C1s (a), S2p (b), O1s (c) peak region, and chemical structure (d).

Pristine Mo(tdf-COCF$_3$)$_3$

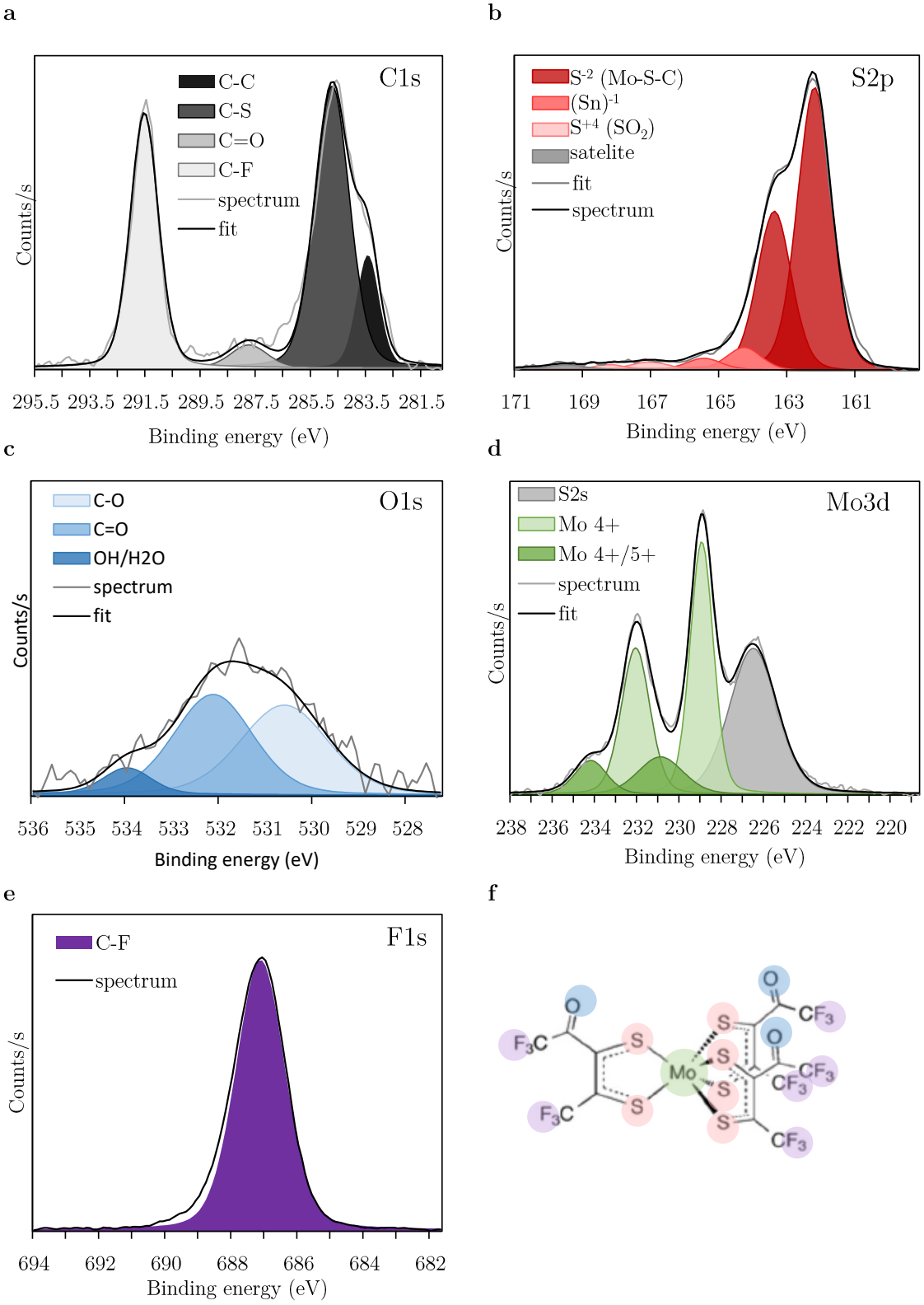

Figure C.2 – XPS spectra for pristine Mo(tfd-COCF$_3$)$_3$: C1s (a), S2p (b), O1s (c), Mo3d (d), F1s (e) peak region, and chemical structure (f).

Additional spectra for PBDTTT-c:Mo(tdf-$COCF_3$)$_3$

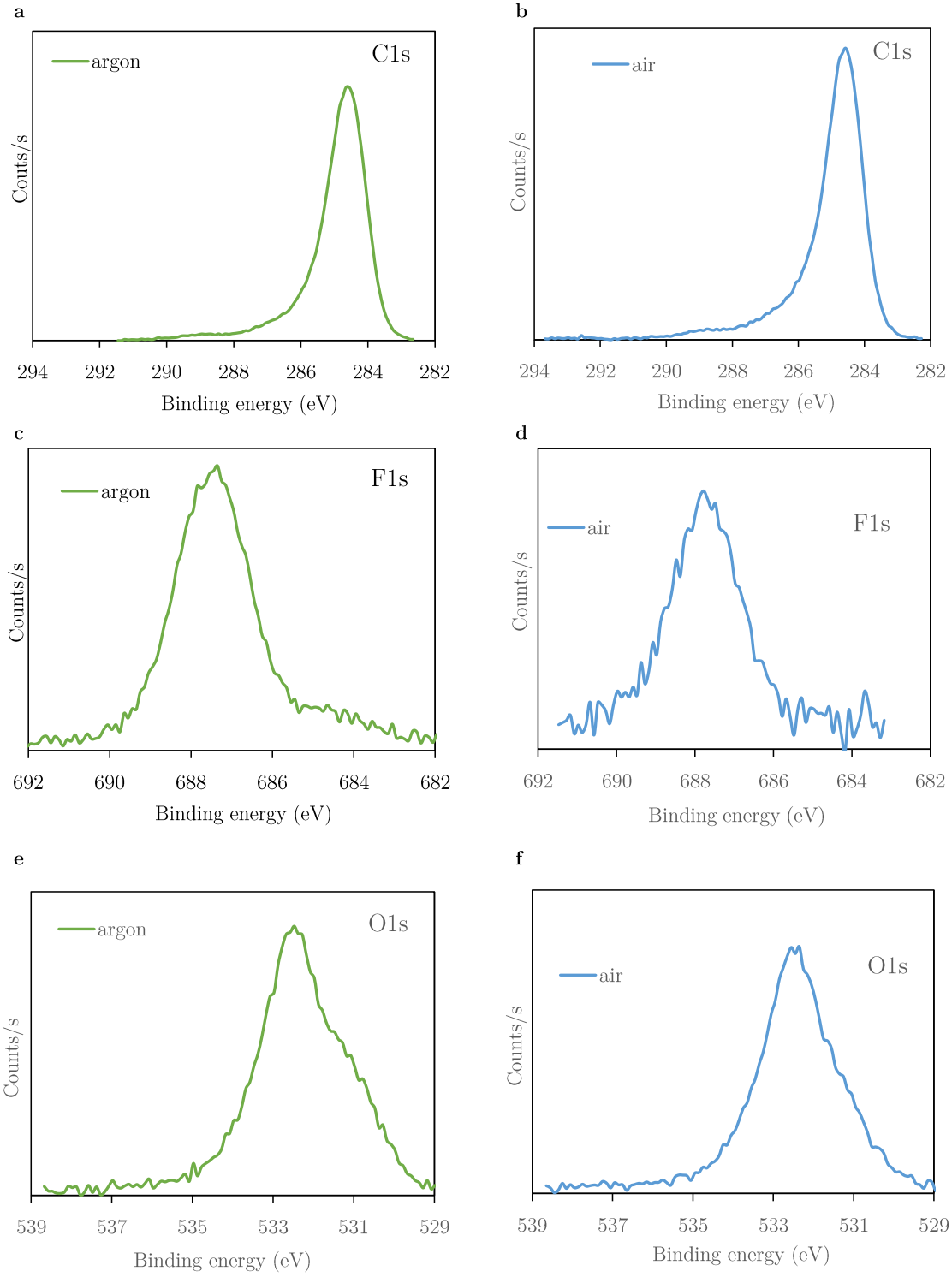

Figure C.3 –XPS spectra of PBDTTT-c:Mo(tfd-$COCF_3$)$_3$ doped layers (25 mol% dopant, 15 nm) exposed to argon atmosphere (a, c, e) and ambient air (b, d, f) overnight: C1s, F1s, and O1s peak region.

Peak fitting details

Table C.1 - XPS peak fitting information for the **Mo3d** peak region of bulk Mo(tfd-$COCF_3)_3$ and PBDTTT-c: Mo(tfd-$COCF_3)_3$ doped layers (25%mol, 15 nm) before and after air exposure.

$Mo(tfd\text{-}COCF_3)_3$					
Peak region Mo3d	S2s	Mo^{4+}		$Mo^{4+/5+}$	
		$(3d_{5/2})$	$(3d_{3/2})$	$(3d_{5/2})$	$(3d_{3/2})$
Position	226.7	229.1	232.3	231.3	234.4
FWHM	2.66	1.30	1.60	2.53	1.80

PBDTTT-c :$Mo(tfd\text{-}COCF_3)_3$ – 20h argon						
Peak region Mo3d	S2s Dopant	S2s polymer	Mo^{4+}		$Mo^{4+/5+}$	
			$(3d_{5/2})$	$(3d_{3/2})$	$(3d_{5/2})$	$(3d_{3/2})$
Position	226.7	228.1	229.4	232.6	231.0	234.1
FWHM	2.66	1.9	1.44	1.54	1.90	2.00
PBDTTT-c :$Mo(tfd\text{-}COCF_3)_3$ -20h air						
Peak region Mo3d	S2s Dopant	S2s polymer	Mo^{4+}		Mo^{6+}	
			$(3d_{5/2})$	$(3d_{3/2})$	$(3d_{5/2})$	$(3d_{3/2})$
Position	226.7	228.1	230.0	233.1	232.0	235.1
FWHM	2.66	1.80	1.30	1.40	1.66	1.76

Table C.2 - XPS peak fitting information for the **S2p** peak region of bulk materials ($Mo(tfd\text{-}COCF_3)_3$, PBDTTT-c, and for PBDTTT-c: $Mo(tfd\text{-}COCF_3)_3$ doped layers (25%mol. 15 nm) before and after air exposure.

PBDTTT-c							
Peak region	C-S				SOx		
S2p	($Sp_{3/2}$)		($Sp_{1/2}$)		($Sp_{3/2}$)		($Sp_{1/2}$)
Position	163.7		164.9		166.3		167.4
FWHM	1.20		1.20		1.30		1.30
$Mo(tfd\text{-}COCF_3)_3$							
Peak region	S^{2-} (S-Mo-C)		$(Sn)^{2-}$		S^{4+} (SO_2)		'Satellite'
S2p	($Sp_{3/2}$)	($Sp_{1/2}$)	($Sp_{3/2}$)	($Sp_{1/2}$)	($Sp_{3/2}$)	($Sp_{1/2}$)	
Position	162.3	163.5	164.6	165.8	167.3	168.5	169.5
FWHM	1.30	1.30	1.30	1.30	1.18	1.18	2.00

PBDTTT-c :$Mo(tfd\text{-}COCF_3)_3$ – 20h argon					
Peak region	C-S		Mo-S-C		'Satellite '
S2p	($Sp_{3/2}$)	($Sp_{1/2}$)	($Sp_{3/2}$)	($Sp_{1/2}$)	
Position	163.7	164.9	162.3	163.5	168.2
FWHM	1.0	1.0	1.3	1.3	1.5
PBDTTT-c :$Mo(tfd\text{-}COCF_3)_3$ – 20h air					
Peak region	C-S		Mo-S-C		'Satellite '
S2p	($Sp_{3/2}$)	($Sp_{1/2}$)	($Sp_{3/2}$)	($Sp_{1/2}$)	
Position	163.7	164.9	162.3	163.5	168.0
FWHM	1.0	1.0	1.3	1.3	1.5

REFERENCES

(1) Millikan, R. A. A Direct Photoelectric Determination of Planck's "h." *Phys. Rev.* **1916**, *7* (3), 355–388. https://doi.org/10.1103/PhysRev.7.355.

(2) Sworakowski, J. How Accurate Are Energies of HOMO and LUMO Levels in Small-Molecule Organic Semiconductors Determined from Cyclic Voltammetry or Optical Spectroscopy? *Synth. Met.* **2018**, *235*, 125–130. https://doi.org/10.1016/j.synthmet.2017.11.013.

(3) Willems, R. E. M.; Weijtens, C. H. L.; Vries, X. de; Coehoorn, R.; Janssen, R. A. J. Relating Frontier Orbital Energies from Voltammetry and Photoelectron Spectroscopy to the Open-Circuit Voltage of Organic Solar Cells. *Adv. Energy Mater.* **2019**, *9* (10), 1803677. https://doi.org/10.1002/aenm.201803677.

(4) Elgrishi, N.; Rountree, K. J.; McCarthy, B. D.; Rountree, E. S.; Eisenhart, T. T.; Dempsey, J. L. A Practical Beginner's Guide to Cyclic Voltammetry. *J. Chem. Educ.* **2018**, *95* (2), 197–206. https://doi.org/10.1021/acs.jchemed.7b00361.

(5) Gritzner, G.; Kuta, J. Recommendations on Reporting Electrode Potentials in Nonaqueous Solvents (Recommendations 1983). *Pure Appl. Chem.* **1984**, *56* (4), 461–466. https://doi.org/10.1351/pac198456040461.

(6) Cardona, C. M.; Li, W.; Kaifer, A. E.; Stockdale, D.; Bazan, G. C. Electrochemical Considerations for Determining Absolute Frontier Orbital Energy Levels of Conjugated Polymers for Solar Cell Applications. *Adv. Mater.* **2011**, *23* (20), 2367–2371. https://doi.org/10.1002/adma.201004554.

(7) Lim, S. H. N.; McKenzie, D. R.; Bilek, M. M. M. Van Der Pauw Method for Measuring Resistivity of a Plane Sample with Distant Boundaries. *Rev. Sci. Instrum.* **2009**, *80* (7), 075109. https://doi.org/10.1063/1.3183503.

(8) Reeves, G. K.; Harrison, H. B. Obtaining the Specific Contact Resistance from Transmission Line Model Measurements. *IEEE Electron Device Lett.* **1982**, *3* (5), 111–113. https://doi.org/10.1109/EDL.1982.25502.

(9) Norrman, K.; Madsen, M. V.; Gevorgyan, S. A.; Krebs, F. C. Degradation Patterns in Water and Oxygen of an Inverted Polymer Solar Cell. *J. Am. Chem. Soc.* **2010**, *132* (47), 16883–16892. https://doi.org/10.1021/ja106299g.

(10) Tietze, M. L.; Rose, B. D.; Schwarze, M.; Fischer, A.; Runge, S.; Blochwitz-Nimoth, J.; Lüssem, B.; Leo, K.; Brédas, J.-L. Passivation of Molecular N-Doping: Exploring the Limits of Air Stability. *Adv. Funct. Mater.* **2016**, *26* (21), 3730–3737. https://doi.org/10.1002/adfm.201505092.

(11) Knop-Gericke, A. X-Ray Photoelectron Spectroscopy. An Introduction to Principles and Practices. By Paul van Der Heide. *Angew. Chem. Int. Ed.* **2012**, *51* (37), 9218–9218. https://doi.org/10.1002/anie.201205395.

(12) Castle, J. E. Practical Surface Analysis by Auger and X-Ray Photoelectron Spectroscopy. D. Briggs and M. P. Seah (Editors). John Wiley and Sons Ltd, Chichester, 1983, 533 Pp., £44.50. *Surf. Interface Anal.* **1984**, *6* (6), 302–302. https://doi.org/10.1002/sia.740060611.